ΛK and Ξ^{-}K$^{\pm}$ Femtoscopy in Pb-Pb Collisions at $\sqrt{s_{\mathrm{NN}}} = 2.76$ TeV from the LHC ALICE Collaboration

Dissertation

Presented in Partial Fulfillment of the Requirements for the Degree Doctor of Philosophy in the Graduate School of The Ohio State University

By

Jesse T. Buxton, M.S., B.S.

Graduate Program in Physics

The Ohio State University

2019

Dissertation Committee:

Professor Thomas J. Humanic, Advisor

Professor Michael Lisa

Professor Ulrich Heinz

Professor Fengyuan Yang

Abstract

The first measurements of the scattering parameters of ΛK pairs in all three charge combinations (ΛK^{+}, ΛK^{-}, and ΛK^{0}_{S}) are presented. The measurements are achieved through a femtoscopic analysis of ΛK correlations in Pb-Pb collisions at $\sqrt{s_{NN}} = 2.76$ TeV from ALICE at the LHC. The femtoscopic correlations result from strong final-state interactions, and are fit with a parametrization allowing for both the characterization of the pair emission source and the measurement of the scattering parameters for the particle pairs. Extensive studies with the THERMINATOR 2 event generator allow for the description of the non-femtoscopic background, resulting mainly from collective effects, with unprecedented precision. Furthermore, this model together with HIJING simulations are used to account for contributions from residual correlations induced by feed-down from resonances. In the experimental data, a striking difference is observed in pairs with low relative momenta ($k^{*} \lesssim 100$ MeV) between the ΛK^{+} and ΛK^{-} correlations, and the ΛK^{0}_{S} system exhibits features between the two. The ΛK^{+} system exhibits a negative real component of the scattering parameter ($\Re f_{0}$), while those of the ΛK^{-} and ΛK^{0}_{S} are positive, although the magnitude of that of the ΛK^{0}_{S} is smaller than that of the ΛK^{-}. The results suggest an effect arising from different quark-antiquark interactions between the pairs ($s\bar{s}$ in ΛK^{+} and $u\bar{u}$ in ΛK^{-}), or from different net strangeness for each system (S=0 for ΛK^{+}, and S=-2 for ΛK^{-}). To investigate further, we conduct a $\Xi^{-}K^{\pm}$ analysis, for which preliminary results are shown. Finally, the ΛK systems exhibit source radii larger than expected from extrapolation from identical particle femtoscopic studies. This effect is interpreted as resulting from the separation in space-time of the single-particle Λ and K source distributions.

To my parents. I would not be who I am without your unwavering and unconditional love. Without you, I would not have the confidence to pursue my dreams. I love you.

Acknowledgments

I would like to thank my advisor, Tom Humanic, for his support and guidance over the past years. Thank you for allowing me the freedom to pursue whatever I found interesting, while keeping me from wandering too far off track. I would also like to thank Mike Lisa for offering additional support and guidance whenever I needed. Thank you to the entire Ohio State Heavy-Ion Physics Research Group, it has been a pleasure working with you all. In particular, I would like to thank Jai Salzwedel for his mentorship; I could not have launched my analysis so quickly without you. I would also like to thank Andrew Kubera for coming to my aid whenever I had any programming or computer issues. Thank you to the ALICE collaboration and the ALICE femtoscopy group. In particular, thank you Laura Fabbietti for all of your help in maturing my analysis. Thank you to all of those at CERN who welcomed me with open arms. I would like to thank The Ohio State University. Go Bucks! Thank you to my friends and family for your love and support. Thank you Bernoulli, you are the best friend anyone could ask for, and such a good and handsome boy.

Finally, thank you to my beautiful fiancée, Faith, for your patience and understanding as I navigated through this stressful time in my life. You are wonderful. I love you.

Vita

November 2, 1987 .... Born - Columbus, Ohio

June 2006 .... Diploma, Worthington Kilbourne High School, Columbus, Ohio

August 2010 .... B.S., Physics and Astronomy, Magna Cum Laude, Honors, Research Distinction,
The Ohio State University, Columbus, Ohio

September 2011 - December 2013 .... Graduate Teaching Associate,
The Ohio State University, Columbus, Ohio

May 2014 .... M.S., Physics,
The Ohio State University, Columbus, Ohio

Janunary 2014 - present .... Graduate Research Associate,
The Ohio State University, Columbus, Ohio

Publications

Shreyasi Acharya et al. "Measuring $\mathrm{K^0_SK^{\pm}}$ interactions using pp collisions at $\sqrt{s} = 7$ TeV". *Phys. Lett.* B790 (2019), pp. 22–34. DOI: 10.1016/j.physletb.2018.12.033. arXiv: 1809.07899 [nucl-ex].

Shreyasi Acharya et al. "Υ suppression at forward rapidity in Pb-Pb collisions at $\sqrt{s_{\mathrm{NN}}} = 5.02$ TeV". *Phys. Lett.* B790 (2019), pp. 89–101. DOI: 10.1016/j.physletb.2018.11.067. arXiv: 1805.04387 [nucl-ex].

Shreyasi Acharya et al. “Centrality and pseudorapidity dependence of the charged-particle multiplicity density in XeXe collisions at $\sqrt{s_{\rm NN}}$ =5.44TeV”. *Phys. Lett.* B790 (2019), pp. 35–48. DOI: 10.1016/j.physletb.2018.12.048. arXiv: 1805.04432 [nucl-ex].

Shreyasi Acharya et al. “Multiplicity dependence of (anti-)deuteron production in pp collisions at $\sqrt{s} = 7$ TeV” (2019). arXiv: 1902.09290 [nucl-ex].

Shreyasi Acharya et al. “Event-shape engineering for the D-meson elliptic flow in mid-central Pb-Pb collisions at $\sqrt{s_{\rm NN}} = 5.02$ TeV”. *JHEP* 02 (2019), p. 150. DOI: 10.1007/JHEP02(2019)150. arXiv: 1809.09371 [nucl-ex].

Shreyasi Acharya et al. “Azimuthal anisotropy of heavy-flavour decay electrons in p-Pb collisions at $\sqrt{s_{NN}} = 5.02$ TeV”. *Phys. Rev. Lett.* 122.7 (2019), p. 072301. DOI: 10.1103/PhysRevLett.122.072301. arXiv: 1805.04367 [nucl-ex].

Shreyasi Acharya et al. “Direct photon production at low transverse momentum in proton-proton collisions at $\sqrt{\mathbf{s}} = \mathbf{2.76}$ and 8 TeV”. *Phys. Rev.* C99.2 (2019), p. 024912. DOI: 10.1103/PhysRevC.99.024912. arXiv: 1803.09857 [nucl-ex].

Shreyasi Acharya et al. “Calibration of the photon spectrometer PHOS of the ALICE experiment” (2019). arXiv: 1902.06145 [physics.ins-det].

Shreyasi Acharya et al. “Measurement of dielectron production in central Pb-Pb collisions at $\sqrt{s_{\rm NN}} = 2.76$ TeV”. *Phys. Rev.* C99.2 (2019), p. 024002. DOI: 10.1103/PhysRevC.99.024002. arXiv: 1807.00923 [nucl-ex].

Shreyasi Acharya et al. “p-p, p-Λ and Λ-Λ correlations studied via femtoscopy in pp reactions at $\sqrt{s} = 7$ TeV”. *Phys. Rev.* C99.2 (2019), p. 024001. DOI: 10.1103/PhysRevC.99.024001. arXiv: 1805.12455 [nucl-ex].

Shreyasi Acharya et al. “Direct photon elliptic flow in Pb-Pb collisions at $\sqrt{s_{NN}} = 2.76$ TeV”. *Phys. Lett.* B789 (2019), pp. 308–322. DOI: 10.1016/j.physletb.2018.11.039. arXiv: 1805.04403 [nucl-ex].

Shreyasi Acharya et al. “Multiplicity dependence of light-flavor hadron production in pp collisions at $\sqrt{s} = 7$ TeV”. *Phys. Rev.* C99.2 (2019), p. 024906. DOI: 10.1103/PhysRevC.99.024906. arXiv: 1807.11321 [nucl-ex].

Shreyasi Acharya et al. “Suppression of $\Lambda(1520)$ resonance production in central Pb-Pb collisions at $\sqrt{s_{\rm NN}} = 2.76$ TeV”. *Phys. Rev.* C99 (2019), p. 024905. DOI: 10.1103/PhysRevC.99.024905. arXiv: 1805.04361 [nucl-ex].

Shreyasi Acharya et al. "Study of J/ψ azimuthal anisotropy at forward rapidity in Pb-Pb collisions at $\sqrt{s_{\rm NN}}$ = 5.02 TeV". *JHEP* 02 (2019), p. 012. DOI: 10.1007/JHEP02(2019)012. arXiv: 1811.12727 [nucl-ex].

Shreyasi Acharya et al. "Charged jet cross section and fragmentation in proton-proton collisions at $\sqrt{s}$ = 7 TeV". *Phys. Rev.* D99.1 (2019), p. 012016. DOI: 10.1103/PhysRevD.99.012016. arXiv: 1809.03232 [nucl-ex].

Shreyasi Acharya et al. "Measurement of D^0, D^+, D^{*+} and D_s^+ production in pp collisions at $\sqrt{s}$ = **5.02 TeV** with ALICE" (2019). arXiv: 1901.07979 [nucl-ex].

Shreyasi Acharya et al. "Event-shape and multiplicity dependence of freeze-out radii in pp collisions at $\sqrt{s} = 7$ TeV" (2019). arXiv: 1901.05518 [nucl-ex].

Shreyasi Acharya et al. "Transverse momentum spectra and nuclear modification factors of charged particles in Xe-Xe collisions at $\sqrt{s_{\rm NN}} = 5.44$ TeV". *Phys. Lett.* B788 (2019), pp. 166–179. DOI: 10.1016/j.physletb.2018.10.052. arXiv: 1805.04399 [nucl-ex].

Shreyasi Acharya et al. "Dielectron and heavy-quark production in inelastic and high-multiplicity protonproton collisions at $\sqrt{s_{NN}}$ = 13TeV". *Phys. Lett.* B788 (2019), pp. 505–518. DOI: 10.1016/j.physletb.2018.11.009. arXiv: 1805.04407 [hep-ex].

Shreyasi Acharya et al. "Real-time data processing in the ALICE High Level Trigger at the LHC" (2018). arXiv: 1812.08036 [physics.ins-det].

Shreyasi Acharya et al. "Charged-particle pseudorapidity density at mid-rapidity in p-Pb collisions at $\sqrt{s_{\rm NN}} = 8.16$ TeV" (2018). arXiv: 1812.01312 [nucl-ex].

Shreyasi Acharya et al. "Jet fragmentation transverse momentum measurements from di-hadron correlations in $\sqrt{s}$ = 7 TeV pp and $\sqrt{s_{\rm NN}}$ = 5.02 TeV p-Pb collisions". *Submitted to: JHEP* (2018). arXiv: 1811.09742 [nucl-ex].

S. Acharya et al. "Transverse momentum spectra and nuclear modification factors of charged particles in pp, p-Pb and Pb-Pb collisions at the LHC". *JHEP* 11 (2018), p. 013. DOI: 10.1007/JHEP11(2018)013. arXiv: 1802.09145 [nucl-ex].

S. Acharya et al. "Measurement of D^0, D^+, D^{*+} and D_s^+ production in Pb-Pb collisions at $\sqrt{s_{\rm NN}}$ = 5.02 TeV". *JHEP* 10 (2018), p. 174. DOI: 10.1007/JHEP10(2018)174. arXiv: 1804.09083 [nucl-ex].

Shreyasi Acharya et al. "Medium modification of the shape of small-radius jets in central Pb-Pb collisions at $\sqrt{s_{\rm NN}}$ = 2.76 TeV". *JHEP* 10 (2018), p. 139. DOI: 10.1007/JHEP10(2018)139. arXiv: 1807.06854 [nucl-ex].

Shreyasi Acharya et al. “Inclusive J/ψ production in XeXe collisions at $\sqrt{s_{NN}} = 5.44$ TeV”. *Phys. Lett.* B785 (2018), pp. 419–428. DOI: 10.1016/j.physletb.2018.08.047. arXiv: 1805.04383 [nucl-ex].

S. Acharya et al. “Azimuthally-differential pion femtoscopy relative to the third harmonic event plane in Pb-Pb collisions at $\sqrt{s_{\mathrm{NN}}} = 2.76$ TeV”. *Phys. Lett.* B785 (2018), pp. 320–331. DOI: 10.1016/j.physletb.2018.06.042. arXiv: 1803.10594 [nucl-ex].

Shreyasi Acharya et al. “Neutral pion and η meson production at mid-rapidity in Pb-Pb collisions at $\sqrt{s_{NN}} = 2.76$ TeV”. *Phys. Rev.* C98.4 (2018), p. 044901. DOI: 10.1103/PhysRevC.98.044901. arXiv: 1803.05490 [nucl-ex].

Shreyasi Acharya et al. “Measurements of low-p_T electrons from semileptonic heavy-flavour hadron decays at mid-rapidity in pp and Pb-Pb collisions at $\sqrt{s_{\mathrm{NN}}} = 2.76$ TeV”. *JHEP* 10 (2018), p. 061. DOI: 10.1007/JHEP10(2018)061. arXiv: 1805.04379 [nucl-ex].

Shreyasi Acharya et al. “Λ_{c}^{+} production in Pb-Pb collisions at $\sqrt{s_{NN}} = 5.02$ TeV”. *Submitted to: Phys. Lett.* (2018). arXiv: 1809.10922 [nucl-ex].

Shreyasi Acharya et al. “Dielectron production in proton-proton collisions at $\sqrt{s} = 7$ TeV”. *JHEP* 09 (2018), p. 064. DOI: 10.1007/JHEP09(2018)064. arXiv: 1805.04391 [hep-ex].

S. Acharya et al. “Anisotropic flow in Xe-Xe collisions at $\sqrt{\mathbf{s}_{\mathrm{NN}}} = \mathbf{5.44}$ TeV”. *Phys. Lett.* B784 (2018), pp. 82–95. DOI: 10.1016/j.physletb.2018.06.059. arXiv: 1805.01832 [nucl-ex].

Shreyasi Acharya et al. “Energy dependence of exclusive J/ψ photoproduction off protons in ultra-peripheral p-Pb collisions at $\sqrt{s_{\mathrm{NN}}} = 5.02$ TeV” (2018). arXiv: 1809.03235 [nucl-ex].

S. Acharya et al. “Anisotropic flow of identified particles in Pb-Pb collisions at $\sqrt{s}_{\mathrm{NN}} = 5.02$ TeV”. *JHEP* 09 (2018), p. 006. DOI: 10.1007/JHEP09(2018)006. arXiv: 1805.04390 [nucl-ex].

Shreyasi Acharya et al. “Constraints on jet quenching in p-Pb collisions at $\sqrt{\mathbf{s_{NN}}}$ = 5.02 TeV measured by the event-activity dependence of semi-inclusive hadron-jet distributions”. *Phys. Lett.* B783 (2018), pp. 95–113. DOI: 10.1016/j.physletb.2018.05.059. arXiv: 1712.05603 [nucl-ex].

Shreyasi Acharya et al. “Neutral pion and η meson production in p-Pb collisions at $\sqrt{s_{\mathrm{NN}}} = 5.02$ TeV”. *Eur. Phys. J.* C78.8 (2018), p. 624. DOI: 10.1140/epjc/s10052-018-6013-8. arXiv: 1801.07051 [nucl-ex].

Shreyasi Acharya et al. “Inclusive J/ψ production at forward and backward rapidity in p-Pb collisions at $\sqrt{s_{\mathrm{NN}}} = 8.16$ TeV”. *JHEP* 07 (2018), p. 160. DOI: 10.1007/JHEP07(2018)160. arXiv: 1805.04381 [nucl-ex].

S. Acharya et al. “Energy dependence and fluctuations of anisotropic flow in Pb-Pb collisions at $\sqrt{s_{\mathrm{NN}}} = 5.02$ and 2.76 TeV”. *JHEP* 07 (2018), p. 103. DOI: 10.1007/JHEP07(2018)103. arXiv: 1804.02944 [nucl-ex].

S. Acharya et al. “Measurement of the inclusive J/ ψ polarization at forward rapidity in pp collisions at $\sqrt{\mathbf{s}} = \mathbf{8}$ TeV”. *Eur. Phys. J.* C78.7 (2018), p. 562. DOI: 10.1140/epjc/s10052-018-6027-2. arXiv: 1805.04374 [hep-ex].

S. Acharya et al. “ϕ meson production at forward rapidity in Pb-Pb collisions at $\sqrt{s_{\mathrm{NN}}} = 2.76$ TeV”. *Eur. Phys. J.* C78.7 (2018), p. 559. DOI: 10.1140/epjc/s10052-018-6034-3. arXiv: 1804.08906 [nucl-ex].

S. Acharya et al. “First measurement of Ξ_{c}^{0} production in pp collisions at $\sqrt{\mathbf{s}} = 7$ TeV”. *Phys. Lett.* B781 (2018), pp. 8–19. DOI: 10.1016/j.physletb.2018.03.061. arXiv: 1712.04242 [hep-ex].

S. Acharya et al. “Longitudinal asymmetry and its effect on pseudorapidity distributions in Pb-Pb collisions at $\sqrt{s_{NN}} = 2.76$ TeV”. *Phys. Lett.* B781 (2018), pp. 20–32. DOI: 10.1016/j.physletb.2018.03.051. arXiv: 1710.07975 [nucl-ex].

Shreyasi Acharya et al. “Prompt and non-prompt J/ψ production and nuclear modification at mid-rapidity in pPb collisions at $\sqrt{\mathbf{s}_{\mathrm{NN}}} = \mathbf{5.02}$ TeV”. *Eur. Phys. J.* C78.6 (2018), p. 466. DOI: 10.1140/epjc/s10052-018-5881-2. arXiv: 1802.00765 [nucl-ex].

Shreyasi Acharya et al. “Analysis of the apparent nuclear modification in peripheral Pb-Pb collisions at 5.02 TeV” (2018). arXiv: 1805.05212 [nucl-ex].

Shreyasi Acharya et al. “Production of the $\rho(770)^{0}$ meson in pp and Pb-Pb collisions at $\sqrt{s_{NN}} = 2.76$ TeV” (2018). arXiv: 1805.04365 [nucl-ex].

Shreyasi Acharya et al. “Two particle differential transverse momentum and number density correlations in p-Pb and Pb-Pb at the LHC” (2018). arXiv: 1805.04422 [nucl-ex].

S. Acharya et al. “Measurement of Z^{0}-boson production at large rapidities in Pb-Pb collisions at $\sqrt{s_{\mathrm{NN}}} = 5.02$ TeV”. *Phys. Lett.* B780 (2018), pp. 372–383. DOI: 10.1016/j.physletb.2018.03.010. arXiv: 1711.10753 [nucl-ex].

S. Acharya et al. “Search for collectivity with azimuthal J/ψ-hadron correlations in high multiplicity p-Pb collisions at $\sqrt{s_{\mathrm{NN}}} = 5.02$ and 8.16 TeV”. *Phys. Lett.* B780

(2018), pp. 7–20. DOI: 10.1016/j.physletb.2018.02.039. arXiv: 1709.06807 [nucl-ex].

Shreyasi Acharya et al. "Λ_c^+ production in pp collisions at $\sqrt{s} = 7$ TeV and in p-Pb collisions at $\sqrt{s_{NN}} = 5.02$ TeV". *JHEP* 04 (2018), p. 108. DOI: 10.1007/JHEP04(2018)108. arXiv: 1712.09581 [nucl-ex].

Shreyasi Acharya et al. "Production of ^{4}He and $^4\overline{\mathrm{He}}$ in Pb-Pb collisions at $\sqrt{s_{\mathrm{NN}}}$ = 2.76 TeV at the LHC". *Nucl. Phys.* A971 (2018), pp. 1–20. DOI: 10.1016/j.nuclphysa.2017.12.004. arXiv: 1710.07531 [nucl-ex].

Shreyasi Acharya et al. "π^0 and η meson production in proton-proton collisions at $\sqrt{s} = 8$ TeV". *Eur. Phys. J.* C78.3 (2018), p. 263. DOI: 10.1140/epjc/s10052-018-5612-8. arXiv: 1708.08745 [hep-ex].

Shreyasi Acharya et al. "*D*-meson azimuthal anisotropy in midcentral Pb-Pb collisions at $\sqrt{\mathbf{s_{NN}}} = \mathbf{5.02}$ TeV". *Phys. Rev. Lett.* 120.10 (2018), p. 102301. DOI: 10.1103/PhysRevLett.120.102301. arXiv: 1707.01005 [nucl-ex].

Shreyasi Acharya et al. "Production of deuterons, tritons, ^{3}He nuclei and their antinuclei in pp collisions at $\sqrt{s} = 0.9$, 2.76 and 7 TeV". *Phys. Rev.* C97.2 (2018), p. 024615. DOI: 10.1103/PhysRevC.97.024615. arXiv: 1709.08522 [nucl-ex].

Shreyasi Acharya et al. "Systematic studies of correlations between different order flow harmonics in Pb-Pb collisions at $\sqrt{s_{NN}} = 2.76$ TeV". *Phys. Rev.* C97.2 (2018), p. 024906. DOI: 10.1103/PhysRevC.97.024906. arXiv: 1709.01127 [nucl-ex].

Shreyasi Acharya et al. "The ALICE Transition Radiation Detector: construction, operation, and performance". *Nucl. Instrum. Meth.* A881 (2018), pp. 88–127. DOI: 10.1016/j.nima.2017.09.028. arXiv: 1709.02743 [physics.ins-det].

Shreyasi Acharya et al. "Constraining the magnitude of the Chiral Magnetic Effect with Event Shape Engineering in Pb-Pb collisions at $\sqrt{s_{\mathrm{NN}}} = 2.76$ TeV". *Phys. Lett.* B777 (2018), pp. 151–162. DOI: 10.1016/j.physletb.2017.12.021. arXiv: 1709.04723 [nucl-ex].

D. Adamov et al. "J/ψ production as a function of charged-particle pseudorapidity density in p-Pb collisions at $\sqrt{s_{NN}} = 5.02$ TeV". *Phys. Lett.* B776 (2018), pp. 91–104. DOI: 10.1016/j.physletb.2017.11.008. arXiv: 1704.00274 [nucl-ex].

S. Acharya et al. "First measurement of jet mass in PbPb and pPb collisions at the LHC". *Phys. Lett.* B776 (2018), pp. 249–264. DOI: 10.1016/j.physletb.2017.11.044. arXiv: 1702.00804 [nucl-ex].

Shreyasi Acharya et al. “Kaon femtoscopy in Pb-Pb collisions at $\sqrt{s_{NN}} = 2.76$ TeV”. *Phys. Rev.* C96.6 (2017), p. 064613. DOI: 10.1103/PhysRevC.96.064613. arXiv: 1709.01731 [nucl-ex].

Shreyasi Acharya et al. “Relative particle yield fluctuations in Pb-Pb collisions at $\sqrt{\mathbf{s}_{\mathbf{NN}}} = \mathbf{2.76}$ TeV”. *Submitted to: Eur. Phys. J.* (2017). arXiv: 1712.07929 [nucl-ex].

Shreyasi Acharya et al. “J/ψ elliptic flow in Pb-Pb collisions at $\sqrt{s_{NN}} = 5.02$ TeV”. *Phys. Rev. Lett.* 119.24 (2017), p. 242301. DOI: 10.1103/PhysRevLett.119.242301. arXiv: 1709.05260 [nucl-ex].

S. Acharya et al. “Charged-particle multiplicity distributions over a wide pseudorapidity range in proton-proton collisions at $\sqrt{s} = 0.9$, 7, and 8 TeV”. *Eur. Phys. J.* C77.12 (2017), p. 852. DOI: 10.1140/epjc/s10052-017-5412-6. arXiv: 1708.01435 [hep-ex].

Shreyasi Acharya et al. “Measuring $K^0_S K^\pm$ interactions using Pb-Pb collisions at $\sqrt{s_{NN}} = 2.76$ TeV”. *Phys. Lett.* B774 (2017), pp. 64–77. DOI: 10.1016/j.physletb.2017.09.009. arXiv: 1705.04929 [nucl-ex].

Shreyasi Acharya et al. “Linear and non-linear flow modes in Pb-Pb collisions at $\sqrt{s_{NN}} = 2.76$ TeV”. *Phys. Lett.* B773 (2017), pp. 68–80. DOI: 10.1016/j.physletb.2017.07.060. arXiv: 1705.04377 [nucl-ex].

Shreyasi Acharya et al. “Measurement of deuteron spectra and elliptic flow in PbPb collisions at $\sqrt{s_{NN}} = 2.76$ TeV at the LHC”. *Eur. Phys. J.* C77.10 (2017), p. 658. DOI: 10.1140/epjc/s10052-017-5222-x. arXiv: 1707.07304 [nucl-ex].

Jaroslav Adam et al. “Centrality dependence of the pseudorapidity density distribution for charged particles in Pb-Pb collisions at $\sqrt{s_{NN}} = 5.02$ TeV”. *Phys. Lett.* B772 (2017), pp. 567–577. DOI: 10.1016/j.physletb.2017.07.017. arXiv: 1612.08966 [nucl-ex].

Shreyasi Acharya et al. “Searches for transverse momentum dependent flow vector fluctuations in Pb-Pb and p-Pb collisions at the LHC”. *JHEP* 09 (2017), p. 032. DOI: 10.1007/JHEP09(2017)032. arXiv: 1707.05690 [nucl-ex].

Jaroslav Adam et al. “Evolution of the longitudinal and azimuthal structure of the near-side jet peak in Pb-Pb collisions at $\sqrt{s_{NN}} = 2.76$ TeV”. *Phys. Rev.* C96.3 (2017), p. 034904. DOI: 10.1103/PhysRevC.96.034904. arXiv: 1609.06667 [nucl-ex].

Jaroslav Adam et al. “Anomalous evolution of the near-side jet peak shape in Pb-Pb collisions at $\sqrt{s_{NN}} = 2.76$ TeV”. *Phys. Rev. Lett.* 119.10 (2017), p. 102301. DOI: 10.1103/PhysRevLett.119.102301. arXiv: 1609.06643 [nucl-ex].

Jaroslav Adam et al. “Insight into particle production mechanisms via angular correlations of identified particles in pp collisions at $\sqrt{\mathrm{s}} = 7$ TeV”. *Eur. Phys. J.* C77.8 (2017), p. 569. DOI: 10.1140/epjc/s10052-017-5129-6. arXiv: 1612.08975 [nucl-ex].

Shreyasi Acharya et al. “Measurement of D-meson production at mid-rapidity in pp collisions at $\sqrt{s} = 7$ TeV”. *Eur. Phys. J.* C77.8 (2017), p. 550. DOI: 10.1140/epjc/s10052-017-5090-4. arXiv: 1702.00766 [hep-ex].

Jaroslav Adam et al. “Measurement of electrons from beauty-hadron decays in p-Pb collisions at $\sqrt{s_{\mathrm{NN}}} = 5.02$ TeV and Pb-Pb collisions at $\sqrt{s_{\mathrm{NN}}} = 2.76$ TeV”. *JHEP* 07 (2017), p. 052. DOI: 10.1007/JHEP07(2017)052. arXiv: 1609.03898 [nucl-ex].

Shreyasi Acharya et al. “Production of muons from heavy-flavour hadron decays in p-Pb collisions at $\sqrt{s_{\mathbf{NN}}} = \mathbf{5.02}$ TeV”. *Phys. Lett.* B770 (2017), pp. 459–472. DOI: 10.1016/j.physletb.2017.03.049. arXiv: 1702.01479 [nucl-ex].

Shreyasi Acharya et al. “Energy dependence of forward-rapidity J/ψ and ψ(2S) production in pp collisions at the LHC”. *Eur. Phys. J.* C77.6 (2017), p. 392. DOI: 10.1140/epjc/s10052-017-4940-4. arXiv: 1702.00557 [hep-ex].

Dagmar Adamova et al. “Production of $\Sigma(1385)^{\pm}$ and $\Xi(1530)^0$ in p-Pb collisions at $\sqrt{s_{NN}} = 5.02$ TeV”. *Eur. Phys. J.* C77.6 (2017), p. 389. DOI: 10.1140/epjc/s10052-017-4943-1. arXiv: 1701.07797 [nucl-ex].

Jaroslav Adam et al. “$\mathrm{K}^*(892)^0$ and $\phi(1020)$ meson production at high transverse momentum in pp and Pb-Pb collisions at $\sqrt{s_{\mathrm{NN}}} = 2.76$ TeV”. *Phys. Rev.* C95.6 (2017), p. 064606. DOI: 10.1103/PhysRevC.95.064606. arXiv: 1702.00555 [nucl-ex].

Dagmar Adamova et al. “Azimuthally differential pion femtoscopy in Pb-Pb collisions at $\sqrt{s_{\mathrm{NN}}} = 2.76$ TeV”. *Phys. Rev. Lett.* 118.22 (2017), p. 222301. DOI: 10.1103/PhysRevLett.118.222301. arXiv: 1702.01612 [nucl-ex].

Jaroslav Adam et al. “Measurement of the production of high-p_{T} electrons from heavy-flavour hadron decays in Pb-Pb collisions at $\sqrt{s_{\mathrm{NN}}} = 2.76$ TeV”. *Phys. Lett.* B771 (2017), pp. 467–481. DOI: 10.1016/j.physletb.2017.05.060. arXiv: 1609.07104 [nucl-ex].

Shreyasi Acharya et al. “Production of π^0 and η mesons up to high transverse momentum in pp collisions at 2.76 TeV”. *Eur. Phys. J.* C77.5 (2017). [Eur. Phys. J.C77,no.9,586(2017)], p. 339. DOI: 10.1140/epjc/s10052-017-5144-7,10.1140/epjc/s10052-017-4890-x. arXiv: 1702.00917 [hep-ex].

Jaroslav Adam et al. “ϕ-meson production at forward rapidity in p-Pb collisions at $\sqrt{s_{\mathrm{NN}}} = 5.02$ TeV and in pp collisions at $\sqrt{s} = 2.76$ TeV”. *Phys. Lett.* B768

(2017), pp. 203–217. DOI: 10.1016/j.physletb.2017.01.074. arXiv: 1506.09206 [nucl-ex].

Jaroslav Adam et al. "Enhanced production of multi-strange hadrons in high-multiplicity proton-proton collisions". *Nature Phys.* 13 (2017), pp. 535–539. DOI: 10.1038/nphys4111. arXiv: 1606.07424 [nucl-ex].

Jaroslav Adam et al. "Flow dominance and factorization of transverse momentum correlations in Pb-Pb collisions at the LHC". *Phys. Rev. Lett.* 118.16 (2017), p. 162302. DOI: 10.1103/PhysRevLett.118.162302. arXiv: 1702.02665 [nucl-ex].

Jaroslav Adam et al. "Measurement of azimuthal correlations of D mesons and charged particles in pp collisions at $\sqrt{s} = 7$ TeV and p-Pb collisions at $\sqrt{s_{\rm NN}} = 5.02$ TeV". *Eur. Phys. J.* C77.4 (2017), p. 245. DOI: 10.1140/epjc/s10052-017-4779-8. arXiv: 1605.06963 [nucl-ex].

Jaroslav Adam et al. "J/ψ suppression at forward rapidity in Pb-Pb collisions at $\sqrt{\mathbf{s_{NN}}} = \mathbf{5.02}$ TeV". *Phys. Lett.* B766 (2017), pp. 212–224. DOI: 10.1016/j.physletb.2016.12.064. arXiv: 1606.08197 [nucl-ex].

Jaroslav Adam et al. "Determination of the event collision time with the ALICE detector at the LHC". *Eur. Phys. J. Plus* 132.2 (2017), p. 99. DOI: 10.1140/epjp/i2017-11279-1. arXiv: 1610.03055 [physics.ins-det].

Jaroslav Adam et al. "W and Z boson production in p-Pb collisions at $\sqrt{s_{NN}} = 5.02$ TeV". *JHEP* 02 (2017), p. 077. DOI: 10.1007/JHEP02(2017)077. arXiv: 1611.03002 [nucl-ex].

Jaroslav Adam et al. "Charged-particle multiplicities in protonproton collisions at $\sqrt{s} = 0.9$ to 8TeV". *Eur. Phys. J.* C77.1 (2017), p. 33. DOI: 10.1140/epjc/s10052-016-4571-1. arXiv: 1509.07541 [nucl-ex].

Jaroslav Adam et al. "Jet-like correlations with neutral pion triggers in pp and central PbPb collisions at 2.76 TeV". *Phys. Lett.* B763 (2016), pp. 238–250. DOI: 10.1016/j.physletb.2016.10.048. arXiv: 1608.07201 [nucl-ex].

Jaroslav Adam et al. "*D*-meson production in *p*-Pb collisions at $\sqrt{s_{NN}}$ =5.02 TeV and in pp collisions at $\sqrt{s}$ =7 TeV". *Phys. Rev.* C94.5 (2016), p. 054908. DOI: 10.1103/PhysRevC.94.054908. arXiv: 1605.07569 [nucl-ex].

Jaroslav Adam et al. "Pseudorapidity dependence of the anisotropic flow of charged particles in Pb-Pb collisions at $\sqrt{s_{\rm NN}} = 2.76$ TeV". *Phys. Lett.* B762 (2016), pp. 376–388. DOI: 10.1016/j.physletb.2016.07.017. arXiv: 1605.02035 [nucl-ex].

Jaroslav Adam et al. “Correlated event-by-event fluctuations of flow harmonics in Pb-Pb collisions at $\sqrt{s_{NN}} = 2.76$ TeV”. *Phys. Rev. Lett.* 117 (2016), p. 182301. DOI: 10.1103/PhysRevLett.117.182301. arXiv: 1604.07663 [nucl-ex].

Jaroslav Adam et al. “Higher harmonic flow coefficients of identified hadrons in Pb-Pb collisions at $\sqrt{s_{NN}} = 2.76$ TeV”. *JHEP* 09 (2016), p. 164. DOI: 10.1007/JHEP09(2016)164. arXiv: 1606.06057 [nucl-ex].

Jaroslav Adam et al. “Measurement of transverse energy at midrapidity in Pb-Pb collisions at $\sqrt{s_{NN}} = 2.76$ TeV”. *Phys. Rev.* C94.3 (2016), p. 034903. DOI: 10.1103/PhysRevC.94.034903. arXiv: 1603.04775 [nucl-ex].

Jaroslav Adam et al. “Multiplicity dependence of charged pion, kaon, and (anti)proton production at large transverse momentum in p-Pb collisions at $\sqrt{s_{\mathbf{NN}}} = 5.02$ TeV”. *Phys. Lett.* B760 (2016), pp. 720–735. DOI: 10.1016/j.physletb.2016.07.050. arXiv: 1601.03658 [nucl-ex].

Jaroslav Adam et al. “Elliptic flow of electrons from heavy-flavour hadron decays at mid-rapidity in Pb-Pb collisions at $\sqrt{s_{\mathrm{NN}}} = 2.76$ TeV”. *JHEP* 09 (2016), p. 028. DOI: 10.1007/JHEP09(2016)028. arXiv: 1606.00321 [nucl-ex].

J. Adam et al. “Measurement of D-meson production versus multiplicity in p-Pb collisions at $\sqrt{s_{\mathrm{NN}}} = 5.02$ TeV”. *JHEP* 08 (2016), p. 078. DOI: 10.1007/JHEP08(2016)078. arXiv: 1602.07240 [nucl-ex].

Jaroslav Adam et al. “Multi-strange baryon production in p-Pb collisions at $\sqrt{s_{\mathbf{NN}}} = 5.02$ TeV”. *Phys. Lett.* B758 (2016), pp. 389–401. DOI: 10.1016/j.physletb.2016.05.027. arXiv: 1512.07227 [nucl-ex].

Jaroslav Adam et al. “Centrality dependence of ψ(2S) suppression in p-Pb collisions at $\sqrt{s_{\mathbf{NN}}} = 5.02$ TeV”. *JHEP* 06 (2016), p. 050. DOI: 10.1007/JHEP06(2016)050. arXiv: 1603.02816 [nucl-ex].

Jaroslav Adam et al. “Centrality dependence of the charged-particle multiplicity density at midrapidity in Pb-Pb collisions at $\sqrt{s_{NN}} = 5.02$ TeV”. *Phys. Rev. Lett.* 116.22 (2016), p. 222302. DOI: 10.1103/PhysRevLett.116.222302. arXiv: 1512.06104 [nucl-ex].

Jaroslav Adam et al. “Measurement of an excess in the yield of J/ψ at very low p_{T} in Pb-Pb collisions at $\sqrt{s_{NN}} = 2.76$ TeV”. *Phys. Rev. Lett.* 116.22 (2016), p. 222301. DOI: 10.1103/PhysRevLett.116.222301. arXiv: 1509.08802 [nucl-ex].

Jaroslav Adam et al. “Differential studies of inclusive J/ and (2S) production at forward rapidity in Pb-Pb collisions at $\sqrt{s_{NN}} = 2.76$ TeV”. *JHEP* 05 (2016), p. 179. DOI: 10.1007/JHEP05(2016)179. arXiv: 1506.08804 [nucl-ex].

Jaroslav Adam et al. “Particle identification in ALICE: a Bayesian approach”. *Eur. Phys. J. Plus* 131.5 (2016), p. 168. DOI: 10.1140/epjp/i2016-16168-5. arXiv: 1602.01392 [physics.data-an].

Jaroslav Adam et al. “Multipion Bose-Einstein correlations in pp,p -Pb, and Pb-Pb collisions at energies available at the CERN Large Hadron Collider”. *Phys. Rev.* C93.5 (2016), p. 054908. DOI: 10.1103/PhysRevC.93.054908. arXiv: 1512.08902 [nucl-ex].

Jaroslav Adam et al. “Centrality dependence of charged jet production in pPb collisions at $\sqrt{s_{\mathrm{NN}}} = 5.02$ TeV”. *Eur. Phys. J.* C76.5 (2016), p. 271. DOI: 10.1140/epjc/s10052-016-4107-8. arXiv: 1603.03402 [nucl-ex].

Jaroslav Adam et al. “Production of K* (892)^0 and ϕ (1020) in pPb collisions at $\sqrt{s_{\mathrm{NN}}}$ = 5.02 TeV”. *Eur. Phys. J.* C76.5 (2016), p. 245. DOI: 10.1140/epjc/s10052-016-4088-7. arXiv: 1601.07868 [nucl-ex].

Jaroslav Adam et al. “Charge-dependent flow and the search for the chiral magnetic wave in Pb-Pb collisions at $\sqrt{s_{NN}} = 2.76$ TeV”. *Phys. Rev.* C93.4 (2016), p. 044903. DOI: 10.1103/PhysRevC.93.044903. arXiv: 1512.05739 [nucl-ex].

Jaroslav Adam et al. “Inclusive quarkonium production at forward rapidity in pp collisions at $\sqrt{s} = 8$ TeV”. *Eur. Phys. J.* C76.4 (2016), p. 184. DOI: 10.1140/epjc/s10052-016-3987-y. arXiv: 1509.08258 [hep-ex].

Jaroslav Adam et al. “Anisotropic flow of charged particles in Pb-Pb collisions at $\sqrt{s_{\mathrm{NN}}} = 5.02$ TeV”. *Phys. Rev. Lett.* 116.13 (2016), p. 132302. DOI: 10.1103/PhysRevLett.116.132302. arXiv: 1602.01119 [nucl-ex].

Jaroslav Adam et al. “Event shape engineering for inclusive spectra and elliptic flow in Pb-Pb collisions at $\sqrt{s_{\mathrm{NN}}} = 2.76$ TeV”. *Phys. Rev.* C93.3 (2016), p. 034916. DOI: 10.1103/PhysRevC.93.034916. arXiv: 1507.06194 [nucl-ex].

Jaroslav Adam et al. “Centrality dependence of the nuclear modification factor of charged pions, kaons, and protons in Pb-Pb collisions at $\sqrt{s_{NN}} = 2.76$ TeV”. *Phys. Rev.* C93.3 (2016), p. 034913. DOI: 10.1103/PhysRevC.93.034913. arXiv: 1506.07287 [nucl-ex].

Jaroslav Adam et al. “Measurement of D$_s^+$ production and nuclear modification factor in Pb-Pb collisions at $\sqrt{s_{\mathrm{NN}}} = 2.76$ TeV”. *JHEP* 03 (2016), p. 082. DOI: 10.1007/JHEP03(2016)082. arXiv: 1509.07287 [nucl-ex].

Jaroslav Adam et al. “Transverse momentum dependence of D-meson production in Pb-Pb collisions at $\sqrt{s_{\mathrm{NN}}} = 2.76$ TeV”. *JHEP* 03 (2016), p. 081. DOI: 10.1007/JHEP03(2016)081. arXiv: 1509.06888 [nucl-ex].

Jaroslav Adam et al. “Measurement of electrons from heavy-flavour hadron decays in p-Pb collisions at $\sqrt{s_{\mathrm{NN}}} = 5.02$ TeV”. *Phys. Lett.* B754 (2016), pp. 81–93. DOI: 10.1016/j.physletb.2015.12.067. arXiv: 1509.07491 [nucl-ex].

Jaroslav Adam et al. “Direct photon production in Pb-Pb collisions at $\sqrt{s_{\mathrm{NN}}} = 2.76$ TeV”. *Phys. Lett.* B754 (2016), pp. 235–248. DOI: 10.1016/j.physletb.2016.01.020. arXiv: 1509.07324 [nucl-ex].

Jaroslav Adam et al. “Centrality evolution of the charged-particle pseudorapidity density over a broad pseudorapidity range in Pb-Pb collisions at $\sqrt{s_{\mathrm{NN}}} = 2.76$ TeV”. *Phys. Lett.* B754 (2016), pp. 373–385. DOI: 10.1016/j.physletb.2015.12.082. arXiv: 1509.07299 [nucl-ex].

Jaroslav Adam et al. “$^{3}_{\Lambda}\mathrm{H}$ and $^{3}_{\overline{\Lambda}}\overline{\mathrm{H}}$ production in Pb-Pb collisions at $\sqrt{s_{\mathrm{NN}}} = 2.76$ TeV”. *Phys. Lett.* B754 (2016), pp. 360–372. DOI: 10.1016/j.physletb.2016.01.040. arXiv: 1506.08453 [nucl-ex].

Jaroslav Adam et al. “Production of light nuclei and anti-nuclei in pp and Pb-Pb collisions at energies available at the CERN Large Hadron Collider”. *Phys. Rev.* C93.2 (2016), p. 024917. DOI: 10.1103/PhysRevC.93.024917. arXiv: 1506.08951 [nucl-ex].

Jaroslav Adam et al. “Multiplicity and transverse momentum evolution of charge-dependent correlations in pp, pPb, and PbPb collisions at the LHC”. *Eur. Phys. J.* C76.2 (2016), p. 86. DOI: 10.1140/epjc/s10052-016-3915-1. arXiv: 1509.07255 [nucl-ex].

Jaroslav Adam et al. “Pseudorapidity and transverse-momentum distributions of charged particles in protonproton collisions at $\sqrt{s} = 13$TeV”. *Phys. Lett.* B753 (2016), pp. 319–329. DOI: 10.1016/j.physletb.2015.12.030. arXiv: 1509.08734 [nucl-ex].

Jaroslav Adam et al. “Azimuthal anisotropy of charged jet production in $\sqrt{s_{\mathrm{NN}}} = 2.76$ TeV Pb-Pb collisions”. *Phys. Lett.* B753 (2016), pp. 511–525. DOI: 10.1016/j.physletb.2015.12.047. arXiv: 1509.07334 [nucl-ex].

Jaroslav Adam et al. “Elliptic flow of muons from heavy-flavour hadron decays at forward rapidity in PbPb collisions at $\sqrt{s_{\mathrm{NN}}} = 2.76$ TeV”. *Phys. Lett.* B753 (2016), pp. 41–56. DOI: 10.1016/j.physletb.2015.11.059. arXiv: 1507.03134 [nucl-ex].

Jaroslav Adam et al. “Forward-central two-particle correlations in p-Pb collisions at $\sqrt{s_{\mathrm{NN}}} = 5.02$ TeV”. *Phys. Lett.* B753 (2016), pp. 126–139. DOI: 10.1016/j.physletb.2015.12.010. arXiv: 1506.08032 [nucl-ex].

Jaroslav Adam et al. “Centrality dependence of pion freeze-out radii in Pb-Pb collisions at $\sqrt{s}_{NN} = 2.76$ TeV”. *Phys. Rev.* C93.2 (2016), p. 024905. DOI: 10.1103/PhysRevC.93.024905. arXiv: 1507.06842 [nucl-ex].

Jaroslav Adam et al. “Study of cosmic ray events with high muon multiplicity using the ALICE detector at the CERN Large Hadron Collider”. *JCAP* 1601 (2016), p. 032. DOI: 10.1088/1475-7516/2016/01/032. arXiv: 1507.07577 [astro-ph.HE].

Jaroslav Adam et al. “Search for weakly decaying $\overline{\Lambda\mathrm{n}}$ and $\Lambda\Lambda$ exotic bound states in central Pb-Pb collisions at $\sqrt{s_{\mathrm{NN}}} = 2.76$ TeV”. *Phys. Lett.* B752 (2016), pp. 267–277. DOI: 10.1016/j.physletb.2015.11.048. arXiv: 1506.07499 [nucl-ex].

Jaroslav Adam et al. “Coherent ψ(2S) photo-production in ultra-peripheral Pb Pb collisions at $\sqrt{s}_{\mathrm{NN}} = 2.76$TeV”. *Phys. Lett.* B751 (2015), pp. 358–370. DOI: 10.1016/j.physletb.2015.10.040. arXiv: 1508.05076 [nucl-ex].

Jaroslav Adam et al. “Centrality dependence of high-p$_T$ D meson suppression in Pb-Pb collisions at $\sqrt{s_{\mathrm{NN}}} = 2.76$ TeV”. *JHEP* 11 (2015). [Addendum: JHEP06,032(2017)], p. 205. DOI: 10.1007/JHEP11(2015)205, 10.1007/JHEP06(2017)032. arXiv: 1506.06604 [nucl-ex].

Jaroslav Adam et al. “Centrality dependence of inclusive J/ production in p-Pb collisions at $\sqrt{s_{\mathrm{NN}}} = 5.02$ TeV”. *JHEP* 11 (2015), p. 127. DOI: 10.1007/JHEP11(2015)127. arXiv: 1506.08808 [nucl-ex].

Jaroslav Adam et al. “One-dimensional pion, kaon, and proton femtoscopy in Pb-Pb collisions at $\sqrt{s_{\mathrm{NN}}}$ =2.76 TeV”. *Phys. Rev.* C92.5 (2015), p. 054908. DOI: 10.1103/PhysRevC.92.054908. arXiv: 1506.07884 [nucl-ex].

Jaroslav Adam et al. “Measurement of jet quenching with semi-inclusive hadron-jet distributions in central Pb-Pb collisions at $\sqrt{s_{\mathrm{NN}}} = 2.76$ TeV”. *JHEP* 09 (2015), p. 170. DOI: 10.1007/JHEP09(2015)170. arXiv: 1506.03984 [nucl-ex].

Jaroslav Adam et al. “Measurement of charm and beauty production at central rapidity versus charged-particle multiplicity in proton-proton collisions at $\sqrt{s} = 7$ TeV”. *JHEP* 09 (2015), p. 148. DOI: 10.1007/JHEP09(2015)148. arXiv: 1505.00664 [nucl-ex].

Jaroslav Adam et al. “Coherent ^{0} photoproduction in ultra-peripheral Pb-Pb collisions at $\sqrt{s_{\mathrm{NN}}} = 2.76$ TeV”. *JHEP* 09 (2015), p. 095. DOI: 10.1007/JHEP09(2015)095. arXiv: 1503.09177 [nucl-ex].

Jaroslav Adam et al. “Precision measurement of the mass difference between light nuclei and anti-nuclei”. *Nature Phys.* 11.10 (2015), pp. 811–814. DOI: 10.1038/nphys3432. arXiv: 1508.03986 [nucl-ex].

Jaroslav Adam et al. “Measurement of charged jet production cross sections and nuclear modification in p-Pb collisions at $\sqrt{s_{\mathrm{NN}}} = 5.02$ TeV”. *Phys. Lett.* B749 (2015), pp. 68–81. DOI: 10.1016/j.physletb.2015.07.054. arXiv: 1503.00681 [nucl-ex].

Jaroslav Adam et al. “Inclusive, prompt and non-prompt J/ψ production at mid-rapidity in Pb-Pb collisions at $\sqrt{s_{\mathrm{NN}}} = 2.76$ TeV”. *JHEP* 07 (2015), p. 051. DOI: 10.1007/JHEP07(2015)051. arXiv: 1504.07151 [nucl-ex].

Jaroslav Adam et al. “Rapidity and transverse-momentum dependence of the inclusive J/ψ nuclear modification factor in p-Pb collisions at $\sqrt{s_{N\ N}} = 5.02$ TeV”. *JHEP* 06 (2015), p. 055. DOI: 10.1007/JHEP06(2015)055. arXiv: 1503.07179 [nucl-ex].

Jaroslav Adam et al. “Centrality dependence of particle production in p-Pb collisions at $\sqrt{s_{\mathrm{NN}}}$= 5.02 TeV”. *Phys. Rev.* C91.6 (2015), p. 064905. DOI: 10.1103/PhysRevC.91.064905. arXiv: 1412.6828 [nucl-ex].

Jaroslav Adam et al. “Measurement of pion, kaon and proton production in protonproton collisions at $\sqrt{s} = 7$ TeV”. *Eur. Phys. J.* C75.5 (2015), p. 226. DOI: 10.1140/epjc/s10052-015-3422-9. arXiv: 1504.00024 [nucl-ex].

Jaroslav Adam et al. “Forward-backward multiplicity correlations in pp collisions at $\sqrt{s} = 0.9, 2.76$ and 7 TeV”. *JHEP* 05 (2015), p. 097. DOI: 10.1007/JHEP05(2015)097. arXiv: 1502.00230 [nucl-ex].

Jaroslav Adam et al. “Measurement of dijet k_T in pPb collisions at $\sqrt{s}_{NN}$=5.02 TeV”. *Phys. Lett.* B746 (2015), pp. 385–395. DOI: 10.1016/j.physletb.2015.05.033. arXiv: 1503.03050 [nucl-ex].

Jaroslav Adam et al. “Measurement of jet suppression in central Pb-Pb collisions at $\sqrt{s_{\mathrm{NN}}} = 2.76$ TeV”. *Phys. Lett.* B746 (2015), pp. 1–14. DOI: 10.1016/j.physletb.2015.04.039. arXiv: 1502.01689 [nucl-ex].

J. Adam et al. “Two-pion femtoscopy in p-Pb collisions at $\sqrt{s_{\mathrm{NN}}} = 5.02$ TeV”. *Phys. Rev.* C91 (2015), p. 034906. DOI: 10.1103/PhysRevC.91.034906. arXiv: 1502.00559 [nucl-ex].

J. T. Buxton and T. J. Humanic. “Hadronic observables from a hadronic rescattering model in $Pb + Pb$ collisions at $\sqrt{s_{NN}} = 2.76$ TeV” (2014). arXiv: 1410.0924 [nucl-ex].

Jesse Buxton and Barbara S. Ryden. “Relative Orientation of Pairs of Spiral Galaxies in the Sloan Digital Sky Survey”. *Astrophys. J.* 756 (2012), p. 135. DOI: 10.1088/0004-637X/756/2/135. arXiv: 1207.4032 [astro-ph.CO].

Fields of Study

Major Field: Physics

Table of Contents

List of Tables

List of Figures

Chapter 1: Introduction

Relativistic heavy-ion physics is an exciting field in which we seek to better understand the fundamental strong force, as well as gain insight into the origins of our Universe, through smashing together particles accelerated to nearly the speed of light. Through the collisions of relativistic heavy-ions, we are able to study strongly interacting matter at energy densities far exceeding that of normal matter. At sufficiently high energy densities, hadronic matter undergoes a transition to a novel state, known as the Quark-Gluon Plasma (QGP), consisting of liberated quarks and gluons. Such a state is exceedingly interesting, as quarks and gluons are typically confined to color neutral objects, and bare color charge has never been directly observed experimentally. The QGP is believed to have existed in the early Universe the first few microseconds after the Big Bang; as such, the collisions of relativistic heavy-ions are often referred to as "Little Bangs".

The theory describing the strong interaction, Quantum Chromodynamics (QCD), is notoriously difficult to handle except in select regimes of weak coupling, where perturbative methods may be applied. The study of the QGP allows us to investigate the strong interaction in the non-perturbative region where it acts strongly! A main goal of the field is to gain a better understanding of normal matter through the reconstruction of the QCD phase diagram. Thus, through the study of the highly complex and chaotic system created in heavy-ion collisions, we seek to gain insight into the basic features of QCD in normal state.

We are, unfortunately, not able to observe the QGP directly. Therefore, we must rely on specific signatures which reveal its presence, and indirect methods and observables to probe it. One such method of probing the system created in heavy-ion collisions is femtoscopy, which is the the topic of this paper. Femtoscopy allows us to study the space-time structure of the evolving system at the femtometer scale (10^{-15} m). We also emphasize the fact that, through the femtoscopic technique, one may extract interaction scattering parameters which would be difficult, if not impossible, to measure otherwise.

The organization of the paper is as follows. Chapter 2 serves as a broad introduction to the physics of relativistic heavy-ion collisions. I will discuss some basic aspects of QCD, and introduce more thoroughly the QGP. Furthermore, this chapter will explore the evolution of the system created in heavy-ion collisions, and present some experimental signatures of the QGP. Chapter 3 will describe the experimental LHC accelerator and the ALICE collaboration, focusing on detectors utilized in this analysis. Chapter 4 will introduce the theoretical groundwork and formalism of femtoscopy, as well as present a few select experimental results utilizing the femtoscopic method. Chapter 5 will explain the experimental details involved in extracting data for use in this analysis, including the event selection, particle reconstruction and identification, formation of the particle pairs, and the construction of the experimental femtoscopic correlation functions. In Chapter 6, the fit method used to model the experimental correlation functions is presented. This includes the treatment of momentum resolution corrections, modeling of contributions from residual correlations induced by feed-down from resonances, and the treatment of the non-femtoscopic backgrounds. This section also includes a discussion of the systematic uncertainties involved in this analysis. Chapter 7 will present and discuss the results from this analysis, and Chapter 8 will summarize and conclude the thesis.

Chapter 2: Relativistic Heavy-Ion Collisions and the Quark-Gluon Plasma

In this section, the basic features of Quantum Chromodynamics and the Quark-Gluon Plasma are introduced. The evolution of the system created in relativistic heavy-ion collisions is described, and a sample of important observables signifying the creation of the QGP and probing its properties is presented.

2.1 Quantum Chromodynamics

Quantum chromodynamics (QCD) is the theory of the strong interaction between quarks and gluons. Quarks are subatomic particles which combine to form hadrons, and gluons are massless bosons exchanged by quarks interacting via the strong force. Its name, QCD, originates from the *color charge* which characterizes its fundamental particles. The color charge in QCD is analogous to the electric charge in the more familiar theory of the electromagnetic interaction, *quantum electrodynamics* (QED). However, within QED there is only one electric charge, whereas in QCD there are three colored charges. Furthermore, in QED many particles carry electric charge, while in QCD no naturally occurring particles carry color. In other words, isolated color has never been observed experimentally, and quarks are always confined to colorless (color-white) composite objects known as hadrons. In addition to this *confinement* property, QCD also exhibits *asymptotic freedom*, both of which are described more below.

Quarks are fermions, which come in six flavors (up (u), down (d), strange (s), charm (c), bottom (b), and top (t)), and three colored degrees of freedom (red (R), blue (B), green (G)). Every particle (be it a quark or a composite object) has a corresponding antiparticle, with the same mass and spin, but opposite quantum numbers (e.g. charge, color, etc.). Elementary hadrons are colorless composite particles made of two or three quarks held together by the strong force, and may be classified as mesons or baryons. Mesons are two quark states, which must be composed of a quark and antiquark, with color and anticolor combining to be colorless. Baryons are composed of three quarks (or three antiquarks), with colors red, green, and blue (antired, antigreen, and antiblue), resulting again in a colorless hadron. Quarks are electrically charged, with fractional charges $(+2/3)e$ (u, c, t), $(-1/3)e$ (d, s, b). However, when discussing the strong interaction with QCD, it is the color charge, not the electric charge, which is relevant.

In QCD, gluons are the spin-1 gauge bosons which mediate the interaction. Just as the electromagnetic force is mediated by the exchange of photons, the strong force is mediated by the exchange of gluons. In the fundamental process $q \to q + g$, the color of the quark may change (its flavor, however, may not). Since color is always conserved, the gluon must carry away the difference in color, which reveals that gluons are *bicolored*. Thus, we have another important difference between QED and QCD: in QED, the photon is electrically neutral, while in QCD, the gluons themselves carry color. As a result, gluons couple directly to other gluons, which makes QCD much more complicated than QED.

The direct gluon-gluon coupling is what essentially gives QCD its interesting properties of asymptotic freedom and confinement. QCD predicts a running of the coupling constant, α_s, which depends on the momentum transferred, Q^2, in the interaction as

$$\alpha_s(Q^2) \propto \frac{1}{\ln(Q^2/\Lambda^2_{QCD})} \xrightarrow{Q^2 \to \infty} 0 \tag{2.1}$$

where Λ (≈ 200 MeV) is a constant defining the scale. The coupling constant exhibits a logarithmic decrease with increasing Q^2. Thus, we see that at large momenta (corresponding to short distances) the coupling becomes small, while for small momenta (corresponding to large distance) the coupling is large. It is oftentimes difficult to perform dynamical calculations in QCD using methods from QED, due to the running of the QCD coupling constant. In QED, the electromagnetic coupling constant is small ($\alpha = 1/137$), while the strong coupling (α_s) constant might be of the order of one. Calculations in QCD may be performed perturbatively (pQCD) only when the coupling is weak, i.e. only for large values of Q^2 (small distances).

From the running of the coupling constant, Eq. 2.1, we can identify the two interesting features of QCD mentioned at the beginning of this section. First, the extremely strong nature of the interaction with increasing separation in related to color confinement. Color confinement is indicated experimentally and by lattice calculations, but has not been formally proven. The second feature, the property of asymptotic freedom, is visible as $\alpha_s \to 0$ as $Q^2 \to \infty$. This means that at very high energies, or short distances, quarks behave as free particles.

2.2 Quark Gluon Plasma

The *Quark-Gluon Plasma* (QGP) is a form of matter in which liberated quarks and gluons, no longer bound to color-white hadrons, comprise the degrees of freedom. Based on the property of asymptotic freedom introduced in Sec. 2.1, many expected that the high energy densities achieved in relativistic heavy-ion collisions would produce a weakly interacting gas of quarks and gluons [1, 2]. However, the experimental data [3–6] contradicted this expectation, as strong hydrodynamic flows and jet quenching were observed. Instead of a weakly interacting gas, the system was found to behave as an almost perfect liquid, requiring instead the constituents to be strongly coupled.

Despite the extremely high temperatures and energy densities involved, the fact that the QGP phase is strongly coupled forces it into the computationally-difficult non-perturbative regime of QCD. Nonetheless, the equilibrium properties of QCD matter may be calculated by means of lattice QCD, which implements the path integral formulation of thermodynamics on a discretized (Euclidean) space-time lattice. Lattice QCD calculations at μ_B=0 demonstrate that QCD matter undergoes a smooth crossover phase transition [7] from a hadronic gas to a QGP at a temperature $T_c = 154 \pm 9$ MeV, corresponding to an energy density of $\epsilon_c = 0.18 - 0.5$ GeV/fm^3 [8].

The main interest in relativistic heavy-ion collisions is to study the QGP phase of matter. However, the system created in such collisions progresses through multiple stages, which complicates the interpretation of how exactly the measured observables relate to the QGP. Overwhelmingly, the information about the system comes from final-state hadrons, which only decouple from the system in the final stages of the collision. Therefore, to understand how the measured observables relate to the QGP, the entire dynamical history of the system must be accurately modeled.

2.3 Heavy-ion collisions

2.3.1 Evolution of system

Within our powerful colliders, we accelerate heavy-ions to nearly the speed of light ($\beta \approx 0.9999998$ for ions in Pb-Pb collisions at $\sqrt{s_{\rm NN}} = 2.76$ TeV), and smash them together with ions from an oppositely traveling beam. When at rest, these nuclei are roughly spherical in shape; however, when traveling at relativistic speeds, the situation is quite different. This is due to the fact that any object in motion will appear Lorentz contracted in the direction parallel to the motion, dictated by the Lorentz factor, γ. For Pb-Pb collisions at $\sqrt{s_{\rm NN}} = 2.76$ TeV, $\gamma \approx 1470$, and the nuclei appear as flattened pancakes.

The nuclei collide into each other, the process of which can proceed in two different ways. Collisions at lower energies have larger stopping power, the result of which is more intuitive and similar to our everyday experience with collisions. In this case, baryons are stopped in middle of the reaction zone, leading to dense baryon-rich matter at midrapidity. Collisions at high energies, such as those studied in the current work, are much more transparent, i.e. they exhibit negligible stopping. The nuclei mostly pass through each other, depositing energy between the two, and leaving two well-separated baryon-rich regions. This is unlike our typical everyday idea of a collision. In such a system, the midrapidity collision fireball is approximately baryon-antibaryon symmetric, i.e. the matter produced has very small net baryon number and approximately zero baryon chemical potential ($\mu_B \approx 0$).

The subsequent evolution of the system created in relativistic heavy-ion collisions may be organized into four stages: pre-hydrodynamic, thermalization, expansion, and decoupling. After the initial collision, the partonic matter created interacts strongly, and quickly reaches a state of approximate local thermal equilibrium. The method through which the system reaches this state is still under debate, and this stage of the collision is broadly described at the pre-hydrodynamic stage. For a successful description of the bulk properties in heavy-ion collisions, the data demand that the hydrodynamical evolution begin very shortly after the collision, implying the pre-hydrodynamic stage exists only for $\tau_{eq} \leq 1\text{fm}/c$ [9].

Once the system reaches approximate local thermal equilibrium, it is well described in the language of relativistic viscous hydrodynamics. Within viscous hydrodynamics, the fluid is assumed to be close to local thermal equilibrium, but small gradients are introduced to allow for deviations from from such a state; therefore, the local equilibrium is never complete. At this point, the system may truly be considered a Quark-Gluon Plasma. The data imply the QGP is a nearly perfect fluid with extremely low viscosity to entropy ratio. The thermal pressure, which acts on the surrounding vacuum, causes the system to expand explosively outward. The hydrodynamic response to the pressure gradients produces a collective flow within the system, in which the constituents are commonly boosted outward.

As the fireball expands in response to the pressure gradients, it cools and its energy density decreases. Once the system reaches $\epsilon_{\text{crit}} \simeq 0.5$ GeV/fm^3, the partons convert to hadrons in a process called hadronization. At essentially the same time, the system reaches chemical freeze-out, at which point the inelastic collisions between particles cease, and the particle abundances are mostly fixed. The abundances can change slightly due to resonance decays (mostly affecting the pion yields), and particle-antiparticle annihilation. The system now, once again, is composed of colorless degrees of freedom, and may be described as a hadronic gas. The hadrons continue to bounce off each other, interacting via elastic collisions, as the system continues to expand and cool. The system eventually becomes so dilute that the hadrons no longer interact elastically, known as kinetic freeze-out, after which the particles free-stream to the detectors.

2.3.2 Event characterization

The dynamics of the system created in a collision depend crucially on the type of collision. More specifically, the characteristics of the system depend on the species of particles involved in the collision, the collision energy, and the size and shape of the initial energy density profile. The first two of the variables described above are easy to control in experiment. The last, namely the size and shape of the initial profile, is not so simply varied with the turn of a knob. Of course, the particle species and collision energy do place basic boundaries on the profile created in these collisions. However, the heavy-ions strike each other with random orientations and at random distances from each other. In some cases, the ions smack straight into each other, and most of the constituent matter is involved in the creation of the resulting system; this is an example of a central collision. In other cases, the ions deliver only a glancing blow to each other, and only a small fraction of the constituents participate; this is an example of a peripheral collision. These two cases will create very different fireballs, and it is important to segregate the events depending on their initial geometry.

In a theoretical description, the overlap region of a collision is described by its impact parameter, $\mathbf{b}$. The impact parameter is defined as the vector pointing from the center of one ion to that of the other. Unfortunately, the length and time-scales involved in heavy ion collisions are far too small for any sort of direct observation of the impact parameter. Thus, we are unable to control the initial geometry as the ions collide randomly with each other, and we are unable to directly observe the impact parameter of the collision. However, all is not lost, as we are able to infer the initial geometry from the data, and consequently group together similar events. In this fashion, we can also treat the initial geometry of the collision as a sort of control variable.

The dynamics of the system are largely dictated by the initial energy density deposited in the interaction region, a quantity which is related to the number of finally observed particles, or multiplicity. The resulting multiplicity is inversely related to the impact parameter of the collision; the average charged-particle multiplicity is assumed to decrease monotonically with increasing impact parameter [10]. The multiplicity is also directly related to the number of participant nucleons (N_{part}) and the number of binary nucleon-nucleon collisions suffered by the participants (N_{coll}). In the field of experimental heavy-ion physics, we use the concept of centrality, which can be determined through the multiplicity, to characterize our collisions. In the case of AA collisions, the centrality is tightly correlated with the impact parameter, and therefore the initial geometry of the collision. Through inference by comparison to simulations, the centrality can be expressed in terms of geometrical parameters, such as the impact parameter, or the number of participating nucleons and binary nucleon-nucleon collisions. In the case of pA and pp collisions, the interpretation is not so straightforward, but multiplicity remains useful in characterizing the events nonetheless.

Typically, the centrality is expressed as a percentage of the total nuclear interaction cross section, σ [11]. Then, the centrality percentile c of an AA collision with impact parameter b is defined by integrating the impact parameter distribution, $\mathrm{d}\sigma/\mathrm{d}b$, as:

$$c(b) = \frac{\int_0^b \frac{\mathrm{d}\sigma}{\mathrm{d}b'} db'}{\int_0^\infty \frac{\mathrm{d}\sigma}{\mathrm{d}b'} db'} = \frac{1}{\sigma_{AA}} \int_0^b \frac{\mathrm{d}\sigma}{\mathrm{d}b'} db' \tag{2.2}$$

As we do not have direct access to the impact parameter, we assume that, on average, the particle multiplicity at midrapidity increases monotonically with the overlap volume (i.e. with centrality). With this assumption, and remembering that small impact parameters correspond to large overlap volumes, we may define the centrality as the fraction of cross section with particle multiplicity above some threshold, N_{ch}. Furthermore, the cross section may be replaced with the number of observed events, n, and the centrality expressed as [10, 12]

$$c(N_{\mathrm{ch}}) \approx \frac{1}{\sigma_{AA}} \int_{N_{\mathrm{ch}}}^\infty \frac{\mathrm{d}\sigma}{\mathrm{d}N'_{\mathrm{ch}}} dN'_{\mathrm{ch}} \approx \frac{1}{N_{\mathrm{ev}}} \int_{N_{\mathrm{ch}}}^\infty \frac{\mathrm{d}n}{\mathrm{d}N'_{\mathrm{ch}}} dN'_{\mathrm{ch}} \tag{2.3}$$

From this expression, we see that the centrality is defined as the percentile of events with the largest multiplicity. The definition is such that the 0–5% centrality bin contains the 5% of all events with the largest final-state multiplicity, and therefore the smallest impact parameters. Similarly, the 90–100% bin contains the 10% of events with the smallest final-state multiplicity, and the largest impact parameters. The terminology can sometimes be confusing. Typically, when using the term centrality, we are referencing how central an event is, which is inversely related to its centrality percentile. Therefore, in moving from peripheral to central events, the terminology is typically that the events are increasing in centrality (instead of saying the events are decreasing in centrality percentile).

Figure 2.1 shows a typical distribution of VZERO amplitudes, which serve as a proxy for the charged particle multiplicity, in Pb-Pb collisions at $\sqrt{s_{\mathrm{NN}}} = 2.76$ TeV

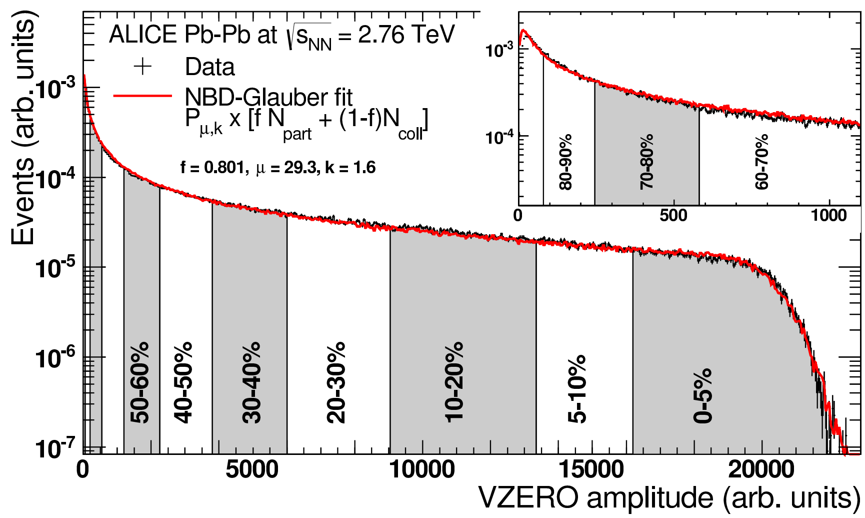

Figure 2.1: Distribution of the sum of the amplitudes int he two VZERO arrays (black histogram) in Pb-Pb collisions at $\sqrt{s_{\rm NN}} = 2.76$ TeV [10]. The red line shows the fit with a Glauber model to the data. The shaded regions indicate the different centrality classes.

(see Sec. 3.2 for a discussion of the VZERO detector). The figure demonstrates the classification of the events into different centrality bins, and also shows the distribution obtained with a model of particle production based on a Glauber description of the nuclear collision [11]. The Glauber model treats the nuclear collision simply as a superposition of binary nucleon-nucleon interactions. For event simulation, a Monte Carlo implementation of the Glauber model is typically utilized [13]. In is simplest form, the nucleon positions within the two nuclei are determined by sampling from the nuclear density function, typically modeled with a Woods-Saxon distribution. The two nuclei are then arranged according to a random impact parameter in the transverse plane. In the collision, the nucleons are propagated with straight-line trajectories, and two nucleons from different nuclei are assumed to collide if the relative (transverse) distance between their centers is less than the radius corresponding to the total inelastic nucleon-nucleon cross section ($d < \sqrt{\sigma_{\rm NN}^{\rm inel}/\pi}$). The inelastic nucleon-nucleon cross section is assumed independent of the number of collisions already suffered by a nucleon.

The Glauber model allows us the estimate both the number of participants, N_{part}, and the total number of binary nucleon-nucleon collisions, N_{coll}: N_{coll} is simply counted, and N_{part} is defined as the total number of target and projectile nucleons having undergone at least one interaction. The soft particle production is assumed to scale with N_{part}, while the hard processes are assumed to scale with N_{coll}. For the multiplicity distribution in a nucleon-nucleon collision, the Negative Binomial Distribution (NBD) is typically used, which has two parameters controlling the mean and width. The number of particle sources is parameterized as a function of N_{part} and N_{coll}, usually as $N_{\mathrm{s}} = fN_{\mathrm{part}} + (1-f)N_{\mathrm{coll}}$, motivated by a two component model, as mentioned above (soft and hard sentence). A fit of this sort is shown in Fig. 2.1.

As demonstrated above, the Glauber model may be used to deduce geometrical properties of the collision. Thus, the centrality can be mapped onto the theoretical impact parameter, as well as the number of participants and number of binary nucleon-nucleon collisions. The centrality determination therefore provides a means by which to compare measurements across various experiments with each other, and with theoretical calculations.

2.4 Observables

The purpose of colliding nuclei at such high energies is to study the hot and dense state of deconfined quarks and gluons, the QGP. However, we are not able to directly observe such a state; long before remnants of the system reach our detectors, the colored degrees of freedom are again trapped within colorless hadrons. Thus, it is from these final-state hadrons that we try to extract information about the initial-state and evolution of the system. Matters are complicated by the fact that the system evolves through multiple distinct stages, which obscure the direct interpretation back to the QGP. Therefore, we must extract the information by comparing experimental observables to models. This leads to a very close relationship between the theorists and experimentalists in the field. Furthermore, the interpretation of a specific measurement, in many cases, relies substantially on its comparison to the same measurement performed in pp and pA collision systems. These comparisons permit us to separate out true final-state effects, resulting from the presence of a strongly coupled system, from initial-state effects. A simple example is comparing an observable in pp collisions to that in AA collisions, scaled by the number of binary nucleon-nucleon interactions from a Glauber model, to see if the AA collision system behaves as a superposition of pp collisions.

The experimental evidence demonstrates a hot, dense, strongly interacting, nearly perfect and almost opaque liquid, the QGP, is created in relativistic heavy-ion collisions. In the following sections a sample of important observables signifying the creation of the QGP and probing its properties is presented.

2.4.1 Charged-particle multiplicity

The measurement of the charged-particle multiplicity, as well as its dependence on event centrality, are typically the first measurements to take place when exploring a new system. The multiplicity is usually expressed in terms of its rapidity density ($\mathrm{d}N_{\mathrm{ch}}/\mathrm{d}y$) or pseudorapidity density ($\mathrm{d}N_{\mathrm{ch}}/\mathrm{d}\eta$). The rapidity ($y$) and pseudorapidity ($\eta$) of a particle are defined as

$$\begin{aligned} y &= \frac{1}{2}\ln\frac{E+p_{\mathrm{L}}}{E-p_{\mathrm{L}}} = \frac{1}{2}\ln\frac{1+\beta_{\mathrm{L}}}{1-\beta_{\mathrm{L}}} \\ \eta &= \frac{1}{2}\ln\frac{|\mathbf{p}|+p_{\mathrm{L}}}{|\mathbf{p}|-p_{\mathrm{L}}} = \frac{1}{2}\ln\frac{1+\cos(\theta)}{1-\cos(\theta)} \end{aligned} \tag{2.4}$$

where E is the energy, p_L the longitudinal component of the momentum, β_L the longitudinal component of the velocity, $|\mathbf{p}|$ the magnitude of the momentum vector, and θ the angle of the momentum vector with respect to the longitudinal direction. Note, pseudorapidity is convenient in that it requires only the direction of the momentum vector, not its magnitude nor the energy of the particle, so no particle identification is needed.

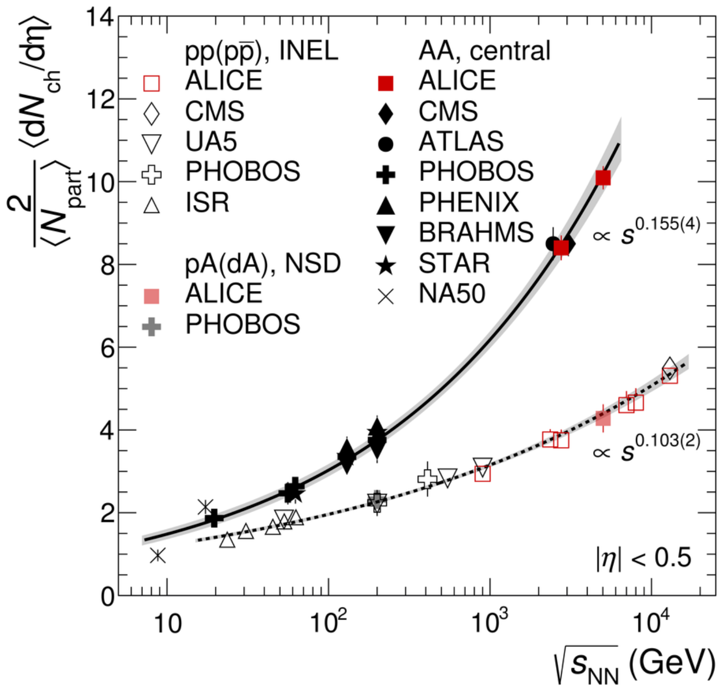

Figure 2.2: Charged-particle pseudorapidity density per participant pair $dN_{ch}/d\eta/(0.5\langle N_{part}\rangle)$ as a function of collision energy, for central Pb-Pb [15–18] and Au-Au [19–23] collisions. Measurements for inelastic pp and p$\bar{p}$ collisions as a functions of $\sqrt{s}$ are also shown [24–26], along with measurements from non-single diffractive p-A and d-A collisions [27, 28]. The power-law dependence for AA and pp(p$\bar{p}$) collisions is shown by solid and dashed lines, respectively, with shaded bands representing the uncertainties on the extracted power-law dependencies. The Pb-Pb measurements from CMS and ATLAS at $\sqrt{s_{NN}} = 2.76$ TeV share slightly shifted horizontally for visibility. Figure from [14]

The collision-energy dependence of $dN_{ch}/d\eta$, normalized to the number of participant pairs, $\langle N_{part}\rangle/2$ (calculated with an MC-Glauber simulation), from pp, pA, and AA collisions is presented in Figure 2.2 [14]. The results from the three LHC experiments are in excellent agreement (measurements from CMS and ATLAS at $\sqrt{s_{NN}}$ = 2.76 TeV are slightly shifted horizontally for visibility). The data reveal that the collision energy dependence of the charged-particle pseudorapidity density per participant pair is well described by a power law, s_{NN}^{α}, for both pp and AA collisions. However, the AA data show a much steeper dependence, with $\alpha = 0.155$, compared to $\alpha = 0.103$ for pp collisions. Not only are the AA data steeper, but they are also more than a factor two higher than the pp data. Therefore, it is clear that AA collisions cannot be simply described as independent superposition of single nucleon-nucleon interactions.

2.4.2 Transverse energy pseudorapidity density

Studying the transverse energy pseudorapidity density at midrapidity, $(\mathrm{d}E_{\mathrm{T}}/\mathrm{d}\eta)|_{\eta=0}$ offers us a quick and simple method to roughly estimate the energy density achieved in the collision system around the time of thermalization. This is thanks to the Bjorken hydrodynamic model, which is based on a longitudinal, transversely isotropic expansion of the medium [29]. Within that model, the energy density, ϵ, is given by

$$\epsilon_{Bj} = \frac{1}{A_{\perp}\tau_0} \frac{\mathrm{d}E_{\mathrm{T}}}{dy}\bigg|_{y=0} \tag{2.5}$$

where $A_{\perp}$ is the transverse overlap area of the colliding nuclei and τ_0 is the parton formation time.

The collision energy dependence of $\mathrm{d}E_{\mathrm{T}}/\mathrm{d}\eta$ at midrapidity, normalized by the number of participant pairs, is shown in Fig. 2.3 [30]. For central Pb-Pb collisions, assuming $A_{\perp} = \pi(7\mathrm{fm})^2$ and $\tau_0 = 1$ fm/c, the energy density extracted is in the range 12-14 GeV/fm^3 [30, 34]. This is roughly 2-3 times that measured by RHIC [3–6], and certainly above the critical energy density predicted for the phase transition, $\epsilon_{\mathrm{c}}(\mu_B = 0) = 0.18 - 0.5$ GeV/fm^3 [8].

The data in Fig. 2.3 are compared to an extrapolation from lower energy data [31], which clearly underestimates the results at the LHC. Results from the EKRT model [32, 33], which combines pQCD minijet production with gluon saturation and hydrodynamics, are also compared to the data. While this model qualitatively described the energy dependence at RHIC and SPS energies, it overestimates the LHC data.

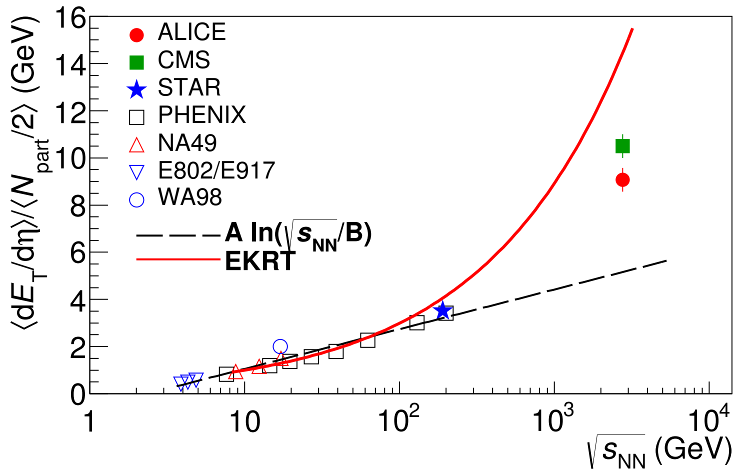

Figure 2.3: $dE_T/d\eta/(0.5\langle N_{part}\rangle)$ at midrapidity vs. $\sqrt{s_{NN}}$ in 0-5% central Pb-Pb collisions at $\sqrt{s_{NN}} = 2.76$ TeV from ALICE [30] and CMS [34], and central collisions at other energies [31, 35, 36]. Note, the NA49 measurement is from the 0-7% centrality class, not the 0-5% class as for all others. Figure from [14]

2.4.3 Identified hadron spectra

The shapes of the experimentally measured p_T spectra reveal valuable information about the system at the time of kinetic decoupling. After hadronization, the particle abundances are mostly stable, as the rates for inelastic processes, which are capable of changing the species identities, are too small to compete with the expansion. However, the cross section for particle interactions is governed by the total cross section, which is comprised of both inelastic and elastic components. The elastic component of the cross section remains large enough for the particles to interact elastically, altering their momentum distributions while keeping their identities intact. At kinetic freeze-out, all low-p_T hadrons have an approximately exponential distribution, dictated by the temperature of the system, blueshifted by the collective flow. This low-p_T shape reveals the thermalized and collectively flowing nature of the system. At higher p_{T} ($\gtrsim$ 3-4 GeV/c), the thermal characteristics give way to a power law shape, as predicted by pQCD [37].

In heavy-ion collisions, the collective expansion leads to a flattening of the transverse momentum spectra, and to a characteristic mass ordering of the inverse slope of the transverse mass (m_{T}) distribution at low-m_{T}. The collective nature of the system acts to equilibrate the velocities of the partons; therefore, in terms of transverse momentum, the heavier particles are affected more strongly by the flow. The radial flow causes a blueshift of the transverse momenta of the final emitted hadrons, pushing them outward in p_{T}-space, and leading to flatter p_{T} distributions, especially at low-p_{T}. The heavier particles, being more affected by the radial flow, are pushed out further than the lighter ones. This leads to the aforementioned flattening of the spectra. The slopes of the p_{T} spectra are affected by the particle masses, and a mass ordering occurs even in the absence of flow; therefore, it is more instructive to demonstrate the effect of flow through the transverse mass spectra, as was done in Ref. [38].

The spectral shapes, including contributions from the thermal and collective flow components, can be investigated within a blast-wave model framework. A typical parameterization assumes a locally thermalized medium, expanding collectively with a common velocity field, with an instantaneous common freeze-out. In such a case, the blast-wave functional form is given by [39]

$$\frac{dN_i}{m_{\mathrm{T}} dm_{\mathrm{T}}} \propto \int_0^R r\, dr\, m_{\mathrm{T}}\, I_0 \left(\frac{p_{\mathrm{T}} \sinh \rho}{T} \right) K_1 \left(\frac{m_{\mathrm{T}} \cosh \rho}{T} \right) \tag{2.6}$$

where the radial flow rapidity ρ, describing the radial velocity profile, is

$$\rho(r) = \tanh^{-1} \beta_{\mathrm{T}}(r) = \tanh^{-1} \left[\left(\frac{r}{R} \right)^n \beta_s \right] \tag{2.7}$$

Here, m_{T} is the transverse mass ($m_{\mathrm{T}} = \sqrt{p_{\mathrm{T}}^2 + m_i^2}$), I_0 and K_1 are the modified Bessel functions, r is the radial distance in the transverse plane, R is the radius of the fireball, β_{T} is the transverse expansion velocity, β_s is the transverse expansion velocity at the surface, and n allows for the variation of the transverse velocity profile.

In both the relativistic and non-relativistic regimes, Eq. 2.6 can be approximated by an exponential distribution

$$\frac{dN_i}{m_{\mathrm{T}} dm_{\mathrm{T}}} \sim \exp\left(-m_{\mathrm{T}}/T_{\mathrm{slope}}\right) \tag{2.8}$$

although with different inverse slopes, T_{slope}, for the two regimes [37, 39, 40]. At large $p_{\mathrm{T}} \sim m_{\mathrm{T}} \gg m_i$, where the emitted hadrons are relativistic, the inverse slope is

$$T_{\mathrm{slope}} = T_f \sqrt{\frac{1 + \langle\beta_{\mathrm{T}}\rangle}{1 - \langle\beta_{\mathrm{T}}\rangle}} \qquad \text{for } p_{\mathrm{T}} \sim m_{\mathrm{T}} \gg m_i \tag{2.9}$$

where $\langle\beta_{\mathrm{T}}\rangle$ is the average transverse flow velocity. Assuming the simple case of a uniform particle density and considering only the transverse geometry, the average is easily found to be [41, 42]

$$\frac{\int_0^R r dr \beta_{\mathrm{T}}(r)}{\int_0^R r dr} = \frac{2}{2+n}\beta_s \tag{2.10}$$

The inverse slope here reflects a standard relativistic blueshift factor towards the observer, which demonstrates that a rapidly expanding source shifts emitted particles to higher momenta, in an m-independent fashion. This asymptotic limit is achieved for m_{T} larger than 1 (2) GeV/c for pions (protons). However, in this region, the non-hydrodynamical power-law behavior also starts to become important.

Non-relativistically, $p_{\mathrm{T}} \ll m_i$, the spectra again have an exponential shape, but instead of a common blueshift, the inverse slope acquires a species dependence

$$T_{\mathrm{slope}} \approx T + \frac{1}{2} m_i \langle\beta_{\mathrm{T}}\rangle^2 \qquad \text{for } p_{\mathrm{T}} \ll m_i \tag{2.11}$$

Thus, for moderate values of m_{T}, the particle mass, m_i, tends to flatten the slope. The above equation shows that the heavier particles gain more momentum from the flow velocity, and their slopes are more flattened.

When studying spectral shapes, one must also keep in mind the contribution from resonance decays. At kinetic freeze-out, these unstable resonances also have an approximately exponential thermal distribution blueshifted by the radial flow. However, before reaching the detectors, the unstable resonances decay, typically producing particles with smaller transverse momenta. This effect works in the opposite direction as radial flow, populating the low-p_{T} region of the distribution, leading to a steeper slope. A majority of the resonances decay by emitting a pion, so this effect is particularly important to consider when analyzing the pion spectrum at low-p_{T}.

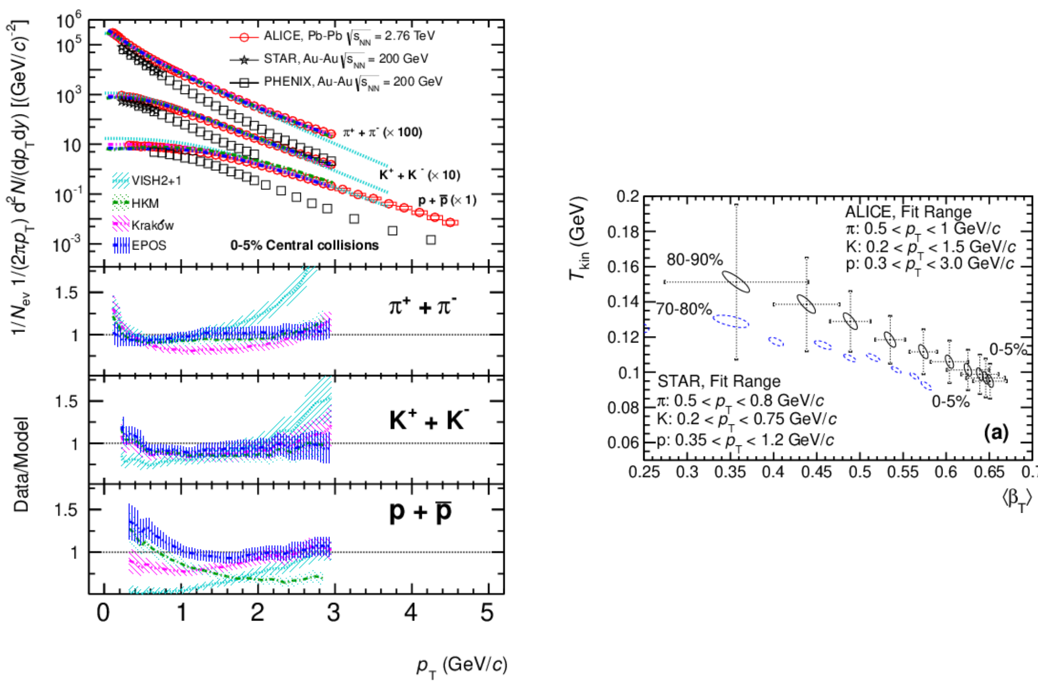

Figure 2.4: (Left) Transverse momentum spectra of $\pi^{\pm}$, $\mathrm{K}^{\pm}$, and $\mathrm{p}(\bar{\mathrm{p}})$ in the 0-5% centrality class from Pb-Pb collisions at $\sqrt{s_{\mathrm{NN}}} = 2.76$ TeV [43] compared to hydrodynamical models and results from RHIC at $\sqrt{s_{\mathrm{NN}}} = 200$ GeV [23, 44]. (Right) Results from blast-wave fits with ALICE (black contours) [43] compared to similar fits at RHIC energies (blue, dashed, contours) [5]. Each confidence contour corresponds to a different centrality class.

Figure 2.4 (left) shows the transverse momentum spectra of $\pi^{\pm}$, $\mathrm{K}^{\pm}$, and $\mathrm{p}(\bar{\mathrm{p}})$ in the 0-5% centrality class from Pb-Pb collisions at $\sqrt{s_{\mathrm{NN}}} = 2.76$ TeV [43] compared to hydrodynamical models and to results from RHIC at $\sqrt{s_{\mathrm{NN}}} = 200$ GeV [23, 44]. The plot shows a change in spectral shapes between RHIC and the LHC, with the protons in particular showing a much flatter distribution at the LHC. Additionally, the mean transverse momentum of the spectra are higher than those measured at RHIC. Both suggest stronger collective radial flow present at the LHC as compared to RHIC. The figure also shows that at low-p_{T} the pion spectra becomes steeper, opposite to the trend observed for the protons and kaons. This is due to the large contribution of resonance decays to the pion spectrum, as previously discussed.

Figure 2.4 (right) presents results from a combined fit of the spectra with the blast-wave function (Eq. 2.6) for both LHC and RHIC results. When interpreting results from a blast-wave fit, it is important remember the relative simplicity of the model, and to keep a few important points in mind. The results from a blast-wave fit generally depend on the particle types and momentum ranges included in the fit, and are especially sensitive to the fit range used for the pions. Furthermore, in general, different particles can decouple from the systems at different times, whereas the model implements a sudden, common, freeze-out for all particles. These types of fits by no means replace a full hydrodynamic calculation, but do offer the ability to compare, with a few simple parameters, different collision systems (be they different in energy, centrality, or species of particles being collided).

The results from Fig. 2.4 show that the extracted average transverse velocity, $\langle \beta_{\mathrm{T}} \rangle$, increases with centrality (from peripheral to central collisions) and from RHIC to the LHC, while the kinetic freeze-out temperature, T_{kin} decreases. The increase in transverse velocity is interpreted as an indication of more rapid expansion in the denser central collisions, and as $\sqrt{s_{\mathrm{NN}}}$ increases. The plot shows that, in comparison to RHIC data for the most central collisions, the extracted freeze-out temperature at the LHC is comparable, while the average flow velocity increases by about 10%. Finally, the fact that more peripheral collisions decouple earlier, at higher freeze-out temperatures and with less transverse flow, is consistent with a shorter lived fireball with stronger flow gradients [37].

2.4.4 Identified particle yields

Instead of studying the shapes of the identified particle spectra, as in Sec. 2.4.3, the relative abundances of the different particle species may be exploited to gain insight into the state of the system around chemical freeze-out. Unlike the momentum distributions studied in Sec. 2.4.3, the particle ratios are expected to be largely insensitive to the underlying processes [40], and effects connected with hydrodynamic flow most cancel in this kind of analysis [45, 46]. Assuming a simple statistical nature of the hadronization process for a medium in thermodynamic equilibrium, the bulk particle production can be described within the framework of thermal (statistical) models based on the grand canonical ensemble [47]. Within such a framework, the conditions at chemical freeze-out can be inferred by fitting the measured particle yields with fit parameters corresponding to the chemical freeze-out temperature (T_{chem}), the baryochemical potential (μ_{B}), and volume (V). This model has its shortcomings, but its simplicity is also very powerful, and serves the purposes for our discussion here.

For a uniform fireball in chemical equilibrium, the particle number density, n_i, is given by [40]

$$n_i = d_i \int \frac{d^3p}{(2\pi)^3} \frac{1}{e^{(E_i-\mu_i)/T} \pm 1} \tag{2.12}$$

where d_i is the spin degeneracy, p the momentum, E the energy, μ_i the chemical potential, and T the temperature. The $+(-)$ is for fermions (bosons). The chemical equilibrium is given by a linear combination of the baryon chemical potential, the strange chemical potential, and the isospin chemical potential [46]

$$\mu_i = \mu_B B_i + \mu_S S_i + \mu_I I_i \tag{2.13}$$

where B_i, S_i, and I_i are the baryon number, strangeness, and the third component of the isospin of the ith hadron, respectively. Within the model, only two parameters,

T and μ_B, are independent. An additional factor, called the strangeness fugacity, γ_s, is sometimes introduced to account for the incomplete strangeness equilibration and to describe the experimental data better.

The comparison of a statistical thermal model with measurements from Pb-Pb collisions at $\sqrt{s_{\mathrm{NN}}} = 2.76$ TeV is shown in Fig. 2.5 [47]. The yields are obtained by integration of the p_{T} spectra, which are typically fit with a blast-wave form (or any other suitable function) to allow the integration to extend below the lowest measured p_{T}. Considering the complexity of a heavy-ion collisions, and the simplicity of the model, the agreement with the data is impressive. The results extracted show a nearly vanishing baryochemical potential ($\mu_{\mathrm{B}} \approx 1$ MeV), as expected in relativistic heavy-ion collisions. The model also shows the chemical freeze-out occurs around $T_{\mathrm{chem}} \approx 157$ MeV, which is rather close to the critical (crossover) temperature in QCD. During the evolution of the system, chemical freeze-out precedes kinetic freeze-out, so the temperature at chemical freeze-out should be higher than that at kinetic freeze-out. Comparing the results here to those in Sec. 2.4.3, we see that this is indeed the case.

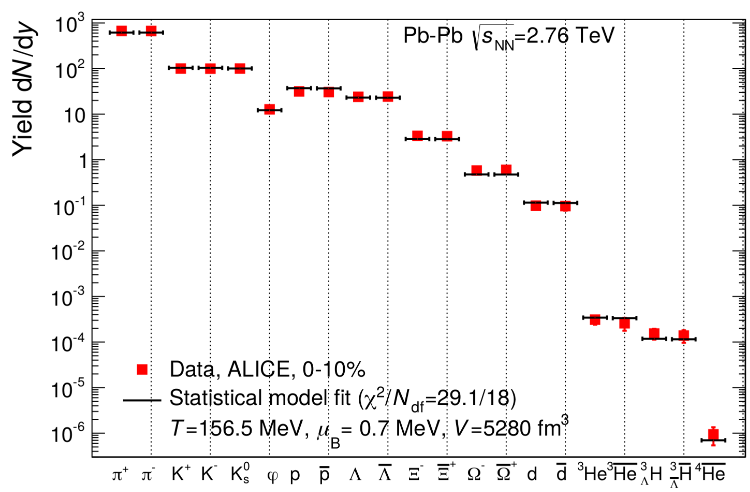

Figure 2.5: Hadron yields in central events (0–10%) from Pb-Pb collisions at $\sqrt{s_{\mathrm{NN}}} = 2.76$ TeV measured with ALICE [43, 48–54] and fit with the statistical hadronization model [47].

2.4.5 Direct photons

Photons provide the most direct probe of the QGP, as they do not couple to the strongly interacting medium, and therefore carry pristine information about the early stages of the collision. However, photons are produced throughout the entire evolution of the system, and measuring isolated direct photon spectra is challenging. Typically, the direct photon yield is extracted on a statistical basis through the comparison of the inclusive photon spectra to the expected background spectra of photons from hadron decays [55–57]. The results from such a measurement performed by the ALICE collaboration are shown in Fig. 2.6[57] for various centralities (arrows represent 90% upper confidence limits). The measurement is accompanied by next-to-leading-order (NLO) perturbative QCD (pQCD) calculations for nucleon-nucleon collisions, all of which have been scaled by the number of binary collisions for the corresponding Pb-Pb collision system.

Above $p_{\mathrm{T}} \gtrsim 5$ GeV/c for all centralities, the data are in good agreement with the pQCD theoretical estimates. There is a clear excess of direct photons in central collisions at low $p_{\mathrm{T}} \lesssim 4$ GeV/c, which might be attributable to thermal photons. Assuming this to be the case, one may fit the spectrum of these thermal photons to extract an effective temperature. This was done by first subtracting the pQCD contribution from one of the theoretical calculations, and fitting the remaining yield with an exponential functions $\propto \exp(-p_{\mathrm{T}}/T_{\mathrm{eff}})$. The extracted inverse slope parameter , i.e. the effective temperature, is $T_{\mathrm{eff}} = 297 \pm 12(\mathrm{stat.}) \pm 41(\mathrm{syst.})$ in the range $0.9 < p_{\mathrm{T}} < 2.1$ for the 0-20% class, and $T_{\mathrm{eff}} = 410 \pm 84(\mathrm{stat.}) \pm 140(\mathrm{syst.})$ in the range $1.1 < p_{\mathrm{T}} < 2.1$ for the 20-40% class.

The simple estimates for the effective temperatures above must not be taken as strictly quantitative results, but rather as rough estimates. Photons originate from all stages of the system's evolution, and careful consideration must be taken when accounting for such effects. A significant contribution originates from blueshifted

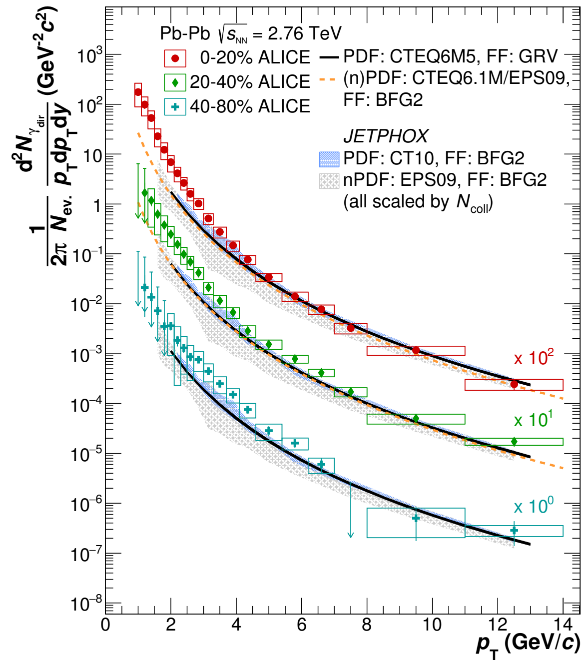

Figure 2.6: Direct photon spectra in Pb-Pb collisions at $\sqrt{s_{\mathrm{NN}}} = 2.76$ TeV in the centrality bins 0-20% (scaled by a factor of 100), 20-40% (scaled by a factor of 10), and 40-80% [57]. The data are compared to NLO pQCD predictions for results from pp collisions, scaled by the number of binary nucleon-nucleon collisions for each centrality class.

photons emitted at late stages of the collision, whose large effective temperatures reflect mostly the strong radial flow generated in the collisions [58]. Therefore, although photons remain as penetrating probes, it is difficult to separate the contributions from the different stages of the system's evolution. The comparison between the medium temperature and the inverse slope parameter is not direct, and the proper interpretation requires a dynamical model which emits photons throughout the entire evolution of the system. Recent calculations employing such sophisticated models suggest the initial temperature to be in the range 350-740 MeV [59–62], well above the critical temperature for a phase transition.

2.4.6 Anisotropic flow

The observation of strong elliptic flow in heavy ion collisions, which is well described with the language of hydrodynamics, was one of the most important discoveries leading to our understanding of the QGP as a strongly coupled plasma of deconfined quarks and gluons [3–6]. Simple arguments based on asymptotic freedom would leave one to naively expect such collisions to produce a weakly coupled gas of quarks and gluons. However, the observation of strong elliptic flow stood in direct opposition to such a simplistic idea: the observed collective phenomena imply the presence of a strongly-interacting medium.

In a relativistic heavy-ion collision, a huge amount of energy is deposited into the interaction region, and large pressure gradients quickly develop between the dense system and the surrounding vacuum. The hydrodynamic response of the system to these pressure gradients causes a collective expansion. In the case of two identical nuclei colliding at non-zero impact parameter (or, the case of deformed nuclei, such as Uranium, colliding centrally and properly aligned), the initial overlap region is anisotropic, and roughly almond shaped. Actually, due to the inherent lumpiness of a nucleus (as well as of the nucleons themselves), even the most central collisions result in anisotropic initial energy density profiles. The efficiency with which the system converts the initial spatial anisotropies into the finally observed anisotropic momentum distribution of the produced particles reveals the nearly ideal nature of the fluid.

Consider, for example, if the produced system behaved as weakly coupled gas-like plasma. In such a case, the constituents would fly around while interacting only rarely and weakly with each other, resulting in a finally observed isotropic distribution. Now, consider the case where the system behaves as a liquid, but with a large viscosity. In this case, the matter will respond hydrodynamically to the initial pressure gradients, but the large viscosity of the fluid will dampen and smooth-out the anisotropies.

Thus, the fact that substantial anisotropies in the azimuthal distribution of particles survive signifies that the produced matter must behave as a liquid with low viscosity.

The azimuthal distribution of produced particles can be described using a general Fourier series decomposition of the particle azimuthal distribution [63, 64],

$$E_i \frac{\mathrm{d}^3 N_i}{\mathrm{d}p^3} = \frac{1}{2\pi} \frac{\mathrm{d}^2 N_i}{p_\mathrm{T} \mathrm{d}p_\mathrm{T} \mathrm{d}y} \left(1 + 2 \sum_{n=1}^{\infty} v_n^i \cos[n(\phi - \Psi_n^i)] \right) \tag{2.14}$$

where E is the energy, p the momentum, p_T the transverse momentum, ϕ the azimuthal angle, and y the rapidity of the particle of species i. The magnitude of each component of the flow is quantified through the harmonic flow coefficient, v_n, with respect to its symmetry plane, Ψ_n. The unity in the above equation corresponds to the isotropic radial flow, and the anisotropic v_n components describe the deformations on top of it. The flow coefficients depend on p_T, y, particle species i (through their rest mass), and impact parameter, and are given by

$$v_n^i(p_\mathrm{T}, y, b) = \langle \cos[n(\phi - \Psi_n^i)] \rangle_{p_\mathrm{T}, b}^i \tag{2.15}$$

where the brackets denote an average over all particles of species i (in the (p_T, y) bin under consideration) in an event, followed by an average over all events within the given centrality bin [37, 65]. We will only explore results from midrapidity, so we suppress the y dependence. If the average in Eq. 2.15 is performed with a single, large p_T bin, one obtains the "p_T-integrated flow".

In non-central collisions, due to the approximate ellipsoidal shape of the overlap region, the second-order flow coefficient, know as *elliptic flow* (v_2), dominates. Early on, v_2 was the only flow coefficient paid much attention; the symmetry of two smooth (Lorentz contracted) nuclei colliding put strong constraints on the spectrum of flow coefficients permitted to be nonzero. Currently, we know that the inherent lumpiness of the colliding nuclei leads to eccentricity harmonics of all orders describing the initial energy density, which drive flow harmonics of all orders. The lumpiness of the reaction zone results from both fluctuations of the nucleon positions within the colliding nuclei, as well as fluctuations of the gluon density profiles within the nucleons.

The harmonic flow planes are not know experimentally, so angular correlations between the finally observed particles must be exploited to estimate the flow coefficients [38, 65]. Two- or multi-particle correlations can be used to directly extract the flow coefficients, or one may estimate the flow planes with a subset of the data before performing the measurement with an independent subset (such as the event-plane or scalar products methods). The extraction of the anisotropic flow coefficients is complicated by the fact that not all angular correlations are collective in origin. There exist so called "non-flow" correlations, which result from effects such as momentum conservation, short-range correlations (like Bose-Einstein effects), resonance decays, Coulomb interactions, and jet correlations [63]. These effects should be reduced in the measurement, or accounted for when interpreting the measured signal.

Generally, the different methods for extracting flow components will have different sensitivity to non-flow contributions and initial state fluctuations. One method to suppress non-flow effects is to introduce a η-gap between the particles in pairs [66], or between the particles used to reconstruct the event planes and those used in the measurement of the flow [67]. Another method is to use multi-particle correlations, which depend on higher moments of the event-by-event v_n distributions, and are known as higher-order cumulants [68]. Assuming non-flow contributions have been successfully eliminated, and assuming $\sigma_{v_n} \ll \langle v_n \rangle$, these higher-order cumulants depend on the σ_{v_n} in a predictable manner, namely [38, 65]

$$v_n\{2\} = \langle v_n \rangle + \frac{1}{2}\frac{\sigma_{v_n}^2}{\langle v_n \rangle} \qquad \text{and} \qquad v_n\{4\} = \langle v_n \rangle - \frac{1}{2}\frac{\sigma_{v_n}^2}{\langle v_n \rangle} \tag{2.16}$$

p_{T}-integrated anisotropic flow

Figure 2.7 presents the p_{T}-integrated elliptic (v_2), triangular (v_3), and quadrangular (v_4) flow components as a function of event centrality for Pb-Pb collisions at both $\sqrt{s_{\mathrm{NN}}} = 5.02$ TeV [66] and 2.76 TeV [69]. The measurements were performed over the p_{T} range $0.2 < p_{\mathrm{T}} < 5.0$ GeV/c, and results are presented using both two-particle (with $|\Delta\eta| > 1$) and multi-particle cumulants methods along with predictions from hydrodynamics models [70, 71]. To better demonstrate the energy evolution of the flow coefficients, the ratios of the 5.02 TeV to 2.76 TeV results are presented in the bottom two panels of the figure.

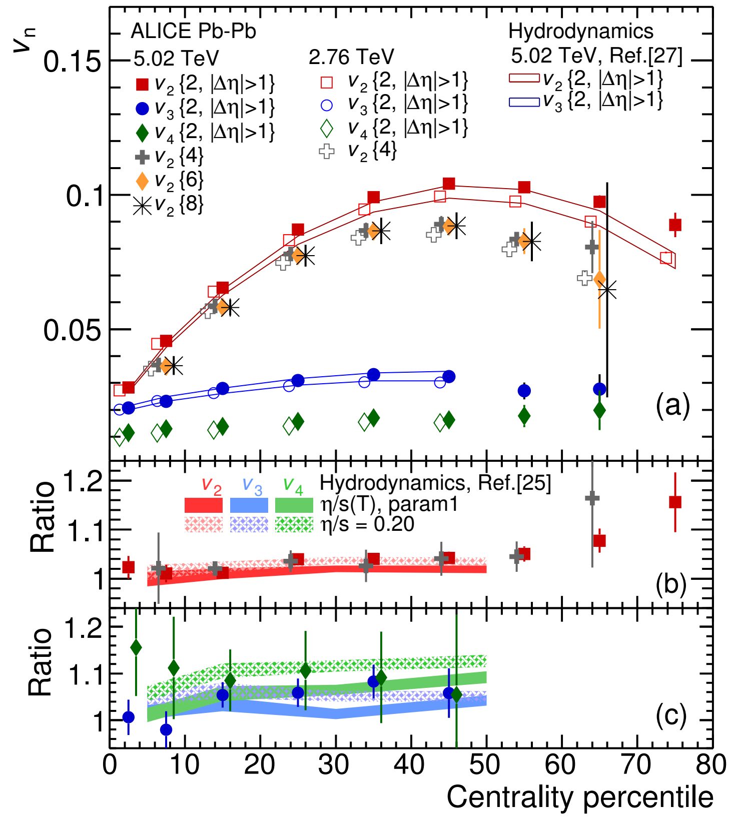

Figure 2.7: Anisotropic flow (v_n) integrated over the $p_{\rm T}$ range $0.2 < p_{\rm T} < 5.0$ GeV/c, as a function of event centrality for Pb-Pb collisions at both $\sqrt{s_{\rm NN}} = 5.02$ TeV [66] and 2.76 TeV [69] measured with ALICE. The plot shows results from both two-particle and multi-particle correlations. The ratios of the data between the two collision energies are shown in (b) for $v_2\{2, |\Delta\eta| > 1\}$ (red) and $v_2\{4\}$ (gray) and (c) for $v_3\{2, |\Delta\eta| > 1\}$ (blue) and $v_4\{2, |\Delta\eta| > 1\}$ (green). Various hydrodynamic calculations are shown [70, 71].

The elliptic flow increases with decreasing centrality, from central to mid-central collisions, as expected from the simple geometric picture of an increasingly spatially elongated source driving stronger elliptic flow. After reaching its maximum value around the 40-50% centrality bin, v_2 decreases. This is contrary to simple intuition that as the collisions become more peripheral, the source becomes even more elongated, and the v_2 signal should continue to increase. With this simple picture, an important consideration is overlooked: namely, as the collisions become peripheral, the system becomes more dilute, and hydrodynamic description becomes less valid [38, 72]. Additionally, the smaller lifetime of peripheral events does not allow the flow enough time to develop [37], and the viscous suppression effects are generally larger in the small fireballs created in such events [73].

Assuming the non-flow contributions are sufficiently suppressed, the plot nicely demonstrates the different dependence of the measurements on flow fluctuations. Referring to Eq. 2.16, the flow fluctuations are expected to give a positive and negative contribution to the two- and multi-particle measurements, respectively; the difference in the two can be used to estimate the effect. Finally, the figure demonstrates that the higher harmonics, v_3 and v_4, exhibit a very weak centrality dependence, which is consistent with their originating primarily from fluctuations. The higher harmonics are also much smaller in magnitude than v_2, except in the most central events, when the v_2 signal also results exclusively from fluctuations.

p_{T}-differential anisotropic flow

The dependence of the elliptic and triangular flow coefficients on transverse momentum, i.e. the p_{T}-differential flow, is presented in Figure 2.8 for events in the 20-30% centrality class of Pb-Pb collisions at $\sqrt{s_{\mathrm{NN}}} = 2.76$ TeV. The elliptic flow is observed to increase almost linearly with p_{T} up to about 3 GeV/c. This behavior is followed by saturation and a decrease observed for all particles and centralities. The position of the maximum depends on the species of particle and centrality bin under consideration. This behaviour demonstrates the gradual breakdown of approximate local thermal equilibrium, and a progressive decoupling from the fluid, for the high-p_{T} particles [37]. The v_3 data are shown together with a hydrodynamical calculation [74] based on iEBE-VISHNU, an event-by-event version of the VISHNU hybrid model

[75], which couples 2+1 dimensional viscous hydrodynamics (VISH2+1) to a hadron cascade model (UrQMD [76]), and uses fluctuating initial conditions with AMPT.

For both v_2 and v_3, a clear mass ordering exists for all centralities at low-p_{T} ($<$ 3 GeV/c); this is also true for higher-order harmonics [77]. This behavior results from the interplay between anisotropic and radial flow. The collective flow tends to equalize the velocities of the particles, so heavier particles gain more in terms of the momentum boost. Thus, for heavier particles, the anisotropic flow signal is pushed out further in p_{T}-space. As a result, for a given value of p_{T} in this regime, heavier particles have smaller v_n.

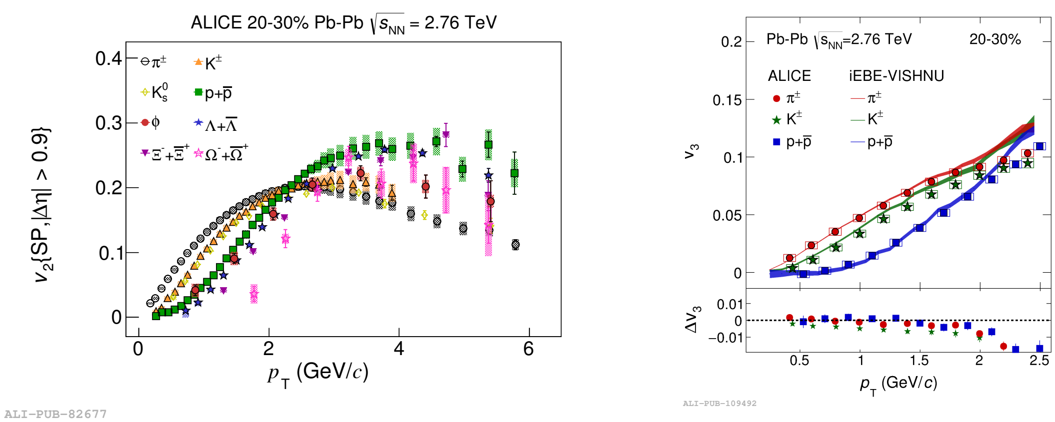

Figure 2.8: p_{T}-differential v_2 (left)[79] and v_3 (right)[77] for identified particles in the 20-30% centrality class of Pb-Pb collisions at $\sqrt{s_{\mathrm{NN}}}$ = 2.76 TeV. Both sets of measurements use the scalar product method [80], although with different implementations. (Right) v_3^{sub} for pion, kaons, and protons compared to v_3 measured with a hydrodynamical calculation [74] based on iEBE-VISHNU [75]. The thickness of the curves reflect the uncertainties of the hydrodynamical calculation. The differences between that data and the model are presented in the lower panel.

At intermediate values of p_{T}, a crossing between baryons and mesons is observed. Above the crossing, particles tend to group according to their type, meson or baryon. This effect is suggested as a sign of quark recombination or coalescence [78]. The ϕ is of particular interest here, as it is a meson, but has a mass similar to that of a proton. Therefore, it can be used to test both the mass ordering and the apparent baryon-meson grouping at intermediate p_{T}. As shown in Fig. 2.8, the ϕ follows the mass-ordered hierarchy at low p_{T}, while at higher values of p_{T} it appears to follow more closely the baryons. In Ref. [79] it was reported that, at intermediate and high p_{T} values of interest, the ϕ appears to follow the band of baryons for central events, while for peripheral events the v_2 values shift progressively to the band of mesons.

2.4.7 Femtoscopy

Femtoscopy is the main focus of this thesis, and is the most direct method for extracting the space-time characteristics of the system produced in heavy-ion collisions. The spatial information extracted with femtoscopy aids in inferences of bulk quantities like pressure, energy density and entropy density. The temporal information and underlying substructure help us to better understand the dynamics of the system. A discussions of the femtoscopic method and results from this ΛK analysis are presented later (Sections 4−7). Furthermore, sample results from other femtoscopic studies, demonstrating the richness of the field, are presented in Sec. 4.4.

The typical goal of a femtoscopic analysis is to extract as much information as possible about the pair emission distributions. The current analyses deviates from this in that extracting the pair emission source for our ΛK is system is somewhat of a secondary goal. The most interesting aspect of the present ΛK analysis is the study of the strong interaction between the Λ and K through the measurement of their nuclear scattering parameters. Interestingly, we find that the $\Lambda\mathrm{K}^{+}$ system behaves quite differently from the $\Lambda\mathrm{K}^{-}$ system.

This investigation of the strong interaction through the measurement of scattering parameters is an ability of femtoscopy that is oftentimes overlooked. This is understandable, as most femtoscopic analyses involve the study of identical particles. Our "bread and butter" analyses are identical $\pi\pi$ correlations. In this case, the correlation signal is overwhelmed by the contribution of quantum statistics (QS), resulting from the symmetrization of the wave-function. The contribution from the Coulomb interaction is a small correction on top of the QS signal, and the strong interaction is essentially invisible. Both the quantum statistical effect and the effect of the Coulomb interaction are well understood, which allows these analyses to focus on the extraction of the source, and to essentially forget about the effect of the strong interaction. In ΛK correlations, both the quantum statistical and Coulomb interaction effects are absent, offering a clear signal from the strong final state interaction effects.

2.4.8 Hard probes

Hard probes provide a powerful means with which to explore the medium created in heavy-ion collisions. Such probes include high transverse momentum particles, jets, heavy flavours and quarkonium states. The large mass and/or energy scales of these probes offers a number of advantages. These probes are produced predominately in hard scatterings (i.e. large momentum transfers $Q^2 \sim p_{\mathrm{T}}^2 \gg 1\mathrm{GeV}^2$) during the initial phases of the collision, and therefore experience the entire evolution of the fireball [37]. Their production is well described using methods of pQCD, so they serve as well-calibrated probes. As these energetic partons traverse the evolving medium, they are expected to lose energy through interactions with the constituents of the matter. The amount of energy loss depends both on the properties of the matter and the path length traversed by the parton. Within the perturbative QCD framework, energy loss is expected to result from both inelastic radiative loss through medium induced gluon radiation, and elastic collisional loss. It is expected that radiative energy loss dominates at high energies, while collisional loss may contribute at lower energies [81].

High-p_T suppression

To signify the effects of the hot and dense QGP matter created in the collisions, a typical strategy is to identify deviations from the baseline established in the absence of such a medium, utilizing proton-proton collisions. The effect is quantified through the nuclear modification factor, R_{AA},

$$R_{AA}(p_{\mathrm{T}}) = \frac{\mathrm{d}N^{AA}(p_{\mathrm{T}}/\mathrm{d}p_{\mathrm{T}})}{\langle N_{\mathrm{coll}}\rangle \mathrm{d}N^{pp}(p_{\mathrm{T}}/\mathrm{d}p_{\mathrm{T}})} \tag{2.17}$$

where N_{coll} is the number of binary nucleon-nucleon collisions, as calculated by a Glauber model. In the absence of nuclear effects, i.e. if the AA system can be treated as a superposition of N_{coll} independent pp collisions, R_{AA} will go to unity (at least for hard processes). When analyzing such a measurement, it is important to remember that soft processes scale with the number of participants, N_{part}, not N_{coll}. This naturally leads to a suppression of R_{AA} in the soft sector.

Figure 2.9 presents the nuclear modification factor in central heavy-ion collisions as a function of p_{T}, $R_{AA}(p_{\mathrm{T}})$, at three difference center-of-mass energies ($\sqrt{s_{\mathrm{NN}}}$). The data show a slightly stronger suppression at the LHC compared to RHIC; for both, the strongest suppression occurs around $p_{\mathrm{T}} \approx$ 6-7 GeV/c, with a suppression factor of approximately 7 at the LHC, and a factor of approximately 5 at RHIC. The figure also nicely demonstrates the expanded capability of producing and measuring hard probes offered by the LHC as compared to RHIC. This extended p_{T} range reveals a new trend inaccessible at RHIC, showing that as p_{T} increases the maximal suppression is followed by an increase in R_{AA}, i.e. the suppression becomes smaller. Nonetheless, the data show that a non-zero suppression remains for all p_{T} measured (CMS has extended the measurement out to $p_{\mathrm{T}} = 300$ GeV/c for Pb-Pb collisions at $\sqrt{s_{\mathrm{NN}}} =$ 5.02 TeV). Thus, even the most energetic particles cannot escape the medium without suffering energy loss.

The LHC experiments have also measured R_{AA} as a function of centrality. The results are as expected when considering the path-length dependence of energy loss: the charged-particle production is progressively less suppressed going from central to peripheral Pb-Pb collisions. One must be somewhat careful when considering such a comparison across centralities, as the dynamics of the created systems vary with centrality. A simpler measurement to digest is R_{AA} measured as a function of azimuthal angle with respect to the event-plane in semi-central collisions. In this

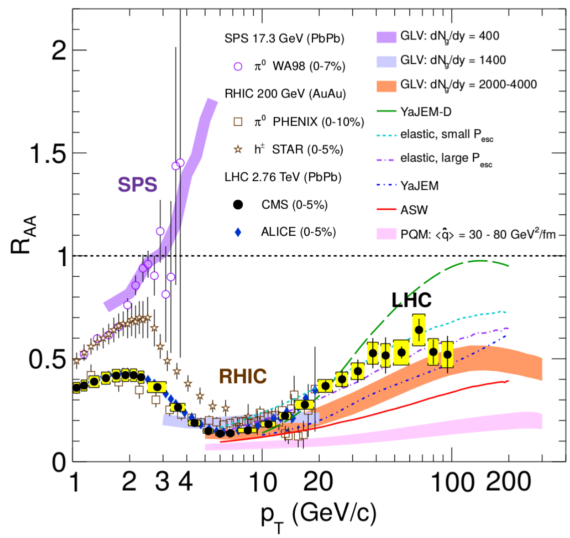

Figure 2.9: Measurement of the nuclear modification factor, R_{AA}, in central heavy-ion collisions as a function of p_{T}. Data are shown for neutral pions (π^0), charged hadrons ($\mathrm{h}^{\pm}$), and charged particles [82–87]. Several theoretical predictions are shown for comparison [33, 88–92]. Figure from [82]

case, one samples events with similar properties, and the overlap geometry of such collisions leads to almond shaped interaction volumes. Considering the path length dependence of parton energy loss, one expects a greater loss for a parton traversing the system out-of-plane as compared to in-plane.

Figure 2.10 presents the measurement of the nuclear modification factors for charged-particles, photons, and W and Z bosons in central (0-5% centrality) Pb-Pb collisions at $\sqrt{s_{\mathrm{NN}}}$ = 2.76 TeV compared to those in pPb collisions at $\sqrt{s_{\mathrm{NN}}}$ = 5.02 TeV. Studying pPb systems here serves to identify the possibility of any initial state effects contributing the the R_{PbPb} measurement. As shown, the R_{pPB} measurement at high-p_{T} is consistent with unity, and therefore absent of any nuclear matter effects. Consequently, the R_{PbPb} measure can be interpreted as resulting from parton energy loss in deconfined QCD matter with negligible contribution from initial state effects. This conclusion is strengthened by the measurement of direct photons and electroweak gauge bosons shown in Fig. 2.10, which are not affected by the hot QCD matter, and whose measurements are consistent with unity.

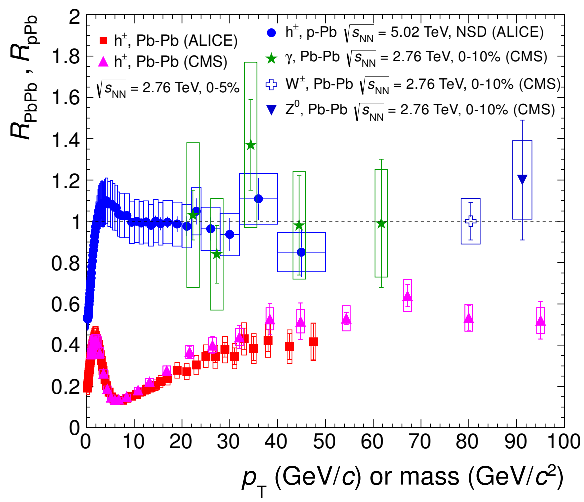

Figure 2.10: Measurement of the nuclear modification factor, R_{pPb}, of charged particles ($\mathrm{h}^{\pm}$) in minimum-bias (NSD) p-Pb collisions at $\sqrt{s_{\mathrm{NN}}} = 5.02$ TeV. For comparison, R_{PbPb} results in Pb-Pb collisions at $\sqrt{s_{\mathrm{NN}}} = 2.76$ TeV are shown for charged particles [82, 93], direct photons [94], Z^0 [95] and $\mathrm{W}^{\pm}$ [96] bosons. Figure from [97]

Jet Quenching

The study of jets is similar in many respects to that of high-p_{T} charged particles, as described above. Hard partons produced early in the collision fragment and hadronize into a collimated spray of particles, called a jet. As stated previously, as these partons traverse the expanding medium, they interact with the constituents of the medium and subsequently lose energy. The study of high-p_{T} charged particles focuses only on the yields of single high-p_{T} tracks. The measurement of jets differs in that the goal is to reconstruct the entire spray of particles originating from the initial hard parton. Jets have an advantage in that their p_{T} and direction of travel are more directly related to that of the initial parton. Using reconstructed jets allows one to more finely investigate how the medium affects the high energy partons which traverse it, in terms of energy loss and angular deflection, as well as opening the door to study how the energy lost by the jet is dispersed and redistributed. Essentially, the study of reconstructed jets expands on the information accessible by simply looking at high-p_{T} particles.

2.4.9 Conclusion

The experimental evidence demonstrates that the QGP is a hot and dense thermalized medium. The QGP behaves as a strongly interacting and nearly perfect liquid which responds to pressure gradients with very little internal friction. As a result, the initial spatial anisotropies in the energy density distribution are converted into anisotropies in the finally observed momentum spectra of the produced particles. The observed hadron momentum spectra and yields reveal information on the chemical composition, temperature, and collective flow patterns of the produced medium. Although the QGP is transparent to electromagnetic probes, it is nearly opaque to even the most energetic colored probes, reaffirming the strongly interacting nature of the medium. The study of hard probes allows us to extract information about the temperature and density of the system at earlier times before decoupling.

The analysis presented in this work focuses on two-particle momentum correlations, which access space-time information of the collision system at kinetic freeze-out. Femtoscopy offers this vital information which are inaccessible through other observables; however, the proper interpretation of femtoscopic measurements relies on knowledge gained through these other measurements. The detailed substructure of the pair source emissions regions extracted through femtoscopy are dictated by the interplay between thermal motion and collective expansion, as will be explored further in Sec. 4.4. Thus, the proper understanding of the QGP as a strongly coupled almost perfect fluid is vital in understanding femtoscopic measurements presented in this work.

Chapter 3: Experimental Set-up

3.1 The Large Hadron Collider at CERN

The ***L**arge **H**adron **C**ollider* (LHC) is currently the world's largest and most powerful particle accelerator and collider, and is operated by the European Organization for Nuclear Research (CERN, from the French ***C**onseil **E**uropéen pour la **R**echerche **N**ucléaire*). CERN and the LHC are located near Geneva, Switzerland, and the 26.7 km beam tunnel of the accelerator straddles the French-Swiss border, 45-170 m underground. The LHC is a synchrotron which uses two separate beam pipes to accelerate particles in opposite directions, crossing the beams at predetermined locations to induce the collisions [98]. Thousands of magnets are utilized to direct the beam around the accelerator, including 1232 dipole magnets 15 m in length which bend the beams, and 392 quadrupole magnets 5-7 m long which focus the beams [99]. To increase the momentum of the particles, the accelerator is equipped with metallic chambers containing an electromagnetic field, know as radiofrequency (RF) cavities, through which charged particles receive an electrical impulse which accelerates them. The collider was designed to reach up to a center-of-mass energy $\sqrt{s} = 14$ TeV for proton-proton (pp) collisions, and up to $\sqrt{s_{\mathrm{NN}}} = 5.5$ TeV for Pb-Pb collisions, where $\sqrt{s_{\mathrm{NN}}}$ is the center-of-mass energy per nucleon pair.

The CERN council granted approval for the LHC project in December of 1994 [98]. The decision to build the LHC at CERN was largely influenced by the presence of the Large Electron-Positron (LEP) collider on the site. For the LEP, the 26.7 km tunnel was already constructed, and could be reused for the LHC. The tunnel geometry, as designed for the LEP, consists of eight crossing points, flanked by long straight sections, and eight arcs. For the LEP, the straight sections contained radiofrequency (RF) cavities which compensated the high synchrotron radiation losses. As a proton machine, such as the LHC, does not suffer as much from the synchrotron radiation, and ideal tunnel would have longer arcs and shorter straight sections. However, the cost-saving advantage outweighed the non-ideal geometry, and the LEP tunnel was reused. In the end, for the LHC only four of the possible eight interaction regions are equipped, and the beam crossings in the remaining four are suppressed to prevent unnecessary disruption of the beams.

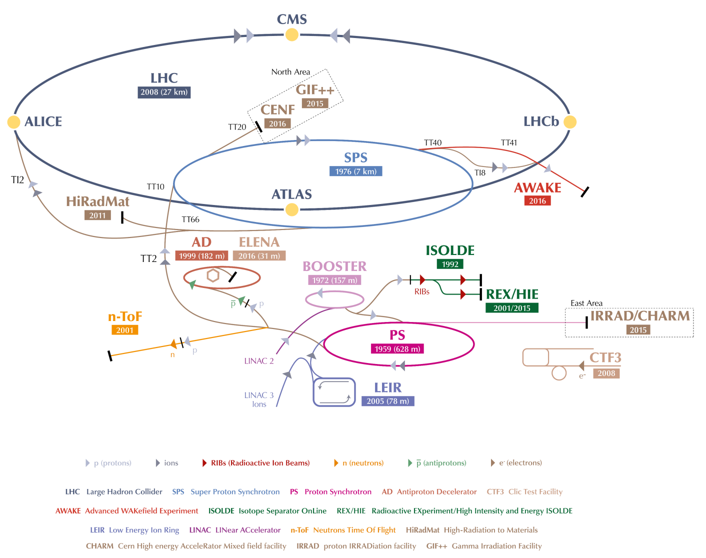

Figure 3.1: LHC schematic and injection chain [100]

The LHC functions as a sequence of accelerators, each accelerating the beam to increasingly higher energies before injecting into the next. Figure 3.1 shows a diagram of the LHC complex. The LHC circulated its first proton beams on September 10 of

2008, but ran for only nine days before suffering an unfortunate magnet quenching accident, causing the operation to be postponed for another year. The first proton-proton collisions were achieved in November of 2009, and on 30 November of 2009 the LHC achieved collisions at an energy of 1.18 TeV per beam, eclipsing the 0.98 TeV per beam capabilities of the Tevatron at Fermilab, making the LHC the world's most powerful collider. In 2010, the LHC reached proton-proton collisions at $\sqrt{s} =$ 7 TeV, and the end of the year saw the first Pb-Pb collisions at $\sqrt{s_{\mathrm{NN}}} = 2.76$ TeV. Since then, the LHC has delivered pp collisions at $\sqrt{s} = 4$ and 13 TeV, pPb collisions at $\sqrt{s_{\mathrm{NN}}} = 5.02$ TeV, and Pb-Pb collisions at 5.02 TeV. For reference, at $\sqrt{s} = 13$ TeV the protons travel at $\sim$ 0.99999999 times the speed of light, and circle the 26.7 km ring in less than 10^{-4} s, or, equivalently, more than 11,000 times per second.

3.2 The ALICE Collaboration

3.2.1 Overview

A L*arge* ***I****on* ***C****ollider* ***E****xperiment*, or ALICE, is one of the four large experiments at the CERN LHC complex, and serves as the dedicated heavy-ion experiment. The purpose of the experiment is to study the physics of strongly interacting matter under extreme conditions of energy density and temperature. Quantum Chromodynamics (QCD), the theory describing the strong-interaction sector of the Standard Model, predicts a transition from normal hadronic matter to a phase of deconfined quarks and gluons at sufficiently high energy density. This phase a matter is known as the Quark-Gluon Plasma (QGP). So, in a general sense, the purpose of the experiment is to study the characteristics of the QGP. Through the study of this matter, we explore the phase diagram of QCD matter, and gain insight to QCD itself. Furthermore, not long after the Big Bang, our universe is believed to have passed through a QGP stage. Therefore, exploring the dynamics of the QGP is exploring the origins of our universe.

The ALICE experiment is designed and optimized to study relativistic nucleus-nucleus (AA) collisions; more specifically, Pb-Pb collisions. However, the physics program also includes the study of proton-proton (pp) and proton-nucleus (pA) collisions. The main motivation for studying these systems is to accumulate reference data against which we can compare our studies. More specifically, these measurements are vital in separating genuine QCD-matter signals from the cold-matter initial and final state effects [12]. However, these systems involve interesting physics in their own right, and the ALICE analyses are complementary to studies conducted by the other LHC experiments.

The ALICE detector was built and is operated by a collaboration which currently includes over 1800 members from 177 institutes in 41 countries. The overall dimensions of the detector are 16 x 16 x 26 m^3, and it weighs approximately 10,000 tons [101]; the impressive scale of the device can be seen in Fig. 3.3 through its comparison to the two reference people in the foreground. The ALICE detector and facilities are located at Point 2 of the LHC in the town of Saint Genis-Pouilly, France. The detector itself is contained in a cavern 52 m below the earth's surface.

Figure 3.2: The main building of the ALICE site, located at Point 2 of LHC, in Sergy, France (bordering the commune of Saint-Genis-Pouilly.) Inside is the ALICE Run Control Centre (ARC), as well as access to the underground cavern, where the detector is housed. Outside, we see three proud (and exhausted) physicists from The Ohio State University.

The ALICE experiment was designed to handle the onslaught from the large particle densities expected in central Pb-Pb collisions at the LHC. The power of the experiment resides in its high detector granularity, low transverse momentum threshold ($p_{\mathrm{T}}^{\mathrm{min}} \approx 0.15$ GeV/c), and excellent particle identification out to 20 GeV/c. The majority of the sub-detectors are situated to measure particles around mid-rapidity ($\eta \approx y \approx 0$, see Eq. 2.4 for definition), the region of lowest net-baryon density and maximum energy density.

The ALICE detector consists of 18 subdetector systems, which can be grouped into three categories: central-barrel detectors, forward detectors, and the muon spectrometer. The central-barrel detectors are embedded in a large solenoid magnet, reused from the L3 experiment at LEP. The L3 solenoid is 12.1 m long with a radius of 5.74 m, and can generate a magnetic field of strength $B = 0.5$ T. The powerful magnet causes the trajectories of the charged particles to bend, and permits the identification and momentum measurement of the particles. The central-barrel covers the pseudorapidity region $|\eta| < 0.9$ and the full azimuth, and is used primarily for particle tracking and identification (PID).

The central-barrel detectors, from inside out, are comprised of the following subdetector systems. The Inner Tracking System (ITS)[102], which performs high-resolution tracking and helps localize the primary event vertex, consists of layers of silicon pixel (SPD), drift (SDD), and strip (SSD) detectors. The cylindrical Time Projection Chamber (TPC)[103] is the main system in the central-barrel for the tracking of charged particles. Next is the Time Radiation detectors (TRD)[104], whose main purpose is to provide electron identification at momenta above 1 GeV/c. Particle identification in the intermediate momentum range is achieved with the Time-Of-Flight detector (TOF)[105, 106]. The High-Momentum Particle Identification Detector (HMPID)[107], as the name suggests, is dedicated to enhancing the PID capability of ALICE beyond the momentum interval attainable through the ITS, TPC, and TOF. The HMPID is based on proximity-focusing Ring Imaging Cherenkov (RICH)

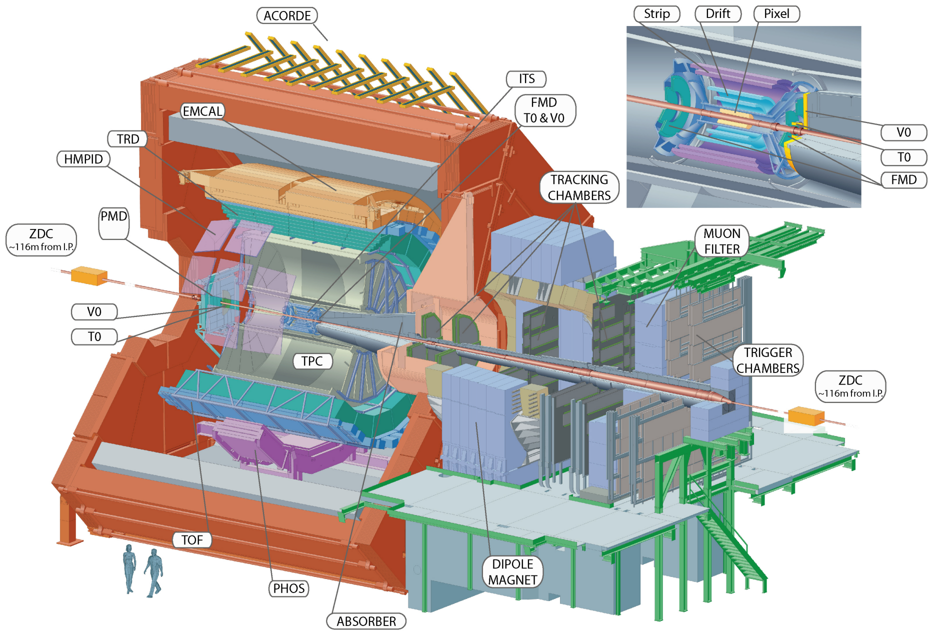

Figure 3.3: Schematic of the ALICE detector [116]

counters, and was designed to allow for the discrimination of π, K, and p up to at least 3 GeV/c. The PHOton Spectrometer (PHOS)[108] is a high-resolution electromagnetic spectrometer, whose main purpose is to provide identification of photons, which also allows for the reconstruction of neutral π^0 mesons. Finally, the ElectroMagnetic Calorimeter (EMCal)[109, 110] focuses on the measurement of high-p_{T} particles, allowing ALICE to explore in more detail the physics of jet quenching. All of these detectors except HMPID, PHOS, and EMCal cover the full azimuth.

The ALICE detector also has a number of subdetectors outside the central η region. Several small detectors, located at small angles, are used primarily for triggering and measuring global event characteristics. The Zero-Degree Calorimeters (ZDC)[111] measures spectator nucleons not participating in the collisions, which allows for the estimation of the number of participants, and therefore the centrality. The Photon Multiplicity Detector (PMD)[112] measures the multiplicity and spatial $(\eta - \phi)$ distribution of photons in the forward pseudo-rapidity region, which can additionally be used to estimate the transverse electromagnetic energy and the event plane. The Forward Multiplicity Detector (FMD)[113] provides charged-particle multiplicity information in the pseudorapidity range $-3.4 < \eta < -1.7$ and $1.7 < \eta < 5.0$, aiding in the determination of the event plane and allowing for the study of multiplicity fluctuations. The VZERO (sometimes called V0)[113] detector, consisting of scintillator counter arrays and covering a pseudorapidity range similar to that of the FMD, is used primarily for event triggering and centrality determination. The T0 [113] detector consists of two Cherenkov counters whose primary task is to provide a start time for the TOF detector.

ALICE can detect and trigger on muons in the forward muon arm, which is located between 2° and 9° from the beam axis on one side of the central barrel. The forward muon arm [114] consists of a complex arrangement of absorbers, a large dipole magnet, and fourteen planes of tracking and triggering chambers. The main purpose of the forward muon arm is the reconstruction of heavy-flavor decays. Finally, the ALICE COsmic Ray DEtector (ACORDE)[115] is an array of scintillator counters placed on the upper surface of the L3 magnet. The purpose of the ACORDE is to provide a fast trigger signal for the commissioning, calibration, and alignment procedures of some of the ALICE tracking detectors. It can also be used, in combination with the TPC, TRD, and TOF, to study high-energy cosmic rays.

3.2.2 Main subdetectors used in this analysis

The ALICE detector is an immense and complex apparatus, worthy of volumes of literature to be sufficiently described. I will not attempt such a feat here, and will only introduce the main components used for the current analysis: ITS, TPC, TOF, and VZERO. For this analysis, events are classified according to their centrality, determined using the VZERO detectors. Charged particle tracking is performed with the TPC and ITS detectors. The ITS is also used for determining the primary collision vertex for each event. The TPC and TOF detectors are utilized in particle identification of reconstructed tracks.

Inner Tracking System (ITS)

The Inner Tracking System (ITS) resides closest to the beam line, and contributes to most all physics measurements conducted by ALICE, as it helps determine the primary collision vertex position with a resolution better than 100 μm [101]. This subdetector is also used to reconstruct the secondary vertices in each collision resulting from the decay of unstable, short-lived, resonances. Furthermore, the ITS is used as a compliment to the Time-Projection Chamber (TPC) for particle tracking and identification. In particular, the ITS is able to extend the tracking and identification of particles with momentum below 200 GeV/c, which do not reach the TPC, and can reconstruct particles traversing dead regions of the TPC. Finally, this subdetector serves to improve the momentum and angular resolution for particles reconstructed by the TPC.

The ALICE ITS consists of six cylindrical layers of silicon detectors arranged coaxially around the beam pipe, at radii between 39 mm and 430 mm [102]. The inner radius is determined by the minimum distance allowed by the beam pipe, while the outer radius ensures the ability to match tracks with those reconstructed in the TPC. All layers cover the rapidity range $|\eta| < 0.9$, while the first layer has a more extended range of $|\eta| < 1.98$ to provide, together with the Forward Multiplicity Detectors (FMD), continuous coverage of the charged-particle multiplicity.

At the time of design, the particle density at the inner layer of the ITS was predicted to reach up to 50 particles per cm^2. With such a high density, and in order to achieve the required impact parameter resolution, the system is designed with Silicon Pixel Detectors (SPD) for the innermost layers, Silicon Drift Detectors (SDD) for the following two layers, and double-sided Silicon micro-Strip Detectors (SDD) in the outermost layers (where the track density is expected to drop below one particle per cm^2). The four outermost layers (SDD and SSD) have an analog readout, and therefore can be used for particle identification through dE/dx measurements in the non-relativistic ($1/\beta^2$) regime.

Time-Projection Chamber (TPC)

The Time-Projection Chamber (TPC) [103, 117] is the main system in the central barrel of the ALICE experiment for tracking charged particles [103]. It is optimized to provide charged particle momentum measurements with good two-track separation, particle identification, and vertex determination. The TPC covers the full azimuth and has a pseudo-rapidity range of $|\eta| < 0.9$. It offers good momentum resolution over a transverse momentum range of 0.1 GeV/$c \lesssim p_{\mathrm{T}} \lesssim 100$ GeV/c.

The TPC consists of a hollow cylinder coaxial with the LHC beams, which is filled with gas and divided into two drift regions by the central electrode located at the axial center. The active volume has an inner radius of about 85 cm, and outer radius of about 250 cm, and a length of about 500 cm along the beam axis. The active volume (~ 90 m^3) is filled with a gas mixture of Ne-CO_2 (90:10). The central electrode is charged to 100 kV, and a voltage dividing network at the surface of the outer and inner cylindrical walls ensures a precise axial electric field of 400 V/cm.

As charged particles pass through the TPC, they ionize the gas along their trajectory. The liberated electrons drift towards the end plates of the cylinder under the influence of the electric field. The maximum distance these electrons must travel is 2.5 m, resulting in a maximum drift time of about 90 μs. The end plates are segmented into $\sim$ 560,000 pads, which register the hits from the drift electrons. The two-dimensional $r\phi$ track projection is obtained directly from the pads, while the distance of the track in the z-direction is determined from the drift time of the liberated electrons. The momentum of a particle can then be determined from the radius of curvature of its track.

Particle identification is achieved by the simultaneous measurement of the specific energy loss ($\mathrm{d}E/\mathrm{d}x$), charge, and momentum of each particle traveling through the detector. The average rate of energy loss is well described by the Bethe-Bloch formula, and for the experimental implementation is typically parametrized as [12, 103]

$$f(\beta\gamma) = \frac{P_1}{\beta^{P_4}}\left[P_2 - \beta^{P_4} - \ln\left(P_3 + \frac{1}{(\beta\gamma)^{P_5}}\right)\right] \tag{3.1}$$

where β is the particle velocity, γ the Lorentz factor, and P_{1-5} are fit parameters. Figure 3.4 shows the experimentally measured $\mathrm{d}E/\mathrm{d}x$ vs. particle momentum in the TPC, showing the separation of the different particle species, and with lines representing to fits using the parametrization in Eq. 3.1.

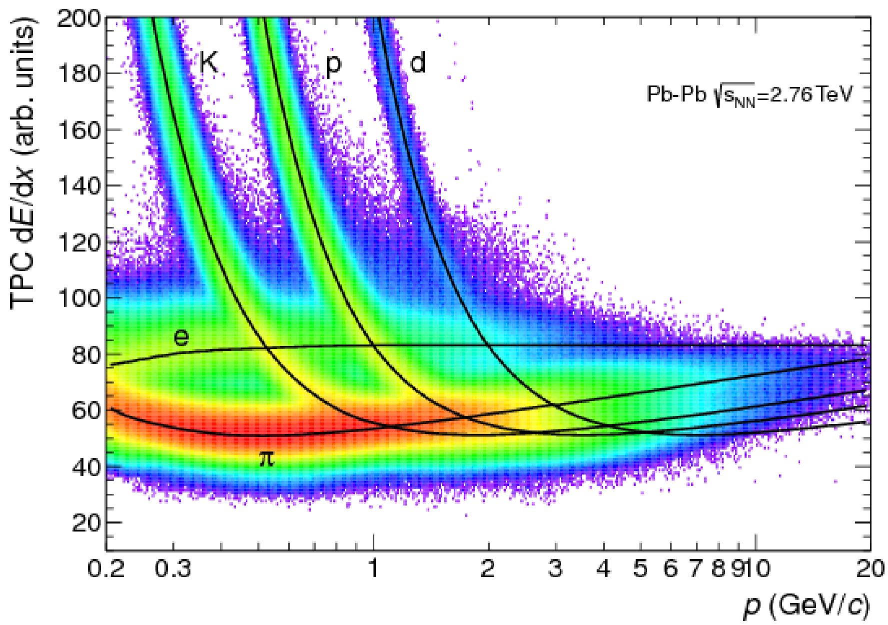

Figure 3.4: Specific energy loss ($\mathrm{d}E/\mathrm{d}x$) in the TPC vs. particle momentum in Pb-Pb collisions at $\sqrt{s_{\mathrm{NN}}} = 2.76$ TeV. The lines show the parametrization of the expected mean energy loss. [12]

Time-Of-Flight (TOF) detector

The Time-of-Flight (TOF) detector [105] is cylindrical in shape with a radius of approximation 3.7 m, covering the full azimuth over the pseudorapidity range $|\eta| < 0.9$. The detector was designed to identify particles in the intermediate momentum region, and consists of a large array of Multigap Resistive Plate Chambers (MRPC).

It has a modular structure with 18 sectors in ϕ, each of which is divided into 5 modules along the beam direction. The TOF detector is able to measure the arrival time of particles with a resolution $\sim$ 80 ps for pions with momentum around 1 GeV/c [12]. This time measurement, together with momentum and track length information measured by the tracking detectors, allows for the calculation of the particle mass. The TOF detector allows particle identification up to $\sim$ 2.5 GeV/c for pions and kaons, and up to 4 GeV/c for protons, with a π/K and K/p separation better than 3σ. Figure 3.5 shows the velocity (β) distribution measured with the TOF detector as a function of particle momentum (measured by the TPC). The figure demonstrates the performance of the detector through the clear separation of the different particle species.

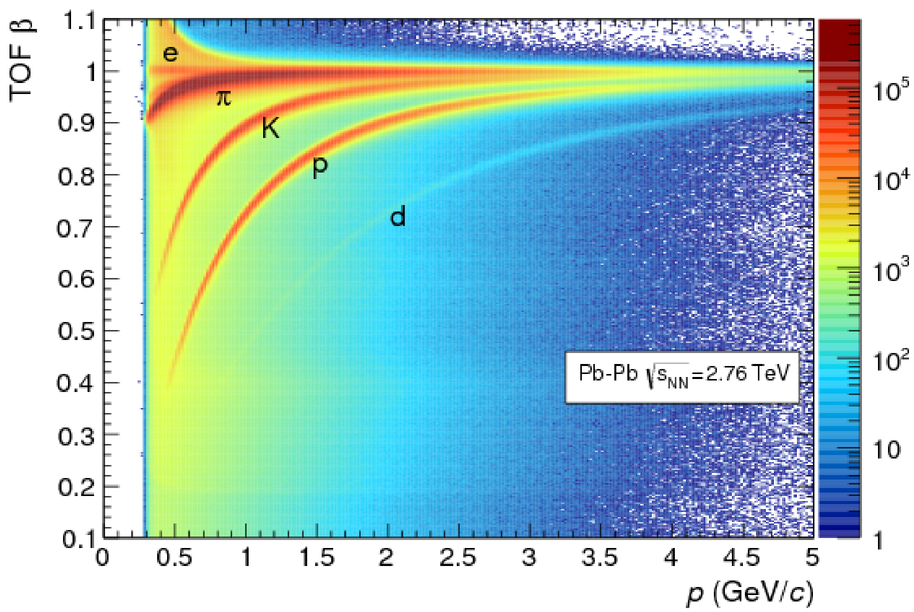

Figure 3.5: Distribution of measured velocity, β, as measured by the TOF detector as a function of momentum in Pb-Pb collisions. [12]

VZERO Detector

The VZERO[1] system is a small angle detector consisting of two circular arrays of 32 scintillator counters, VZERO-A and VZER0-C, installed on either side of interaction point (for a more detailed description, see Refs. [101, 118, 119]). Each array covers the full azimuth and is segmented in four rings radially, each of which is divided into eight sections azimuthally. For collisions at the nominal vertex ($z = 0$), the counters measure charged particles in the pseudorapidity ranges $2.8 < \eta < 5.1$ (VZERO-A) and $-3.7 < \eta < -1.7$ (VZERO-C). The detector records both the amplitude and the arrival time of signals produced by the charged particles.

The VZERO serves a few main functions within the ALICE architecture. It provides triggering (minimum bias or centrality trigger) for the central barrel detectors in pp and Pb-Pb collisions. The dependence between the signal recorded by the VZERO (as the sum of VZERO-A and VZERO-C amplitudes) and the number of emitted particles is monotone, which allows the detector to serve as an indicator of centrality through the event multiplicity (see Sec. 2.3.2). Through cuts on the numbers of fired counters and on the total charge, the system is able to provide rough centrality triggers. The detector is also able to measure azimuthal distributions, which are important for estimating the reaction planes in Pb-Pb collisions. Finally, the VZERO is able to separate beam-beam interactions from background events (e.g. from beam-gas interactions), either at trigger level or in offline analyses. The identification of the background events is possible through the measurement of the time-of-flight difference between the two VZERO-A and VZERO-C detectors.

[1] In ALICE physics papers, this is sometimes referred to as the V0 detector. To avoid any confusion with V0 particles, which is a general term for a neutral particle decaying into two charged daughter tracks (e.g. Λ and K^0_S), we use the VZERO notation.

Chapter 4: Femtoscopy

4.1 Introduction

Femtoscopy is an experimental method used to extract spatio-temporal information about the systems created in particle collisions. With this method, one exploits two-particle (or higher) relative-momentum correlations to probe the space-time freeze-out structure of the dynamic matter at the femtometer scale (10^{-15} m). The first application exploiting a similar technique came in the 1950s in the field of astrophysics. Hanbury-Brown and Twiss utilized correlations of radio-wavelength photons to extract angular sizes of stars and other celestial bodies [120, 121]. Independently in 1960, correlations between identical pions were shown to be sensitive to the source dimensions in proton-antiproton collisions, the so called "GGLP effect" (the study was done by Goldhaber, Goldhaber, Lee, and Pais with the Bevatron at Lawrence Berkeley National Lab) [122]. Throughout the 1970s the method was refined, and other classes or correlations were shown to be useful for such measurements, such as the strong and Coulomb interactions. The GGLP and HBT effects differ in their theoretical framework, but are quite similar both in their techniques and in the information they extract. In the end, "HBT interferometry" emerged as the preferred nomenclature within the nuclear community for such measurements. Today, the terms femtoscopy and HBT interferometry are oftentimes used interchangeably. However, to many, HBT refers specifically to femtoscopic measurements conducted with identical bosons, as was done in the original analyses. In a more general sense, the term femtoscopy includes any measurement utilizing particle correlations to extract spatio-temporal information.

4.2 Theoretical formalism

4.2.1 Theoretical correlation function construction

The two-particle correlation function used in femtoscopy is defined as the ratio of the Lorentz-invariant two-particle and single-particle spectra [123, 124]

$$C_{ab}(\mathbf{p_a}, \mathbf{p_b}) = \frac{E_a E_b \frac{dN_{ab}}{d^3p_a d^3p_b}}{\left(E_a \frac{dN_a}{d^3p_a}\right)\left(E_b \frac{dN_b}{d^3p_b}\right)} \tag{4.1}$$

The goal of analyzing such experimentally measured correlation functions is the extraction of space-time characteristics of the expanding system. The single-particle distributions in the denominator of Eq. 4.1 can be related to the single-particle emission function, $s(x,p)$, as

$$E_a \frac{dN_a}{d^3p_a} = \int d^4x_a s(x_a, p_a) \tag{4.2}$$

The single-particle emissions function is a single-particle Wigner density, which gives the probability of emitting a particle of momentum p from a space-time point x. If we assume that the emission process is initially uncorrelated, then the pair source distribution may be expressed as the product of the single-particle source functions, $S_{ab}(x_a, p_a, x_b, p_b) = s_a(x_a, p_a)s_b(x_b, p_b)$. The two-particle distribution may then be written as

$$E_a E_b \frac{dN_{ab}}{d^3p_a d^3p_b} = \int d^4x_a d^4x_b s_a(x_a, p_a) s_b(x_b, p_b) |\Psi(x_a, p_a, x_b, p_b)|^2 \tag{4.3}$$

where the two-particle wave-function, Ψ, includes the proper (anti)symmetrization for the case of identical particles. This leads to the following form of the correlation function:

$$C_{ab}(\mathbf{p_a}, \mathbf{p_b}) = \frac{\int d^4x_a d^4x_b s_a(p_a, x_a) s_b(p_b, x_b) |\Psi(x_a, p_a, x_b, p_b)|^2}{\int d^4x_a s_a(p_a, x_a) \int d^4x_b s_b(p_b, x_b)} \tag{4.4}$$

Note, the derivation so far assumes that higher order (anti)symmetrization can be neglected; the modification to the single-particle spectra (and to the two-particle correlation function) was found to be negligible for heavy-ion femtoscopic measurement, for which the freeze-out phase-space density is well below unity [123].

It is more convenient to express the correlation function in terms of the total momentum, $\mathbf{P}$, and relative momentum $\boldsymbol{k}^*$, where the four-vectors P^μ and k^μ are

$$\begin{aligned} P^\mu &\equiv p_a^\mu + p_b^\mu \\ k^\mu &= \frac{(p_a - p_b)^\mu}{2} - \frac{(p_a - p_b) \cdot P}{2P^2} P^\mu \end{aligned} \tag{4.5}$$

The last term in the definition of k^μ projects out the temporal component in the two-particle rest frame [125]. In the pair rest frame (PRF), where $\mathbf{P} = 0$, this reduces to $k^\mu = (0, \boldsymbol{k}^*)$. Therefore, $\boldsymbol{k}^*$ is the momentum of the first particle in the PRF, and half the pair relative momentum in that frame. Throughout the remainder of this document, all variables with an asterisks (*) refer to their values in the PRF. For the case of identical particle femtoscopy, instead of k^μ, one typically studies the correlations as a function of the pair relative momentum, $q^\mu = 2k^\mu$. Note, $(p_a - p_b) \cdot P = |p_a|^2 - |p_b|^2 = m_a^2 - m_b^2$. Therefore, for identical particle analyses, k^μ reduces to the more friendly form, $k^\mu = \frac{1}{2}(p_a - p_b)$.

Due to the fact that the measured particles are on-shell, P and k are orthogonal:

$$\begin{aligned} P^\mu k_\mu &= (p_a + p_b)^\mu \left(\frac{(p_a - p_b)_\mu}{2} - \frac{(p_a - p_b) \cdot P}{2P^2} P_\mu \right) \\ &= \frac{1}{2}(m_a^2 - m_b^2) - \frac{(p_a - p_b) \cdot P}{2P^2} P^2 \\ &= \frac{1}{2}(m_a^2 - m_b^2) - \frac{1}{2}(m_a^2 - m_b^2) = 0 \\ \Rightarrow P^\mu k_\mu &= 0 \end{aligned} \tag{4.6}$$

However, the momentum combinations P and k will generally be off-shell, $P_0 \neq E(\mathbf{P})$ (i.e. $(E_a + E_b) \neq \sqrt{(m_a + m_b)^2 + \mathbf{P}^2}$). Introducing the center-of-mass four-coordinate R and relative separation r [126]

$$\begin{aligned} R &= \left[(p_a \cdot P) x_a + (p_b \cdot P) x_b \right] / P^2 \\ r &= x_a - x_b \end{aligned} \tag{4.7}$$

Eq. 4.4 may be written as

$$C_{ab}(\mathbf{P},\mathbf{k}) = \frac{\int d^4x_a d^4x_b s_a(\frac{p_1\cdot P}{P^2}P + k, x_a) s_b(\frac{p_2\cdot P}{P^2}P - k, x_b)|\Psi(r,k)|^2}{\int d^4x_a s_a(\frac{p_1\cdot P}{P^2}P + k, x_a)\int d^4x_b s_b(\frac{p_2\cdot P}{P^2}P - k, x_b)} \tag{4.8}$$

which, for identical particles, reduces to

$$C_{ab}(\mathbf{P},\mathbf{k}) = \frac{\int d^4x_a d^4x_b s_a(\frac{P}{2} + k, x_a) s_b(\frac{P}{2} - k, x_b)|\Psi(r,k)|^2}{\int d^4x_a s_a(\frac{P}{2} + k, x_a)\int d^4x_b s_b(\frac{P}{2} - k, x_b)} \tag{4.9}$$

Next, we impose the smoothness approximation [127], which assumes that the source function has a sufficiently weak momentum dependence at low-k, and implies

$$\begin{aligned} s_a\left(\frac{p_a\cdot P}{P^2}P + k, x_a\right) &\approx s_a\left(\frac{p_a\cdot P}{P^2}P, x_a\right) \equiv s_a(\bar{p}_a, x_a) \\ s_b\left(\frac{p_b\cdot P}{P^2}P - k, x_b\right) &\approx s_b\left(\frac{p_b\cdot P}{P^2}P, x_b\right) \equiv s_b(\bar{p}_b, x_b) \end{aligned} \tag{4.10}$$

Therefore, the two-particle relative momentum correlation function may be written theoretically by the Koonin-Pratt equation [128, 129]

$$\begin{aligned} C_{ab}(\mathbf{P},\mathbf{k}^*) &= \int d^3r^* S_{\mathbf{P}}(\mathbf{r}^*)|\Psi(\mathbf{k}^*,\mathbf{r}^*)|^2 \\ S_{\mathbf{P}}(\mathbf{r}^*) &\equiv \frac{\int d^4x_a d^4x_b s_a(\bar{p}_a, x_a) s_b(\bar{p}_b, x_b)\delta(\mathbf{r}^* - \mathbf{x}^*{}_a + \mathbf{x}^*{}_b)}{\int d^4x_a d^4x_b s_a(\bar{p}_a, x_a) s_b(\bar{p}_b, x_b)} \end{aligned} \tag{4.11}$$

where $S_{\mathbf{P}}(\mathbf{r}^*)$ is the pair source distribution, $\Psi_{\mathbf{k}^*}(\mathbf{r}^*)$ is the two-particle wave-function, and k^* is the momentum of one particle in the pair rest frame. $S_{\mathbf{P}}(\mathbf{r}^*)$ is normalized to unity ($\int d^3r^* S_{\mathbf{P}}(\mathbf{r}^*) = 1$), and gives the emission probability density for two particles of pair momentum $\mathbf{P}$ at relative distance $\mathbf{r}^*$ in the PRF when averaged over all emission times. The probability of emitting a single particle of momentum p from space-time point x is $s(p,x)$, and is evaluated at a momentum such the total momentum is $\mathbf{P}$ and each particle has the same velocity [125] (i.e. $\bar{p}_i = [p_i \cdot P/P^2]P$). Equation 4.11 reveals the limitations of femtoscopy; at best, we are able to probe the distribution of relative positions of particles with identical velocities and total momentum $\mathbf{P}$ as they move in an asymptotic state. Therefore, we do not measure the enture size of the source, but rather the "regions of homogeneity" [130].

λ factor

In experiment, the measured correlation function can be distorted by two distinct contaminations. In addition to containing primary particles of interest, the final sample of pairs will unavoidably contain misidentified particles and particles originating from resonance decays. Residual correlations from resonance feed-down can affect the correlation non-trivially, as will be discussed in Sec. 6.2. However, for now, we assume that the contaminations described above result simply in pairs of uncorrelated particles in our sample. In such a case, the contaminations lead to an attenuation of the femtoscopic signal observed in the correlation function, which is typically accounted for experimentally by introducing a λ parameter into the fit. The λ parameter may be introduced in Eq. 4.11 by dividing the source distribution into correlated and uncorrelated contributions, $S(\mathbf{r}^*) = \lambda S_{\text{corr.}} + (1-\lambda)S_{\text{uncorr.}}$, where both $S_{\text{corr.}}$ and $S_{\text{uncorr.}}$ integrate to unity. The uncorrelated pairs introduce a random signal, which integrates to unity, and Eq. 4.11 becomes

$$C(\mathbf{P}, \mathbf{k}^*) = (1-\lambda) + \lambda \int S(\mathbf{r}^*)|\Psi(\mathbf{k}^*, \mathbf{r}^*)|^2 d^3\mathbf{r}^* \tag{4.12}$$

In the case of a system with degenerate states, e.g. due to (iso)spin, the above equation is slightly altered, and becomes

$$C(\mathbf{P}, \mathbf{k}^*) = (1-\lambda) + \lambda \sum_S \rho_S \int S(\mathbf{r}^*)|\Psi^S(\mathbf{k}^*, \mathbf{r}^*)|^2 d^3\mathbf{r}^* \tag{4.13}$$

where ρ_S is the normalized emission probability for the state S with pair wave-function Ψ^S.

4.2.2 Coordinate system

In most femtoscopic analyses, a Cartesian coordinate system is used (however, utilizing spherical coordinates has many advantages, and will likely become more prevalent in the field moving forward, see Sec. 4.3.1). Within the Cartesian representation, one defines the coordinate axes such that the pair momentum, $\mathbf{P}$, has only two non-zero components

$$\mathbf{P} = (P_\perp, 0, P_\parallel) \tag{4.14}$$

This is the *out-side-long* prescription. The *longitudinal* (or *long*) axis is chosen to be aligned with the beam. The transverse momentum vector, $\mathbf{P}_\mathrm{T}$ (i.e. the projection of the total momentum onto a plane perpendicular to the beam), defines the *outward* (or *out*) direction. Finally, the *sideward* (or *side*) axis is orthogonal to the other two.

Typically, the correlation function in relativistic heavy-ion collisions is presented in either the **L**ongitudinally **C**o-**M**oving **S**ystem (LCMS) or the **P**air **R**est **F**rame (PRF). The LCMS system is defined such that the pair's total momentum in the longitudinal direction vanishes. In boost-invariant systems, observables expressed in the LCMS frame are independent of $P_\parallel$, and the source has reflection symmetry about the r_long=0 plane. The PRF is defined such that the total momentum of the pair vanishes. The PRF can be obtained from the LCMS frame by a Lorentz boost in the outward direction. The PRF is commonly used in non-identical particle studies, and is the frame in which the two-particle relative wave-function is most conveniently expressed.

4.2.3 Gaussian parameterization

In order to extract the spatio-temporal information about the homogeneity regions, a Gaussian source function is typically used. This form is able to capture the bulk properties of the emitting source with a minimal number of parameters. The most general form on a Gaussian source is of the form [131, 132]

$$S(x, \mathbf{P}) \propto \exp\left[-\frac{1}{2}\tilde{x}^\mu(\mathbf{P}) B_{\mu\nu}(\mathbf{P}) \tilde{x}^\nu(\mathbf{P})\right] \tag{4.15}$$

where

$$\begin{aligned} \tilde{x}^\mu(\mathbf{P}) &= x^\mu - \bar{x}^\mu(\mathbf{P}) \\ \bar{x}^\mu(\mathbf{P}) &= \langle x^\mu \rangle \\ (B^{-1})_{\mu\nu}(\mathbf{P}) &= \langle \tilde{x}_\mu \tilde{x}_\nu \rangle \end{aligned} \tag{4.16}$$

and brackets $\langle f \rangle$ denote the average over the emission function

$$\langle f(x) \rangle = \frac{\int d^4x f(x) S(x,P)}{\int d^4x S(x,P)} \tag{4.17}$$

Therefore, $\bar{x}^\mu(\mathbf{P})$ is the effective source center, i.e. the point of maximum probability of emission with momentum $\mathbf{P}$, and $\tilde{x}^\mu(\mathbf{P})$ is the offset from the center.

In general, for a multivariate normal distribution of dimension d

$$f(\mathbf{x}) = \frac{1}{(2\pi)^{d/2}|\mathbf{\Sigma}|^{1/2}} \exp\left\{-\frac{1}{2}(\mathbf{x}-\boldsymbol{\mu})^T\mathbf{\Sigma}^{-1}(\mathbf{x}-\boldsymbol{\mu})\right\} \tag{4.18}$$

there are a total of $\frac{1}{2}d(d+3)$ independent parameters. Within the mean vector $\boldsymbol{\mu}$ there are d independent parameters, and within the symmetric covariance matrix $\mathbf{\Sigma}$ there are $\frac{1}{2}d(d+1)$ independent parameters. Therefore, for our implementation here, the most general form includes 14 independent parameters: 10 parameters for the symmetric matrix $B_{\mu\nu}$, and 4 parameters for offsets $\bar{x}^\mu$. As the source depends only on the distribution of relative spatial coordinates in the pair frame, only 9 parameters remain: the vector difference between average emission points, and a symmetric 3×3 covariance matrix [125]. The diagonal components of the matrix represent the Gaussian widths, while the off-diagonal elements describe the orientation of the three dimensional ellipse [123]. In many cases, reflection symmetries can be used to eliminate certain terms. A diagram highlighting a three-dimensional source with tilt in the out-long and out-side directions is shown in Fig. 4.1.

4.2.4 Identical and non-interacting particles

In this section, I will specifically focus on femtoscopy with identical and non-interacting pions. The purpose here is two-fold. First, identical pion correlations have historically been the most prevalent studies within femtoscopy. Second, although the process responsible for their correlation signal is less intuitive, the math involved with two non-interacting and identical spin-0 bosons is greatly simplified, and the implications of the results more intuitive. These analyses are typically done with charged pions ($\pi^\pm$), largely due to the difficulty in detecting their neutral brothers

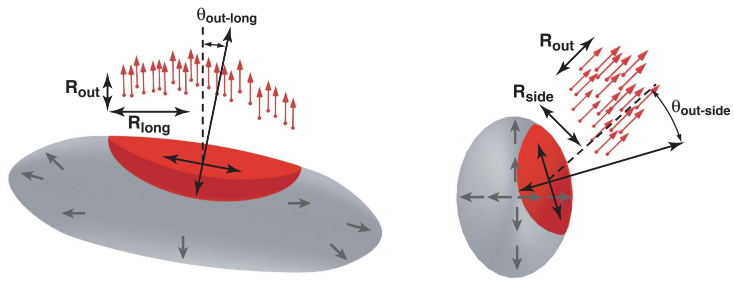

Figure 4.1: A cartoon demonstrating the emission picture for non-central heavy-ion collisions [123]. The figure shows that different length scales are possible in the different directions, as well as the fact that the principal axes need not perfectly align with the out-side-long axes. The figure highlights a source with out-long and out-side cross terms. The left shows a snapshot from alongside of the beam, and right right shows a view looking directly down the beam pipe.

(π^0). Although these pairs interact via both the Coulomb and strong interactions, treating them solely based on their quantum statistical properties captures the major features of their correlation functions.

For identical, non-interacting pions, the properly symmetrized two-particle wave-function Ψ, takes the form:

$$\begin{aligned}\Psi_{\pi\pi} &= \frac{1}{\sqrt{2}}\left(\psi_{p_1p_2}+\psi_{p_2p_1}\right)\\ &= \frac{1}{\sqrt{2}}\left(e^{-ip_1\cdot x_1}e^{-ip_2x_2}+e^{-ip_2\cdot x_1}e^{-ip_1x_2}\right)\\ &= \frac{1}{\sqrt{2}}e^{-i\frac{P}{2}\cdot(x_1+x_2)}\left(e^{-ik\cdot r}+e^{ik\cdot r}\right)\end{aligned} \tag{4.19}$$

where $P = p_1 + p_2$, $k = \frac{1}{2}(p_1 - p_2)$, and $r = x_1 - x_2$. The modulus of the two-particle wave-function squared, $|\Psi_{\pi\pi}|^2$, is easily found to be:

$$\begin{aligned}|\Psi_{\pi\pi}|^2 &= \frac{1}{2}\left[e^{-i\frac{P}{2}\cdot(x_1+x_2)}\left(e^{-ik\cdot r}+e^{ik\cdot r}\right)\right]\left[e^{i\frac{P}{2}(x_1+x_2)}\left(e^{ikr}+e^{-ikr}\right)\right]\\ &= 1+\cos(2k\cdot r)\end{aligned} \tag{4.20}$$

This clearly shows that the signal will be enhanced at low relative momenta.

The case is very different for identical fermions, where the overall wave-function is antisymmetric. For example, when dealing with a pair of identical spin-$\frac{1}{2}$ particles, let's say two neutrons for the purpose of this demonstration (nn), the situation is slightly more complicated due to the fact that the system can be in a spin singlet ($S = 0$ and antisymmetric) or triplet ($S = 1$ and symmetric) state. In general, the wave-function will be a linear combination of these component states, with weights proportional to the probability of observing each state. In the case of unpolarized emission, the weights are proportional to the statistical spin factors, $2S + 1$, giving a ratio for singlet to triplet of 1:3 in this case. The state vector for two identical spin-$\frac{1}{2}$ particles must be antisymmetric; therefore, the symmetric spin triplet state must combine with an antisymmetric spatial component, and the antisymmetric spin singlet state with a symmetric spatial component, for the overall state to be antisymmetric. Assuming unpolarized emission, the modulus of the wave-function squared for the nn system is

$$|\Psi_{nn}|^2 = \frac{1}{2}\left[\frac{1}{4}|\psi^{S=0}_{-k^*_{nn}} + \psi^{S=0}_{k^*_{nn}}|^2 + \frac{3}{4}|\psi^{S=1}_{-k^*_{nn}} - \psi^{S=1}_{k^*_{nn}}|^2\right] \tag{4.21}$$

where $S = 0$ is the spin singlet state, and $S = 1$ the triplet state. This form was used in fitting the pp correlation function in Ref. [133]. In the case of non-interacting particles, we have $\psi^{S=0}_{k^*_{nn}} = \psi^{S=1}_{k^*_{nn}} = e^{-i\frac{P}{2}\cdot(x_1+x_2)}e^{-ik\cdot r}$, and therefore

$$|\Psi_{nn}|^2 = \frac{1}{4}\left[1 + \cos(2k\cdot r)\right] + \frac{3}{4}\left[1 - \cos(2k\cdot r)\right] \quad = 1 - \frac{1}{2}\cos(2k\cdot r) \tag{4.22}$$

The triplet state overpowers the singlet state with the 3:1 ratio, and therefore the correlation function will have a minimum as $k \to 0$. However, we see that the presence of the singlet spin state saves the signal from going to zero, as one might naively guess with a system of identical fermions.

Of course, up to this point in the section, only the two-particle wave-functions have been discussed. To understand our femtoscopic correlation functions, the wave-function must be integrated over the pair emission source distribution. Taking our Gaussian ansatz (Eq. 4.15), plugging it into our expression for the correlation function (Eq. 4.11), assuming the appropriate wave-function for identical non-interacting bosons, the correlation function takes the general form

$$C(\mathbf{q},\mathbf{P}) = 1 + \exp\left[-q^\mu q^\nu \langle \tilde{x}_\mu \tilde{x}_\nu \rangle(\mathbf{P})\right]. \tag{4.23}$$

For identical non-interacting spin-1/2 fermions, the correlation function instead would be

$$C(\mathbf{q},\mathbf{P}) = 1 - \frac{1}{2}\exp\left[-q^\mu q^\nu \langle \tilde{x}_\mu \tilde{x}_\nu \rangle(\mathbf{P})\right]. \tag{4.24}$$

From the above expressions, it is obvious that we cannot extract the pair source size, but only the second moment of the effective source distribution of particles with momentum $\mathbf{P}$. Furthermore, as mentioned previously, femtoscopy is not able to measure the entire source, but only the regions of homogeneity. Or, in the words of Ref. [124], femtoscopy measures the size of the system through a filter of wavelength $\mathbf{P}$.

To relate the correlation function in Eq. 4.23 to experimental data, we must eliminate one of the four components of q via the mass shell constraint. This causes a non-trivial mixing of spatial and temporal components of the extracted radii. In the following, the Greek indices (μ,ν) run over four-vectors and vary from 0 to 3, while Roman indices (i,j) run over three-vectors and vary from 1 to 3. The mass-shell constraint (see Eq. 4.6), implies

$$\begin{aligned} &P^\mu q_\mu = 0 \\ &\Rightarrow q^0 = \frac{\mathbf{P}\cdot\mathbf{q}}{P^0} \equiv \boldsymbol{\beta}\cdot\mathbf{q} = \beta^i q^i = -\beta_i q^i \end{aligned} \tag{4.25}$$

where $\boldsymbol{\beta} \equiv \boldsymbol{P}/P^0$ describes the velocity of the pair. Eq. 4.25 can then be used to rewrite $q^\mu q^\nu \langle \tilde{x}_\mu \tilde{x}_\nu \rangle(\mathbf{P})$ as

$$\begin{aligned} q^\mu q^\nu \langle \tilde{x}_\mu \tilde{x}_\nu \rangle &= q^\mu q^0 \langle \tilde{x}_\mu \tilde{x}_0 \rangle + q^\mu q^j \langle \tilde{x}_\mu \tilde{x}_j \rangle \\ &= q^0 q^0 \langle \tilde{x}_0 \tilde{x}_0 \rangle + q^i q^0 \langle \tilde{x}_i \tilde{x}_0 \rangle + q^0 q^j \langle \tilde{x}_0 \tilde{x}_j \rangle + q^i q^j \langle \tilde{x}_i \tilde{x}_j \rangle \\ &= (-\beta_i q^i)(-\beta_j q^j)\langle \tilde{x}_0 \tilde{x}_0 \rangle + 2q^i(-\beta_j q^j)\langle \tilde{x}_i \tilde{x}_0 \rangle + q^i q^j \langle \tilde{x}_i \tilde{x}_j \rangle \\ &= q^i q^j \left\{ \langle \tilde{x}_i \tilde{x}_j \rangle - 2\beta_j \langle \tilde{x}_0 \tilde{x}_i \rangle + \beta_i \beta_j \langle \tilde{x}_0 \tilde{x}_0 \rangle \right\} \\ &= q^i q^j \langle \left(\tilde{x}_i - \beta_i \tilde{t}\right)\left(\tilde{x}_j - \beta_j \tilde{t}\right) \rangle \end{aligned} \tag{4.26}$$

Therefore, the correlation function in Eq. 4.23 may be written as

$$
\begin{aligned}
C(\mathbf{q},\mathbf{P}) &= 1 + \exp\left[-q^i q^j R_{ij}^2(\mathbf{P})\right] \\
R_{ij}^2(\mathbf{P}) &= \langle(\tilde{x}_i - \beta_i \tilde{t})(\tilde{x}_j - \beta_j \tilde{t})\rangle(\mathbf{P})
\end{aligned}
\tag{4.27}
$$

The symmetric matrix $R_{ij}^2(\mathbf{P})$ has six independent coefficients, which are functions of three variables: the pair rapidity, the magnitude of $P_\perp$ and its azimuthal angle with respect to the impact parameter $\mathbf{b}$ [124]. In the out-side-long (osl) coordinate system, the diagonal elements are

$$
\begin{aligned}
R_{11}^2(\mathbf{P}) &= R_o^2(\mathbf{P}) = \langle(\tilde{x}_o - \beta_\perp \tilde{t})^2\rangle(\mathbf{P}) \\
R_{22}^2(\mathbf{P}) &= R_s^2(\mathbf{P}) = \langle \tilde{x}_s^2 \rangle(\mathbf{P}) \\
R_{33}^2(\mathbf{P}) &= R_l^2(\mathbf{P}) = \langle(\tilde{x}_l - \beta_l \tilde{t})^2\rangle(\mathbf{P})
\end{aligned}
\tag{4.28}
$$

and the off diagonal elements are

$$
\begin{aligned}
R_{12}^2(\mathbf{P}) &= R_{os}^2(\mathbf{P}) = \langle(\tilde{x}_s - \beta_\perp \tilde{t})\tilde{x}_s\rangle(\mathbf{P}) \\
R_{23}^2(\mathbf{P}) &= R_{sl}^2(\mathbf{P}) = \langle \tilde{x}_s(\tilde{x}_l - \beta_l \tilde{t})\rangle(\mathbf{P}) \\
R_{13}^2(\mathbf{P}) &= R_{ol}^2(\mathbf{P}) = \langle(\tilde{x}_o - \beta_\perp \tilde{t})(\tilde{x}_l - \beta_l \tilde{t})\rangle(\mathbf{P})
\end{aligned}
\tag{4.29}
$$

From these equations, it is clear that the femtoscopic radii mix the space-time characteristics of the source in a nontrivial way.

4.2.5 Final state interactions

Consider a pair of identical particles with four-momenta p_1 and p_2, spin $j_1 = j_2 = j$, in space-time points x_1 and x_2. We assume the interaction may depend on the total spin state S of the system, where S can take on values $j_1 + j_2, j_1 + j_2 - 1, ..., j_1 - j_2$, which simplifies to $2j \geq S \geq 0$ for the case of identical particles. The modulus squared of the two particle wave-function, $|\Psi|^2$, receives contributions from each spin state with corresponding two-particle wave-function ψ^S. If ρ_S is the normalized probability for a state with total spin S ($\sum_S \rho_S = 1$), $|\Psi|^2$ may be written as

$$
\begin{aligned}
|\Psi|^2 = \frac{1}{2} &\sum_{S=\text{even (odd)}} \rho_S \left|\psi_{p_1 p_2}^S(x_1, x_2) + (-1)^S \psi_{p_2 p_1}^S(x_1, x_2)\right|^2 \\
+ \frac{1}{2} &\sum_{S=\text{odd (even)}} \rho_S \left|\psi_{p_1 p_2}^S(x_1, x_2) - (-1)^S \psi_{p_2 p_1}^S(x_1, x_2)\right|^2
\end{aligned}
\tag{4.30}
$$

for bosons (fermions). For the case of unpolarized emission, $\rho_S = (2S+1)/[(2j_1+1)(2j_2+1)]$, which for identical particles reduces to $\rho_S = (2S+1)/(2j+1)^2$.

Equation 4.30 maintains the proper overall symmetrization of the two-particle wave-functions, which is the combination of the spin and spatial components, and must always be symmetric for bosons and antisymmetric for fermions. The spin state for a pair of bosons (fermions) with $S = \text{even}\,(\text{odd})$ is symmetric, while that for a boson (fermion) pair with $S = \text{odd}\,(\text{even})$ is antisymmetric (symmetric). Eq. 4.30 takes care of the necessary symmetrization regardless of whether the particles are bosons or fermions, and regardless of the spin state (see Table 4.1). For instance, since the spin state for a boson pair with $S = \text{even}$ is symmetric, the accompanying spatial component given in Eq. 4.30 is also symmetric to keep the overall wave-function symmetric. The spin state for a fermion with $S = \text{odd}$ is symmetric, so the accompanying spatial component given in Eq. 4.30 is antisymmetric to make the overall wave-function antisymmetric.

	S	Ψ_{spin}	Ψ_{spatial}	Ψ_{total}
Bosons	Even	Symm	Symm	Symm
	Odd	Anti	Anti	Symm
Fermions	Even	Anti	Symm	Anti
	Odd	Symm	Anti	Anti

Table 4.1: Demonstration of the symmetrization of the spatial component (Ψ_{spatial}) of the wave-function from Eq. 4.30 maintaining the proper symmetrization of the total wave-function for both fermions and bosons in spin state S. In the table, Symm=symmetric and Anti=antisymmetric.

If we simplify matters by assuming unpolarized emission with identical particles whose final state interaction does not depend on their spin state, instead of Eq. 4.30, we have [134]

$$
\begin{aligned}
|\Psi|^2 = & \frac{j+1}{2(2j+1)} \left|\psi_{p_1p_2}(x_1,x_2) + (-1)^{2j}\psi_{p_2p_1}(x_1,x_2)\right|^2 \\
& + \frac{j}{2(2j+1)} \left|\psi_{p_1p_2}(x_1,x_2) - (-1)^{2j}\psi_{p_2p_1}(x_1,x_2)\right|^2
\end{aligned}
\tag{4.31}
$$

where $(j+1)/(2j+1)$ and $j/(2j+1)$ are the fractions of even (odd) and odd (even) identical two-particle spin states, respectively, for spin-j bosons (fermions). Using these equations, for the case of non-interacting spin-0 identical particles (see App. D.1), we recover Eq. 4.20, as we should. For the case of interacting identical spin-1/2 particles, we instead have Eq. 4.21, and for the case of non-interacting identical spin-1/2 particles we have Eq. 4.22.

Strong Interaction Only

For the case of interacting particles, the non-symmetrized two-particle wave-function, ψ, may be written as [134]

$$\psi_{p_1p_2}(x_1,x_2) = e^{-iP\cdot R}\left(e^{-ik\cdot r} + \phi_{p_1p_2}(r)\right) \tag{4.32}$$

where, P and k are the total and relative momentum as defined in Eq. 4.5, R and r are the center-of-mass coordinate and relative separation as defined in Eq. 4.7. Here, $\phi_{p_1p_2}(r)$ describes the final state interactions (FSI) of the particles. The interaction only depends on the relative position and motion of the two particles, not the center-of-mass motion. Accordingly, the factor $e^{-iP\cdot R}$ drops out when calculating $|\psi|^2$, so we omit it from the rest of the discussion. Assuming that the range of the interaction potential is smaller than the distance between the emission points, $\phi_{p_1p_2}(r)$ may be expressed as [134]

$$\phi_{p_1p_2}(r) = f(k^*)\Phi_{p_1p_2}(r) \tag{4.33}$$

where, in the effective range approximation, $f(k^*)$ is of the form

$$f(k^*) = \left(\frac{1}{f_0} + \frac{1}{2}d_0k^{*2} - ik^*\right)^{-1} \tag{4.34}$$

where k^* is $|\boldsymbol{k}^*|$. Furthermore, if we assume the magnitude of the momentum difference is much smaller than the mass of the particles ($k^* \ll m$), and that the particles are emitted at the same time in the pair rest frame, $\Phi_{p_1p_2}(r)$ reduces to

$$\Phi_{p_1p_2}(r) = \frac{e^{ik^*r}}{r} \tag{4.35}$$

In other words, $\Phi_{p_1p_2}(r)$ is a diverging spherical wave. Therefore, we have $\psi_{p_1p_2} = e^{-ik^*\cdot r} + \phi_{p_1p_2}(r)$, where $\phi_{p_1p_2}(r)$ is independent of the directions of the vectors $\boldsymbol{k}^*$ and $\boldsymbol{r}$ [135].

Assuming the final state interactions are independent of the spin state, for identical interacting particles, Eq. 4.31 becomes (see App. D.2)

$$|\Psi|^2 = 1 + g_0 \cos(2k \cdot r) + g_i \left\{ |\phi_{p_1p_2}(r)|^2 + 2\Re[\phi_{p_1p_2}(r)] \cos(k \cdot r) \right\} \tag{4.36}$$

where $g_0 = (-1)^{2j}/(2j+1)$ and $g_i = 1 + g_0$.

For non-identical interacting particles, where we need not worry about the symmetrization of the wave-function, we have (see Appendix D.3):

$$\begin{aligned} |\Psi_{p_1p_2}|^2 &= 1 + |f(k^*)\Phi_{p_1p_2}|^2 + e^{ik\cdot x} f(k^*)\Phi_{p_1p_2} + e^{-ik\cdot x}\tilde{f}(k^*)\tilde{\Phi}_{p_1p_2} \\ &= 1 + |f(k^*)\Phi_{p_1p_2}|^2 + 2\Re[f(k^*)\Phi_{p_1p_2}]\cos(k\cdot r) - 2\Im[f(k^*)\Phi_{p_1p_2}]\sin(k\cdot r) \end{aligned} \tag{4.37}$$

where $\tilde{f}(k^*)$ and $\tilde{\Phi}_{p_1p_2}(r)$ are the complex conjugates of $f(k^*)$ and $\Phi_{p_1p_2}(r)$.

If we allow the interaction, and therefore the two-particle wave-function, to depend on the total spin S of the system (but not on the spin projections), things change slightly. Instead of grouping all odd and even total spins together, as was done in deriving Eqs. 4.36 and 4.37, we need to keep track of their individual contributions, as their wave-functions will be different. When combining all of the various states with different spin, they must be combined with a weight factor ρ_S, the normalized emission probability for such a state ($\sum_S \rho_S = 1$). In this case, we find (see Appendix D.4)

$$
\begin{aligned}
|\Psi|^2 = 1 &+ \left(\sum_{S=\text{even}} \rho_S - \sum_{S=\text{odd}} \rho_S\right) \cos(2k \cdot r) \\
&+ 2 \sum_{S=\text{even}} \rho_S \left\{|\phi^S_{p_1p_2}(r)|^2 + 2\Re[\phi^S_{p_1p_2}(r)] \cos(k \cdot r)\right\} \\
= 1 &+ g'_0 \cos(2k \cdot r) + 2 \sum_{S=\text{even}} \rho_S \left\{|\phi^S_{p_1p_2}(r)|^2 + 2\Re[\phi^S_{p_1p_2}(r)] \cos(k \cdot r)\right\}
\end{aligned} \tag{4.38}
$$

where $g'_0 = \sum_{S=\text{even}} \rho_S - \sum_{S=\text{odd}} \rho_S$. In the case of unpolarized emission for identical particle pairs, $\rho_S = (2S+1)/(2j+1)^2$, and we have $g'_0 = g_0 = (-1)^{2j}/(2j+1)$.

The case of interacting non-identical particles can be written down immediately from Eq. 4.37

$$
|\Psi_{p_1p_2}|^2 = \sum_S \rho_S \left\{1 + |\phi^S_{p_1p_2}|^2 + 2\Re[\phi^S_{p_1p_2}] \cos(k \cdot r) - 2\Im[\phi^S_{p_1p_2}] \sin(k \cdot r)\right\} \tag{4.39}
$$

where $\phi_{p_1p_2}(r) = f(k^*)\Phi_{p_1p_2}(r)$, and for the case of unpolarized emission, $\rho_S = (2S+1)/[(2j_1+1)(2j_2+1)]$.

Now, up to this point, we have discussed only the wave-functions. Within femtoscopy, this essentially amounts to assuming point-like sources. In the more realistic scenario, the correlation function should be averaged over the space-time distribution of particle sources. This is done through the Koonin-Pratt equation, Eq. 4.11, introduced in Sec. 4.2.1. In the case of one-dimensional analyses, a spherically symmetric Gaussian pair emission source in the PRF with size R_{inv} is often assumed

$$
S(r) \propto \exp\left[-\frac{r^2}{4R^2_{\text{inv}}}\right]. \tag{4.40}
$$

As a side note, a more realistic source would allow for different radii in the out, side and long directions. Furthermore, for non-identical particle femtoscopy between species a and b, each single-particle source should be given unique offsets, $\mu_{a,i}$ and

$\mu_{b,i}$, where i=o,s,l. In such a case the pair emission source would be

$$S_{ab}(\mathbf{r}) \propto \int \exp\left(-\frac{(r_{a,\text{out}}-\mu_{a,\text{out}})^2}{2R_{a,\text{out}}^2}-\frac{(r_{a,\text{side}}-\mu_{a,\text{side}})^2}{2R_{a,\text{side}}^2}-\frac{(r_{a,\text{long}}-\mu_{a,\text{long}})^2}{2R_{a,\text{long}}^2}\right)$$
$$\times \exp\left(-\frac{(r_{b,\text{out}}-\mu_{b,\text{out}})^2}{2R_{b,\text{out}}^2}-\frac{r_{b,\text{side}}-\mu_{b,\text{side}})^2}{2R_{b,\text{side}}^2}-\frac{r_{b,\text{long}}-\mu_{b,\text{long}})^2}{2R_{b,\text{long}}^2}\right)$$
$$\times\, \delta(r_{\text{out}}-r_{a,\text{out}}+r_{b,\text{out}})dr_{a,\text{out}}dr_{b,\text{out}}$$
$$\times\, \delta(r_{\text{side}}-r_{a,\text{side}}+r_{b,\text{side}})dr_{a,\text{side}}dr_{b,\text{side}}$$
$$\times\, \delta(r_{\text{long}}-r_{a,\text{long}}+r_{b,\text{long}})dr_{a,\text{long}}dr_{b,\text{long}} \tag{4.41}$$

Using the results from Appendix C.2, we find

$$\begin{aligned} S_{ab}(\mathbf{r}) \propto\, & \exp\left(-\frac{[r_{\text{out}}-(\mu_{a,\text{out}}-\mu_{b,\text{out}})]^2}{2(R_{a,\text{out}}^2+R_{b,\text{out}}^2)}\right) \\ & \times \exp\left(-\frac{[r_{\text{side}}-(\mu_{a,\text{side}}-\mu_{b,\text{side}})]^2}{2(R_{a,\text{side}}^2+R_{b,\text{side}}^2)}\right) \\ & \times \exp\left(-\frac{[r_{\text{long}}-(\mu_{a,\text{long}}-\mu_{b,\text{long}})]^2}{2(R_{a,\text{long}}^2+R_{b,\text{long}}^2)}\right) \end{aligned} \tag{4.42}$$

which demonstrates $\mu_{ab,i} = \mu_{a,i} - \mu_{b,i}$, and $R_{ab,i}^2 = R_{a,i}^2 + R_{b,i}^2$ [136]. Due to azimuthal symmetry and symmetry about midrapidity, the relative shifts in the side and long directions vanish ($\mu_{ab,\,side} \approx 0$ and $\mu_{ab,\,long} \approx 0$), and only an asymmetry in the out direction remains. Therefore, the source becomes,

$$\begin{aligned} S_{ab}(\mathbf{r}) \propto\, & \exp\left(-\frac{[r_{\text{out}}-(\mu_{a,\text{out}}-\mu_{b,\text{out}})]^2}{2(R_{a,\text{out}}^2+R_{b,\text{out}}^2)}\right) \\ & \times \exp\left(-\frac{r_{\text{side}}^2}{2(R_{a,\text{side}}^2+R_{b,\text{side}}^2)}\right) \\ & \times \exp\left(-\frac{r_{\text{long}}^2}{2(R_{a,\text{long}}^2+R_{b,\text{long}}^2)}\right) \end{aligned} \tag{4.43}$$

In the case of identical particle analyses, where the Gaussian offsets are zero and the single-particle sources are obviously described by the same radii, the two-particle source is related by a factor $\sqrt{2}$ to the single-particle sizes, as described above ($R_{aa}^2 = 2R_a^2$).

We return to our treatment of a one dimensional femtoscopic study with a spherically symmetric source of width R_{inv} (Eq. 4.40). In the absence of Coulomb effects, with the assumptions and approximations used above (including unpolarized emission), utilizing Eq. 4.11 results in a 1D femtoscopic correlation function which can be calculated analytically as

$$C(k^*) = 1 + C_{QI}(k^*) + C_{FSI}(k^*) \tag{4.44}$$

C_{QI} describes plane-wave quantum interference:

$$C_{QI}(k^*) = \alpha \exp(-4k^{*2}R^2) \tag{4.45}$$

where $\alpha = (-1)^{2j}/(2j+1)$ (i.e. $\alpha = g_0$) for identical particles with spin j, and $\alpha = 0$ for non-identical particles. For all analyses presented in this study, $\alpha = 0$. C_{FSI} describes the s-wave strong final state interaction between the particles

$$C_{FSI}(k^*) = \sum_S \rho_S \left[\frac{1}{2} \left| \frac{f^S(k^*)}{R} \right|^2 \left(1 - \frac{d_0^S}{2\sqrt{\pi}R} \right) + \frac{2\Re f^S(k^*)}{\sqrt{\pi}R} F_1(2k^*R) - \frac{\Im f^S(k^*)}{R} F_2(2k^*R) \right] \tag{4.46}$$

where $\rho_S = (2S+1)/[(2j_1+1)(2j_2+1)]$ and

$$F_1(z) = \int_0^z \frac{e^{x^2-z^2}}{z} dx \qquad F_2(z) = \frac{1-e^{-z^2}}{z} \tag{4.47}$$

where R is the source size, $f(k^*)$ is the s-wave scattering amplitude, f_0 is the complex scattering length, and d_0 is the effective range of the interaction.

With the inclusion of the λ parameter through Eq. 4.12, one obtains

$$\begin{aligned} C(k^*) &= (1-\lambda) + \lambda\left[1 + C_{QI}(k^*) + C_{FSI}(k^*)\right] \\ &= 1 + \lambda[C_{QI}(k^*) + C_{FSI}(k^*)] \end{aligned} \tag{4.48}$$

Inclusion of the Coulomb Interaction

The introduction of the Coulomb interaction into the framework complicates matters, and the correlation functions no longer have the nice analytic form from the previous subsection. Additionally, we can no longer describe the wave-function as the superposition of an incoming plane and outgoing spherical waves, as the long-range Coulomb interaction modifies both [126, 137]. In such a case, including both the strong and Coulomb interactions, the two-particle wave-function may be written as [126]

$$\Psi_{\mathbf{k}^*}(\mathbf{r}^*) = e^{i\delta_c}\sqrt{A_c(\eta)}[e^{-i\mathbf{k}^*\cdot\mathbf{r}^*}F(-i\eta, 1, i\xi) + f_c(k^*)\frac{\tilde{G}(\rho,\eta)}{r^*}] \tag{4.49}$$

where $\rho = k^*r^*$, $\eta = (k^*a_c)^{-1}$, $\xi = \mathbf{k}^*\cdot\mathbf{r}^* + k^*r^* \equiv \rho(1+\cos\theta^*)$, and $a_c = (\mu z_1 z_2 e^2)^{-1}$ is the two-particle Bohr radius, with z_1 and z_2 the charges of the two particles (including the appropriate signs) in terms of the elementary charge e, and μ is the reduced mass $\mu = (m_1 + m_2)/m_1 m_2$. δ_c is the Coulomb s-wave phase shift, $A_c(\eta)$ is the Coulomb penetration factor, $\tilde{G} = \sqrt{A_c}(G_0 + iF_0)$ is a combination of the regular (F_0) and singular (G_0) s-wave Coulomb functions. $f_c(k^*)$ is the s-wave scattering amplitude:

$$f_c(k^*) = \left[\frac{1}{f_0} + \frac{1}{2}d_0 k^{*2} - \frac{2}{a_c}h(\eta) - ik^*A_c(\eta)\right]^{-1} \tag{4.50}$$

where the "h-function", $h(\eta)$, is expressed through the digamma function, $\psi(z) = \Gamma'(z)/\Gamma(z)$ as:

$$h(\eta) = 0.5[\psi(i\eta) + \psi(-i\eta) - \ln(\eta^2)] \tag{4.51}$$

Even with a nice Gaussian form of the source distribution, the use of the wave-function in Eq. 4.49 within our femtoscopic framework will not result in a nice analytic form. One solution to building the correlation function is to numerically integrate the Koonin-Pratt equation (Eq. 4.11). A second option is to proceed by simulating particle pairs and averaging the modulus squared of their wave-functions to solve the integral (as discussed in Sec. 6.5). In testing the numerical integration and pair simulation methods within a strong-only interaction scenario, we found the two to be consistent.

Calculating a correlation function by way of numerically integrating or simulating pairs in Eq. 4.12 is numerically costly and time consuming. Furthermore, in many cases, the effects of both the Coulomb and strong interactions are essentially a correction on top of the powerful correlations resulting from quantum statistical effects (this is not true for, e.g. our $\Xi^-K^\pm$ study). In most cases, the strong interaction is ignored, and the Coulomb interaction is accounted for by introducing a correction term, $K_{\rm Coul}$ [138, 139], as

$$C(\boldsymbol{q}) = (1-\lambda) + \lambda K_{\rm Coul}(\boldsymbol{q})\left(1 + e^{-q_i q_j R_{ij}^2}\right) \tag{4.52}$$

Initially, the $K_{\rm Coul}$ was modeled with the Gamow factor, $G(\eta)$

$$G(\eta) = \frac{2\pi\eta}{e^{2\pi\eta}-1} \tag{4.53}$$

which is the result achieved when integrating a Coulomb-only wave-function (i.e. Eq. 4.49 without the f_c term) over pointlike sources ($S(\boldsymbol{r}^*) = \delta(\boldsymbol{r}^*)$). However, this approximation is not great, and with improvements in data quality and CPU speed, it has been replaced with more accurate representations. One common method for treating the Coulomb interaction involves using the measured unlike-sign particle pairs to approximate the Coulomb effect in like-sign pairs [139]. In another method, the Gamow factor is replaced by a calculation using the Coulomb-only wave-function for a finite Gaussian source. Typically, with this method an estimated source size is used to calculate $K_{\rm Coul}$, and then $K_{\rm Coul}$ is kept constant during the actual fitting procedure. This process could then continue in an iterative fashion, where the fit gives a better estimate of the source size, which is then used to calculate a new value of $K_{\rm Coul}$, which is included in the new fit, etc. However, especially in the case of including both the Coulomb and strong interactions, the most accurate representation remains numerically solving Eq. 4.12 with Ψ from Eq. 4.49. With processing capabilities continuing to increase, and through parallel-programming with increasingly powerful and less expensive GPUs available to consumers, the full calculation should be pursued.

4.3 Experimental correlation functions

In practice, the correlation function is typically formed experimentally as

$$C(k^*) = \mathcal{N}\frac{A(k^*)}{B(k^*)} \tag{4.54}$$

where $A(k^*)$ is the signal distribution, $B(k^*)$ is the reference distribution, and $\mathcal{N}$ is a normalization parameter. $B(k^*)$ is used to divide out the phase-space effects, and, in an ideal world, this process leaves only the femtoscopic signal visible in the experimental correlation function. The femtoscopic signal results from the spatially-dependent two-particle relative wave-function, which vanishes as $k^* \to \infty$. Assuming this to be the only signal in the data, the correlation function approaches a constant value at large-k^*, and is typically normalized to unity in that region. In this analysis, we observe a large non-femtoscopic background (to be discussed more in Sec. 6.3), which prohibits our correlation functions from approaching a constant value (out to at least $k^* = 2$ GeV/c, which is well beyond the signal region). Therefore, for this analysis, the normalization parameter is chosen such that the mean value of the correlation function equal unity for $k^* \in [0.32, 0.4]$ GeV/c (just outside of the signal region).

In practice, $A(k^*)$ is constructed by binning in k^* pairs from the same event. Ideally, $B(k^*)$ is similar to $A(k^*)$ in all respects excluding the presence of femtoscopic correlations [123]. Furthermore, $B(k^*)$ should account for effects such as detector acceptance and efficiency, and fluctuations in reaction-plane orientation, multiplicity, and vertex position [125]. This is most naturally achieved by building $B(k^*)$ with pairs of particles originating from different events, known as the mixed event technique [140]. In forming the reference distribution, it is important to mix only similar events; mixing events with different phase-spaces can result in an unreliable reference, and can introduce artificial signals into the correlation function. Other techniques exist for constructing reference distributions; most notably, one may use same-event pairs after rotating one particle in the pair by 180° in the transverse plane (see Sec. 5.7.2 for more details).

4.3.1 Spherical harmonic decomposition

In femtoscopic analyses, it can be beneficial to the expand the measured correlations and extracted sources in spherical harmonics (SH) [141–143]. This method is advantageous because it allows one to encode the full three-dimensional (3D) information of the correlation function into a small set of one-dimensional (1D) plots. Note that, in general, the perfect description of the correlation function requires an infinite set of (l, m) components; however, the intrinsic symmetries of the pair distribution result in most of the components vanishing. Additionally, of the non-vanishing components, only those with small l contain important information for our purposes.

The correlation function, binned in spherical coordinates, can be expanded into spherical harmonics as

$$C(q,\theta,\phi) = \sqrt{4\pi}\sum_{l=0}^{\infty}\sum_{m=-l}^{l}\left(A_{l,m}(q)Y_{l,m}(\cos\theta,\phi)\right) \tag{4.55}$$

where the coefficients of the expansion, $A_{l,m}(q)$ are functions of q. Exploiting the orthonormality of the $Y_{l,m}$ harmonics, we can isolate the individual expansion coefficients as

$$A_{l,m}(q) = \frac{1}{4\pi}\int_0^{4\pi} d\Omega_{\hat{\mathbf{q}}} C(\mathbf{q}) Y^*_{l,m}(\Omega_{\hat{\mathbf{q}}}) \tag{4.56}$$

One method for constructing the spherical harmonic decomposition is to store the numerator and denominator distributions in spherical coordinates first, to form the correlation function second, and finally to extract the coefficients of the expansion. This method, while conceptually more simple, does not exploit the full potential offered through the decomposition. Namely, the necessary construction of 3D histograms negates the low-statistics advantage of the 1D representations. To exploit the full advantage offered, a new technique to represent the correlation function in spherical harmonics was developed [143]. With the technique, both the numerator and denominator are stored directly in spherical harmonics (as 1D, not 3D, histograms), and a method to calculate the correlation function directly was presented. We used this technique in the decomposition of our ΛK correlation functions, shown in Appendix B.

Assuming a 3D Gaussian source with unique radii in the three directions (R_{out}, R_{side}, R_{long}), and allowing for a non-zero shift in the outward direction (μ_{out}), i.e.

$$S(\mathbf{r}) \propto \exp\left(-\frac{(r_{\mathrm{out}} - \mu_{\mathrm{out}})^2}{2R_{\mathrm{out}}^2} - \frac{r_{\mathrm{side}}^2}{2R_{\mathrm{side}}^2} - \frac{r_{\mathrm{long}}^2}{2R_{\mathrm{long}}^2}\right) \tag{4.57}$$

the main femtoscopic information is contained in the following four components: C_0^0, $\Re C_1^1$, $\Re C_0^2$, and $\Re C_2^2$ [136]. The coefficient C_0^0 quantifies the overall angle-integrated strength of the correlation function, similar to that studied in our 1D analyses. The $\Re C_1^1$ term is sensitive to the asymmetry in the outward direction, a component interesting for non-identical particle studies. $\Re C_1^0$ is sensitive to any asymmetry in the long direction, which should be zero for analyses at midrapidity from collisions between identical particles. $\Re C_0^2$ contains information about the relative magnitude of the longitudinal to transverse radii, and $\Re C_2^2$ component is most sensitive to the $R_{\mathrm{out}}/R_{\mathrm{side}}$ ratio.

The C_0^0 and $\Re C_1^1$ components from a spherical harmonic decomposition of the correlation functions from a $\pi^{\mathrm{ch}}\mathrm{K}^{\mathrm{ch}}$ analysis can be found in Fig. 4.6 in Sec. 4.4.4. Spherical harmonic decompositions of the ΛK systems studied in this thesis can be found in Appendix B.

4.4 Experimental results in femtoscopy

Femtoscopy is a rich field which has evolved past its original use of roughly demonstrating the overall scale of the system created in particle collisions. Current studies are able to extract the size, shape, and orientation of the pair emission regions, as demonstrated qualitatively in Fig. 4.1. The momentum and species dependence of femtoscopic measurements affirm the collective nature of the hot and dense matter created in heavy-ion collisions. Through azimuthally sensitive femtoscopy, we are able to investigate the final spatial anisotropy of the particle emitting sources, giving us more insight into the evolution of the created system. Femtoscopy offers us the ability to estimate important time scales involved in heavy-ion collisions, including the total time to reach kinetic decoupling, as well as the lifetime, or suddenness, or particle emission. As highlighted in this paper, femtoscopy offers us a unique environment in which to measure nuclear scattering parameters. Finally, through non-identical particle femtoscopy, we are able to study the space-time separation of the single-particle source emitting regions.

4.4.1 Source sizes

For the systems measured from heavy-ion collisions, femtoscopy can only offer a measurement of the homogeneity regions, not the size of the entire fireball. Nonetheless, we can still get a sense of the overall system size and volume at kinetic freeze-out by looking at such measurements. Typically, the volume of the system is quantified as the product of the three femtoscopic radii, $R_{\mathrm{out}}R_{\mathrm{side}}R_{\mathrm{long}}$, measured with low-$p_{\mathrm{T}}$ pions. Pions are the most bountiful finally emitted hadrons in the collisions, and the use of low-p_{T} particles allows for the extraction of the largest regions of homogeneity (below we show that increasing the pair transverse momentum decreases the extracted femtoscopic radii). Such measurements are presented in Fig. 4.2, which shows $R_{\mathrm{out}}R_{\mathrm{side}}R_{\mathrm{long}}$ for pion analyses in heavy-ion collisions at the LHC [144] and lower energies [23, 145–153], as a function of the charged-particle pseudorapidity density. As shown in the figure, the system created at the LHC is about twice as large as that at RHIC.

Instead of looking at the overall "volume" extracted using low-p_{T} particles, it is also interesting to study how the femtoscopic radii evolve with momentum and centrality, as shown in Fig. 4.3. The evolution with centrality is easy to understand: as the size of the system grows in more central collisions, so do the regions of homogeneity. The femtoscopic substructure is dictated by the interplay between thermal motion and collective expansion [123, 125]. A stronger expansion results in larger

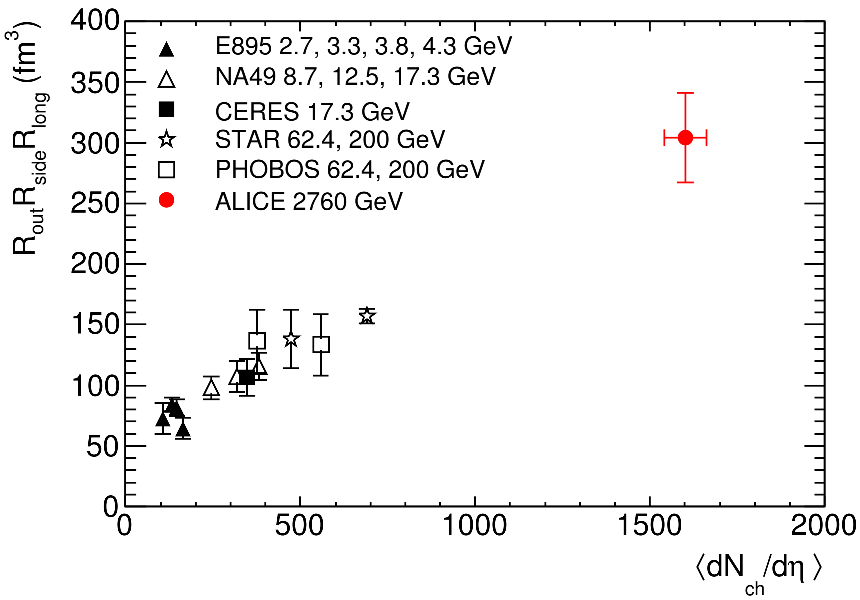

Figure 4.2: The product of the three pion radii, $R_{\text{out}}R_{\text{side}}R_{\text{long}}$, as a function of $\langle dN_{\text{ch}}/d\eta\rangle$. The ALICE results [144] is compared to those for central gold and lead collisions at lower energies at the AGS [145], SPS [146–148], and RHIC [23, 149–153]. Figure from [144].

pressure gradients, which tend to reduce the regions of homogeneity. A higher temperature produces the opposite effect, as it broadens the momentum spectra through thermal smearing, thus increasing the regions of homogeneity [37]. Heavier particles are less affected by the temperature of the system, and more sensitive to the collective effects.

The hydrodynamic flow present in the evolving system causes the decrease of the femtoscopic radii with increasing pair transverse momentum, $k_{\text{T}} = |\boldsymbol{p}_{\text{T},1} + \boldsymbol{p}_{\text{T},2}|/2$. The collective motion creates an *x-p correlation* between the average momentum of the particles and their space-time position [37]. Thus, the collective flow causes particles emitted from spatially separated parts of the collision region to move away from each other. As discussed previously, the random thermal motion helps to increase the spatial region from which particles with similar velocities are emitted. As the momentum of the pair increases, the spatially correlated region becomes smaller, and the random thermal motion is less effective in acting against the focusing power of

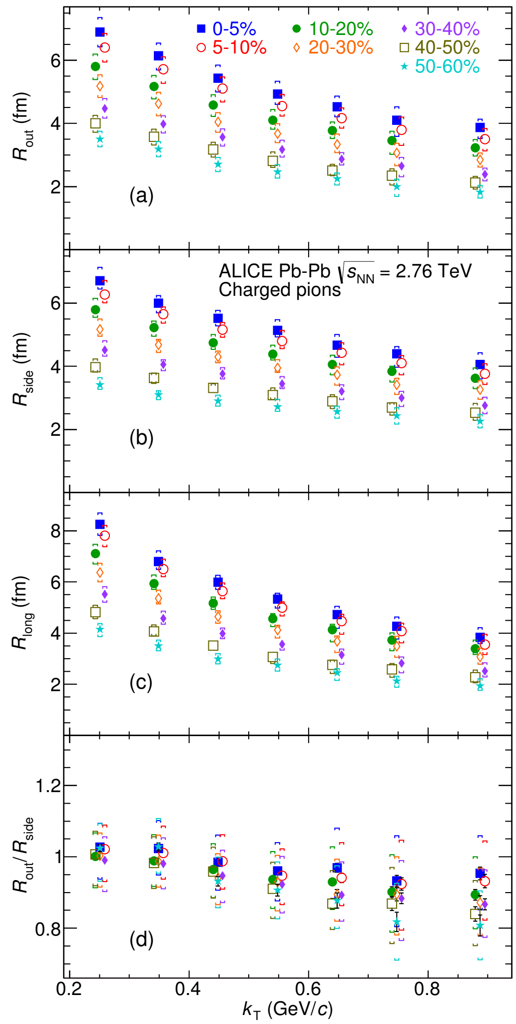

Figure 4.3: Identical charge pion femtoscopic radii in Pb-Pb collisions at $\sqrt{s_{NN}} = 2.76$ TeV [154]. The radii are shown as a function of pair transverse momentum, k_T, for various centrality bins. For visibility, the points for centralities 5-10%, 10-20%, 30-40%, and 40-50% have been shifted horizontally.

the flow. This effect is nicely demonstrated in Fig. 4.3, as the radii are observed to decrease with increasing k_T.

4.4.2 Time scales

Within a hydrodynamic inspired picture, the decoupling time of hadrons at midrapitiy may be estimated, as the size of the particle emitting region is inversely proportional to the gradients of the expanding medium. Within a boost invariant system, the longitudinal radius most directly accesses the freeze-out time of the system. Quantitatively, the kinetic decoupling time can be estimated assuming thermal emission of a boost invariant system with instantaneous freeze-out at proper time τ_f. Under such assumptions, the freeze-out time is estimated by fitting the m_{T}-dependence of R_{long} with

$$R^2_{\mathrm{long}}(m_{\mathrm{T}}) = \tau_f^2 \frac{T}{m_T} \frac{K_2(m_T/T)}{K_1(m_T/T)} \qquad m_{\mathrm{T}} = \sqrt{m^2 + k_{\mathrm{T}}^2} \tag{4.58}$$

where m is the particle mass, T the kinetic freeze-out temperature (taken to be 120 MeV in [144]), and K_1 and K_2 are the integer order modified Bessel functions [155]. Using R_{long}, the decoupling time extracted by ALICE was 10-11 fm/c in central Pb-Pb collisions at $\sqrt{s_{\mathrm{NN}}} = 2.76$ TeV [144].

4.4.3 Anisotropic freeze-out structure

Azimuthally sensitive femtoscopic analyses measure oscillations in the extracted femtoscopic radii as a function of emission angle with respect to the harmonic flow symmetry planes. These analyses have typically been performed with respect to the second harmonic event plane, but analyses with respect to the third order plane have been published by the PHENIX collaboration at RHIC [156], and recently by the ALICE collaboration at the LHC [157]. Azimuthally differential femtoscopic analyses are the coordinate-space analog of the anisotropic flow measurements, and provide important complementary information about the particle source.

The azimuthal dependence of the femtoscopic sources with respect to the flow planes originates from anisotropies in the collective flow gradients. The measurement of the radii with respect to the elliptic flow plane provides information on the evolution of the system shape. In non-central collisions, the large initial spatial anisotropy is driven towards isotropy by the anisotropic flow. The extent to which the initial spatial anisotropy is modified is dictated by the amount of flow in the system and the properties of the medium. With knowledge of the final spatial anisotropy of the shape at freeze-out, together with the strength of the anisotropic flow and an estimate of the initial geometry (from, for instance, a Glauber model), it is possible to estimate the time required for the system to evolve from its initial to final shape. Such estimates yield results consistent with those using R_{long}, as discussed above (Sec. 4.4.2)[158].

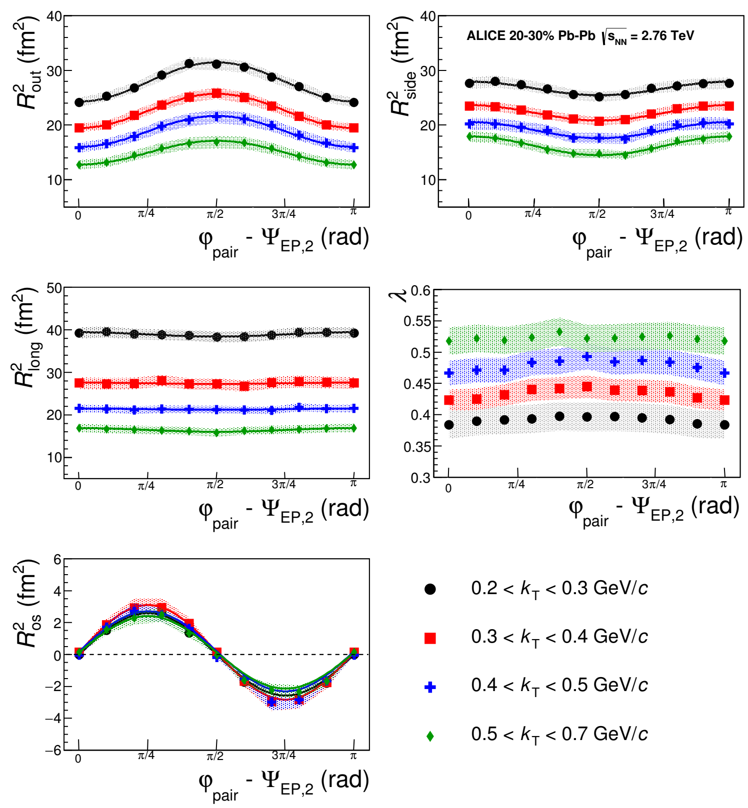

Figure 4.4: Azimuthally differential pion femtoscopy in Pb-Pb collisions at $\sqrt{s_{\mathrm{NN}}} = 2.76$ TeV [159]. The figure shows the azimuthal dependence of R^2_{out}, R^2_{side}, R^2_{long}, R^2_{os} and λ as a function of $\Delta\varphi = \varphi_{\mathrm{pair}} - \Psi_{\mathrm{EP},2}$. The results are for the 20-30% centrality bin over k_{T} ranges 0.2-0.3 (black circles), 0.3-0.4 (red squares), 0.4-0.5 (blue crosses), and 0.5-0.7 (green diamonds) GeV/c. The bands indicate systematic errors, and the results are not corrected for event-plane resolution ($\approx$ 85%-95%).

Figure 4.4 presents results from an azimuthally differential pion femtoscopic analysis for the 20-30% centrality bin from Pb-Pb collisions at $\sqrt{s_{\mathrm{NN}}} = 2.76$ TeV [159]. The anisotropic shape transverse to the beam direction elicits $\cos(n\varphi_{\mathrm{pair}})$ (n even) oscillations in the R^2_{out}, R^2_{side}, and R^2_{os} terms, as shown. The strong in-plane expansion is not able to fully convert the initial out-of-plane geometry. The figure shows no oscillations for R^2_{long} and λ, and the study reports R^2_{ol} and R^2_{sl} to be consistent with zero, as expected due to symmetry.

The results in Fig. 4.4, together with results from other centralities, were fit with a simple functional form allowing for the extraction of the average radii and the amplitudes of the oscillations. The average radii obtained were found to be consistent with the previous, non-azimuthally dependent, measurements [154]. The relative oscillations of R^2_{out} and R^2_{side} were shown to decrease from semi-central to central collisions (i.e. from the studied 40-50% bin to the 0-5% bin), as one expects from a progressively rounder source.

4.4.4 Non-identical particle femtoscopy

In addition to providing information about the size of the pair emission regions, non-identical particle femtoscopy gives us access to the emission asymmetries between different species of particles. These asymmetries exist in both space and time, and are intimately related to the collective nature of the system. Namely, heavier particles are less affected by random thermal motion, and are more strongly confined by the collective flow. As a result, higher-m_{T} particles originate from smaller regions of homogeneity, and their emission points reside further away in the "out" direction [160]. This effect is demonstrated in Fig. 4.5. An additional shift in time can result from the fact that different species kinematically decouple from the system at different times, depending on their interaction cross sections. Significant feed-down from resonance decays can also contribute a time delay.

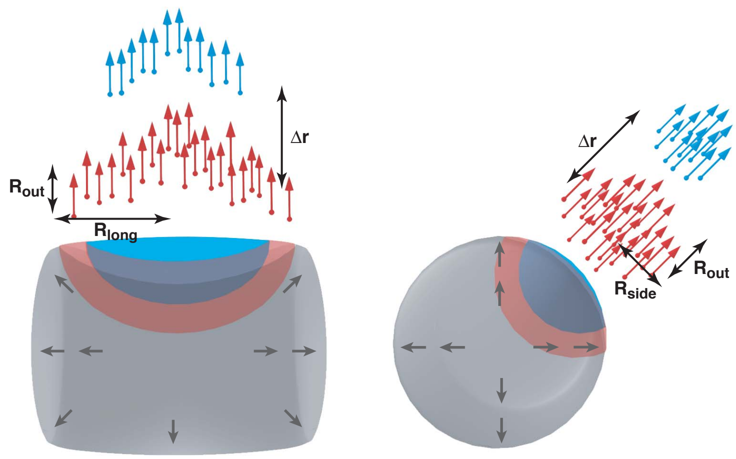

Figure 4.5: A cartoon demonstrating the emission picture for non-identical particle femtoscopy studies [123]. The figure shows the emission zones for higher mass (blue) and lower mass (red) particles. The left shows a snapshot from alongside of the beam, and right right shows a view looking directly down the beam pipe. Heavier particles are less affected by random thermal motion, and their sources are more strongly dictated by collective flow. The heavier particles are more confined to a smaller region towards the surface.

Figure 4.6 [161] presents recent results from a $\pi^{\mathrm{ch}}\mathrm{K}^{\mathrm{ch}}$ femtoscopic analyses conducted with Pb-Pb collisions at $\sqrt{s_{\mathrm{NN}}} = 2.76$ TeV. The analysis studies the emission asymmetry between the π and K sources through a spherical harmonic decomposition of the correlation functions. The correlation functions (the C_0^0 and $\Re C_1^1$ components of which are shown in the left of Fig. 4.6) were fit using the CorrFit program [162], and the extracted radii and emission asymmetries are shown in the right of Fig. 4.6. As shown, both the extracted radii and asymmetries increase with particle multiplicity, and the asymmetries are shown the be negative, implying that the pions are emitted closer to the center of the source, and/or earlier than the kaons. The extracted asymmetries are between $\mu_{\mathrm{out}} \approx -2$ to -4 fm, which is somewhat smaller than the results reported by STAR for πK correlations in central Au-Au collisions at $\sqrt{s_{\mathrm{NN}}} =$ 130 GeV [163].

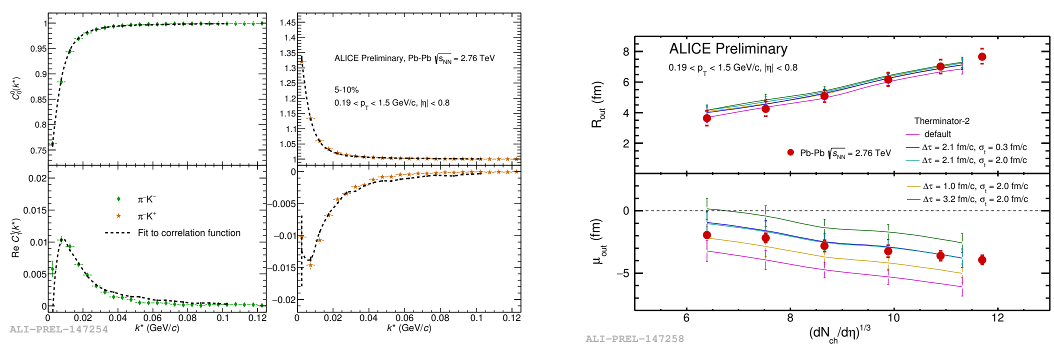

Figure 4.6: $\pi^{\rm ch}{\rm K}^{\rm ch}$ femtoscopy with spherical harmonics in Pb-Pb collision at $\sqrt{s_{\rm NN}} = 2.76$ TeV [161]. (Left) The C_0^0 (top) and $\Re C_1^1$ (bottom) components from a spherical harmonic decomposition of the correlation functions for like-sign $\pi^-{\rm K}^-$ (green diamonds) and unlike-sign $\pi^-{\rm K}^+$ (orange stars) pairs. Fits to the data using the CorrFit program [162] are shown as dashed lines. (Right) Source size (top) and emission asymmetry (bottom) as a function of $({\rm d}N_{\rm ch}/{\rm d}\eta)^{1/3}$ together with results using the THERMINATOR 2 generator with default and selected values of additional time delays for kaons (where $\Delta\tau$ and σ_t are the mean and width of the Gaussian distribution used for drawing the emission delay values).

Chapter 5: Data Selection and Correlation Function Construction

5.1 Data sample and software

The events utilized in this analysis were taken from the LHC11h (AOD145) dataset, which was recorded during the 2011 Pb-Pb run. Approximately 40 million combined central, semi-central, and minimum bias events were analyzed. Runs from both positive (++) and negative (−−) ALICE dipole magnetic field polarity settings were used. Accumulating dating from both field configurations allows for important consistency checks, as the physics results in this analysis should not depend on the detector's magnetic field polarity. Approximately two-thirds of the runs included in this analysis were taken with the magnetic field in the negative configuration, and one-third were taken with the positive configuration. The runlist used is:
170593, 170572, 170388, 170387, 170315, 170313, 170312, 170311, 170309, 170308, 170306, 170270, 170269, 170268, 170230, 170228, 170207, 170204, 170203, 170193, 170163, 170159, 170155, 170091, 170089, 170088, 170085, 170084, 170083, 170081, 170040, 170027, 169965, 169923, 169859, 169858, 169855, 169846, 169838, 169837, 169835, 169591, 169590, 169588, 169587, 169586, 169557, 169555, 169554, 169553, 169550, 169515, 169512, 169506, 169504, 169498, 169475, 169420, 169419, 169418, 169417, 169415, 169411, 169238, 169167, 169160, 169156, 169148, 169145, 169144, 169138, 169099, 169094, 169091, 169045, 169044, 169040, 169035, 168992, 168988, 168826, 168777, 168514, 168512, 168511, 168467, 168464, 168460, 168458, 168362,

168361, 168342, 168341, 168325, 168322, 168311, 168310, 168115, 168108, 168107, 168105, 168076, 168069, 167988, 167987, 167985, 167920, 167915

Analyses were also performed on the LHC12a17a_fix (AOD149) Monte Carlo HIJING events for certain checks, for generation of response matrices in the treatment of momentum resolution effects (Sec. 6.1), and for the estimation of reconstruction efficiencies for use in estimating λ parameters (Sec. 6.2). The THERMINATOR 2 event generator was utilized for certain aspects, such as generation of transform matrices describing feed-down contributions from resonances and the estimation of λ parameters (Sec. 6.2), as well as for modeling the non-femtoscopic background (Sec. 6.3).

The analysis was performed on the PWGCF analysis train using AliRoot v5-09-29-1 and AliPhysics vAN-20180505-1. The main classes utilized include: AliFemtoVertexMultAnalysis, AliFemtoEventCutEstimators, AliFemtoESDTrackCutNSigmaFilter, AliFemtoV0TrackCutNSigmaFilter, AliFemtoXiTrackCut, AliFemtoV0PairCut, AliFemtoV0TrackPairCut, AliFemtoXiTrackPairCut, and AliFemtoAnalysisLambdaKaon. All of these classes are contained in /AliPhysics/PWGCF/FEMTOSCOPY/AliFemto and /AliPhysics/PWGCF/FEMTOSCOPY/AliFemtoUser directories.

5.2 Event selection and mixing

The events utilized in this analysis were recorded during the 2011 Pb-Pb run, and were collected using the minimum bias, semi-central (0–50% centrality) and central (0–10%) triggers. The primary collision vertex for each event is required to be within ± 10 cm of the center of the TPC along the beam direction. This cut reduces contamination from background events (e.g. beam-gas interactions or parasitic collisions from debunched ions [10]), and allows for use of the full range of ALICE acceptance. Finally, to be included in the analysis, an event must contain at least one Λ hyperon and at least one K meson.

The AliFemtoEventReaderAODChain class is used to read the events. Centrality flattening, a procedure which flattens out the multiplicity distribution within a given centrality class, is not used as it does not influence the observed correlation functions significantly. FilterBit(7) is applied, which enforces TPC-only tracks constrained to the primary vertex. The centrality is determined by the "V0M" method of AliCentrality, set by calling SetUseMultiplicity(kCentrality) in AliFemtoEventReaderAOD. The analysis is performed with 0–10%, 10–30%, and 30–50% centrality bins. The event mixing is handled by the AliFemtoVertexMultAnalysis class, which only mixes events with like vertex position and centrality. Events are binned both in primary vertex positions (2 cm bin width) and in centrality (5% bin width), and only events within a given bin are mixed. Each event is mixed with $N_{\mathrm{mix}} = 5$ others for the construction of the reference distribution.

We utilize the SetPrimaryVertexCorrectionTPCPoints switch, which essentially re-centers each collision vertex at $z = 0.$. More specifically, after the event binning, a vertex correction is applied to each event, in which the primary vertex position is subtracted from the TPC track positions for each particle in the event. Subsequently, the tracks in an event are all measured relative to the event vertex, instead of the center of the TPC. This effectively gives each event the same primary vertex position, which is important for the implementation of the average separation cut in mixed-event pairs.

5.3 $\mathrm{K}^{\pm}$ track selection

Charged kaons are identified using the AliFemtoESDTrackCutNSigmaFilter class. The single-particle selection criteria used to select charged kaon candidates are summarized in Tables 5.2 and 5.3. $\mathrm{K}^{\pm}$ track detection utilizes both TPC and TOF detectors, and tracks within the range $0.14 < p_{\mathrm{T}} < 1.5$ GeV/c are accepted. As we are interested in primary particles originating from the primary vertex, to reduce the number of secondaries in our sample (for instance, charged particles produced in the detector material, particles from weak decays, etc.), we establish a maximum cut on the distance-of-closest-approach (DCA) of the track the the primary vertex. This restriction is realized by imposing a DCA cut in both the transverse and beam directions.

Particle identification (PID) was performed using both the TPC and TOF detectors via the Nσ method. With the Nσ method, each track is assigned N$\sigma_{i,\mathrm{TPC}}$ and N$\sigma_{i,\mathrm{TOF}}$ values quantifying the number of Gaussian widths away from the mean of the distribution for particle species i in the TPC and TOF, respectively. These Nσ values are then used as cut values in the selection of particle species of interest. We additionally include methods to reduce the contamination in our $\mathrm{K}^{\pm}$ samples from electrons and pions. The specifics for these cuts are contained in Table 5.2.

The purity of the $\mathrm{K}^{\pm}$ collections is estimated using the HIJING MC data, for which the true identity of each reconstructed $\mathrm{K}^{\pm}$ particle is known. Therefore, the purity may be estimated as:

$$Purity(K^{\pm}) = \frac{N_{true}}{N_{reconstructed}} \tag{5.1}$$

We find Purity(K^{+}) $\approx$ Purity(K^{-}) $\approx$ 97%. The approximate numbers of $\mathrm{K}^{\pm}$ in the final collections are shown in Table 5.1.

Centrality	K^{+}	K^{-}
0–10%	3.9×10^{8}	3.6×10^{8}
10–30%	1.2×10^{8}	1.1×10^{8}
30–50%	4.7×10^{7}	4.3×10^{7}

Table 5.1: Approximate number of $\mathrm{K}^{\pm}$ mesons in samples

$K^{\pm}$ **selection**

Kinematic range	
$\vert\eta\vert$	< 0.8
p_{T}	$0.14 < p_{\mathrm{T}} < 1.5$ GeV/c
Track quality and selection	
FilterBit	7
Number of clusters in the TPC	> 80
χ^2/N_{DOF} for (ITS, TPC) clusters	$<$ (3.0, 4.0)
DCA to primary vertex (XY, Z)	$<$ (2.4, 3.0) cm
Remove particles with any kink labels	true
Nσ to primary vertex	< 3.0
$K^{\pm}$ identification	
PID Probabilities	
K	> 0.2
(π, μ, p)	$<$ (0.1, 0.8, 0.1)
Most probable particle type (fMostProbable =)	Kaon (3)
TPC and TOF Nσ Cuts	
$p < 0.4$ GeV/c	$N_{\sigma K,\mathrm{TPC}} < 2$
$0.4 < p < 0.45$ GeV/c	$N_{\sigma K,\mathrm{TPC}} < 1$
$0.45 < p < 0.80$ GeV/c	$N_{\sigma K,\mathrm{TPC}} < 3$ $N_{\sigma K,\mathrm{TOF}} < 2$
$0.80 < p < 1.0$ GeV/c	$N_{\sigma K,\mathrm{TPC}} < 3$ $N_{\sigma K,\mathrm{TOF}} < 1.5$
$p > 1.0$ GeV/c	$N_{\sigma K,\mathrm{TPC}} < 3$ $N_{\sigma K,\mathrm{TOF}} < 1$

Table 5.2: $K^{\pm}$ selection

$K^{\pm}$ selection - Misidentification Cuts

Electron Rejection: Reject if		$N_{\sigma e^{-},TPC} < 3$
Pion Rejection: Reject if:		
$p < 0.65$ GeV/c	TOF and TPC available	
	$N_{\sigma\pi,TPC} < 3$ $N_{\sigma\pi,TOF} < 3$	
	Only TPC available	
	$p < 0.5$ GeV/c	$N_{\sigma\pi,TPC} < 3$
	$0.5 < p < 0.65$ GeV/c	$N_{\sigma\pi,TPC} < 2$
$0.65 < p < 1.5$ GeV/c	$N_{\sigma\pi,TPC} < 5$ $N_{\sigma\pi,TOF} < 3$	
$p > 1.5$ GeV/c	$N_{\sigma\pi,TPC} < 5$ $N_{\sigma\pi,TOF} < 2$	

Table 5.3: $K^{\pm}$ selection - misidentification cuts

5.4 V0 selection

5.4.1 General V0 reconstruction

$\Lambda(\overline{\Lambda})$ and K^0_S particles are electrically neutral, and cannot be directly detected, but must instead be reconstructed through their decay products, i.e. daughters. This process is illustrated in Figure 5.1, and the main cuts used are shown in Table 5.5 (Λ and $\overline{\Lambda}$) and Table 5.7 (K^0_S). In general, particles which are topologically reconstructed in this fashion are called V0 particles. The decay channel $\Lambda \rightarrow p\pi^-$ was used for the identification of Λ hyperons (and, similarly the charge-conjugate decay for the $\overline{\Lambda}$ identification), and $K^0_S \rightarrow \pi^+\pi^-$ for the identification of K^0_S mesons.

To construct a V0 particle, the charged daughter tracks must first be identified. Aside from typical kinematic and PID cuts (using TPC and TOF detectors), the daughter tracks are exposed to a minimum cut on their impact parameter with respect to the primary vertex. The daughters of a V0 particle should not originate from the primary vertex, but rather from the decay vertex of the V0, hence the minimum

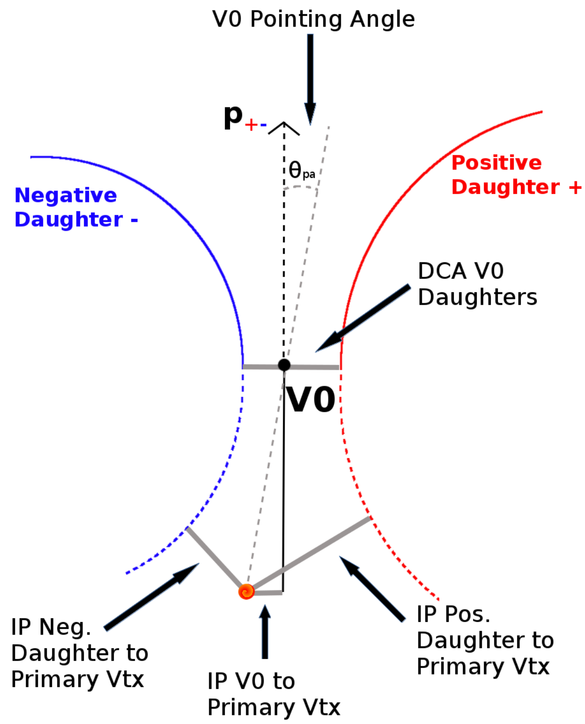

Figure 5.1: V0 Reconstruction

cut imposition. The decay vertex of the V0 is assumed to be the point of closest approach between the daughter tracks. To help ensure quality, a maximum value cut is demanded on the distance-of-closest-approach between the daughters (DCA V0 Daughters). The positive and negative daughter tracks are combined to form the V0 candidate, the momentum of which is simply the sum of the momenta of the daughters (calculated at the DCA).

A minimum transverse momentum cut on the V0 candidate is introduced to reduce contamination from fake candidates. Opposite to that of the daughter tracks, the V0 candidate is exposed to a maximum cut on its impact parameter with respect to the primary vertex. In this case, we want our V0 candidates to be primary, hence the maximum cut imposition. To further strengthen our selection of primary V0 candidates, we impose a selection on the pointing angle, θ_{pa}, between the V0 momentum and the vector pointing from the primary vertex to the secondary V0 decay vertex. We want the V0 candidate's momentum to point back to the primary decay vertex, and therefore a small θ_{pa} is desirable; we achieve this by appointing a minimum value on $\cos(\theta_{\mathrm{pa}})$ ("Cosine of pointing angle" in Tables 5.5 and 5.7).

On occasion, $\Lambda(\overline{\Lambda})$ particles are misidentified as $\mathrm{K^0_S}$, and vice versa. To attempt to remove these contaminations without throwing away good candidates, we impose a set of misidentification cuts. The intent of these cuts is to judge whether a candidate is more likely a $\Lambda(\overline{\Lambda})$ or a $\mathrm{K^0_S}$, and they are implemented as described below (the effects of which can be seen in Figures 5.2 and 5.3). For a given V0, we calculate the mass assuming different identities (Λ, $\overline{\Lambda}$, $\mathrm{K^0_S}$) of the candidate; the mass assuming $\mathrm{K^0_S}$ hypothesis ($m_{\mathrm{inv,\,K^0_S\,hyp.}}$) is calculated assuming $\pi^+\pi^-$ daughters, the mass assuming Λ hypothesis ($m_{\mathrm{inv,\,\Lambda\,hyp.}}$) is calculated assuming $\mathrm{p}\pi^-$ daughters, and the mass assuming $\overline{\Lambda}$ hypothesis ($m_{\mathrm{inv,\,\bar{\Lambda}\,hyp.}}$) is calculated assuming $\bar{p}\pi^+$ daughters. In addition to the notation just introduced, in the following, $m_{\mathrm{PDG,\,K^0_S}}$ and $m_{\mathrm{PDG,\,\Lambda(\bar{\Lambda})}}$ denote the particle masses of the $\mathrm{K^0_S}$ and $\Lambda(\overline{\Lambda})$, respectively, as recorded by the Particle Data Group [164].

For $\Lambda(\overline{\Lambda})$ selection, a candidate is assumed to be misidentified and is rejected if all of the following criteria are satisfied:

1. $\left|m_{\mathrm{inv,\,K^0_S\,hyp.}} - m_{\mathrm{PDG,\,K^0_S}}\right| < 9.0\ \mathrm{MeV}/c^2$

2. The daughter particles pass daughter cuts intended for $\mathrm{K^0_S}$ reconstruction

    (a) Λ selection

        i. p daughter passes π^+ cuts intended for $\mathrm{K^0_S}$ reconstruction

        ii. π^- daughter passes π^- cuts intended for $\mathrm{K^0_S}$ reconstruction.

    (b) $\overline{\Lambda}$ selection

        i. π^+ daughter passes π^+ cuts intended for $\mathrm{K^0_S}$ reconstruction

        ii. $\bar{\mathrm{p}}$ daughter passes π^- cuts intended for $\mathrm{K^0_S}$ reconstruction.

3. $\left|m_{\mathrm{inv,\,K^0_S\,hyp.}} - m_{\mathrm{PDG,\,K^0_S}}\right| < \left|m_{\mathrm{inv,\,\Lambda(\bar{\Lambda})\,hyp.}} - m_{\mathrm{PDG,\,\Lambda(\bar{\Lambda})}}\right|$

Similarly, for K^0_S selection, a candidate is rejected if all of the following criteria are satisfied for the Λ case, or for the $\overline{\Lambda}$ case:

1. $\left|m_{\mathrm{inv},\,\Lambda(\bar{\Lambda})\,\mathrm{hyp.}} - m_{\mathrm{PDG},\,\Lambda(\bar{\Lambda})}\right| < 9.0\ \mathrm{MeV}/c^2$
2. The daughter particles pass daughter cuts intended for $\Lambda(\overline{\Lambda})$ reconstruction
   (a) π^+ daughter passes $\mathrm{p}(\pi^+)$ daughter cut intended for $\Lambda(\overline{\Lambda})$ reconstruction
   (b) π^- daughter passes $\pi^-(\bar{\mathrm{p}})$
3. $\left|m_{\mathrm{inv},\,\Lambda(\bar{\Lambda})\,\mathrm{hyp.}} - m_{\mathrm{PDG},\,\Lambda(\bar{\Lambda})}\right| < \left|m_{\mathrm{inv},\,K^0_S\,\mathrm{hyp.}} - m_{\mathrm{PDG},\,K^0_S}\right|$

At this stage, we have a collection of V0 candidates satisfying all of the aforementioned cuts. However, this collection is still polluted by fake V0s, for which the daughter particles happen to pass all of our cuts, but which do not actually originate from a V0. Although the two daughter particles appear to reconstruct a V0 candidate, they are lacking one critical requirement: the system invariant mass does not match that of our desired V0 species (these can be seen outside of the mass peaks in Fig. 5.4). Therefore, as our final single-particle cut, we require the invariant mass of the V0 candidate to fall within the mass peak of our desired species. Note, however, that some fake V0s still make it past this final cut, as their invariant mass also happens to fall without our acceptance window.

Occasionally, we encounter a situation where two V0 candidates share a common daughter. Both of these candidates cannot be real V0s, and including both could introduce an artificial signal into our data. To avoid any auto-correlation effects, for each event, we impose a single-particle shared daughter cut on each collection of V0 candidates. This cut iterates through the V0 collection to ensure that no daughter is claimed by more than one V0 candidate. If a shared daughter is found between two V0 candidates, that candidate with a smaller DCA to primary vertex is kept while the other is excluded from the analysis.

The specific cuts used to reconstruct our $\Lambda(\overline{\Lambda})$ and K^0_S populations, along with plots showing the effect of the misidentification cuts, are shown in the following sections.

5.4.2 Λ reconstruction

The cuts shown in Table 5.5, in addition to the misidentification and shared daughter cuts presented in Sec. 5.4.1, are used to select good $\Lambda(\overline{\Lambda})$ candidates. Figure 5.2a shows the mass assuming K^0_S hypothesis for the Λ collection, i.e. assuming the daughters are $\pi^+\pi^-$ instead of $p^+\pi^-$. Figure 5.2b shows a similar plot, but is for the $\overline{\Lambda}$ collection, i.e. assume the daughters are $\pi^+\pi^-$ instead of $\pi^+\bar{p}^-$. The K^0_S contamination is visible, although not profound, in both, in the slight peaks around $m_{\rm inv} = 0.497$ GeV/c^2.

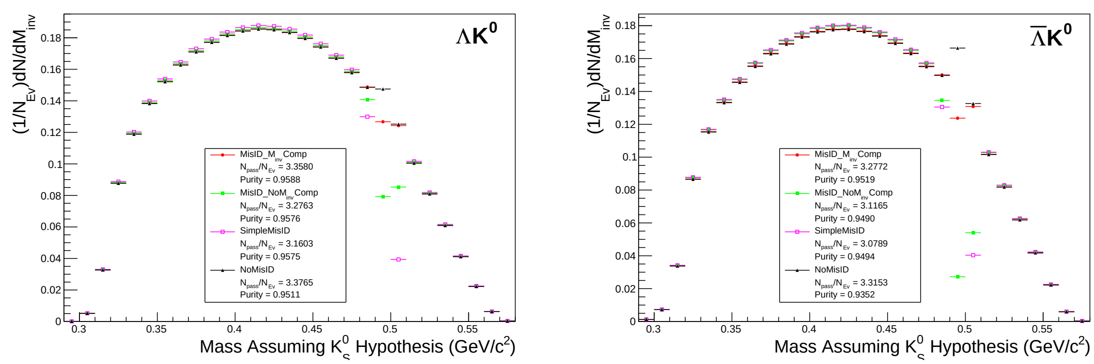

(a) Mass assuming K^0_S-hypothesis for Λ collection, i.e. assume the daughters are $\pi^+\pi^-$ instead of $p^+\pi^-$.

(b) Mass assuming K^0_S-hypothesis for $\overline{\Lambda}$ collection, i.e. assume the daughters are $\pi^+\pi^-$ instead of $\pi^+\bar{p}^-$.

Figure 5.2: Mass assuming K^0_S-hypothesis for V0 candidates passing all Λ (left) and $\overline{\Lambda}$ (right) cuts. The "NoMisID" distribution (black triangles) does not attempt to remove misidentified K^0_S; the slight peak around $m_{\rm inv} = 0.5$ GeV/c^2 contains misidentified K^0_S particles in our $\Lambda(\overline{\Lambda})$ collection. "SimpleMisID" (pink squares) simply cuts out the entire peak. "MisID_M$_{\rm inv}$Comp" (red circles) and "MisID_NoM$_{\rm inv}$Comp" (green squares) use the misidentification cuts outlined in the text with and without, respectively, implementing the final $m_{\rm inv}$ comparison step.

If one simply cuts out the entire peak, good Λ particles will be lost. Ideally, the Λ selection and $\mathrm{K^0_S}$ misidentification cuts are selected such that the peak is removed from this plot while leaving the underlying distribution continuous. To attempt to remove these $\mathrm{K^0_S}$ contaminations without throwing away good Λ and $\overline{\Lambda}$ particles, the misidentification cuts introduced in Sec. 5.4.1 were imposed (the effects of which are visible in Fig. 5.2). The approximate numbers of Λ and $\overline{\Lambda}$ hyperons in the final collections are shown in Table 5.4.

Centrality	Λ	$\overline{\Lambda}$
0–10%	5.7×10^7	5.5×10^7
10–30%	1.8×10^7	1.8×10^7
30–50%	6.9×10^6	6.7×10^6

Table 5.4: Approximate number of Λ and $\overline{\Lambda}$ hyperons in samples

5.4.3 $\mathrm{K^0_S}$ reconstruction

The cuts shown in Table 5.7, in addition to the misidentification and shared daughter cuts presented in Sec. 5.4.1, are used to select good $\mathrm{K^0_S}$ candidates. As can be seen in Figure 5.3, some misidentified Λ and $\overline{\Lambda}$ particles contaminate our $\mathrm{K^0_S}$ sample. Figure 5.3a shows the mass assuming Λ-hypothesis for the $\mathrm{K^0_S}$ collection, i.e. assume the daughters are $\mathrm{p}^+\pi^-$ instead of $\pi^+\pi^-$. Figure 5.3b is similar, but shows the mass assuming $\overline{\Lambda}$-hypothesis for the collection, i.e. assume the daughters are $\pi^+\bar{p}^-$ instead of $\pi^+\pi^-$. The Λ contamination can be seen in Fig. 5.3a, and the $\overline{\Lambda}$ contamination in Fig. 5.3b, in the peaks around $m_{\mathrm{inv}} = 1.115$ GeV/c^2. Additionally, the $\overline{\Lambda}$ contamination is visible in Fig. 5.3a, and the Λ contamination visible in Fig. 5.3b, in the region of excess around $1.65 < m_{\mathrm{inv}} < 2.1$ GeV/c^2. This is confirmed as the number of misidentified Λ particles in the sharp peak of Fig. 5.3a (misidentified

Λ reconstruction		
$\lvert\eta\rvert$		< 0.8
p_{T}		> 0.4 GeV/c
$\lvert m_{\mathrm{inv}} - m_{\mathrm{PDG}}\rvert$		< 3.8 MeV
DCA to prim. vertex		< 0.5 cm
Cosine of pointing angle		> 0.9993
OnFlyStatus		false
Decay Length		< 60 cm
Shared Daughter Cut		true
Misidentification Cut		true
Daughter Cuts (π and p)		
$\lvert\eta\rvert$		< 0.8
Number of clusters in the TPC		> 80
Daughter status		kTPCrefit
DCA πp Daughters		< 0.4 cm
π-specific cuts		
p_{T}		> 0.16 GeV/c
DCA to prim vertex		> 0.3 cm
TPC and TOF Nσ Cuts		
$p < 0.5$ GeV/c		N$\sigma_{\mathrm{TPC}} < 3$
$p > 0.5$ GeV/c	if TOF & TPC available	N$\sigma_{\mathrm{TPC}} < 3$ & N$\sigma_{\mathrm{TOF}} < 3$
	else	N$\sigma_{\mathrm{TOF}} < 3$
p-specific cuts		
p_{T}		$> 0.5(p)$ $[0.3(\bar{p})]$ GeV/c
DCA to prim vertex		> 0.1 cm
TPC and TOF Nσ Cuts		
$p < 0.8$ GeV/c		N$\sigma_{\mathrm{TPC}} < 3$
$p > 0.8$ GeV/c	if TOF & TPC available	N$\sigma_{\mathrm{TPC}} < 3$ & N$\sigma_{\mathrm{TOF}} < 3$
	else	N$\sigma_{\mathrm{TOF}} < 3$

Table 5.5: Λ reconstruction

$\overline{\Lambda}$ particles in the sharp peak of Fig. 5.3b) approximately equals the excess found in the $1.65 < m_{\rm inv} < 2.1$ GeV/c^2 region of Fig. 5.3a (Fig. 5.3b).

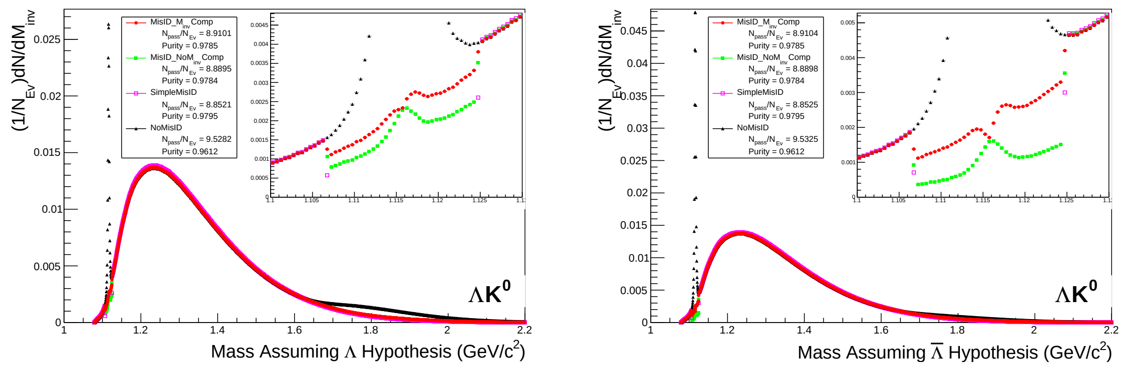

(a) Mass assuming Λ-hypothesis for $\mathrm{K^0_S}$ collection, i.e. assume the daughters are $p^+\pi^-$ instead of $\pi^+\pi^-$.

(b) Mass assuming $\overline{\Lambda}$-hypothesis for $\mathrm{K^0_S}$ collection, i.e. assume the daughters are $\pi^+\bar{p}^-$ instead of $\pi^+\pi^-$.

Figure 5.3: Mass assuming Λ-hypothesis (left) and $\overline{\Lambda}$-hypothesis (right) for $\mathrm{K^0_S}$ collection. The "NoMisID" distribution (black triangles) does not attempt to remove misidentified Λ and $\overline{\Lambda}$; the peak around $m_{\rm inv} = 1.115$ GeV/c^2 contains misidentified Λ (left) and $\overline{\Lambda}$ (right) particles in our $\mathrm{K^0_S}$ collection. "SimpleMisID" (pink squares) simply cuts out the entire peak. "MisID_M$_{\rm inv}$Comp" (red circles) and "MisID_NoM$_{\rm inv}$Comp" (green squares) use the misidentification cuts outlined in the text with and without, respectively, implementing the final $m_{\rm inv}$ comparison step. Also note, the relative excess of the "NoMisID" distribution around $1.65 < m_{\rm inv} < 2.1$ GeV/c^2 shows misidentified $\overline{\Lambda}$ (left) and Λ (right) particles in our $\mathrm{K^0_S}$ collection.

The peaks around $m_{\rm inv} = 1.115$ GeV/c^2 in Figure 5.3 contain both misidentified $\Lambda(\overline{\Lambda})$ particles and good $\mathrm{K^0_S}$. If one simply cuts out the entire peak, some good $\mathrm{K^0_S}$ particles will be lost. Ideally, the $\mathrm{K^0_S}$ selection and $\Lambda(\overline{\Lambda})$ misidentification cuts can be selected such that the peak is removed from this plot while leaving the underlying distribution continuous. To attempt to remove these Λ and $\overline{\Lambda}$ contaminations without throwing away good $\mathrm{K^0_S}$ particles, the misidentification cuts introduced in Sec. 5.4.1 were imposed (the effects of which are visible in Fig. 5.3). The approximate numbers of $\mathrm{K^0_S}$ mesons in the final collections are shown in Table 5.6.

Centrality	K^0_S
0–10%	1.4×10^8
10–30%	4.6×10^7
30–50%	1.8×10^7

Table 5.6: Approximate number of K^0_S mesons in samples

<table>
<tr><th colspan="3">K^0_S reconstruction</th></tr>
<tr><td colspan="2">$|\eta|$</td><td>< 0.8</td></tr>
<tr><td colspan="2">p_T</td><td>> 0.2 GeV/c</td></tr>
<tr><td colspan="2">$|m_{inv} - m_{PDG}|$</td><td>< 17 MeV</td></tr>
<tr><td colspan="2">DCA to prim. vertex</td><td>< 0.3 cm</td></tr>
<tr><td colspan="2">Cosine of pointing angle</td><td>> 0.9993</td></tr>
<tr><td colspan="2">OnFlyStatus</td><td>false</td></tr>
<tr><td colspan="2">Decay Length</td><td>< 30 cm</td></tr>
<tr><td colspan="2">Shared Daughter Cut</td><td>true</td></tr>
<tr><td colspan="2">Misidentification Cut</td><td>true</td></tr>
<tr><th colspan="3">$\pi^{\pm}$ Daughter Cuts</th></tr>
<tr><td colspan="2">$|\eta|$</td><td>< 0.8</td></tr>
<tr><td colspan="2">Number of clusters in TPC</td><td>> 80</td></tr>
<tr><td colspan="2">Daughter Status</td><td>kTPCrefit</td></tr>
<tr><td colspan="2">DCA $\pi^+\pi^-$ Daughters</td><td>< 0.3 cm</td></tr>
<tr><td colspan="2">p_T</td><td>> 0.15 GeV/c</td></tr>
<tr><td colspan="2">DCA to prim vertex</td><td>> 0.3 cm</td></tr>
<tr><td colspan="3">TPC and TOF Nσ Cuts</td></tr>
<tr><td colspan="2">$p < 0.5$ GeV/c</td><td>N$\sigma_{TPC} < 3$</td></tr>
<tr><td rowspan="2">$p > 0.5$ GeV/c</td><td>if TOF & TPC available</td><td>N$\sigma_{TPC} < 3$ & N$\sigma_{TOF} < 3$</td></tr>
<tr><td>else</td><td>N$\sigma_{TOF} < 3$</td></tr>
</table>

Table 5.7: K^0_S reconstruction

5.4.4 V0 purity estimation

In order to obtain a true and reliable signal, one must ensure good purity of the V0 collection. The purity of the collection is calculated as

$$Purity = \frac{Signal}{Signal + Background}. \tag{5.2}$$

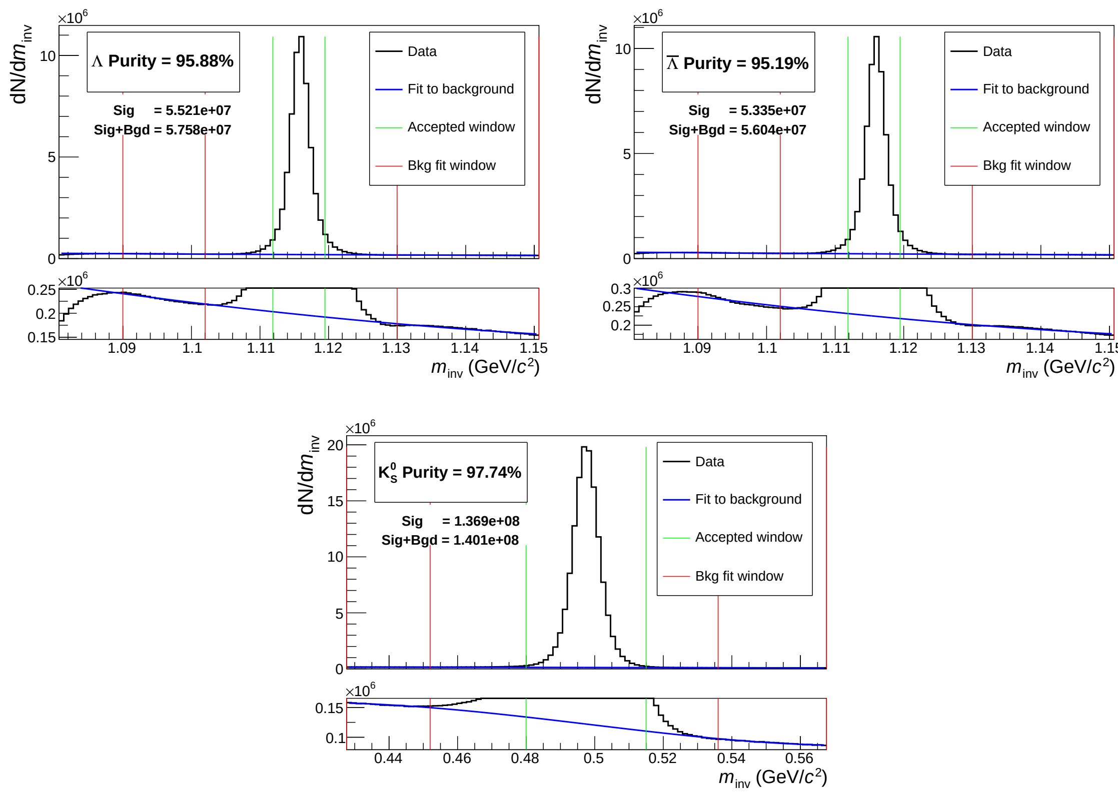

Figure 5.4: Invariant mass ($m_{\rm inv}$) distribution for all Λ (top left), $\overline{\Lambda}$ (top right), and $\rm K^0_S$ (bottom) candidates immediately before the final invariant mass cut. The bottom figures are zoomed to show the background with fit. The vertical green lines represent the $m_{\rm inv}$ cuts used in the analyses, the red vertical lines delineate the regions over which the background was fit, and the blue line shows the background fit.

To access both the signal and background, the invariant mass distribution ($m_{\rm inv}$) of all V0 candidates must be constructed immediately before the final invariant mass cut, as shown in Fig. 5.4 for Λ, $\overline{\Lambda}$ and $\rm K^0_S$ candidates in the 0–10% centrality bin.

Fig. 5.4a presents the $p\pi^-$ invariant mass distribution showing the Λ peak, Fig. 5.4b presents the $\bar{p}\pi^+$ invariant mass distribution showing the $\overline{\Lambda}$ peak, and Fig. 5.4c presents the $\pi^+\pi^-$ invariant mass distribution showing the K^0_S peak. As shown in Figure 5.4, the background is fit (with a polynomial) outside of the peak region of interest to obtain an estimate for the background within the region. Within the m_{inv} cut limits, the background is assumed to be the region below the fit while the signal is that above the fit. The Λ and $\overline{\Lambda}$ purities were found to be $\approx 95\%$, and the K^0_S purity was found to be $\approx 98\%$.

5.4.5 V0 purity background estimation

As previously discussed in Sec. 5.4.4, the backgrounds in the m_{inv} distributions are modeled by a polynomial which is fit outside of the final cut region in an attempt to estimate the background within the cut region. As this estimate of the background under the mass peak is vital for our estimate of our V0 purity, it is important for us to ensure that our estimate is accurate. More specifically, it is necessary that we ensure the background is well described by a polynomial fit within the cut region, which matches continuously and smoothly to the region outside of our cut.

To better understand our background, we studied V0 candidates reconstructed with daughters from different events. These mixed-event V0s certainly do not represent real, physical V0s (a single V0 cannot have daughters living in two different events!), but rather represent a large portion of the background creeping into our analysis. The standard AliFemto framework is not equipped to handle this situation, as most are not interested in these fake-V0s. Therefore, we built a new class, AliFemtoV0PurityBgdEstimator, to handle our needs. In addition to finding fake-V0s using mixed-event daughters, we also used our new class to find real-V0s using same-event daughters.

Figure 5.5 shows the results of our study. In the figures, the black points, marked "Data", correspond to V0s found using the standard V0-finder, and to the V0s used

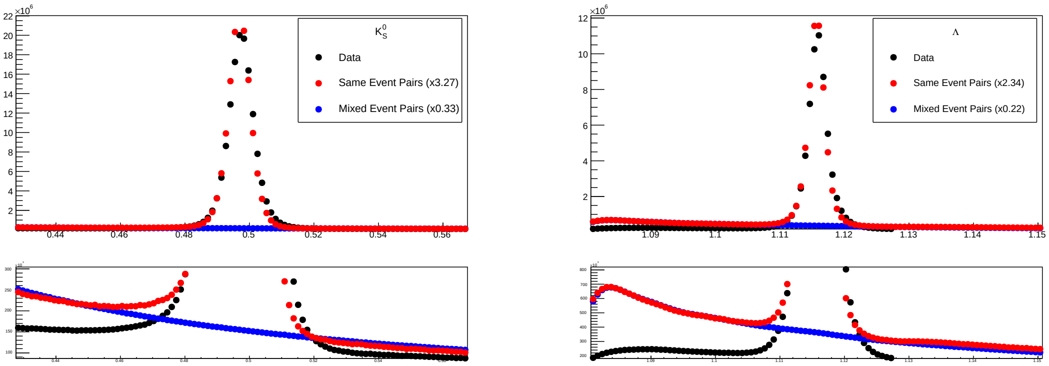

(a) K^0_S (b) Λ

Figure 5.5: V0 Purity Background Estimation. The black points, marked "Data", correspond to real V0s found using the standard V0-finder (i.e. the V0s used in my analyses). The red points, marked "Same Event Pairs", show real V0s reconstructed with our personal V0-finder in AliFemtoV0PurityBgdEstimator. These data are scaled by a factor (listed in the legend) to match their $Signal + Background$ value in the cut region with that of the data. The blue points, marked "Mixed Event Pairs", show fake-V0s reconstructed with our personal V0-finder using mixed-event daughters. The blue points are scaled by a factor (listed in the legend) to closely match the red points in the side-band region.

in my analyses. The red and blue points utilize our personal V0-finder (i.e. AliFemtoV0PurityBgdEstimator). The red points show real-V0s reconstructed using same-event daughters, and the blue points show fake-V0s reconstructed using mixed-event daughters. Both the red and blue points have been scaled by different factors (listed in the legends) to nicely align all three data on a single plot.

Figure 5.5 shows that our personal V0-finder does a good, but not perfect, job of matching the shape of the m_{inv} plots obtained from the data. The scale factor listed in the legend reveals that we are only finding 1/3 - 1/2 of the V0s found by the standard V0-finder. These two points are not of concern, as our purpose here is to gain a sense of the broad shape of the background. It is revealed in Fig. 5.5, when studying the red and blue points, that the background distribution within the mass peak region is simply a smooth connection of the backgrounds outside of the cut region, as we assumed. Therefore, our method of fitting the background outside of the cut region and extrapolating to the cut region is justified.

5.5 Ξ^- reconstruction

The reconstruction of Ξ^- particles is one level above V0 reconstruction in complexity. V0 particles are topologically reconstructed by searching for the charged daughters into which they decay. With Ξ^- particles, we search for the Λ (V0) and π^- (track) daughters into which the Ξ^- decays. We will refer to the π in the preceding sentence as the "bachelor π".

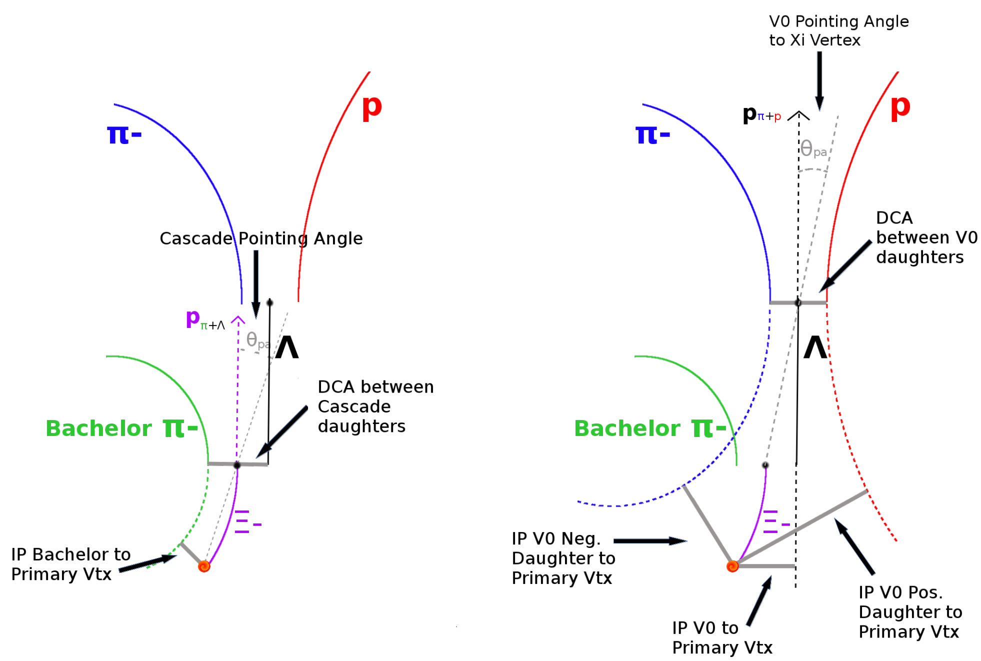

Figure 5.6: (Left) Ξ^- reconstruction (DCA to primary vertex for Ξ^- not shown). (Right) Ξ^- daughter reconstruction.

The cuts shown in Table 5.8 were used to select good Ξ^- ($\overline{\Xi}^+$) candidates. Furthermore, we excluded any candidate in which the bachelor π was also claimed as a daughter of the Λ (implemented in AliFemtoXiTrackPairCut class). Finally, a shared daughter cut, similar to that for V0s discussed in Sec. 5.4.1, was implemented. More specifically, this cut iterates through the Ξ^- collection to ensure that no daughter is claimed by more than one Ξ^- candidate. If a shared daughter is found between two Ξ^- candidates, that candidate with a smaller DCA to primary vertex is kept while the other is excluded from the analysis.

The purity of our Ξ^- and $\overline{\Xi}^+$ collections were calculated just as those of our V0 collections (see Sec. 5.4). Figure 5.7, which is used to calculate the purity, shows the m_{inv} distribution of our $\Xi^-(\overline{\Xi}^+)$ candidates just before the final m_{inv} cut. We estimate our purities to be Purity(Ξ^-) $\approx$ 90% and Purity($\overline{\Xi}^+$) $\approx$ 92%.

<table>
<tr><th colspan="3">Ξ reconstruction</th></tr>
<tr><td colspan="2">$|\eta|$</td><td>< 0.8</td></tr>
<tr><td colspan="2">p_{T}</td><td>> 0.8 GeV/c</td></tr>
<tr><td colspan="2">$|m_{\mathrm{inv}} - m_{\mathrm{PDG}}|$</td><td>$< 3.0$ MeV</td></tr>
<tr><td colspan="2">DCA to prim. vertex</td><td>< 0.3 cm</td></tr>
<tr><td colspan="2">Cosine of pointing angle</td><td>> 0.9992</td></tr>
<tr><th colspan="3">Λ daughter cuts</th></tr>
<tr><td colspan="2">DCA to prim. vertex</td><td>> 0.2 cm</td></tr>
<tr><td colspan="2">Cosine of pointing angle</td><td>> 0.0</td></tr>
<tr><td colspan="2">Cosine of pointing angle to Ξ decay vertex</td><td>> 0.9993</td></tr>
<tr><td colspan="2">OnFlyStatus</td><td>false</td></tr>
<tr><td colspan="3">All other Λ and corresponding (π and p) daughter cuts are same as in primary Λ selection, and can be found in Sec. 5.4.2</td></tr>
<tr><th colspan="3">Bachelor π cuts</th></tr>
<tr><td colspan="2">$|\eta|$</td><td>< 0.8</td></tr>
<tr><td colspan="2">p_{T}</td><td>> 0.0 GeV/c</td></tr>
<tr><td colspan="2">DCA to prim. vertex</td><td>> 0.1 cm</td></tr>
<tr><td colspan="2">Number of clusters in the TPC</td><td>> 70</td></tr>
<tr><td colspan="2">Daughter status</td><td>kTPCrefit</td></tr>
<tr><td colspan="3">TPC and TOF Nσ Cuts</td></tr>
<tr><td colspan="2">$p < 0.5$ GeV/c</td><td>N$\sigma_{\mathrm{TPC}} < 3$</td></tr>
<tr><td rowspan="2">$p > 0.5$ GeV/c</td><td>if TOF & TPC available</td><td>N$\sigma_{\mathrm{TPC}} < 3$ & N$\sigma_{\mathrm{TOF}} < 3$</td></tr>
<tr><td>else</td><td>N$\sigma_{\mathrm{TOF}} < 3$</td></tr>
</table>

Table 5.8: Ξ^- reconstruction

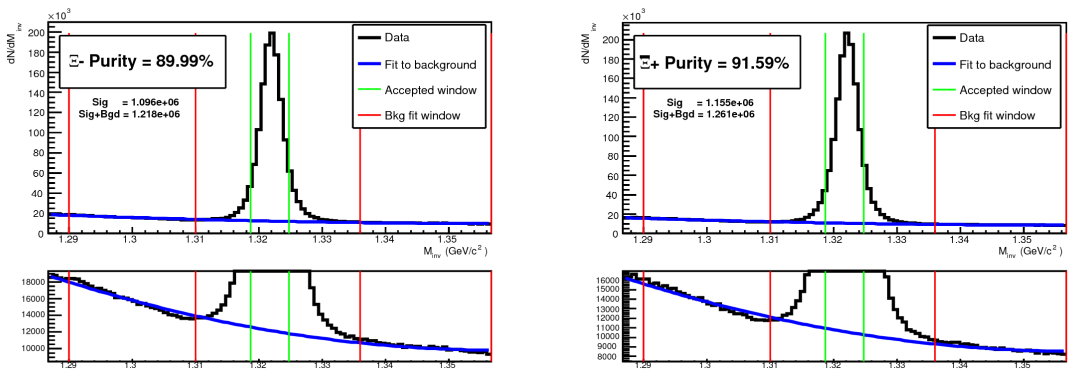

Figure 5.7: Invariant mass (m_{inv}) distribution for all Ξ^- (left) and $\overline{\Xi}^+$ (right) candidates immediately before the final invariant mass cut. The bottom figures are zoomed to show the background with fit. The vertical green lines represent the m_{inv} cuts used in the analyses, the red vertical lines delineate the regions over which the background was fit, and the blue line shows the background fit.

5.6 Pair selection

The femtoscopic analysis of two-particle correlation functions relies on the proper formation of particle pairs. In particular, contamination from pairs constructed with split or merged tracks, and pairs sharing daughters, can introduce artificial signals into the correlation functions, obscuring the actual physics. In an effort to remove such contaminations, we impose two main pair cuts: a shared daughter cut, and an average separation ($\overline{|\mathbf{\Delta r}|}$) cut.

The purpose of the shared daughter cut is to ensure the first particle in the pair is uniquely separated from the second. For pairs formed of two V0s (e.g. ΛK^0_S), this cut is implemented by removing all pairs which share a daughter. For example, in the ΛK^0_S analysis, if the Λ and K^0_S in a potential pair claim the same π^- daughter, the pair is excluded from the analysis. For a pair formed of a single V0 and a charged track (e.g. $\Lambda K^\pm$), the cut removes all pairs in which the charged track is also claimed as a daughter of the V0. This mistake could only occur if, for instance, either a $K^\pm$ is misidentified as a π or p and used in the V0 reconstruction, or a π or p is misidentified as a $K^\pm$ in the $K^\pm$ selection. In the case of a pair formed from a charged Ξ^- and a charged track (e.g. $\Xi^- K^\pm$), the cut removes all pairs in which the charged track is also claimed as a daughter of the Ξ^-, be it the bachelor-π daughter directly, or a daughter of the Λ daughter (a granddaughter of the Ξ^-). In the $\Xi^- K^\pm$ analysis, as in the $\Lambda K^\pm$ case, this could only occur if there was misidentification of a $K^\pm$ as a π or p, or vice versa.

The purpose of the average separation cut is to remove splitting and merging effects, and it is employed in the following way. To calculate the average separation between two tracks, the spatial separation is determined at several points throughout the TPC (every 20 cm radially from 85 cm to 245 cm), and the results are averaged. For the ΛK^0_S analysis, which involves two V0 particles, a minimum average separation cut of 6 cm between the like-charge daughters in the pairs is imposed (for example, between the p daughter of the Λ and the π^+ daughter of the K^0_S). For the $\Lambda K^\pm$

analyses, a minimum average separation cut of 8 cm is enforced between the $K^{\pm}$ and the Λ daughter sharing the same charge (for example, in the ΛK^{+} analysis, between the p daughter of the Λ and the K^{+}). Finally, for the $\Xi^{-}K^{\pm}$ analysis, a minimum average separation cut of 8 cm is enforced between any daughter of the Ξ^{-} sharing the same charge as the $K^{\pm}$ in the pair (for example, the the $\Xi^{-}K^{-}$ analysis, between the π^{-} granddaughter which decayed from the Λ daughter and the K^{-}, and between the bachelor-π^{-} daughter and the K^{-}).

The motivation for the values used in the $\overline{|\Delta \mathbf{r}|}$ cuts can be see in Figures 5.8, 5.9, and 5.10, in which average separation correlation functions are presented. The average separation correlation functions, $C(\overline{|\Delta \mathbf{r}|})$, are formed just as for our relative-momentum correlation functions, but instead of k^{*} we bin in $\overline{|\Delta \mathbf{r}|}$. Looking at $C(\overline{|\Delta \mathbf{r}|})$ for like-charge tracks, at the lowest average separation we see an enhancement due to track splitting, followed by (at slightly higher average separation) a suppression due to track merging. When the average separation correlation function stabilizes to unity, these effects are no longer abundant, and we choose our cut value. Splitting and merging effects between oppositely charged tracks was found to be negligible, therefore no cuts on unlike-charge tracks were imposed. To summarize:

Average Separation Cuts ($\overline{|\Delta \mathbf{r}|}$)

(a) ΛK^{0}_{S} Analyses

- $\overline{|\Delta \mathbf{r}|} > 6.0$ cm for like-charge sign daughters
- No cut for unlike-charge daughters

(b) $\Lambda K^{\pm}$ Analyses

- $\overline{|\Delta \mathbf{r}|} > 8.0$ cm for daughter of $\Lambda(\overline{\Lambda})$ sharing charge sign of $K^{\pm}$
- No cut for unlike-charge

(c) $\Xi^{-}K^{\pm}$ Analyses

- $\overline{|\Delta \mathbf{r}|} > 8.0$ cm for any daughter of Ξ sharing charge sign of $K^{\pm}$
- No cut for unlike-charge

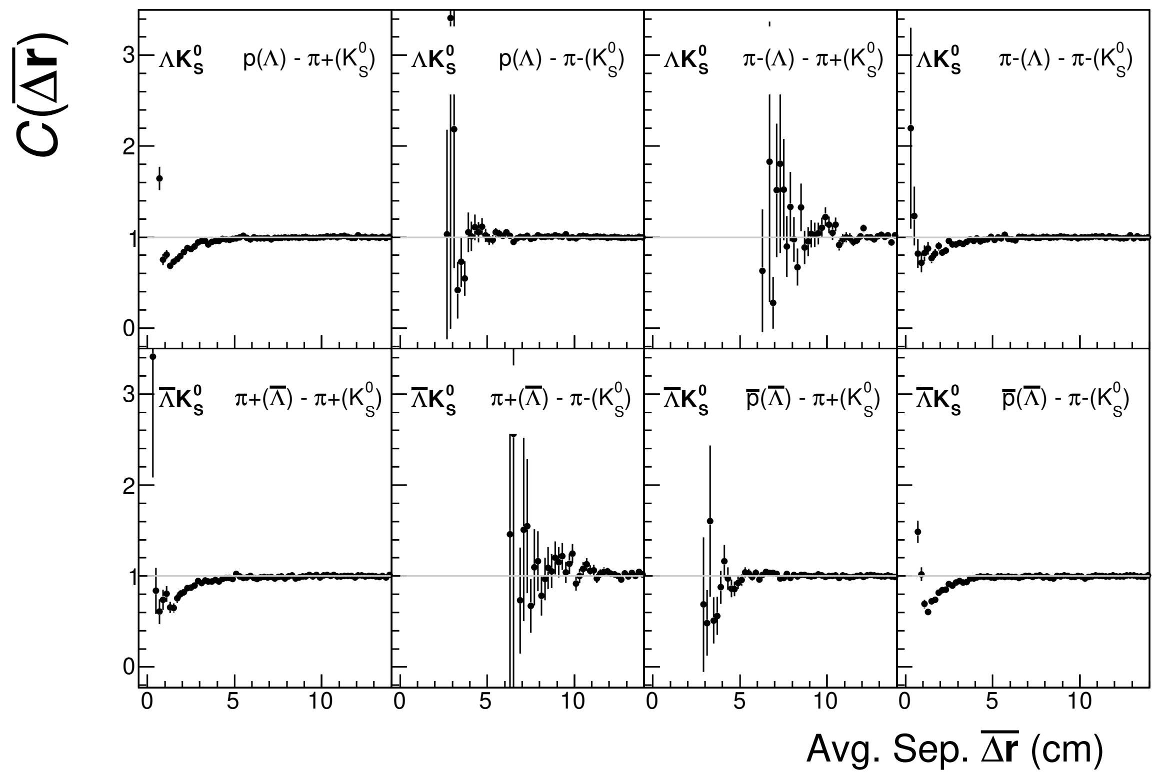

Figure 5.8: Average separation ($\overline{|\Delta \mathbf{r}|}$) correlation functions between the daughters of $\Lambda(\overline{\Lambda})$ hyperons and the daughters of K^0_S mesons in the $\Lambda(\overline{\Lambda})K^0_S$ analyses. The top row shows results from the ΛK^0_S system, and the bottom shows the $\overline{\Lambda}K^0_S$ system. The text in the top right of each subfigure indicates the daughters studied, and the mother of each daughter is shown in parentheses "()"; e.g. the top left shows the $\overline{|\Delta \mathbf{r}|}$ correlation between the p daughter of the Λ and the π^+ daughter of the K^0_S.

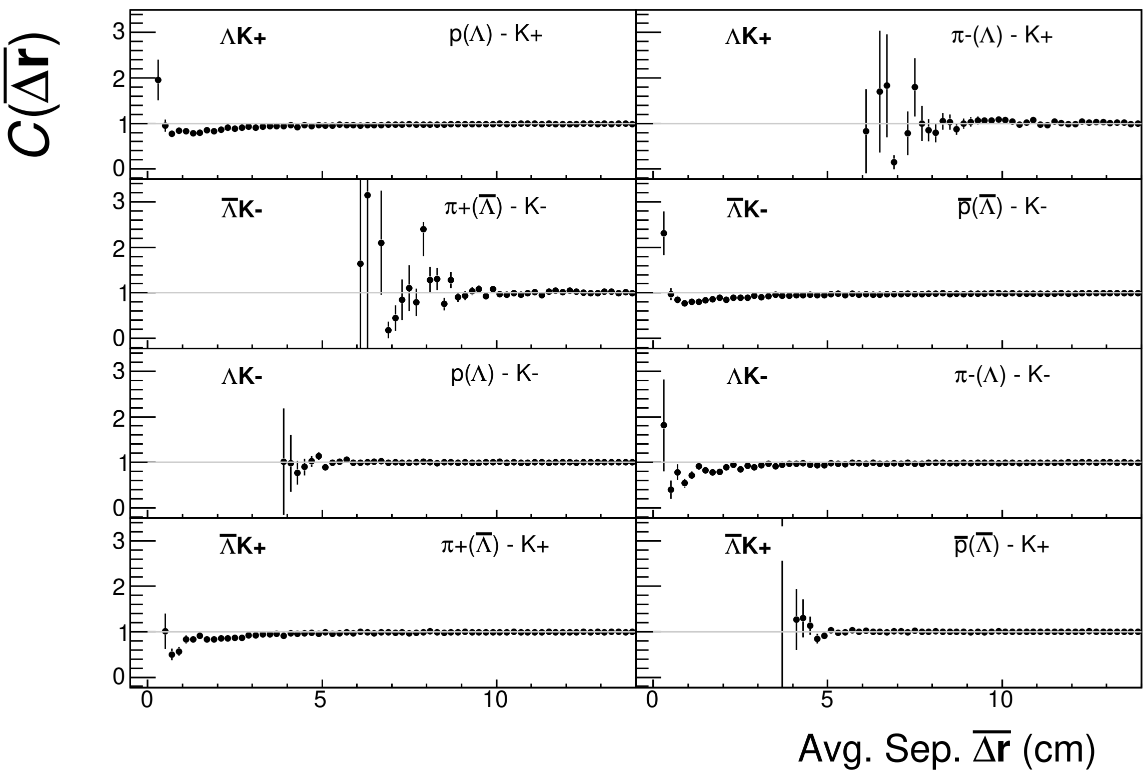

Figure 5.9: Average separation ($\overline{|\Delta\mathbf{r}|}$) correlation functions between the daughters of $\Lambda(\overline{\Lambda})$ hyperons and the $K^{\pm}$ mesons in the $\Lambda(\overline{\Lambda})K^{\pm}$ analyses. The rows differentiate the analysis; from top to bottom: ΛK^{+}, $\overline{\Lambda}K^{-}$, ΛK^{-}, $\overline{\Lambda}K^{+}$. The text in the top right of each subfigure indicates the particle tracks studied, and, if applicable, the mother of a given particle is shown in parentheses "()"; e.g. the top left shows the $\overline{|\Delta\mathbf{r}|}$ correlation between the p daughter of the Λ and the K^{+}.

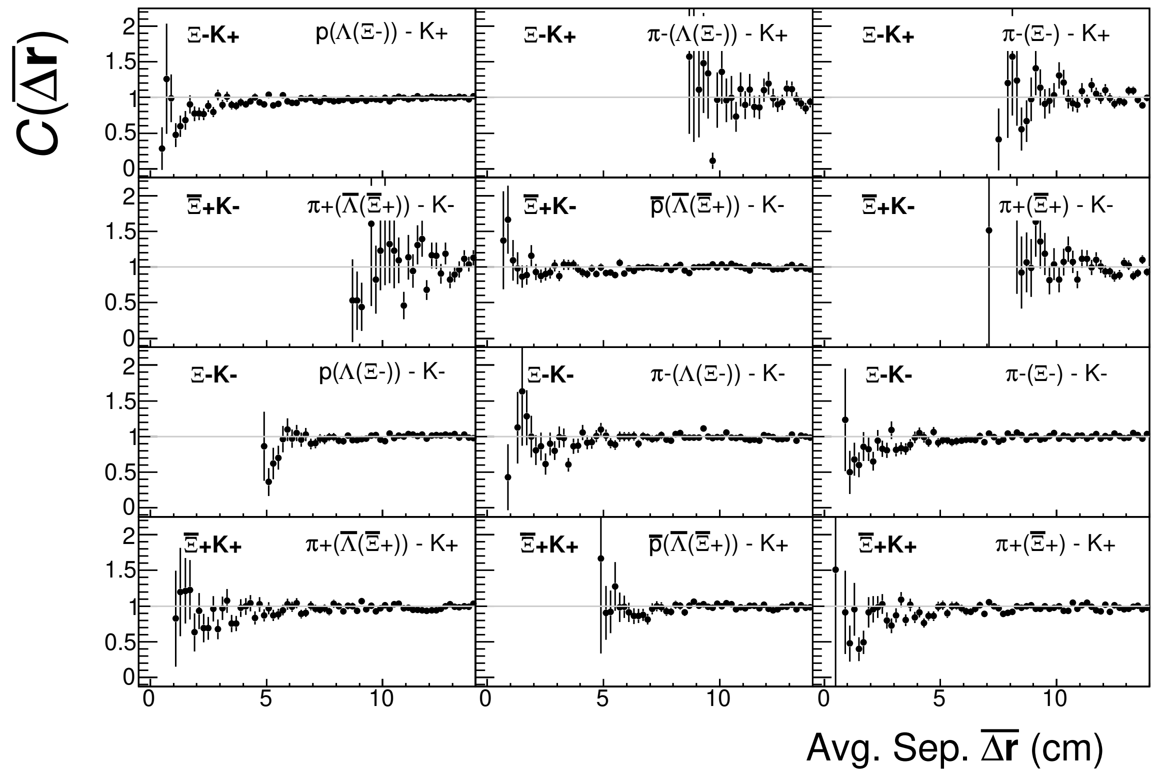

Figure 5.10: Average separation ($\overline{|\Delta \mathbf{r}|}$) correlation functions between the daughters and granddaughters of Ξ hyperons and $K^{\pm}$ mesons in the $\Xi^{-}(\overline{\Xi}^{+})K^{\pm}$ analyses. The rows differentiate the analysis; from top to bottom: $\Xi^{-}K^{+}$, $\overline{\Xi}^{+}K^{-}$, $\Xi^{-}K^{-}$, $\overline{\Xi}^{+}K^{+}$. The text in the top right of each subfigure indicates the particle tracks studied, and, if applicable, the mother of a given particle is shown in parentheses "()"; e.g. the top left shows the $\overline{|\Delta \mathbf{r}|}$ correlation between the p granddaughter of the Ξ^{-} (i.e. the p daughter of the Λ which decayed from the Ξ^{-}) and the K^{+}. As a second example, the top right shows the $\overline{|\Delta \mathbf{r}|}$ correlation between the bachelor-π^{-} daughter of the Ξ^{-} and the K^{+}.

5.7 Correlation functions

This analysis studies the relative momentum correlations of both ΛK and $\Xi^-K^\pm$ pairs using the two-particle correlation function, defined as $C(k^*) = A(k^*)/B(k^*)$, where $A(k^*)$ is the signal distribution, $B(k^*)$ is the reference (or background) distribution, and k^* is the momentum of one of the particles in the pair rest frame. In practice, $A(k^*)$ is constructed by binning in k^* pairs from the same event. $B(k^*)$ is used to divide out the phase-space effects, leaving only the femtoscopic effects in the correlation function. Therefore, ideally $B(k^*)$ is similar to $A(k^*)$ in all respects excluding the presence of femtoscopic correlations [123].

This analysis presents correlation functions for three centrality bins (0–10%, 10–30%, and 30–50%), and is pair transverse momentum ($k_{\mathrm{T}} = 0.5|\mathbf{p}_{\mathrm{T},1} + \mathbf{p}_{\mathrm{T},2}|$)[1] integrated (i.e. not binned in k_{T}) due to limited statistics. The correlation functions are constructed separately for the two ALICE dipole magnetic field configurations (positive ++, and negative −−), and were checked for consistency. The correlation functions are kept separate during the fitting process, and are combined using a weighted average when plotting, where the weight is the number of numerator pairs in the normalization range.

5.7.1 Typical correlation function construction

In practice, $B(k^*)$ is typically obtained by forming mixed-event pairs [140], i.e. particles from a given event are paired with particles from $\mathrm{N}_{mix}(= 5)$ other events. In forming the background distribution, it is important to mix only similar events; mixing events with different phase-spaces can result in an unreliable background distribution, and can introduce artificial signals in the correlation function. Therefore, in this analysis, we bin our events both in primary vertex location (2 cm bin width)

[1] The notation is a bit confusing, as this k_{T} value is not related to the relative momentum vector k^μ introduced in Eq. 4.5. However, this is the most commonly used notation, so we adopt it here.

and in centrality (5% bin width), and we only mix events within a given bin; i.e. we only mix events of like centrality and of like primary vertex location.

Figures 5.11, 5.12, 5.13 show the correlation functions for all centralities studied for $\Lambda K^+(\bar{\Lambda}K^-)$, $\Lambda K^-(\bar{\Lambda}K^+)$, and $\Lambda(\bar{\Lambda})K^0_S$, respectively. All are normalized in the range $0.32 < k^* < 0.4$ GeV/c. It is interesting to note that the average of the $\Lambda K^+(\bar{\Lambda}K^-)$ and $\Lambda K^-(\bar{\Lambda}K^+)$ correlation functions is consistent with our $\Lambda K^0_S(\bar{\Lambda}K^0_S)$ measurement (see also Fig. 7.3 in Sec. 7.1.1). The figures show a significant non-femtoscopic background, i.e. the correlation function deviates from unity outside of the femtoscopic signal region, observable in the figures at $k^* \gtrsim 0.4$ GeV/c, and more pronounced in the more peripheral events. The non-femtoscopic background will be discussed further in Sec. 6.3.

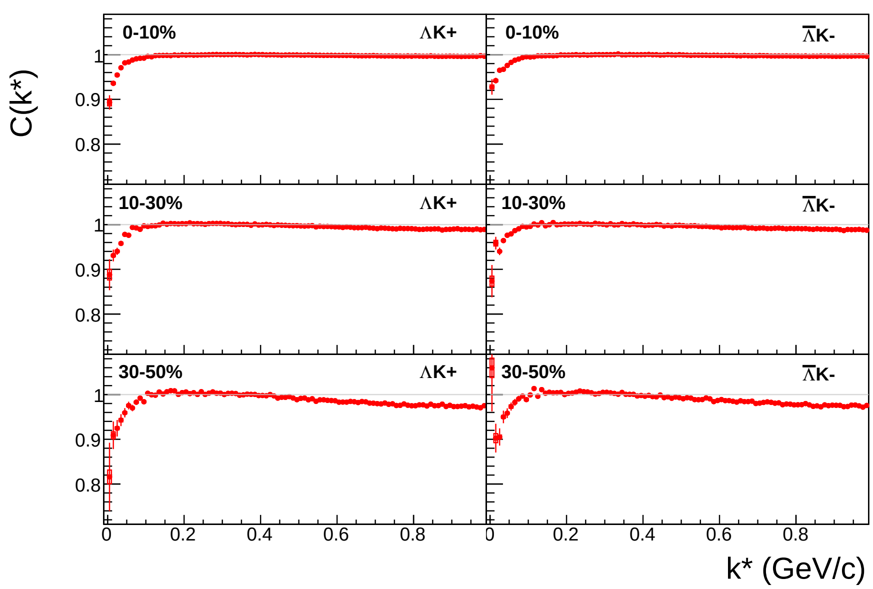

Figure 5.11: ΛK^+ (left) and $\bar{\Lambda}K^-$ (right) correlations for 0–10% (top), 10–30%(middle), and 30–50%(bottom) centralities.

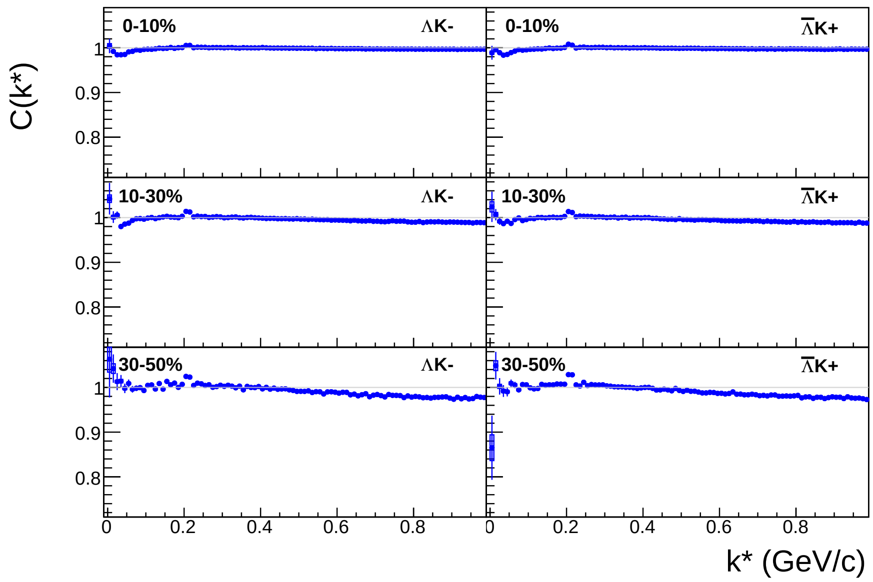

Figure 5.12: ΛK^- (left) and $\overline{\Lambda}K^+$ (right) correlations for 0–10% (top), 10–30%(middle), and 30–50%(bottom) centralities. The peak at $k^* \approx 0.2$ GeV/c is due to the Ω^- (and, to a much smaller extent, the $\Xi(1690)$ resonances.

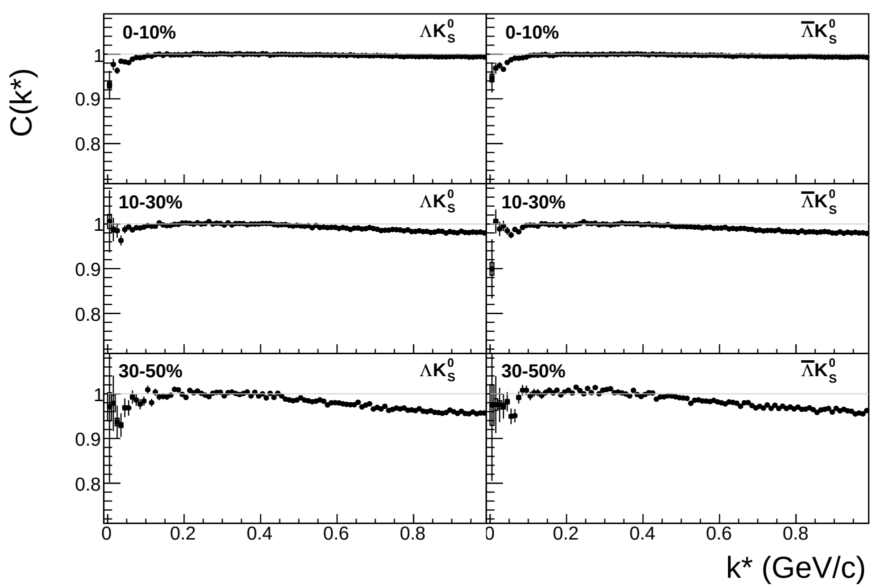

Figure 5.13: ΛK^0_S (left) and $\overline{\Lambda}K^0_S$ (right) correlations for 0–10% (top), 10–30%(middle), and 30–50%(bottom) centralities.

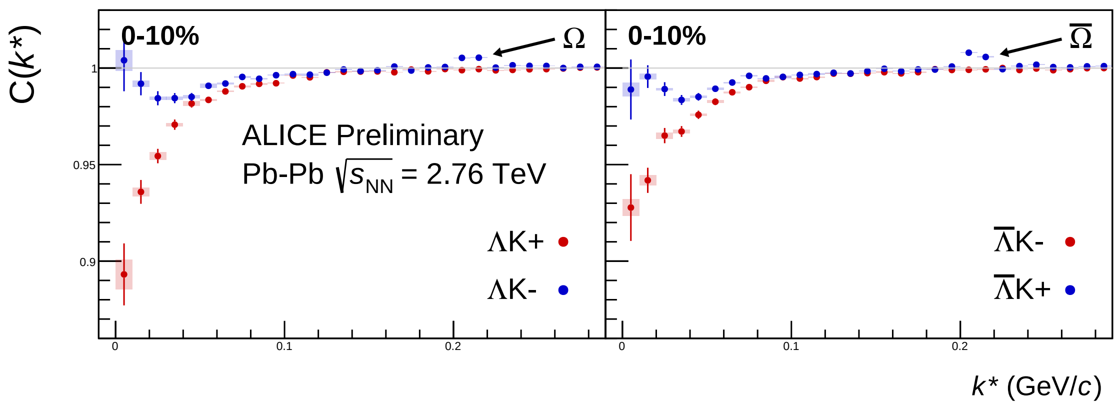

Figure 5.14: Correlation Functions: ΛK^+ vs. ΛK^- ($\overline{\Lambda}K^+$ vs. $\overline{\Lambda}K^-$) for 0–10% centrality. The peak in ΛK^-($\overline{\Lambda}K^+$) at $k^* \approx 0.2$ GeV/c is due to the Ω^- (and likely the $\Xi(1690)$ resonance, although to a much smaller extent). The lines represent the statistical errors, while boxes represent systematic errors.

5.7.2 Stavinskiy correlation function construction

The purpose of our investigation of the "Stavinskiy method" [165] is to attempt to rid the correlation functions of the non-femtoscopic background. More specifically, our intent is to handle background contributions from elliptic flow, and other sources having reflection symmetry in the transverse plane. With the Stavinskiy method, mixed-event pairs are not used for the reference distribution ($B(k^*)$); instead, same-event *pseudo-pairs*, formed by rotating one particle in a real pair by 180° in the transverse plane, are used as a reference. This rotation rids the pairs of any femtoscopic correlation, while maintaining correlations due to elliptic flow (and other suitably symmetric contributors).

Note, one must be somewhat careful when applying this Stavinskiy method. We found that, in order to obtain correct results, we had to run our pseudo-pairs through the same pair cuts used in our analyses. In an ideal world, our pair cut would only remove truly bad pairs resulting from splitting, merging, etc. In the real world, the pair cut always throws out some of the good with the bad. Therefore, for the pseudo-pairs to form a reliable background, they too must experience the pair cut, and the loss of "good" pseudo-pairs.

The results of correctly and incorrectly implementing such a procedure, compared to the normal correlation function construction (Sec. 5.7.1), are shown in Figures 5.15 - 5.17. In all cases, results from the incorrect implementation are shown in magenta, and the correct implementation in green. The figures show the Stavinskiy method does a very good job of ridding the $\Lambda\mathrm{K}^{\pm}$ correlations of their non-femtoscopic backgrounds. We also see the procedure does not work as well on the $\Lambda\mathrm{K}^0_{\mathrm{S}}$ system. We find that the improper implementation of the method, in which the pseudo-pairs are not exposed to the appropriate pairs cuts, affect mainly our $\Lambda\mathrm{K}^+$ & $\overline{\Lambda}\mathrm{K}^-$ analysis (Fig. 5.15). Fit results obtained using that Stavinskiy method can be found in App. A.1.

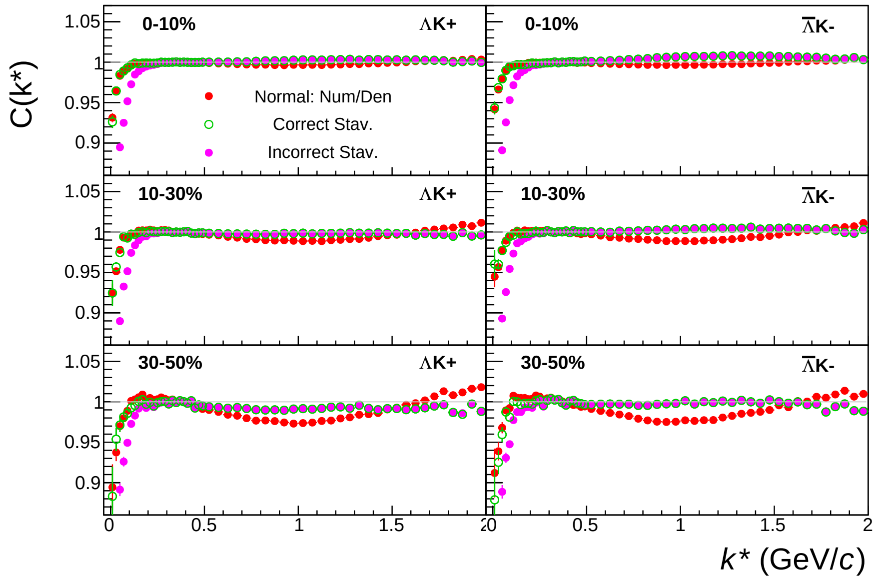

Figure 5.15: ΛK^+ and $\overline{\Lambda}K^-$ correlation functions built using the Stavinskiy method, both correctly (green, open) and incorrectly (magenta, closed), compared to the standard method (red, closed) for 0–10%, 10–30%, and 30–50% centralities. See text for details.

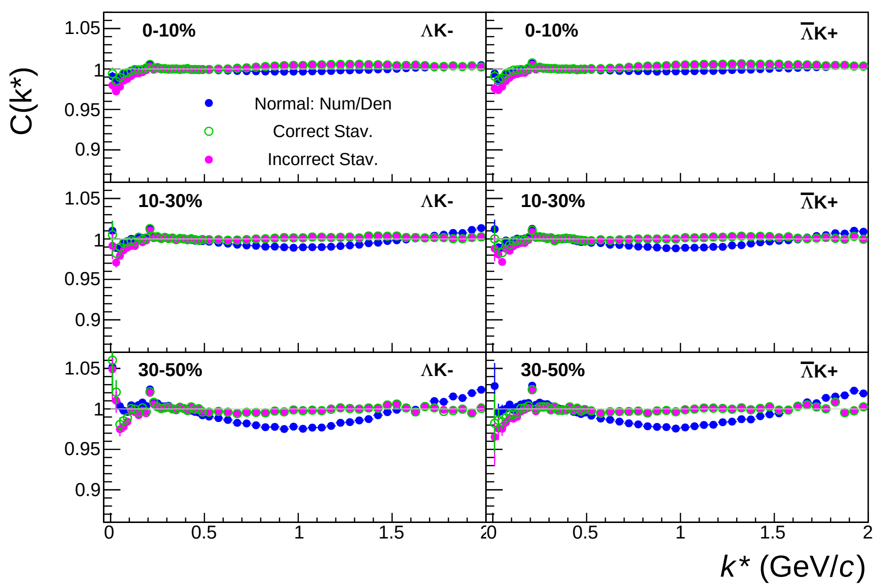

Figure 5.16: ΛK^- and $\overline{\Lambda}K^+$ correlation functions built using the Stavinskiy method, both correctly (green, open) and incorrectly (magenta, closed), compared to the standard method (blue, closed) for 0–10%, 10–30%, and 30–50% centralities. See text for details.

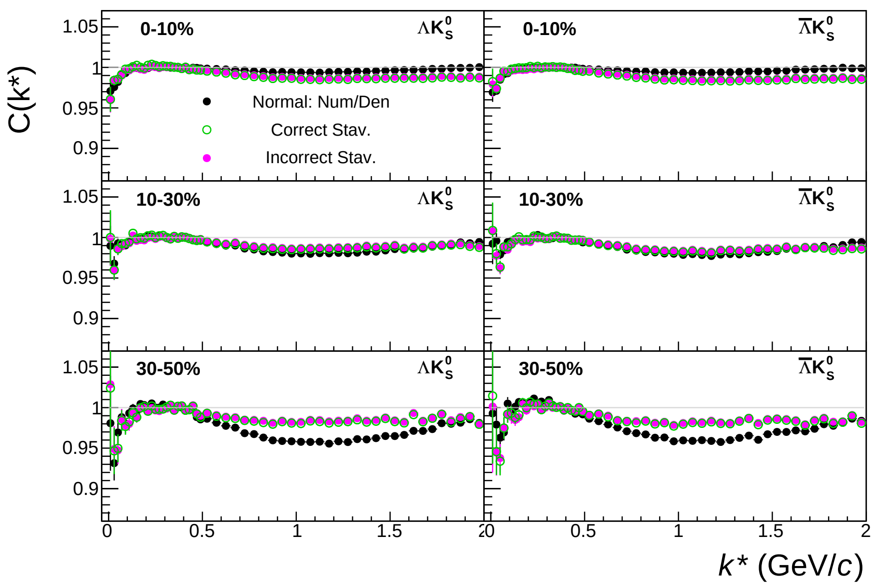

Figure 5.17: ΛK^0_S and $\overline{\Lambda} K^0_S$ correlation functions built using the Stavinskiy method, both correctly (green, open) and incorrectly (magenta, closed), compared to the standard method (black, closed) for 0–10%, 10–30%, and 30–50% centralities. See text for details.

Chapter 6: Fitting Procedure

In this chapter, we discuss the methods used for fitting our ΛK and Ξ^{-}K$^{\pm}$ correlation functions. We begin with a discussion of the finite track momentum resolution of our detectors, and how we account for such effects in our fit. We then discuss the inclusion of residual correlations resulting from the feed-down of resonances into our ΛK system. The observation of a large non-femtoscopic background signal in our correlation functions is presented, including an explanation of the underlying cause, as well as its treatment within our fit procedure. Finally, we summarize the methods used to fit the ΛK and Ξ^{-}K$^{\pm}$ systems, and we end with a discussion of the systematic uncertainties of our results.

6.1 Momentum resolution corrections

Finite track momentum resolution causes the reconstructed momentum of a particle to smear around the true value. This, of course, also holds true for V0 particles. The effect is propagated up to the pairs of interest, which causes the reconstructed relative momentum (k^{*}_{Rec}) to differ from the true relative momentum (k^{*}_{True}). Smearing of the momentum typically will result in a suppression of the signal. More specifically, the smearing will broaden the signal, which would cause a decrease in the extracted radius of the system. The effect of finite momentum resolution can be investigated using the MC HIJING data, for which both the true (k^{*}_{True}) and reconstructed (k^{*}_{Rec}) momenta are available.

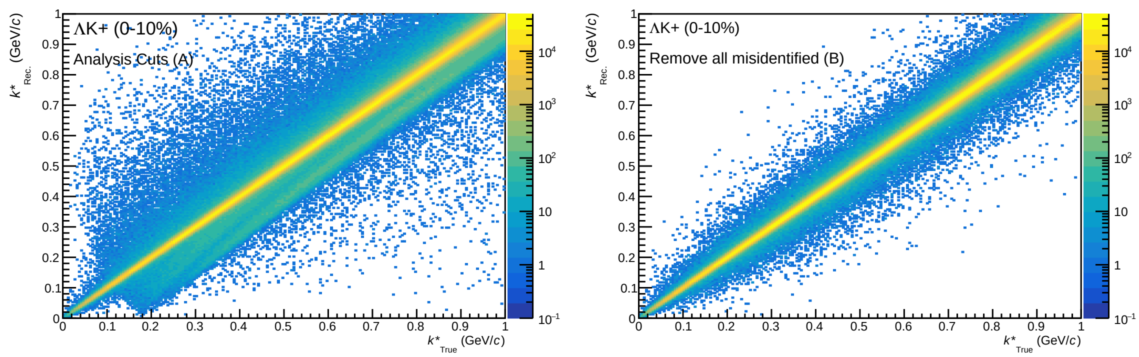

Figure 6.1: Sample k^*_{True} vs. k^*_{Rec} plots from MC HIJING events for ΛK$^+$ 0–10% analyses. The left figure shows results which utilize the cuts in our analysis, and in the right all pairs with a misidentified particle have been removed. In the left figure, the structure which appears around $k^*_{\mathrm{Rec}} = k^*_{\mathrm{True}}$- 0.15 GeV/$c$ is mainly caused by K$^0_{\mathrm{S}}$ contamination in our $\Lambda(\overline{\Lambda})$ sample. The remaining structure not distributed about $k^*_{\mathrm{Rec}} = k^*_{\mathrm{True}}$ is due to π and e contamination in our K$^{\pm}$ sample.

Figure 6.1 shows sample k^*_{True} vs. k^*_{Rec} plots for ΛK$^+$ 0–10% analyses generated with the MC HIJING and GEANT 3 simulations. The left figure shows results which utilize the cuts in our analysis, and in the right all pairs with one or more misidentified particles have been removed. If there are no contaminations in our pair collection, the left plot in Figure 6.1 should match the right; this is mostly true in our analyses. However, there are some interesting features in Fig. 6.1 (left) which demonstrate a small (notice the log-scale on the z-axis) contamination in our pair collection. The structure around $k^*_{\mathrm{Rec}} = k^*_{\mathrm{True}}$- 0.15 GeV/$c$ is mainly caused by K$^0_{\mathrm{S}}$ contamination in our $\Lambda(\overline{\Lambda})$ sample. The remaining structure not distributed about $k^*_{\mathrm{Rec}} = k^*_{\mathrm{True}}$ is due to π and e contamination in our K$^{\pm}$ sample.

Information gained from looking at k^*_{Rec} vs k^*_{True} can be used to apply corrections to account for the effects of finite momentum resolution on the correlation functions. A typical method ("Ratio" method) involves using the MC HIJING data to build two correlation functions, $C_{\mathrm{Rec}}(k^*)$ and $C_{\mathrm{True}}(k^*)$, using the generator-level momentum (k^*_{True}) and the measured detector-level momentum (k^*_{Rec}). The data is then corrected by multiplying by the ratio, $C_{\mathrm{True}}/C_{\mathrm{Rec}}$, before fitting. This essentially unsmears the data, which then can be compared directly to theoretical predictions and fits. Although this is conceptually simple, there are a couple of big disadvantages to this method. First, HIJING does not incorporate final-state interactions, so weights must be used when building same-event (numerator) distributions. These weights account for the interactions, and, in the absence of Coulomb interactions, can be calculated using Eq. 4.44. Of course, these weights are valid only for a particular set of fit parameters. Therefore, in the fitting process, during which the fitter explores a large parameter set, the corrections will not remain valid. As such, applying the momentum resolution correction and fitting becomes a long and drawn-out iterative process. An initial parameter set is obtained (through fitting without momentum resolution corrections, theoretical models, or a good guess), the MC data is analyzed to obtain the correction factor, the data is fit using the correction factor, a refined parameter set is extracted, the MC data is analyzed again to obtain the new correction factor, etc. This process continues until the parameter set stabilizes.

The second issue with the "Ratio" method concerns statistics. With the HIJING data readily available, we were not able to generate the statistics necessary to use the raw $C_{\mathrm{True}}/C_{\mathrm{Rec}}$ ratio. The ratio was not stable, and when applied to the data, obscured the signal. Attempting to fit the ratio to generate the corrections also proved problematic. However, as HIJING does not include final-state interactions, the standard same-event and mixed-event pairs are very similar (with the exception of things like energy and momentum conservation, etc). Therefore, one may artificially increase the statistics by building the numerator distribution with mixed-event pairs. This corresponds, more or less, to simply running the weight generator through the detector framework.

In a second approach, referred to as the "Matrix method", information gained from looking at k^*_{Rec} vs k^*_{True} is exploited to generate response matrices. The response matrix describes quantitatively how each k^*_{Rec} bin receives contributions from multiple k^*_{True} bins, and can be used to account for the effects of finite momentum resolution. Figure 6.1 shows an example of a response matrix. With this approach, the resolution correction is applied on-the-fly during the fitting process by propagating the theoretical fit correlation function ($C_{\mathrm{Fit}}(k^*_{\mathrm{True}})$) through the response matrix, according to:

$$C_{\mathrm{Fit}}(k^*_{\mathrm{Rec}}) = \frac{\sum\limits_{k^*_{\mathrm{True}}} M_{k^*_{\mathrm{Rec}},k^*_{\mathrm{True}}} C_{\mathrm{Fit}}(k^*_{\mathrm{True}})}{\sum\limits_{k^*_{\mathrm{True}}} M_{k^*_{\mathrm{Rec}},k^*_{\mathrm{True}}}} \tag{6.1}$$

where $M_{k^*_{\mathrm{Rec}},k^*_{\mathrm{True}}}$ is the response matrix, $C_{\mathrm{Fit}}(k^*_{\mathrm{True}})$ is the theoretic fit function binned in k^*_{True}, and the denominator normalizes the result. Equation 6.1 describes that, for a given k^*_{Rec} bin, the observed value of $C(k^*_{\mathrm{Rec}})$ is a weighted average of all $C(k^*_{\mathrm{True}})$ values, where the weights are the normalized number of counts in the [k^*_{Rec}, k^*_{True}] bin.

Here, the momentum resolution correction is applied to the fit, not the data. In other words, during the fit the theoretical correlation function is smeared just as real data would be, as opposed to unsmearing the data. This may not be ideal for the theorist attempting to compare a model to experimental data, but it leaves the experimental data unadulterated. The current analyses use this "Matrix" method to apply momentum resolution corrections because of two major advantages. First, the MC HIJING data must be analyzed only once, and no assumptions about the fit are needed. Second, the momentum resolution correction is applied on-the-fly by the fitter, delegating the iterative process to a computer instead of the user.

The two methods described above, "Ratio" and "Matrix", should reproduce the same results. This was tested by first assuming a parameter set and building the C_{True} and C_{Rec} correlation functions needed for the "Ratio" method. A test correlation function was built using the parameter set, and both correction methods ("Ratio" and "Matrix") were applied to study their effect, the results of which are presented in Fig. 6.2. In the figure, the "Ratio" method is shown with circle markers, while the "Matrix" method is shown with triangles. Furthermore, black/gray points utilize a course binning in comparison to the finer binning used for the red points. Looking at the black/gray data, the two methods initially show an apparent discrepancy. However, the red data points a much closer together, and we conclude that any difference in the two methods is due to binning effects, i.e. the two methods converge as the bin size is decreased.

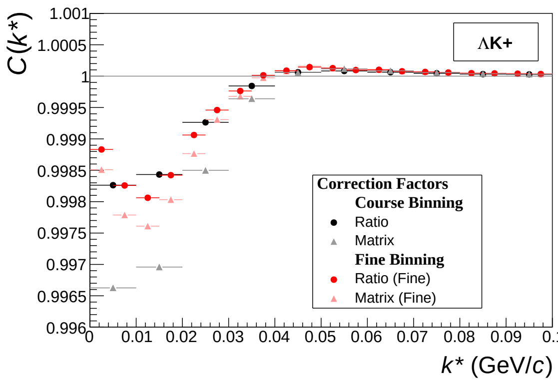

(a) ΛK$^+$

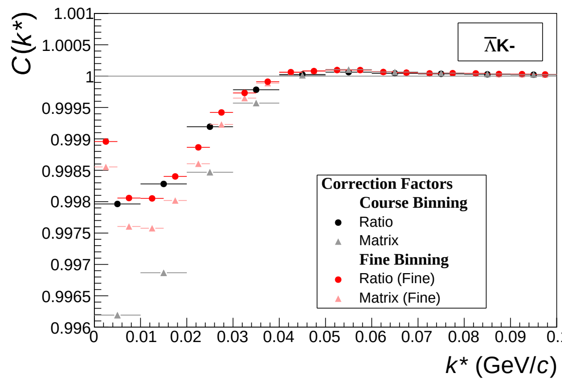

(b) $\overline{\Lambda}$K$^-$

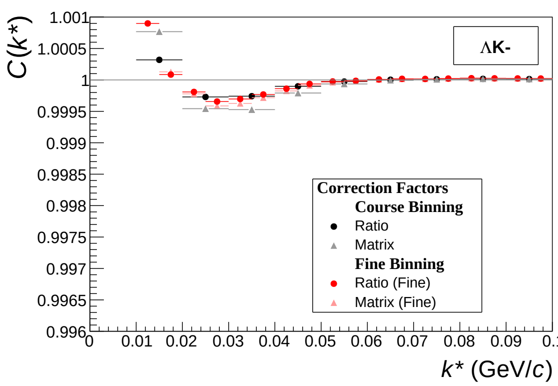

(c) ΛK$^-$

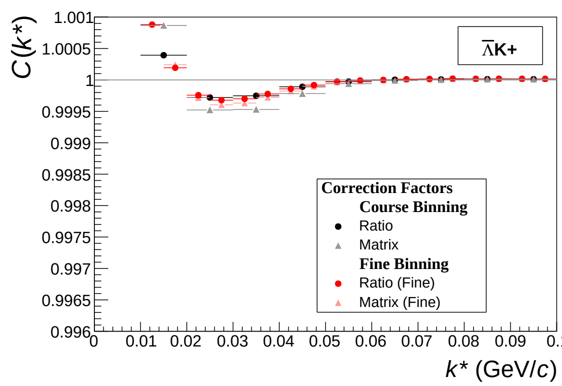

(d) $\overline{\Lambda}$K$^+$

Figure 6.2: Comparison of the two methods, “Ratio” and “Matrix”, for accounting for momentum resolution effects with HIJING. The “Ratio” method is shown with circle markers, while the “Matrix” method is shown with triangles. Black points utilize a course binning, while a finer binning was used for the red points.

6.2 Residual correlations

The purpose of this analysis is study the interaction and scale of the emitting source of the primary ΛK pairs. However, in practice, obtaining a pure sample of primary ΛK pairs is impossible to achieve; some of the selected particles originate as decay products from other resonances, and some of the final pairs contain a misidentified member. In both cases, these contribute to the finally observed correlation function, and obscure its relation to the primary ΛK system. The contributions from fake pairs, which contain at least one misidentified member, are assumed to average to unity, in which case they simply attenuate the femtoscopic signal.

Those pairs containing daughters from decayed resonances carry information about the parent system. In effect, the correlation between the parents will be visible, although smeared out, in the daughters' signal. This is termed a residual correlation resulting from feed-down. For this analysis, a portion of the selected Λ hyperons decay from Σ^0, Ξ^0, Ξ^- and $\Sigma^{*(+,-,0)}(1385)$ parents, and some of the K mesons decay from $\mathrm{K}^{*(+,-,0)}(892)$ parents. Residual correlations are important in an analysis when three criteria are met [166]: i) the parent correlation signal is large, ii) a large fraction of pairs in the sample originate from the particular parent system, and iii) the decay momenta are comparable to the expected correlation width in k^*. The contributions from the primary correlation, residual correlations, and fake pairs on the finally measure data is shown schematically in Figure 6.3.

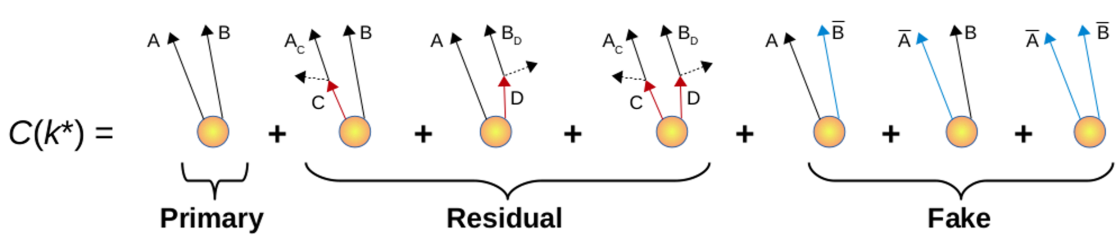

Figure 6.3: A schematic representation of the contributions to the finally measured data from the primary correlation, residual correlations, and fake pairs.

Inclusion of residual contributions in the fit

As it is difficult for us to eliminate these residual correlations from our analyses, we must attempt to account for them in our fit. The genuine ΛK correlation function may be combined with the contributions from residual feed-down and misidentified particles to obtain the finally measured signal [166]:

$$\begin{aligned} C_{\text{measured}}(k^*_{\Lambda\text{K}}) &= 1 + \lambda'_{\Lambda\text{K}}[C_{\Lambda\text{K}}(k^*_{\Lambda\text{K}}) - 1] + \sum_{i,j} \lambda'_{ij}[C_{ij}(k^*_{\Lambda\text{K}}) - 1] \\ \lambda'_{ij} &= \lambda_{\text{Fit}}\lambda_{ij} \\ \sum_{i,j} \lambda'_{ij} &= \lambda_{\text{Fit}} \sum_{i,j} \lambda_{ij} = \lambda_{\text{Fit}} \end{aligned} \tag{6.2}$$

where the ΛK term represents the genuine ΛK correlation, and the ij terms denote the contributions from residual feed-down and possible impurities. More specifically, $C_{ij}(k^*_{\Lambda\text{K}})$ is the correlation function between parents of particle species i and j, expressed in terms of the relative momentum of the observed daughter ΛK pair. The λ_{ij} parameters serve as weights dictating the strength of the parent contribution to the daughter pair, and are normalized to unity. The individual λ_{ij} are fixed (and whose values can be found in Tables 6.2 and 6.3), but the parameter λ_{Fit} is left free. The λ_{Fit} parameter serves as an overall normalization shared by all contributors.

In order to obtain the parent correlation function expressed in the relative momentum of the daughter pair, $C_{ij}(k^*_{\Lambda K})$, oa transform matrix is needed. The transform matrix describes the decay kinematics of the parent system into the daughter, and maps the k^* of the parent pair onto that of the daughter pair. Using this matrix, the transformed residual correlation function can be obtained as

$$C_{ij}(k^*_{\Lambda\text{K}}) \equiv \frac{\sum\limits_{k^*_{ij}} C_{ij}\left(k^*_{ij}\right) T\left(k^*_{ij}, k^*_{\Lambda\text{K}}\right)}{\sum\limits_{k^*_{ij}} T\left(k^*_{ij}, k^*_{\Lambda\text{K}}\right)} \tag{6.3}$$

where T is the transform matrix, $C_{ij}\left(k^*_{ij}\right)$ is the parent correlation function, and $C_{ij}\left(k^*_{\Lambda\text{K}}\right)$ is the parent correlation function expressed in the relative momentum of the daughter pair.

The transform matrix is generated with the THERMINATOR 2 [167] simulation. It is formed for a given parent system, ij, by taking all ΛK pairs originating from ij, calculating the relative momentum of the parents (k^*_{ij}) and daughters ($k^*_{\Lambda\mathrm{K}}$), and filling a two-dimensional histogram with the values. The transform matrix is essentially an unnormalized probability distribution mapping the k^* of the parent pair to that of the daughter pair when one or both parents decay. An example of such transform matrices can be found in Figures 6.4 and 6.5.

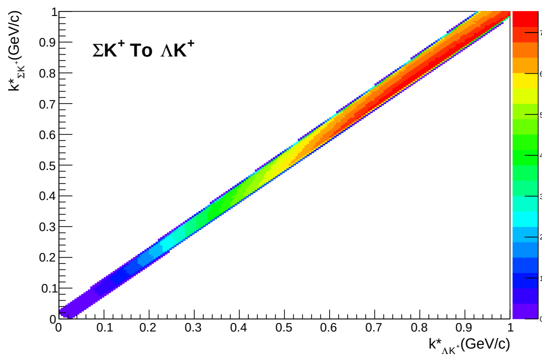

(a) Transform matrix for $\Sigma\mathrm{K}^+$ pairs into $\Lambda\mathrm{K}^+$

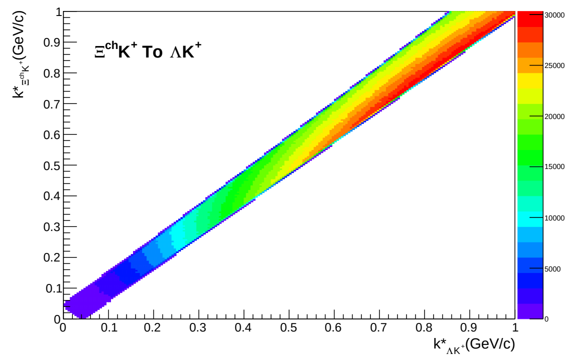

(b) Transform matrix for $\Xi^-\mathrm{K}^+$ pairs into $\Lambda\mathrm{K}^+$

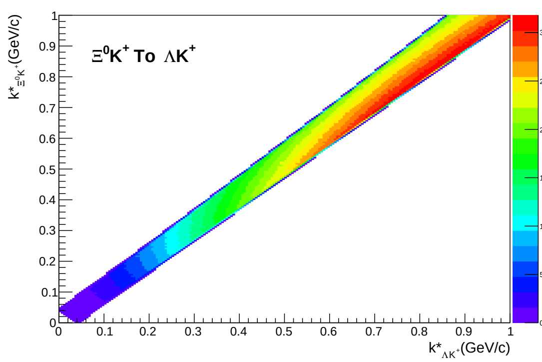

(c) Transform matrix for $\Xi^0\mathrm{K}^+$ pairs into $\Lambda\mathrm{K}^+$

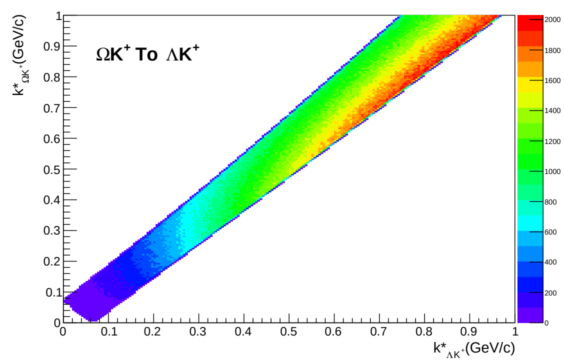

(d) Transform matrix for $\Omega^-\mathrm{K}^+$ pairs into $\Lambda\mathrm{K}^+$

Figure 6.4: Sample Transform Matrices generated with THERMINATOR for $\Lambda\mathrm{K}^+$ Analysis

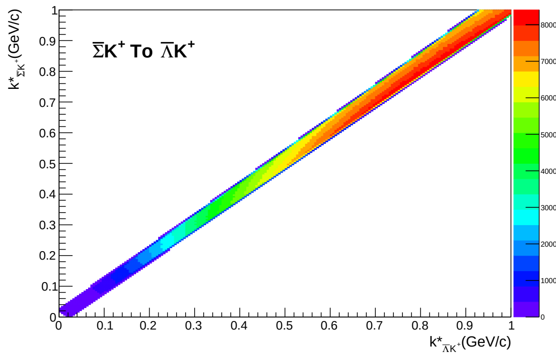

(a) Transform matrix for $\overline{\Sigma}$K$^+$ pairs into $\overline{\Lambda}$K$^+$

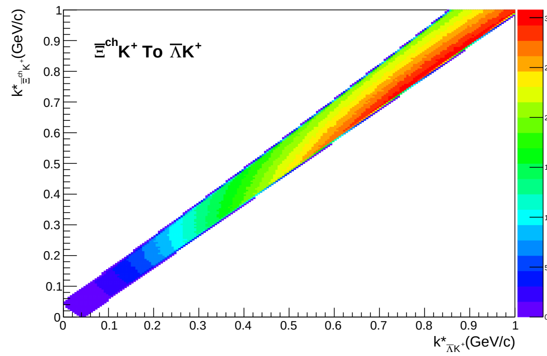

(b) Transform matrix for $\overline{\Xi}^+$K$^+$ pairs into $\overline{\Lambda}$K$^+$

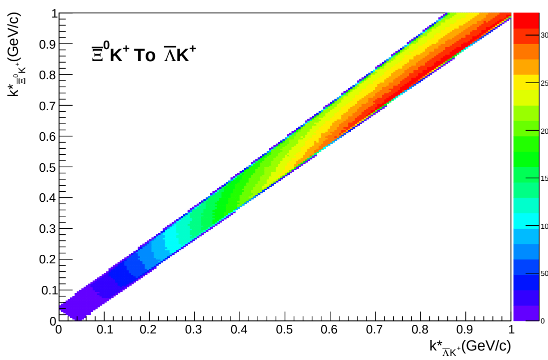

(c) Transform matrix for $\overline{\Xi}^0$K$^+$ pairs into $\overline{\Lambda}$K$^+$

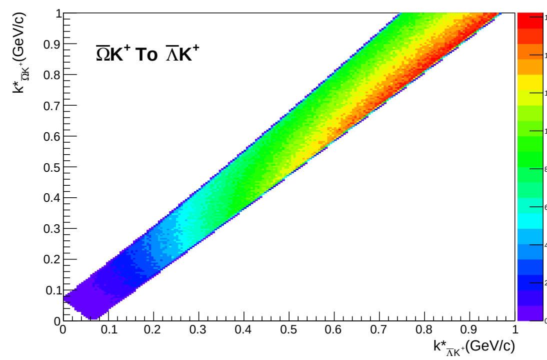

(d) Transform matrix for $\overline{\Omega}^+$K$^+$ pairs into $\overline{\Lambda}$K$^+$

Figure 6.5: Sample Transform Matrices generated with THERMINATOR for $\overline{\Lambda}$K$^+$ Analysis

Estimation of the λ parameters

We can group the types of pairs contributing to our finally observed correlation functions into three broad categories: primary pairs, residual contributors, and other pairs. The primary pairs are the pairs of interest whose signal we want to measure. The residual contributors and other pairs muddle the finally observed signal.

Femtoscopic analyses are sensitive to the pair emission structure at kinetic freeze-out. Therefore, in the eyes of femtoscopy, any particle born from a resonance decay before last rescattering is seen as primary. Within the THERMINATOR 2 simulation, we find that, aside from those which are primary, our Λ hyperons and K mesons decay from a a large number of resonances ($\sim$50 Λ parent species, and $\sim$70 K parent species). From the $\sim$3500 possible contributors feeding down into our ΛK system, only 10 individual pairs contribute significantly. These ten are: Σ^0K, Ξ^-K, Ξ^0K, Σ^{*+}K, Σ^{*-}K, Σ^{*0}K, ΛK*, Σ^0K*, Ξ^-K*, Ξ^0K*. However, it is important to remember that THERMINATOR 2 does not include a hadronic rescattering phase, and therefore models more closely the case of free streaming after chemical freeze-out. As previously stated, femtoscopy is sensitive to the source after kinetic freeze-out, so care needs to be taken in deciding which pairs will contribute to the experimental correlation functions. It is clear that the first three, which decay by the electromagnetic or weak interaction, need to be included in our treatment of residual correlation effects. These three, with a decay length of $\sim 10^4$ fm for the Σ^0 and decay lengths on the order of centimeters ($\sim 10^{13}$ fm) for Ξ^- and Ξ^0, will survive until after last hadronic rescattering to affect the finally observed ΛK correlation function. For the remaining seven, which decay via the strong interaction, the situation is not as clear; the Σ^* and K* have proper decay lengths $c\tau \approx 5$ fm and 4 fm, respectively. Although some of the Σ^* and K* will decay after kinetic freeze-out, we expect that most will decay before. Therefore, in the eyes of femtoscopy, most of the ΛK pairs originating from Σ^*K and ΛK* are primary.

With the arguments presented above, out of the ten top parent systems feeding down into our final ΛK pairs (as estimated with THERMINATOR 2), we expect residual effects to survive from only three, the Σ^0K, Ξ^-K, Ξ^0K systems. Therefore, we include only these three in our final fit algorithm, and assume the other seven contribute to our primary pair samples. However, as mentioned above, within the THERMINATOR 2 simulation there are still $\sim$3490 parent systems which feed-down into the final ΛK pairs. Some of these parent systems will decay to ΛK pairs before kinetic freeze-out, and should be treated as primary, but others will not. For these remaining possible contributors, we use the proper decay length of the parents to judge whether or not the daughter pair should be treated as primary. More specifically, if both parents in the pair have a proper decay length $\tau < \tau_{\max}$, then the daughter pair is considered primary; for our final results, we have chosen $c\tau_{\max} = 10$ fm. If either parent has $\tau > \tau_{\max}$, the daughter pair contributes to the "Other" category when calculating λ parameters. This "Other" category contains pairs which are not considered primary, and which do not originate from the three residual contributor systems included in the fit. For this hodgepodge of pair systems, all with different two-particle interactions and single-particle source distributions, we assume the net correlation effect averages to unity.

The choice of $c\tau_{\max} = 10$ fm is somewhat arbitrary, and (as long as $c\tau_{\max} \geq 6$ fm, described below) the exact value used makes little difference on the final results. The choice shifts pairs between the "Primary" and "Other" groups, as is demonstrated in Table 6.1, where $\lambda_{\mathrm{Primary}}$ and λ_{Other} are shown for $c\tau_{\max} = 6$, 10, and 100 fm. The majority of parents contributing to our Λ and K samples decay via the strong interaction with proper decay lengths less than a few fm, and whose daughters should always be considered primary. The notable exceptions with proper decay lengths above a few fm, aside from the previously described Σ^* and K^*, are: $\phi(1020)$, $\Lambda(1520)$, $\Lambda(1670)$, $\Xi(1690)$, $\Xi(1820)$, $\Xi(2030)$ (the ϕ decay length is $\sim$50 fm, and the others are all below 15 fm). None of these contribute substantially to our ΛK population, so changing the exact value of $c\tau_{\max}$ will not drastically change our λ parameters. One final exception is the Ω^-, which decays weakly on the order of a few cm. Decaying long after kinetic freeze-out, the Ω^- contributes a residual signal to our ΛK pairs; however, the number of Λ originating from the Ω^- is an order of magnitude below the Σ^0, Ξ^-, and Ξ^0 contributions, and we ignore the Ω^- in our treatment of the residuals (i.e. pairs with a Λ originating from an Ω^- are sorted into the "Other" category).

As described above, as long as $c\tau_{\max}$ is chosen ≥ 6 fm, the resultant λ parameters, and ultimately our finally extracted fit values, do not change drastically. The value $c\tau_{\max} = 6$ fm serves as a type of threshold because any choice above that value

$c\tau_{\mathrm{max}}$ (fm)	Primary	Other
6	0.502	0.250
10	0.527	0.226
100	0.565	0.189

Table 6.1: "Primary" and "Other" λ values for the ΛK^+ correlation functions for the cases $c\tau_{\mathrm{max}} = 6, 10, 100$ fm, in which three residual contributors are included. The other λ parameters are not shown, as they do not change for the different value of $c\tau_{\mathrm{max}}$ in the table. The sum of $\lambda_{\mathrm{Primary}}$ and λ_{Other} is not exactly the same in each case due to the difference reconstruction efficiencies between the two groups (see Fig. 6.6).

maintains the daughters of Σ^* and K^* parents in the primary category. Physically, choosing $c\tau_{\mathrm{max}}$ above 6 fm is reasonable; however, it is also interesting to assume the Σ^* and K^* survive until after last rescattering and to study the effect of their inclusion in our fit procedure. Results from such a procedure is shown in Appendix A.3, where we lowered the value of $c\tau_{\mathrm{max}}$ to 4 fm and included contributions from $\Sigma^{*+}K$, $\Sigma^{*-}K$, $\Sigma^{*0}K$, ΛK^*, $\Sigma^0 K^*$, $\Xi^- K^*$, $\Xi^0 K^*$ in our treatment of the residuals.

The λ_{ij} parameters dictate the strength of the parent contribution to the daughter pair. Therefore, the λ_{ij} parameter for parent system ij can be estimated as the total number of ΛK pairs in our experimental sample originating from ij (N_{ij}) divided by the total number of ΛK pairs (N_{Total}):

$$\lambda_{ij} = \frac{N_{ij}}{N_{Total}} \tag{6.4}$$

The particle yields can be estimated using THERMINATOR 2 simulation ($N_{ij}^{\scriptscriptstyle THERM}$), while the reconstruction efficiencies (RE_{ij}) are estimated with MC HIJING data, which has been run through GEANT to simulate the detector response (the results of which are shown in Fig. 6.6).

Using the THERMINATOR 2 and MC HIJING simulations, the λ_{ij} parameters are estimated as

$$\lambda_{ij} = \frac{N_{ij}}{N_{Total}} = \frac{N_{ij}^{\scriptscriptstyle THERM} RE_{ij}^{\scriptscriptstyle HIJING}}{\sum\limits_{\alpha\beta} N_{\alpha\beta}^{\scriptscriptstyle THERM} RE_{\alpha\beta}^{\scriptscriptstyle HIJING}} \tag{6.5}$$

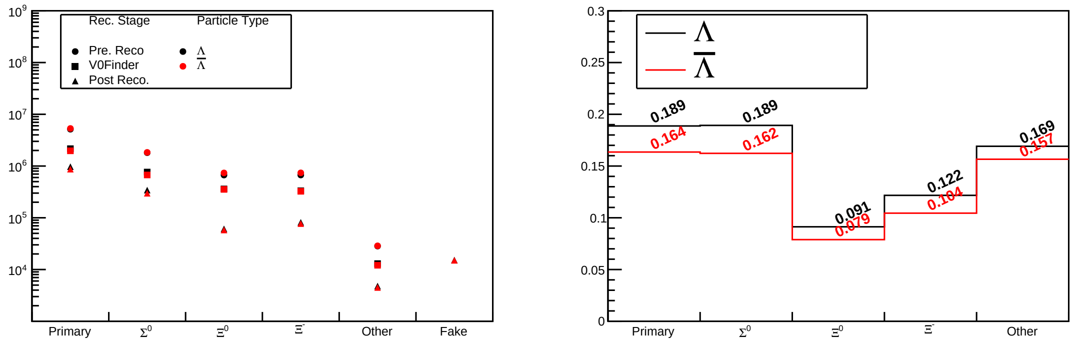

(a) Reconstruction Efficiencies (3 Residuals)

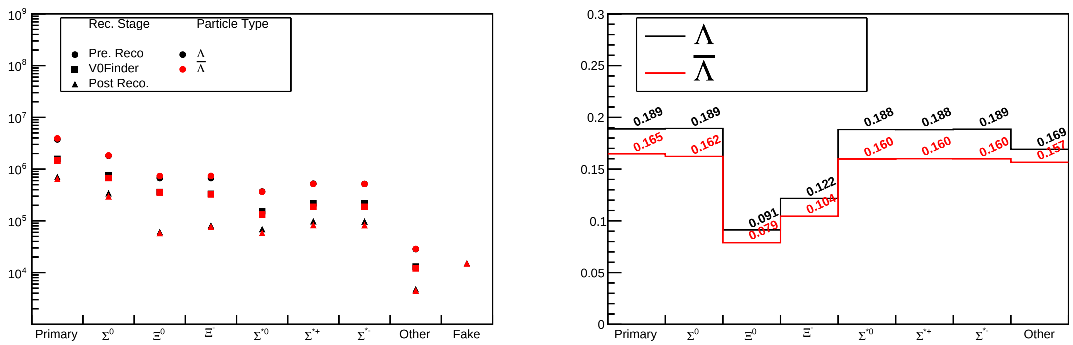

(b) Reconstruction Efficiencies (10 Residuals)

Figure 6.6: Reconstruction Efficiencies

The λ_{ij} values used can be found in Table 6.2, for the case $c\tau_{\text{max}} = 10$ fm, in which three residual contributors are included, and in Table 6.3 for the case $c\tau_{\text{max}} = 4$ fm, in which ten residual contributors are included. In the tables, we also list the λ_{ij} values used for "Other" and "Fakes". The "Other" category contains pairs which are not primary, and which do not originate from the (three or ten) residual pairs included in the fit, as described above. The "Fakes" category represents pairs that are mistakenly identified as ΛK. To estimate this λ_{Fakes} value, we assumed that the number of fake pairs was equal to the total number of pairs multiplied by the Λ purity (i.e. assuming perfect purity for the kaons); or, more simply, $\lambda_{\text{Fakes}} = 1.0$ - Purity(Λ). For both of these contributors ("Other" and "Fakes"), we assume that the correlations average to unity, and therefore do not contribute to the final correlation function (aside from reducing the signal).

ΛK^+		$\bar{\Lambda} K^-$		ΛK^-		$\bar{\Lambda} K^+$	
Source	**λ value**	**Source**	**λ value**	**Source**	**λ value**	**Source**	**λ value**
Primary	0.527	Primary	0.526	Primary	0.526	Primary	0.527
$\Sigma^0 K^+$	0.111	$\bar{\Sigma}^0 K^-$	0.110	$\Sigma^0 K^-$	0.110	$\bar{\Sigma}^0 K^+$	0.111
$\Xi^0 K^+$	0.039	$\bar{\Xi}^0 K^-$	0.035	$\Xi^0 K^-$	0.038	$\bar{\Xi}^0 K^+$	0.036
$\Xi^- K^+$	0.050	$\bar{\Xi}^+ K^-$	0.046	$\Xi^- K^-$	0.050	$\bar{\Xi}^+ K^+$	0.046
Other	0.226	Other	0.235	Other	0.228	Other	0.233
Fakes	0.048	Fakes	0.048	Fakes	0.048	Fakes	0.048

ΛK^0_S		$\bar{\Lambda} K^0_S$	
Pair System	**λ value**	**Pair System**	**λ value**
Primary	0.543	Primary	0.544
$\Sigma^0 K^0_S$	0.120	$\bar{\Sigma}^0 K^0_S$	0.120
$\Xi^0 K^0_S$	0.042	$\bar{\Xi}^0 K^0_S$	0.039
$\Xi^- K^0_S$	0.054	$\bar{\Xi}^+ K^0_S$	0.050
Other	0.194	Other	0.199
Fakes	0.048	Fakes	0.048

Table 6.2: λ values for the individual components of the ΛK correlation functions for the case $c\tau_{\mathrm{max}} = 10$ fm, in which three residual contributors are included. The values were obtained with THERMINATOR 2 and HIJING simulations, as detailed in the text.

Modeling of the parent systems

In practice, we model the parent system (ex. $\Sigma^0 K^+$), and run the parent correlation function through the appropriate transform matrix to determine the contribution to the daughter signal (ex. ΛK^+). In an ideal world, we would simply look up the parent interaction in some table, input this into our model, and form the parent correlation function. Unfortunately, the world in which we live is not perfect, such a table does not exists, and little is know about the interaction between the particles in the residual contributing pairs of this study. Introducing a unique set of scattering parameters and radii for each residual system would introduce a large number of

ΛK^+		$\overline{\Lambda}K^-$		ΛK^-		$\overline{\Lambda}K^+$	
Source	**λ value**	**Source**	**λ value**	**Source**	**λ value**	**Source**	**λ value**
Primary	0.180	Primary	0.180	Primary	0.179	Primary	0.181
Σ^0K^+	0.116	$\overline{\Sigma}^0K^-$	0.114	Σ^0K^-	0.115	$\overline{\Sigma}^0K^+$	0.116
Ξ^0K^+	0.040	$\overline{\Xi}^0K^-$	0.037	Ξ^0K^-	0.040	$\overline{\Xi}^0K^+$	0.037
Ξ^-K^+	0.052	$\overline{\Xi}^+K^-$	0.047	Ξ^-K^-	0.052	$\overline{\Xi}^+K^+$	0.048
$\Sigma^{*+}K^+$	0.054	$\overline{\Sigma}^{*-}K^-$	0.051	$\Sigma^{*+}K^-$	0.053	$\overline{\Sigma}^{*-}K^+$	0.051
$\Sigma^{*-}K^+$	0.048	$\overline{\Sigma}^{*+}K^-$	0.050	$\Sigma^{*-}K^-$	0.048	$\overline{\Sigma}^{*+}K^+$	0.050
$\Sigma^{*0}K^+$	0.048	$\overline{\Sigma}^{*0}K^-$	0.045	$\Sigma^{*0}K^-$	0.048	$\overline{\Sigma}^{*0}K^+$	0.045
ΛK^*	0.046	$\overline{\Lambda K}^*$	0.047	$\Lambda\overline{K}^*$	0.046	$\overline{\Lambda}K^*$	0.047
Σ^0K^*	0.041	$\overline{\Sigma}^0\overline{K}^*$	0.041	$\Sigma^0\overline{K}^*$	0.041	$\overline{\Sigma}^0K^*$	0.041
Ξ^0K^*	0.014	$\overline{\Xi}^0\overline{K}^*$	0.013	$\Xi^0\overline{K}^*$	0.014	$\overline{\Xi}^0K^*$	0.013
Ξ^-K^*	0.018	$\overline{\Xi}^+\overline{K}^*$	0.017	$\Xi^-\overline{K}^*$	0.018	$\overline{\Xi}^+K^*$	0.017
Other	0.295	Other	0.310	Other	0.299	Other	0.307
Fakes	0.048	Fakes	0.048	Fakes	0.048	Fakes	0.048

ΛK^0_S		$\overline{\Lambda}K^0_S$	
Pair System	**λ value**	**Pair System**	**λ value**
Primary	0.192	Primary	0.193
$\Sigma^0K^0_S$	0.125	$\overline{\Sigma}^0K^0_S$	0.124
$\Xi^0K^0_S$	0.043	$\overline{\Xi}^0K^0_S$	0.040
$\Xi^-K^0_S$	0.056	$\overline{\Xi}^+K^0_S$	0.052
$\Sigma^{*+}K^0_S$	0.058	$\overline{\Sigma}^{*+}K^0_S$	0.055
$\Sigma^{*-}K^0_S$	0.052	$\overline{\Sigma}^{*-}K^0_S$	0.054
$\Sigma^{*0}K^0_S$	0.052	$\overline{\Sigma}^{*0}K^0_S$	0.048
ΛK^*	0.022	$\overline{\Lambda}K^*$	0.022
Σ^0K^*	0.019	$\overline{\Sigma}^0\overline{K}^*$	0.019
Ξ^0K^*	0.007	$\overline{\Sigma}^0\overline{K}^*$	0.006
Ξ^-K^*	0.009	$\overline{\Sigma}^0\overline{K}^*$	0.008
Other	0.318	Other	0.330
Fakes	0.048	Fakes	0.048

Table 6.3: λ values for the individual components of the ΛK correlation functions for the case $c\tau_{\max} = 4$ fm, in which ten residual contributors are included. The values were obtained with THERMINATOR 2 and HIJING simulations, as detailed in the text.

additional fit parameters, for which we do not have enough constraints, and would cause our fitter to be too unconstrained to yield trustworthy results. Therefore, for this analysis, we assume all residual pairs have the same source size as the daughter ΛK pair. Furthermore, we assume Coulomb-neutral residual pairs share the same scattering parameters as the daughter pair. Therefore, for Coulomb-neutral pairs, such as Σ^0K and Ξ^0K, $C_{ij}(k^*_{ij})$ is calculated from Eq. 4.44, with the help of Eq. 4.46; $C_{ij}(k^*_{\Lambda K})$ is then obtained by transforming $C_{ij}(k^*_{ij})$ with Eq. 6.3, using the appropriate transform matrix.

For residual pairs affected by both the strong and Coulomb interactions, things are a bit more complicated. This is due to the fact that, for the case of both strong and Coulomb interactions, we no longer have a nice analytical form with which to construct our fit functions. Generating a correlation function including both is also time consuming, as described further in Sec. 6.5. This increase in formation time is not an issue in generating single correlation functions, however, it does become a problem when including the method in the fit process, where thousands of generated correlation functions are needed (the parallelization of the process across a large number of GPU cores, to drastically decrease run-time, is currently underway). Therefore, when modeling Ξ^-K$^\pm$ residual correlations, we use the experimental Ξ^-K$^\pm$ data; in this case, there is no need to make any assumptions about scattering parameters or source sizes. The downside is that, especially in the 30-50% centrality bin, the statistics are low and error bars large. For the other cases with strong and Coulomb interactions, we assume the strong interaction is negligible, and generate the parent correlation assuming a Coulomb-only scenario (see Sec. 6.5 for more details). This approximation is well justified here as a Coulomb-only description of the system describes, reasonably well, the broad features of the Ξ^-K$^\pm$ correlation; the strong interaction is necessary for the fine details. However, as these correlations are run through a transform matrix, which largely flattens out any fine details, a Coulomb-only description is sufficient.

In practice, the Coulomb-only scenario is achieved by first building a large number of Coulomb-only correlations for various radii and λ parameter values, and interpolating from this grid during the fitting process. This allows us to generate the correlations functions with the speed needed to converge on fit results within a reasonable amount of time. We find consistent results between using the Ξ^{-}K data and the Coulomb-only interpolation method. When quantifying the $\Xi^{-}K^{\pm}$ residual contribution, the experimental $\Xi^{-}K^{\pm}$ data is always used. When the number of residual pairs used is increased to 10, so that contributors such as $\Sigma^{*+}K^{-}$ enter the picture, the Coulomb-only interpolation method is used.

Two examples of how very different transform matrices can alter a correlation function are shown in Figures 6.7 and 6.8 below. These figures were taken using parameter values obtained from fits to the data. In the top left figure of each, the input correlation function (closed symbols) is shown together with the output, transformed, correlation function (open symbols). In the bottom left, the transformed correlation is shown by itself (with zoomed y-axis); this is especially helpful when the λ parameter is very small, in which case the contribution in the top left can look flat, but the zoomed-in view in the bottom left shows the structure. The right plot in each figure shows the transform matrix.

Concerning the radii of the residual parent pairs, it was suggested that these should be set to smaller values than those of the daughter pair. In the interest of minimizing the number of parameters in the fitter, we tested this by introducing an m_{T}-scaling of the parents' radii. The motivation for this scaling comes from the approximate m_{T}-scaling of the radii observed for identical particle femtoscopic analyses in Fig. 7.2. To achieve this scaling, we assume the radii follow an inverse-square-root distribution: $R_{AB} = \alpha m_{\mathrm{T}}^{-1/2}$. Then, it follows that we should scale the parent radii as:

$$R_{AB} = R_{\Lambda \mathrm{K}} \left(\frac{m_{\mathrm{T},AB}}{m_{\mathrm{T},\Lambda \mathrm{K}}} \right)^{-1/2} \tag{6.6}$$

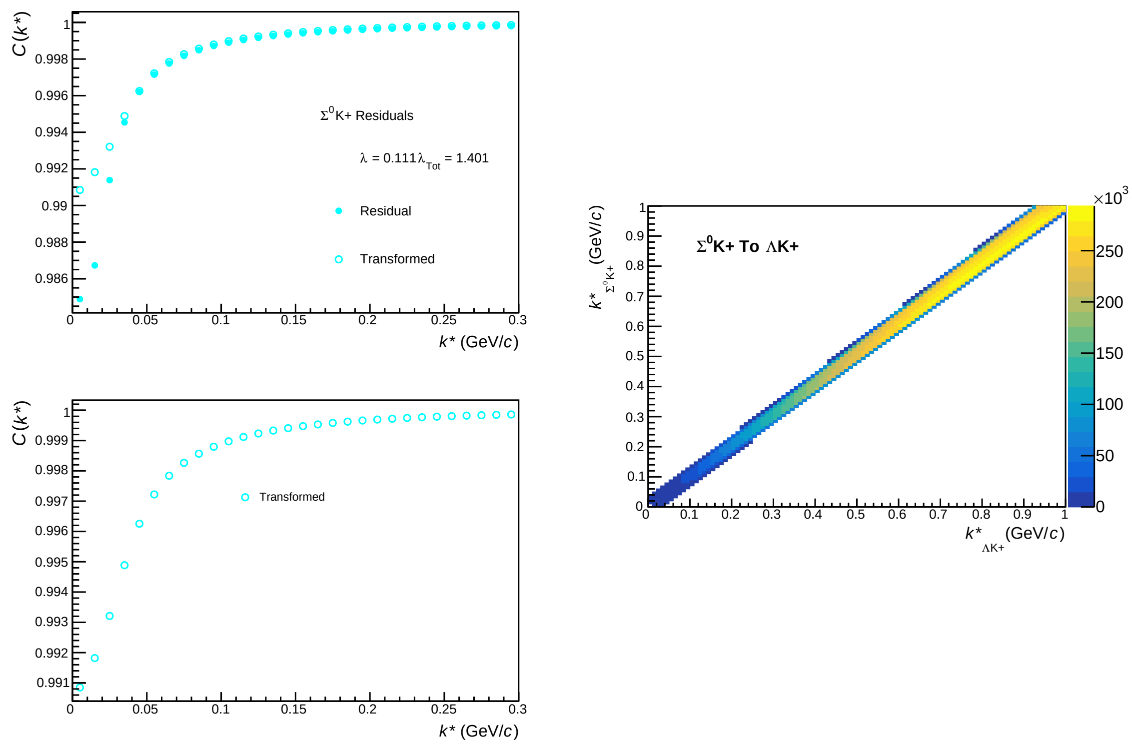

Figure 6.7: $\Sigma^0\mathrm{K}^+$ Transform. These figures were taken using parameter values obtained from fits to the data. In the top left figure, the input correlation function (closed symbols) is shown together with the output, transformed, correlation function (open symbols). In the bottom left, the transformed correlation is shown by itself. The right figure shows the transform matrix.

The values of m_T for each pair system were taken from THERMINATOR 2. As the fitter dances around parameter space and selects a new radius for the ΛK system, the radii of the residuals is simply the ΛK radius scaled by the appropriate factor, given above (Eq. 6.6). In the end, this scaling factor made no significant difference in our fit results, so this complication is omitted in our final results. Note that this is not surprising, as the most extreme scaling factor was, in the case of using 10 residual systems, between $\Lambda\mathrm{K}^+$ with $m_{\mathrm{T},\Lambda\mathrm{K}^+} \approx 1.4$ GeV/c^2 and $\Xi^-\mathrm{K}^*$ with $m_{\mathrm{T},\Xi^-\mathrm{K}^*} \approx 1.8$ GeV/c^2, resulting in a scale factor of ≈ 0.9.

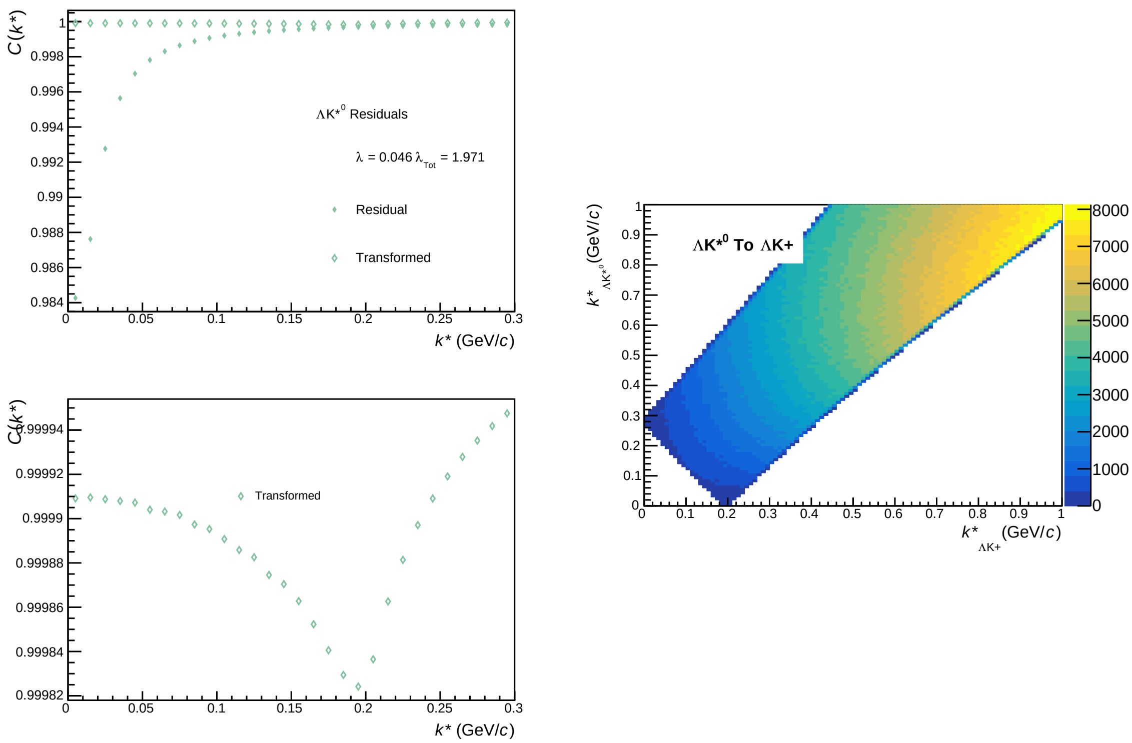

Figure 6.8: ΛK^{*0} Transform. These figures were taken using parameter values obtained from fits to the data. In the top left figure, the input correlation function (closed symbols) is shown together with the output, transformed, correlation function (open symbols). In the bottom left, the transformed correlation is shown by itself. The right figure shows the transform matrix.

6.3 Non-femtoscopic background

We observe a significant non-femtoscopic, non-flat, background in all of our correlations outside of the signal region ($k^* \gtrsim 0.3$ GeV/c). This background increases with decreasing centrality, is the same amongst all $\Lambda K^{\pm}$ pairs, and is more pronounced in the ΛK^0_S system, as can be seen in Fig. 6.9.

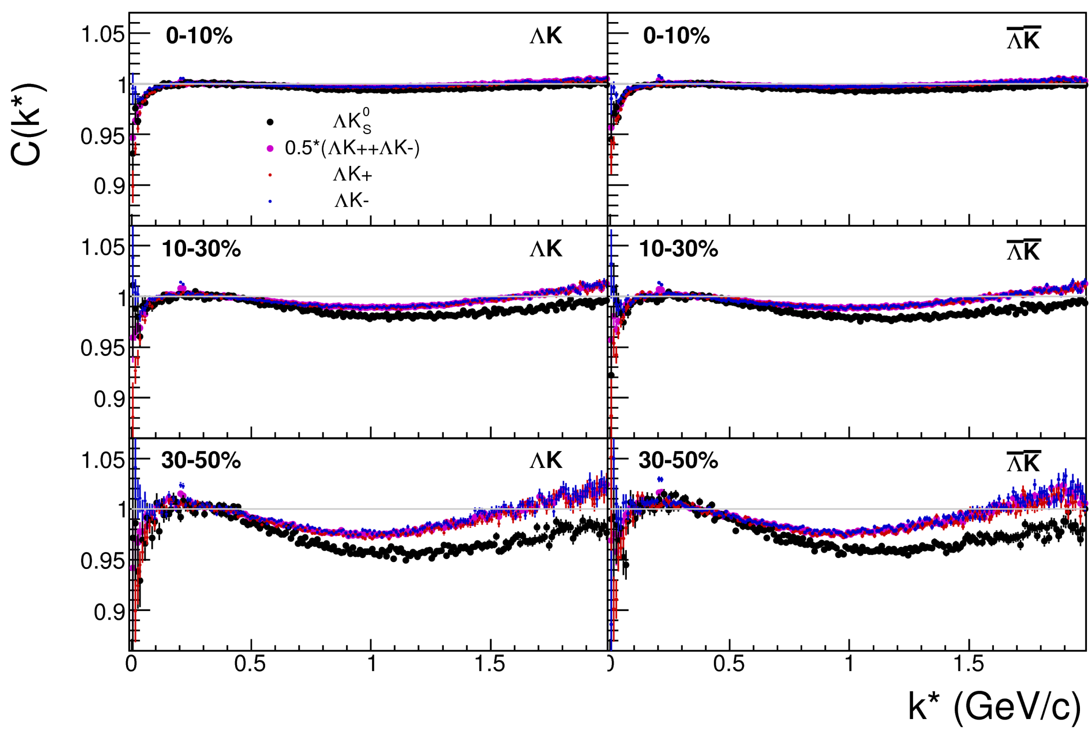

Figure 6.9: A comparison on the non-femtoscopic backgrounds observed in our our ΛK experimental data.

It is suggested that this background effect is due primarily to particle collimation associated with elliptic flow [168]. More specifically, these backgrounds result from mixing events with unlike event-plane angles (Ψ_{EP}). As explained in Ref. [168], when elliptic flow is present, all particles are more likely to be emitted in a specific direction (in-plane). Therefore, the difference in momenta for pairs of particles tends to be smaller, compared to the case of no flow. For mixed-event pairs, the two events used do not share an event-plane, and therefore there is no collimation effect in the pairs from flow. As a result, pairs with larger momentum difference are more likely when mixed-events are used (in the denominator of the correlation function), causing the correlation function to dip below unity. In general, the observation of the correlation function below unity, at a given k^*, means it is more probable to find a pair at that k^* when the daughters are taken from mixed-events, as compared to when they are taken from the same event. This same reasoning suggests that the background should lead to an enhancement at low-k^*. Furthermore, it appears that that the observed enhancement at $k^* \gtrsim 1.5$ GeV/c is also be due to collective effects, as explained later in this section.

The behavior of the non-femtoscopic background is needed in the low-k^* femtoscopic signal region, but a clean view of it is only accessible outside of such a region. From the arguments above, it appears a solution to the background issue is to align the event-planes before mixing events, but this is easier said than done. Unfortunately, we cannot simply rotate each event to artificially align their event-planes and rid ourselves of this mixing effect, as our azimuthal angle acceptance is not perfectly uniform, and we have only finite event-plane resolution. With better resolution, another option would be to bin events in Ψ_{EP} and only mix events within a given bin. We pursued this direction, as shown in Fig. 6.10, and observed a slight decrease in the background (closed cyan points); however, going to finer binning, we saw no additional reduction in the background (open magenta points), signaling that we had reached the limits dictated by the resolution. In the end, we are forced to model the background and include it into our fit procedure.

Implementation of THERMINATOR 2

The THERMINATOR 2 simulation has been shown to reproduce the non-femtoscopic background features in a πK analysis [168], so we utilize it here to investigate further

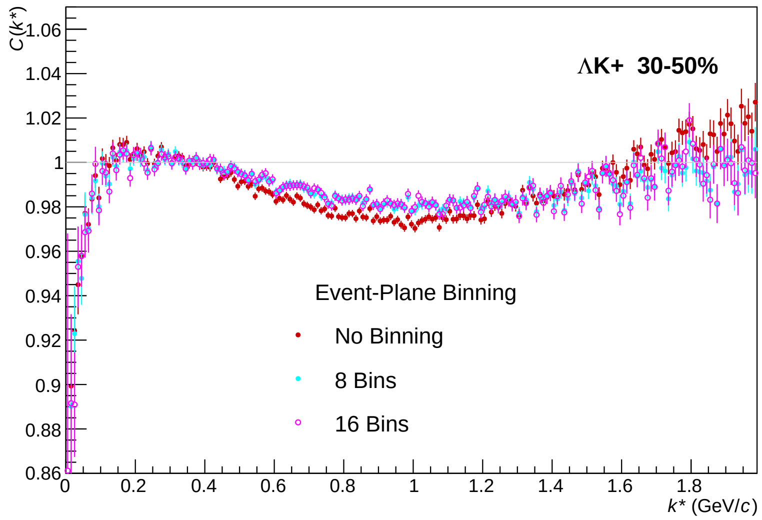

Figure 6.10: Effect of binning the reference distribution, $B(k^*)$, in Ψ_{EP} with no (red, closed), eight (cyan, closed), and 16 (magenta, open) bins. The data shown are for the $\Lambda\mathrm{K}^+$ analysis in the 30-50% centrality bin.

the background features in the ΛK systems. THERMINATOR 2 is a Monte Carlo event generator designed to study the statistical production of particles in relativistic heavy-ion collisions [167]. Given a freeze-out hypersurface and velocity profile, THERMINATOR 2 performs a statistical hadronization via the Cooper-Frye formalism. The model does not include hadronic rescattering, but does include the propagation and decay of a large number of hadronic resonances. For this analysis, the Lhyquid3v freeze-out hypersurface obtained from a (3+1)-dimensional viscous hydrodynamics calculation was used (this hypersurface is not packaged with the public code, but was obtained via correspondence with the THERMINATOR 2 authors). Through the use of this hypersurface, collective expansion effects are included in the simulation. An example of the elliptic flow signals in the simulation are shown in Figure 6.11, which presents $v_2(p_{\mathrm{T}})$ from the model implemented with an impact parameter $b = 8$ fm.

Before presenting and discussing results from the THERMINATOR 2 simulation, it is important to discuss how our correlation functions are constructed with the

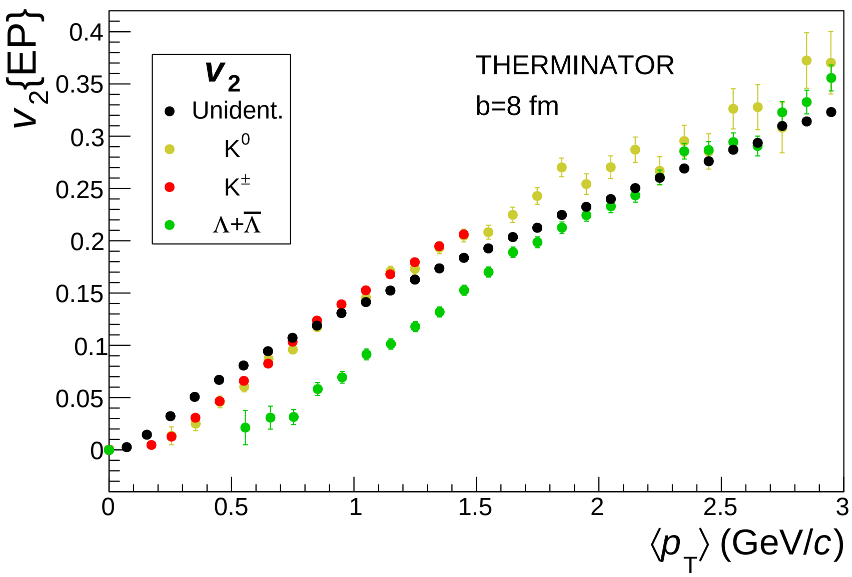

Figure 6.11: Elliptic flow coefficients (v_2) as a function of p_{T} from the THERMINATOR 2 simulation with impact parameter $b = 8$ fm for all unidentified particles (black), $\mathrm{K}^0_{\mathrm{S}}$ (gold), $\mathrm{K}^{\pm}$ (red), and $\Lambda(\overline{\Lambda})$ (green). The same kinematic cuts used in the femtoscopic study are used here, explaining why, for instance, the $\mathrm{K}^{\pm}$ signal is only measured to $p_{\mathrm{T}} = 1.5$ GeV/c. The measurement was performed with the event-plane method with a pseudorapidity gap of $\Delta\eta > 0.2$ between the tracks used to calculate v_2 and those used to the event-plane determination.

simulation data. The simulation does not include any final state interaction effects, so the femtoscopic correlation effect must be introduced by hand. This is achieved during the construction of particle pairs through a weighting technique. The same-event particle pairs are weighted by the modulus squared of the appropriate two-particle wave-function, $|\Psi|^2$ (using the equations from Sec. 4.2.5), when building the signal distributions (numerators). This essentially introduces the two-particle interaction into these pairs, and is achieved by assuming a set of scattering parameters for the system under consideration. The mixed-event pairs, which should be absent of interactions, receive unit weights ($= 1$) when constructing the reference distributions (denominators).

By default, the THERMINATOR 2 simulation constructs all events with event-plane angles aligned along the laboratory x-axis ($\Psi_{\mathrm{EP}} = 0$). This is troublesome for a couple of reasons. First, in experiment we are given events which are randomly oriented, so the situation in the model is not realistic. Second, the non-femtoscopic background effect results primarily from mixing events with unlike event-plane angles, as described above. Therefore, using the standard THERMINATOR 2 simulation with all event-planes aligned, one does not observe any non-femtoscopic background. In order to produce such a signal, and better match the simulation to the experimental environment, we issue each simulated event a random Ψ_{EP}.

We summarize here our construction of correlation functions from the simulated THERMINATOR 2 data. To introduce a femtoscopic signal into the correlation functions, the numerator pairs are weighted with $|\Psi|^2$, after assuming a set of scattering parameters for each pair system. If we are interested in studying only the non-femtoscopic backgrounds, the numerator weights are set to unity. In order to introduce the non-femtoscopic background, we randomly orient each event, as given in experiment. If we want to eliminate the non-femtoscopic background, we keep the standard THERMINATOR 2 output of all event-plane angles aligned along the laboratory x-axis.

Results with THERMINATOR 2

Figure 6.12a shows that the THERMINATOR 2 simulation does a good job of describing the difference in background between the $\Lambda\mathrm{K}^{\pm}$ and $\Lambda\mathrm{K}^0_{\mathrm{S}}$ systems observed in the data (see Fig. 6.9). The figure presents the non-femtoscopic backgrounds (i.e. numerator weights set to unity) obtained from the simulation for the $\Lambda\mathrm{K}^{+}$ (red), $\Lambda\mathrm{K}^{-}$ (blue), and $\Lambda\mathrm{K}^0_{\mathrm{S}}$ (black) correlation functions. The model also demonstrates that the difference in $\Lambda\mathrm{K}^{\pm}$ and $\Lambda\mathrm{K}^0_{\mathrm{S}}$ backgrounds is due mainly to a difference in kinematic cuts, not due to any interesting physics, highlighted in Figure 6.12b. For Fig. 6.12b, restrictions were imposed on the p_{T} of the $\mathrm{K}^0_{\mathrm{S}}$ to more closely match the $\mathrm{K}^{\pm}$ cuts, and the resulting backgrounds are shown to align much better. Therefore, we conclude that the difference in backgrounds between $\Lambda\mathrm{K}^{\pm}$ and $\Lambda\mathrm{K}^0_{\mathrm{S}}$ observed in our experimental data is simply due to a difference in kinematic cuts between $K^{\pm}$ and K^0_S particles.

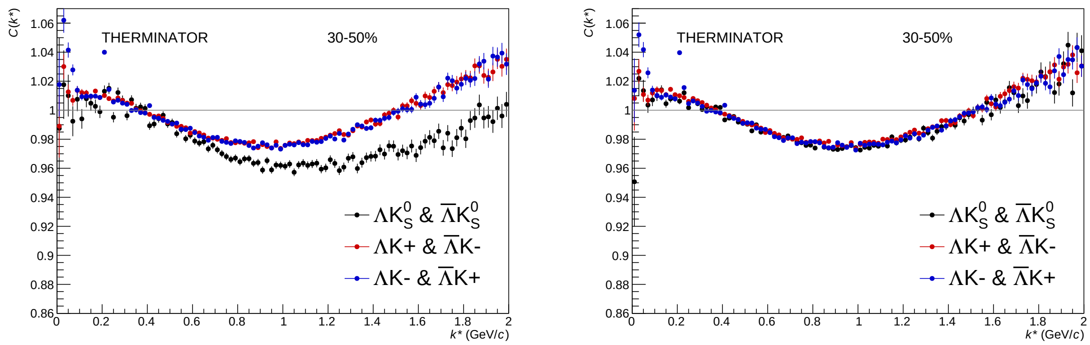

(a) THERMINATOR standard results

(b) THERMINATOR results after upper-p_{T} cut placed on K^0_S to more closely match $K^{\pm}$

Figure 6.12: THERMINATOR 2 simulation for ΛK^+ (red), ΛK^- (blue), and ΛK^0_S (black). In 6.12a, we show the standard THERMINATOR 2 results. THERMINATOR 2 does a good job describing qualitatively the different between the $\Lambda K^{\pm}$ and ΛK^0_S backgrounds. In 6.12b, an upper-p_{T} cut was placed on the K^0_S particles to more closely match the $K^{\pm}$ kinematic cuts. After this tweak, the $\Lambda K^{\pm}$ and ΛK^0_S backgrounds agree much better.

We find that, after issuing each simulated event a random Ψ_{EP}, THERMINATOR 2 does an exceptional job of describing our data. Furthermore, the simulation showed the non-femtoscopic background affects the correlation function as a separable scale factor (Fig 6.14, discussed below). Figure 6.13 shows the THERMINATOR 2 simulation (green) together with experimental data (red, blue, black). The figure also shows a 6^{th}-order polynomial fit to the simulation (green), as well as the fit polynomial scaled to match the data (red, blue, black). The simulation will be used quantitatively in our fit procedure for the $\Lambda K^{\pm}$ systems, as described at the end of this section.

Figure 6.14 shows three correlation functions generated using different implementations of the THERMINATOR 2 simulation ("Cf w/o Bgd (A)", "Cf w. Bgd (B)", "Bgd(C)"), as well as two histograms describing the relation between the three ("Ratio (B/C)", "1+Diff(B-C)"). "Cf w/o Bgd (A)" shows a correlation function with a

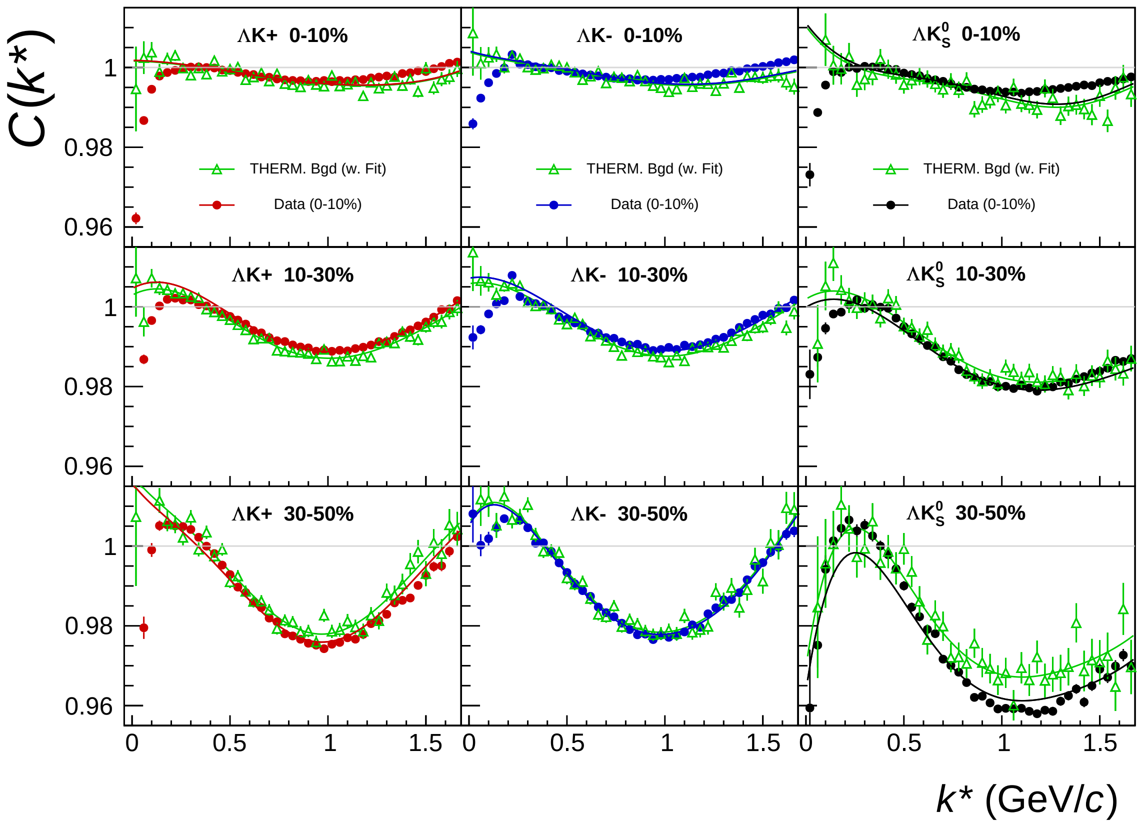

Figure 6.13: THERMINATOR 2 simulation (green) together with experimental data (red, blue, or black). Results are shown for ΛK^{+} (left), ΛK^{-} (middle), and ΛK^0_S (right). A 6^{th}-order polynomial fit to the simulation is shown as a solid green line. This polynomial is scaled to match the experimental data. The polynomial fit with scale factor applied is drawn in a color matching the experimental data (red, blue, black).

femtoscopic correlation, but without background (i.e. the signal distributions were weighted with $|\Psi|^2$, and for all events $\Psi_{\mathrm{EP}} = 0$). The second correlation, "Cf w. Bgd (B)", shows a correlation function with both a femtoscopic correlation and a background (i.e. the signal distributions were weighted with $|\Psi|^2$, and a random Ψ_{EP} was generated for each event), which most closely matches our situation in experiment. Finally, "Bgd (C)", shows a correlation function with a non-femtoscopic background, but no femtoscopic correlation (i.e. the signal distributions were weighted with unity, and a random Ψ_{EP} was generated for each event).

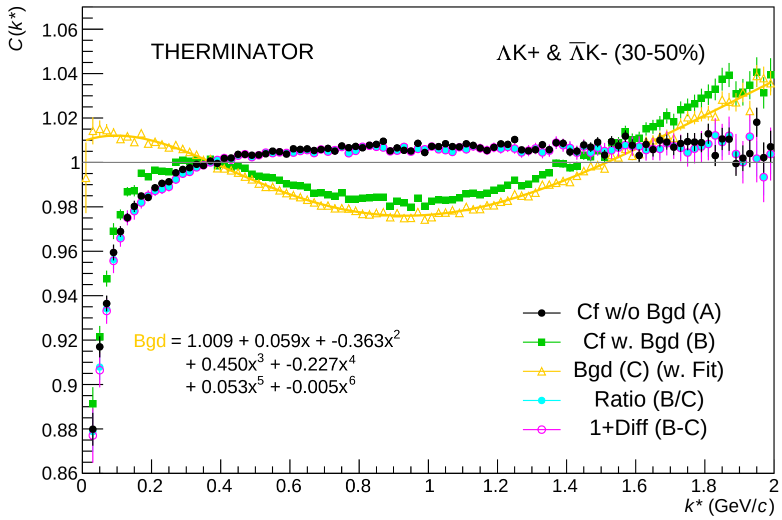

Figure 6.14: Correlation with background decomposition with THERMINATOR. "Cf w/o Bgd (A)" shows a correlation function with a femtoscopic correlation, but without background. "Cf w. Bgd (B)", shows a correlation function with both a femtoscopic correlation and a background (most closely matches our situation in experiment). "Bgd (C)", shows a correlation function with a non-femtoscopic background, but no femtoscopic correlation, i.e. background only.

The main conclusion from Fig. 6.14 is that the non-femtoscopic background affects the correlation function as a separable scale factor. This is seen through the fact that the black points match the cyan points; or, equivalently:

$$Cfw/oBgd = \frac{Cfw.Bgd}{Bgd} \rightarrow C_{theory} = \frac{C_{exp}}{F_{Bgd}} \rightarrow C_{exp} = C_{theory} \cdot F_{Bgd} \tag{6.7}$$

We expect this behavior to be roughly the same in the experimental data, as the hydrodynamic hypersurface used in the simulation contains a collective expansion similar to that observed in experiment.

The description by THERMINATOR 2 of the non-femtoscopic backgrounds in the $\Lambda K^{\pm}$ systems is remarkable, as shown in Fig. 6.13, and can be used in a quantitative fashion to help fit the data. More specifically, the non-femtoscopic backgrounds are modeled by 6$^{\text{th}}$-order polynomial fits to the THERMINATOR 2 simulation for the $\Lambda K^{\pm}$ analyses, as suggested in Ref. [168]; one polynomial for each centrality class.

The form of each polynomial was set before use with the experimental data by fitting to the THERMINATOR 2 simulation, as shown in Fig. 6.13. At the time of the fit, each polynomial could only be adjusted by a simple scale factor to best match the background in the data.

The description of the ΛK^0_S is good at a qualitative level, but not quantitatively good enough to be utilized in our fit. As such, we use a linear form to model the background in the ΛK^0_S system, as was done with the $K^0_S K^0_S$ analysis in Ref. [133]. The background for each correlation function was fixed before use in the signal region by fitting a linear form to the region $0.6 < k^* < 0.9$ GeV/c. In all cases, the non-femtoscopic background correction was applied as a scale factor.

Effect of different anisotrpic flows

As a majority contribution of the non-femtoscopic background results from anisotropic flow, it is interesting to study how different flows affect the background. Furthermore, the arguments given above for the elliptic flow producing the non-femtoscopic background are true for any flow harmonic; the elliptic flow is dominant (except for the most central of collisions), so its contribution dominates the observed background in experiment. In any case, it is interesting to inspect the background produced by different flow harmonics; therefore, we study separately the effect of a significant elliptic and a significant triangular flow signal. Additionally, if the non-femtoscopic background is due to the anisotropic flow, the effect should disappear when the anisotropic flow disappears (this conclusion is already implied by the weakening of the signal in central events).

The effects of different anisotropic flows are investigated in Figure 6.15, which shows the effect of substantial elliptic (v_2) and triangular (v_3) anisotropic flow, as well as the absence of anisotropic flow, on the observed non-femtoscopic background with the THERMINATOR 2 simulation data for an impact parameter $b = 5$ fm. Here, we are interested only in studying the background effects, so unity weights were used in the construction of the signal distribution. For the simulation presented in the figure, the v_n signal was obtained by replacing the emission angle (ϕ) of each particle in the model with a value drawn from the distribution $P(\phi) = \frac{1}{2}\left[1 + \cos(n\phi)\right]$. Note, using the emission supplied by the model, the extracted v_2 (see Fig. 6.11) and v_3 values are nonzero, but we use this artificial procedure because we are interested in studying the effects of flow in extreme cases. This procedure has the added benefit of providing a more controlled measurement. The flow signal was turned off in the simulation by drawing the emission angles randomly.

As shown in Fig. 6.15, turning off the anisotropic flow eliminates the non-femtoscopic background. The figure also shows an interesting difference in the backgrounds resulting from elliptic and triangular flow. The differences in these signals, and more specifically the difference in their periodicity, helps in the interpretation of each. The anisotropic flow initially leads to an enhancement at low-k^*; this is understood from the particle collimation arguments provided above. After the enhancement, the observed suppression is also explained above as resulting from the particle collimation combined with the mixing of events with unlike Ψ_{EP} angles. The cause of the next rise in the signal was not immediately obvious (although, the fact that the signal disappears with vanishing anisotropic flow clearly demonstrates the effect is still due to the flow). However, the fact that the background resulting from v_3 rises but then falls again illuminates the situation. For the case of elliptic flow, the results suggest the rise in the background after $k^* \sim 0.75$ GeV/c is due to a surplus in the signal distribution of particles with angular separation 180° in the transverse plane as compared to the mixed events (with randomly oriented Ψ_{EP}), following the periodic nature of the elliptic flow. For the case of triangular flow, the second enhancement occurs at lower k^* (compared to the case of elliptic flow) because the v_3 symmetry has a period of 120°.

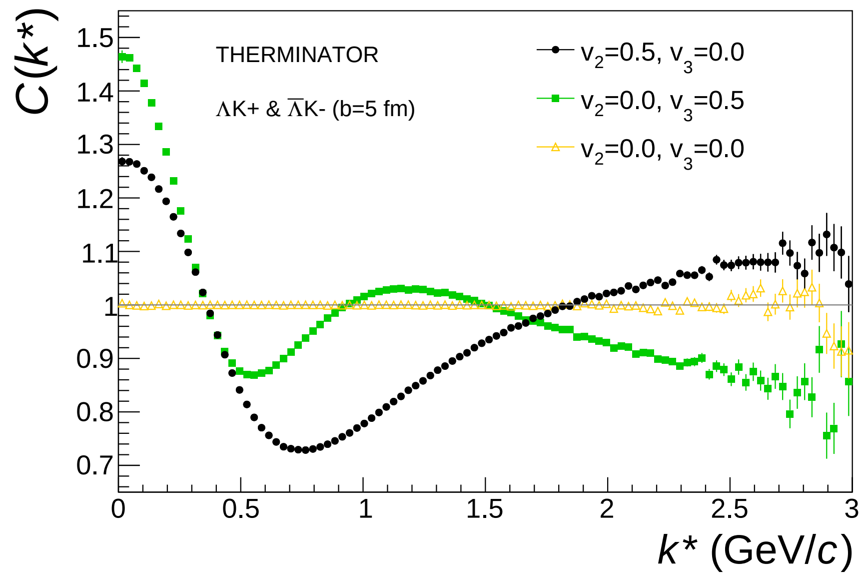

Figure 6.15: Effects of substantial elliptic (black) and triangular (green) anisotropic flow on the observed non-femtoscopic background. The case of vanishing anisotropic flow is also shown (gold).

Stavinskiy method with THERMINATOR 2

An alternative approach to treating the non-femtoscopic background is to instead attempt to eliminate it. The background may be effectively reduced by forming the reference distribution ($B(k^*)$) with the "Stavinskiy method" [165], as introduced in Sec. 5.7.2. With the Stavinskiy method, mixed-event pairs are not used for the reference distribution; instead, same-event pseudo-pairs, formed by rotating one particle in a real pair by 180° in the transverse plane, are used. This rotation rids the pairs of any femtoscopic correlation, while maintaining correlations due to elliptic flow (and other suitably symmetric contributors).

Figure 6.16 demonstrates the use of the Stavinskiy method with THERMINATOR 2. In the figure, unit weights are used for all numerators, so no femtoscopic signal is included, only background effects. The black points show an ideal, experimentally unreachable, situation of aligning all of the event-plane angles. With THERMINATOR 2, when the event-planes are aligned, the background signal is killed. The green

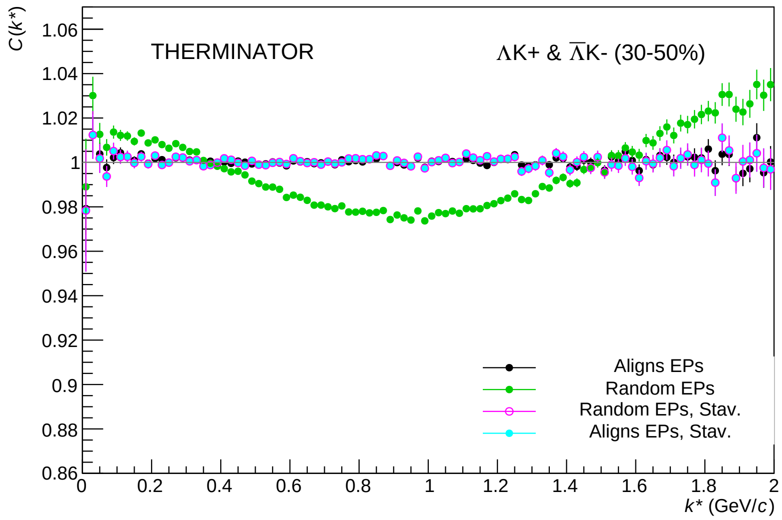

Figure 6.16: The use of the Stavinskiy method with THERMINATOR 2. Unit weights were used for all numerators. The black points show the case of aligning all of the event-plane angles. The green points show a more experimentally realistic situation of random event-plane angles. The purple and blue points shown the affect of applying the Stavinskiy method to the black and green points, respectively.

points show the case of random event-plane angles, a situation more closely matching that of experiment. The purple points shown the affect of applying the Stavinskiy method to the case of random event-planes. The figure shows that this method effectively kills the non-flat background (i.e. the procedure takes the green points to the purple). Finally, the blue points show the effect of applying the Stavinskiy method when all of the event-planes are aligned. This shows that the Stavinskiy method does not introduce any signal to an already flat background. The effect of using the Stavinskiy method for our experimental ΛK correlation functions can be seen in Sec. 5.7.2.

6.4 ΛK fitter

The code developed to fit the data is called "LednickyFitter", and utilizes the ROOT TMinuit implementation of the MINUIT fitting package. In short, given a function with a number of parameters, the fitter explores the parameter space searching for the minimum of the function. In this implementation, the function to be minimized should represent the difference between the measured and theoretical correlation functions. However, a simple χ^2 test is inappropriate for fitting correlation functions, as the ratio of two Poisson distributions does not result in a Poisson distribution. Instead, a log-likelihood fit function of the following form is used [123]:

$$\chi^2_{PML} = -2\left[A\ln\left(\frac{C(A+B)}{A(C+1)}\right) + B\ln\left(\frac{A+B}{B(C+1)}\right)\right] \tag{6.8}$$

where A is the experimental signal distribution (numerator), B is the experimental reference distribution (denominator), and C is the theoretical fit correlation function. Therefore, we use Eq. 6.8 as the statistic quantifying the quality of the fit.

The fit procedure relies on the framework introduced in Sec. 4.2.5. The Lednický and Lyuboshitz analytical model [134] is employed to model all correlation functions in which the Coulomb interaction is absent, i.e. Eqs. 4.46–4.48. The parameters included in the generation of a correlation function are: λ, R, f_0 ($\Re f_0$ and $\Im f_0$ separately), d_0, and normalization N. The methods used to model correlation functions whose particles interact via the Coulomb force are described in Sec. 6.5.

With our procedure, we are able to share parameters between different analyses and fit all simultaneously. A given pair and its conjugate (e.g. ΛK^+ and $\overline{\Lambda}K^-$) always share scattering parameters ($\Re f_0$, $\Im f_0$, d_0). However, the three distinct systems (ΛK^+, ΛK^-, and ΛK^0_S) are assumed to have unique scattering parameters which are allowed to differ from each other. We assume the pair emission source for a given centrality class is similar between all analyses; therefore, for each centrality, all ΛK analyses share a common radius parameter. We assume the same is true for the overall normalization λ_{Fit} parameters in Eq. 6.2. Finally, each correlation function has a unique normalization parameter.

All correlation functions are normalized in the range $0.32 < k^* < 0.40$ GeV/c, and fit in the range $0.0 < k^* < 0.30$ GeV/c. For the ΛK^- analysis, the region $0.19 < k^* < 0.23$ GeV/c is excluded from the fit to exclude the bump caused by the Ω^- resonance.

For each pair system, we account for contributions from three residual contributors, as discussed in Sec. 6.2, and whose individual λ_{ij} values are listed in Table 6.2. The cases of zero and ten residual contributors were also investigated to study the effect on the extracted fits (see App. A). However, the inclusion of contributions from (Σ^0K, Ξ^0K, Ξ^-K) $\rightarrow$ ΛK most realistically models the system, as described further in Sec. 6.2, and the case of three residual contributors was chosen for the final results. We account for effects of finite track momentum resolution, as outlined in Sec. 6.1. The non-femtoscopic backgrounds are modeled using the THERMINATOR 2 simulation for the ΛK$^\pm$ analyses, and with a linear form for the ΛK$^0_\mathrm{S}$ system, as described in Sec. 6.3.

To summarize, the complete fit function is constructed as follows:

1. The uncorrected, primary, correlation function, $C_{\Lambda\mathrm{K}}(k^*_{\mathrm{True}})$, is constructed using Eqs. 4.44 and 4.46

2. The correlation functions describing the parent systems which contribute residually are obtained using:

    - Eqs. 4.44 and 4.46 for the case of Coulomb-neutral pairs
    - Ξ^-K$^\pm$ experimental data for Ξ^-K$^\pm$ contributions
    - a Coulomb-only curve, with the help of methods introduced in Sec. 6.5, for other pairs including the Coulomb interaction

3. The residual contributions to the ΛK correlation function are found by running each parent correlation function through the appropriate transform matrix, via Eq. 6.3

4. The primary and residual correlations are combined, via Eq. 6.2 with Tab. 6.2, to form $C'_{Fit}(k^*_{\mathrm{True}})$

5. The correlation function is corrected to account for momentum resolution effects using Eq. 6.1, to obtain $C'_{\mathrm{Fit}}(k^*_{\mathrm{Rec}})$

6. Finally, the non-flat background correction, $F_{\mathrm{Bgd}}(k^*_{\mathrm{Rec}})$ is applied, and the final fit function is obtained, $C_{\mathrm{Fit}}(k^*_{\mathrm{Rec}}) = C'_{\mathrm{Fit}}(k^*_{\mathrm{Rec}}) * F_{\mathrm{Bgd}}(k^*_{\mathrm{Rec}})$

Figures 7.4, 7.5, and 7.6 show experimental data with fits, assuming three residual contributors, for all studied centralities, for $\Lambda\mathrm{K}^+(\overline{\Lambda}\mathrm{K}^-)$, $\Lambda\mathrm{K}^-(\overline{\Lambda}\mathrm{K}^+)$, and $\Lambda\mathrm{K}^0_\mathrm{S}(\overline{\Lambda}\mathrm{K}^0_\mathrm{S})$, respectively. For the cases of no and ten residual contributors, see Appendix A.

6.5 $\Xi^-\mathrm{K}^\pm$ fitter

When fitting the $\Xi^-(\overline{\Xi}^+)\mathrm{K}^\pm$ results, it is necessary to include both strong and Coulomb interaction effects. In this case, Equation 4.46 is no longer valid, and, in fact, there is no analytical form with which to fit. We therefore must take a more basic approach, and integrate Eq. 4.11 by hand, using the wave-function given in Eqs. 4.49–4.51. To achieve this, one has two options. The first option is to numerically integrate Eq. 4.13. The second option is to simulate a large sample of particle pairs, calculate the wave-function describing the interaction, and average to obtain the integral. Having no experience with either of these options, we elected the latter of simulating pairs. The code developed to achieve this functionality is called "CoulombFitter". Currently, in order to generate the statistics needed for a stable fit, we find that $\sim 10^4$ simulated pairs per 10 MeV k^* bin are necessary. The nature of this process means that the "CoulombFitter" takes much longer to run than the "LednickyFitter" of Section 6.4.

As stated before, to generate a fit correlation function, we must simulate a large number of pairs, calculate the wave-function, and average $|\Psi|^2$ over all pairs in a given k^* bin. Essentially, we calculate Equation 4.13 by hand:

$$
\begin{aligned}
C(\mathbf{k}^*) &= (1-\lambda) + \lambda \sum_S \rho_S \int S(\mathbf{r}^*)|\Psi^S_{\mathbf{k}^*}(\mathbf{r}^*)|^2 d^3\mathbf{r}^* \\
\longrightarrow C(|\mathbf{k}^*|) \equiv C(k^*) &= (1-\lambda) + \lambda \sum_S \rho_S \langle|\Psi^S(\mathbf{k}^*_\mathbf{i}, \mathbf{r}^*_\mathbf{i})|^2\rangle_i
\end{aligned}
\tag{6.9}
$$

where $\langle\rangle_i$ represents an average over all pairs in a given k^* bin. Unfortunately, with this analysis, we are not sensitive to, and therefore not able to distinguish between, the iso-spin singlet and triplet states. We proceed with our analysis, but the results must be interpreted as iso-spin averaged scattering parameters.

In summary, for a given k^* bin, we must draw $N_{pairs} \sim 10^4$ pairs, and for each pair:

1. Draw a random $\mathbf{r}^*$ vector according to our Gaussian source distribution $S(\mathbf{r}^*)$
2. Draw a random $\boldsymbol{k}^*$ vector satisfying the $|\boldsymbol{k}^*|$ restriction of the bin
   - We draw from real k^* vectors obtained from the data
   - However, we find that drawing from a distribution flat in k^* gives similar results
3. Construct the wave-function Ψ

After all pairs for a given k^* bin are simulated and wave-functions obtained, the results are averaged to give the fit result.

Construction of the wave-functions, Equation 4.49, involves a number of complex functions not included in standard C++ or ROOT libraries (namely, $h(\eta)$, $\tilde{G}(\rho, \eta)$, and $F(-i\eta, 1, i\xi)$). These functions were even difficult to find and implement from elsewhere. Our solution was to embed a Mathematica kernel into our C++ code to evaluate these functions. However, having Mathematica work on-the-fly with the fitter was far too time consuming (the fitter would have taken days, maybe weeks to finish). Our solution was to use Mathematica to create matrices representing these functions for different parameter values. During fitting, these matrices are then used to interpolate the results of the complicated functions, which are subsequently used to build the wave-functions. This method decreases the running time dramatically, and we are now able to generate results in under ~ 1 hour.

6.6 Systematic errors

In order to understand the systematic uncertainties of our data, the analysis code was run many times using slightly different values for a number of important cuts, and the results were compared. To quantify the systematic errors on the data, all correlation functions built using all varied cut values were bin-by-bin averaged, and the resulting variance of each bin was taken as the systematic error. The cuts included in the systematic study, as well as the values used in the variations, are shown in Tab. 6.4 (ΛK^0_S), Tab. 6.5 ($\Lambda K^\pm$) and Tab. 6.6 ($\Xi^- K^\pm$). Note, the central value corresponds to that used in the analysis.

Similarly, the fit parameters extracted from all of these correlation functions were averaged, and the resulting variances were taken as the systematic errors for the fit parameters. As with the systematic errors on the data, this was performed for all varied cut values. Additionally, a systematic analysis was done on our fit method through varying our k^* fit range, as well as varying our modeling of the non-femtoscopic background. Our choice of k^* fit range was varied by $\pm$ 25%. As previously stated, the non-femtoscopic backgrounds are modeled using the THERMINATOR 2 simulation for the $\Lambda K^\pm$ analyses, and with a linear form for the ΛK^0_S system. To study the contribution of this choice to our systematic errors, we modeled the backgrounds of all of our systems by fitting to the data with a with a linear, quadratic, and Gaussian form. Additionally, we modeled the backgrounds of all systems with a polynomial fit to the THERMINATOR 2 simulation, scaled to match the data. The resulting uncertainties in the extracted parameter sets were combined with our uncertainties arising from our particle and pair cuts.

ΛK^0_S systematics

DCA to PV $\Lambda(\overline{\Lambda})$	$<$ [4, 5, 6] mm
DCA to PV K^0_S	$<$ [2, 3, 4] mm
DCA $\Lambda(\overline{\Lambda})$ Daughters	$<$ [3, 4, 5] mm
DCA K^0_S Daughters	$<$ [2, 3, 4] mm
$\cos(\theta_{PA})$ $\Lambda(\overline{\Lambda})$ to PV	$>$ [0.9992, 0.9993, 0.9994]
$\cos(\theta_{PA})$ K^0_S to PV	$>$ [0.9992, 0.9993, 0.9994]
DCA to PV of $p(\bar{p})$ Daughter of $\Lambda(\overline{\Lambda})$	$>$ [0.5, 1, 2] mm
DCA to PV of $\pi^-(\pi^+)$ Daughter of $\Lambda(\overline{\Lambda})$	$>$ [2, 3, 4] mm
DCA to PV of π^+ Daughter of K^0_S	$>$ [2, 3, 4] mm
DCA to PV of π^- Daughter of K^0_S	$>$ [2, 3, 4] mm
$\overline{\mathbf{\Delta r}}$ of Like-Charge Daughters	$>$ [5, 6, 7] cm

Table 6.4: ΛK^0_S systematics. In the table, the shorthand used is as follows: PA = pointing angle; PV = primary vertex; DCA = distance of closest approach; $\overline{\mathbf{\Delta r}}$ = average separation

$\Lambda K^\pm$ systematics

DCA $\Lambda(\overline{\Lambda})$ to PV	$<$ [4, 5, 6] mm
DCA $\Lambda(\overline{\Lambda})$ Daughters	$<$ [3, 4, 5] mm
$\cos(\theta_{PA})$ $\Lambda(\overline{\Lambda})$ to PV	$>$ [0.9992, 0.9993, 0.9994]
DCA to PV of $p(\bar{p})$ Daughter of $\Lambda(\overline{\Lambda})$	$>$ [0.5, 1, 2] mm
DCA to PV of $\pi^-(\pi^+)$ Daughter of $\Lambda(\overline{\Lambda})$	$>$ [2, 3, 4] mm
$\overline{\mathbf{\Delta r}}$ of $\Lambda(\overline{\Lambda})$ Daughter with Same Charge as $K^\pm$	$>$ [7, 8, 9] cm
DCA to PV in Transverse Plane of $K^\pm$	$<$ [1.92, 2.4, 2.88]
DCA to PV in Longitudinal Direction of $K^\pm$	$<$ [2.4, 3.0, 3.6]

Table 6.5: $\Lambda K^\pm$ systematics. In the table, the shorthand used is as follows: PA = pointing angle; PV = primary vertex; DCA = distance of closest approach; $\overline{\mathbf{\Delta r}}$ = average separation.

$\Xi^{-}K^{\pm}$ systematics

DCA to PV $\Xi(\bar{\Xi})$	$<$ [2, 3, 4] mm
DCA $\Xi(\bar{\Xi})$ Daughters	$<$ [2, 3, 4] mm
$\cos(\theta_{PA})$ $\Xi(\bar{\Xi})$ to PV	$>$ [0.9991, 0.9992, 0.9993]
$\cos(\theta_{PA})$ $\Lambda(\overline{\Lambda})$ to $\Xi(\bar{\Xi})$ DV	$>$ [0.9992, 0.9993, 0.9994]
DCA to PV bachelor π	$>$ [0.5, 1, 2] mm
DCA to PV $\Lambda(\overline{\Lambda})$	$>$ [1, 2, 3] mm
DCA $\Lambda(\overline{\Lambda})$ Daughters	$<$ [3, 4, 5] mm
DCA to PV of $p(\bar{p})$ Daughter of $\Lambda(\overline{\Lambda})$	$>$ [0.5, 1, 2] mm
DCA to PV of $\pi^{-}(\pi^{+})$ Daughter of $\Lambda(\overline{\Lambda})$	$>$ [2, 3, 4] mm
$\overline{\mathbf{\Delta r}}$ of $\Lambda(\overline{\Lambda})$ Daughter and $K^{\pm}$ with like charge	$>$ [7, 8, 9] cm
$\overline{\mathbf{\Delta r}}$ of Bachelor π and $K^{\pm}$ with like charge	$>$ [7, 8, 9] cm
DCA to PV in Transverse Plane of $K^{\pm}$	$<$ [1.92, 2.4, 2.88]
DCA to PV in Longitudinal Direction of $K^{\pm}$	$<$ [2.4, 3.0, 3.6]

Table 6.6: $\Xi^{-}K^{\pm}$ systematics. In the table, the shorthand used is as follows: PA = pointing angle; PV = primary vertex; DV = decay vertex; DCA = distance of closest approach; $\overline{\mathbf{\Delta r}}$ = average separation.

Chapter 7: Results

7.1 Results: ΛK^0_S and $\Lambda K^{\pm}$

In the following sections, we present our final results, for which three residual contributors are assumed ($c\tau_{\mathrm{max}} = 10$ fm, see Sec. 6.2). Results for the cases of ten residual contributors and no residual correlations may be found in Appendices A.3 and A.4, respectively. Furthermore, comparisons of results obtained using different variations of the fit method can be found in Appendix A.1.

For the results shown, unless otherwise noted, the following hold true: All correlation functions are normalized in the range $0.32 < k^* < 0.40$ GeV/c, and fit in the range $0.0 < k^* < 0.30$ GeV/c. For the ΛK^- and $\overline{\Lambda} K^+$ analyses, the region $0.19 < k^* < 0.23$ GeV/c is excluded from the fit to exclude the bump caused by the Ω^- resonance. The non-femtoscopic backgrounds for the $\Lambda K^{\pm}$ systems are modeled by a 6^{th}-order polynomial fit to THERMINATOR 2 simulation, while those for the ΛK^0_S are fit with a simple linear form. All analyses are fit simultaneously across all centralities, with a single radius and normalization λ parameter for each centrality bin. Scattering parameters ($\Re f_0$, $\Im f_0$, d_0) are shared between pair-conjugate systems, but assumed unique between the different ΛK charge combinations (i.e. a parameter set describing the ΛK^+ & $\overline{\Lambda} K^-$ system, a second set describing the ΛK^- & $\overline{\Lambda} K^+$ system, and a third for the ΛK^0_S & $\overline{\Lambda} K^0_S$ system). Each correlation function receives a unique normalization parameter. The fits are corrected for finite momentum resolution effects, non-femtoscopic backgrounds, and residual correlations resulting from the feed-down from resonances.

Lines and boxes on the experimental data represent statistical and systematic errors, respectively. In the figures showing experimental correlation functions with fits, the black solid curve shows the primary (ΛK) contribution to the fit (i.e. $1 + \lambda'_{\Lambda\mathrm{K}} C_{\Lambda\mathrm{K}}(k^*_{\Lambda\mathrm{K}})$ in Eq. 6.2). The green curve shows the fit to the non-femtoscopic background (with a polynomial fit to the THERMINATOR 2 simulation for the $\Lambda\mathrm{K}^{\pm}$ systems, and a linear form fit to the data for the $\Lambda\mathrm{K}^0_\mathrm{S}$). The purple curve shows the final fit after all residual contributions have been included, and momentum resolution and non-flat background corrections have been applied. The extracted fit values with uncertainties are printed as (fit value) $\pm$ (statistical uncertainty) $\pm$ (systematic uncertainty).

Figure 7.1 nicely collects and summarizes all of our extracted fit parameters. In the summary plot, we show the extracted scattering parameters in the form of a $\Im f_0$ vs $\Re f_0$ plot, which includes the d_0 values to the right side. We also show the λ_{Fit} vs. radius parameters for all three of our studied centrality bins. The extracted fit parameters are also collected in Table 7.1. Figure 7.2 presents our extracted fit radii, along with those of other systems previously analyzed by ALICE [133], as a function of pair transverse mass (m_T).

Centrality	λ	R
0–10%	1.40 ± 0.63 (stat.) ± 0.17 (sys.)	6.24 ± 0.92 (stat.) ± 0.66 (sys.)
10–30%	0.90 ± 0.34 (stat.) ± 0.17 (sys.)	4.41 ± 0.50 (stat.) ± 0.39 (sys.)
30–50%	1.00 ± 0.34 (stat.) ± 0.22 (sys.)	3.51 ± 0.44 (stat.) ± 0.28 (sys.)

System	$\Re f_0$	$\Im f_0$	d_0
ΛK^+ & $\bar{\Lambda} K^-$	-0.49 ± 0.19 (stat.) ± 0.12 (sys.)	0.42 ± 0.22 (stat.) ± 0.12 (sys.)	-0.55 ± 2.22 (stat.) ± 1.76 (sys.)
ΛK^- & $\bar{\Lambda} K^+$	0.19 ± 0.15 (stat.) ± 0.08 (sys.)	0.29 ± 0.17 (stat.) ± 0.08 (sys.)	-7.80 ± 6.15 (stat.) ± 6.10 (sys.)
ΛK^0_S & $\bar{\Lambda} K^0_S$	0.09 ± 0.15 (stat.) ± 0.06 (sys.)	0.53 ± 0.28 (stat.) ± 0.13 (sys.)	-2.59 ± 1.47 (stat.) ± 3.59 (sys.)

Table 7.1: Fit Results ΛK, with 3 residual correlations included. The fit procedure is as described in the text. The fit is done on the data with only statistical error bars. The errors marked as “stat.” are those returned by MINUIT. The errors marked as “sys.” are those which result from my systematic analysis (as outlined in Section 6.6).

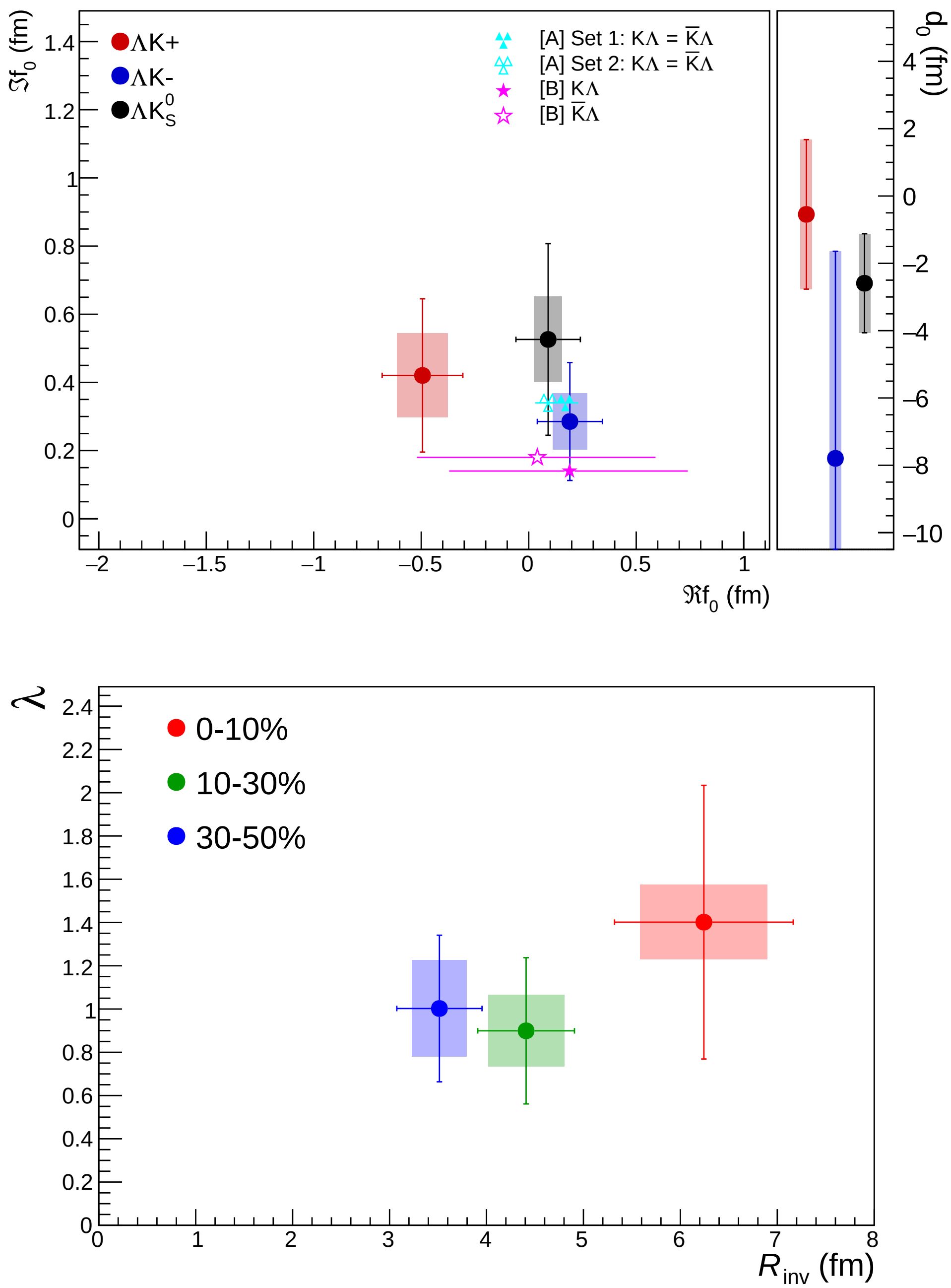

Figure 7.1: Extracted fit parameters for the case of 3 residual contributors for all of our ΛK systems. [Top]: $\Im f_0$ vs. $\Re f_0$, together with d_0 to the right. [Bottom]: λ vs. Radius for the 0–10% (blue), 10–30% (green), and 30–50% (red) centrality bins. In the fit, all ΛK systems share common radii. The color scheme used in the panel is consistent with that in Fig. 7.2. The cyan ([A] = Ref. [169]) and magenta ([B] = Ref. [170]) points show theoretical predictions made using chiral perturbation theory.

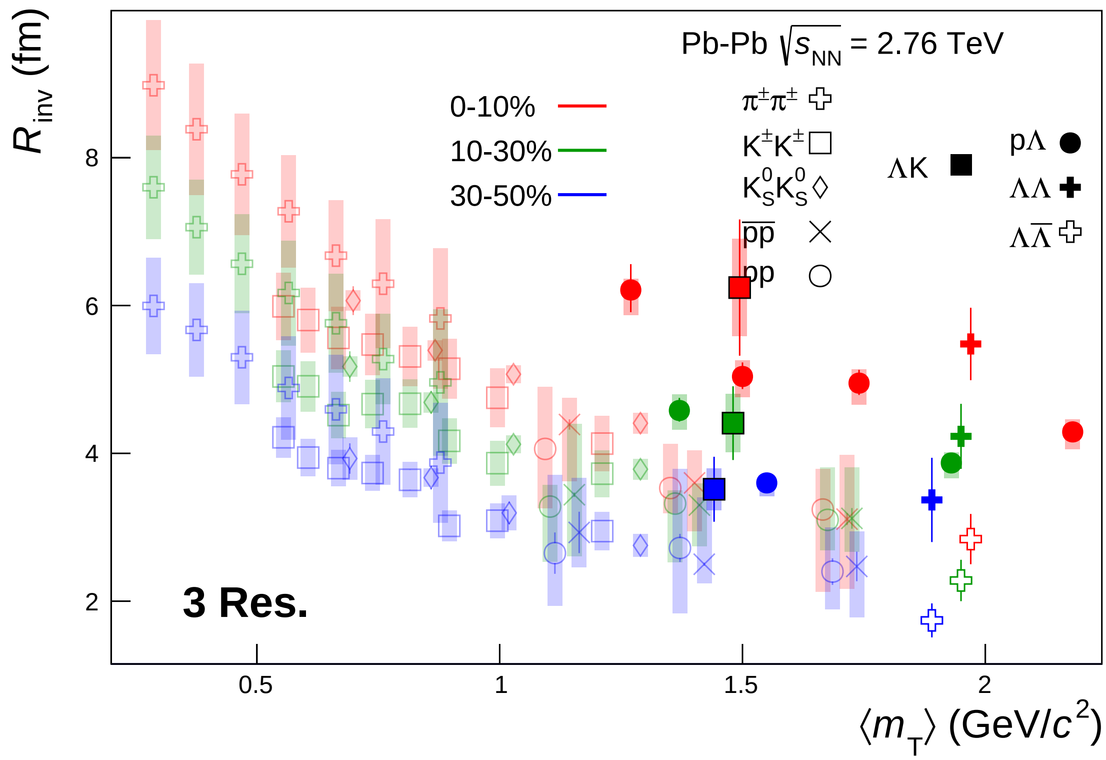

Figure 7.2: 3 residual correlations in ΛK fits. Extracted R_{inv} fit parameters as a function of pair transverse mass (m_{T}) for various pair systems over several centralities. The ALICE published data [133] are shown with transparent, open symbols. The new ΛK results are shown with opaque, filled symbols. The m_{T} value for the ΛK system is an average of those for the ΛK^+, $\overline{\Lambda}K^-$, and ΛK^0_S systems.

7.1.1 Correlation functions with fits

Figure 7.3 highlights the interesting differences and similarities between the three ΛK systems. In the left panels of Fig. 7.3, the pair-conjugate systems have been combined, and the three ΛK charge combinations are plotted together in the different centrality bins. The figures demonstrate that the correlation effect appears at similar k^* values for all systems. Moving from high-k^* downward, the initial suppression in the signal is due to the positive imaginary component of the scattering parameters, $\Im f_0$, which describes the inelastic scattering channels. Continuing to lower values of k^*, the three ΛK systems diverge. The negative real component of the scattering parameter, $\Re f_0$, in the ΛK^+ system causes the suppression of the signal to continue and to increase in magnitude. A negative $\Re f_0$ indicates that the strong interaction is acting repulsively in the ΛK^+ system. For the ΛK^- system, as one moves to lower values of k^*, the suppression decreases and eventually turns to an enhancement. This is due to the positive $\Re f_0$ value in the ΛK^- system, indicating that the strong interaction acts attractively. The attractive nature of the strong interaction is also visible in the ΛK^0_S system, although to a smaller extent compared the the ΛK^- data.

The right panels of Fig. 7.3 show the average of all $\Lambda K^\pm$ correlation functions (i.e. $\Lambda K^+ \oplus \overline{\Lambda} K^- \oplus \Lambda K^- \oplus \overline{\Lambda} K^+$) in magenta compared to $\Lambda K^0_S \oplus \overline{\Lambda} K^0_S$ in black. The figure shows that the average of all $\Lambda K^\pm$ results in a correlation function which is similar to that of the ΛK^0_S. It is suggested that the K^0_S may behave somewhat as the average of the K^+ and K^-. The quark content of the K^+ is $u\bar{s}$, and that of the K^- is $\bar{u}s$. The K^0_S is a mixture of the netural K^0 and $\overline{K}^0$ states, and is represented with quark content $\frac{1}{\sqrt{2}}[d\bar{s} + \bar{d}s]$. Therefore, in terms of its electric charge and strangeness content, the K^0_S is a type of average of the K^+ and K^-; however, the charged kaons contain (anti)up quarks, while the K^0_S contains (anti)down quarks.

Figures 7.4, 7.5, and 7.6 show the experimental correlation functions with fits, assuming 3 residual contributors ($c\tau_{\max} = 10$ fm, see Sec. 6.2), for all ΛK systems

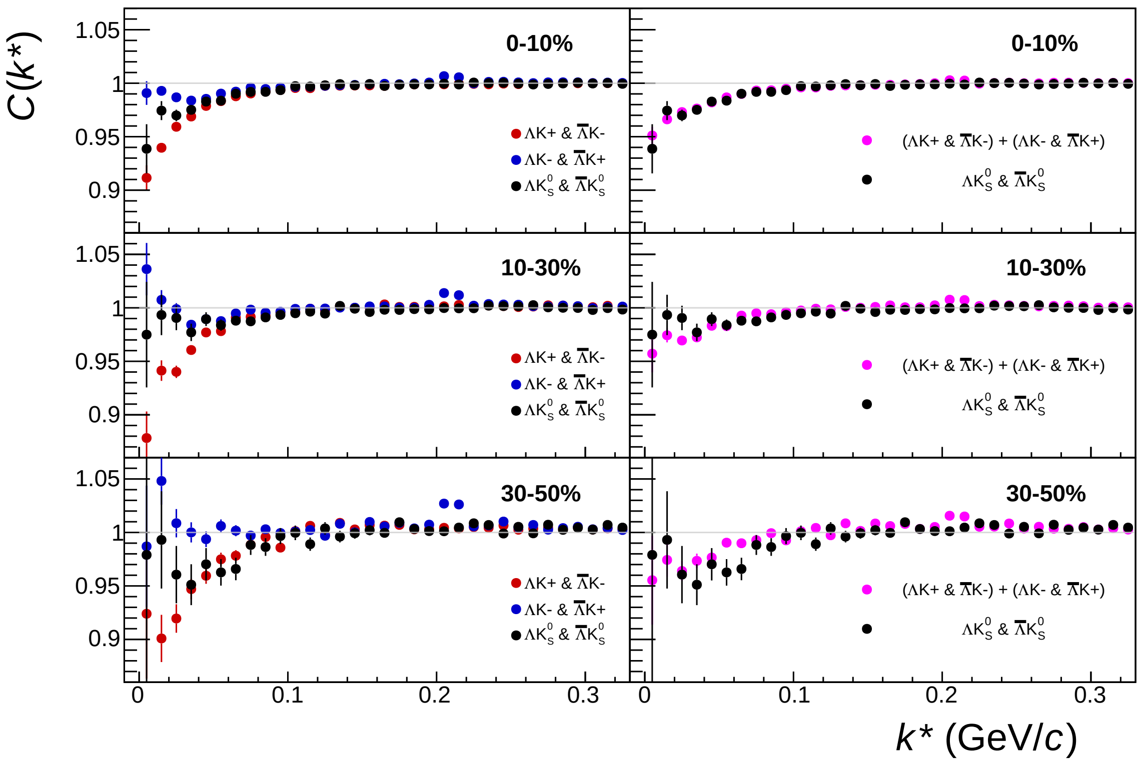

Figure 7.3: Comparison of the ΛK correlation functions for the 0–10% (top), 10–30% (middle), and 30–50% (bottom) centrality bins. In the left column, the pair-conjugate systems have been combined, with $\Lambda K^{+} \oplus \overline{\Lambda}K^{-}$ in red, $\Lambda K^{-} \oplus \overline{\Lambda}K^{+}$ in blue, and $\Lambda K^0_S \oplus \overline{\Lambda}K^0_S$ in black. In the right column, the $\Lambda K^{+} \oplus \overline{\Lambda}K^{-}$ and $\Lambda K^{-} \oplus \overline{\Lambda}K^{+}$ correlation functions are combined and presented in magenta.

(ΛK^{+}, ΛK^{-}, and ΛK^0_S, respectively) in all studied centralities (0–10%, 10–30%, 30–50%). The parameter sets extracted from the fits can be found in Table 7.1. Figures with a wider range in k^*, showing better the non-femtoscopic backgrounds, may be found in Appendix A. Also contained in the appendix are plots demonstrating the contributions from the residuals, as well as results assuming 10 and no residual contributors.

In Figures 7.4 – 7.9, the pair system (e.g. ΛK^{+}) data is shown in the left column, and the charge conjugate pair system (e.g. $\overline{\Lambda}K^{-}$) in the right. The results are grouped according to analysis type in Figs. 7.4 – 7.6, where the the pair system is shown on the left with its conjugate on the right, and the rows differentiate the centrality bins

(0–10% in the top, 10–30% in the middle, and 30–50% in the bottom). In Figs. 7.7–7.9 the figures are grouped together by centrality bin, and the rows differentiate the ΛK charge combinations. The lines on the data represent the statistical errors, while the boxes represent the systematic errors. The fit procedure is as described in the text; in short, all systems are fit simultaneously with shared radii, while each [ΛK^+, ΛK^-, ΛK^0_S] maintains a unique set of scattering parameters. The black solid line represents the primary ΛK component of the fit. The green line shows the fit to the non-flat background. The purple curves show the fit after all residuals' contributions have been included, and momentum resolution and non-flat background corrections have been applied. The extracted fit values with uncertainties are printed in the top left panel of each figure.

Results grouped by analysis type

The following figures (Figs. 7.4–7.6) contain the fit results together with data, grouped together by analysis type (ΛK^+ & $\overline{\Lambda}K^-$, ΛK^- & $\overline{\Lambda}K^+$, ΛK^0_S & $\overline{\Lambda}K^0_S$). In these figures, the pair system is shown on the left with its conjugate on the right, and the rows differentiate the centrality bins (0–10% in the top, 10–30% in the middle, and 30–50% in the bottom)

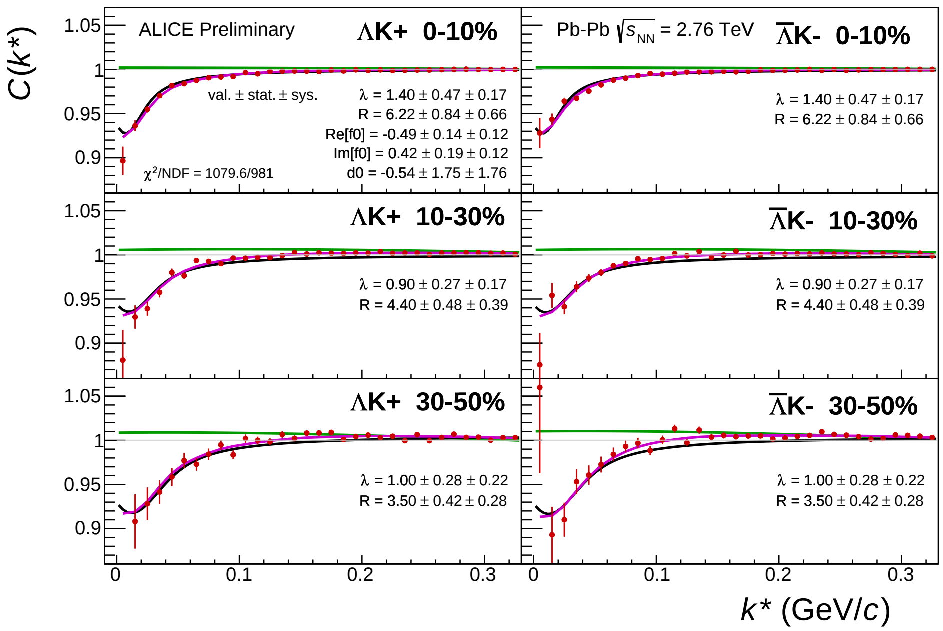

Figure 7.4: Fit results for the ΛK^+ (left) and $\bar{\Lambda}K^-$ (right) data in all centrality bins (0–10% in the top, 10–30% in the middle, and 30–50% in the bottom). See text for details.

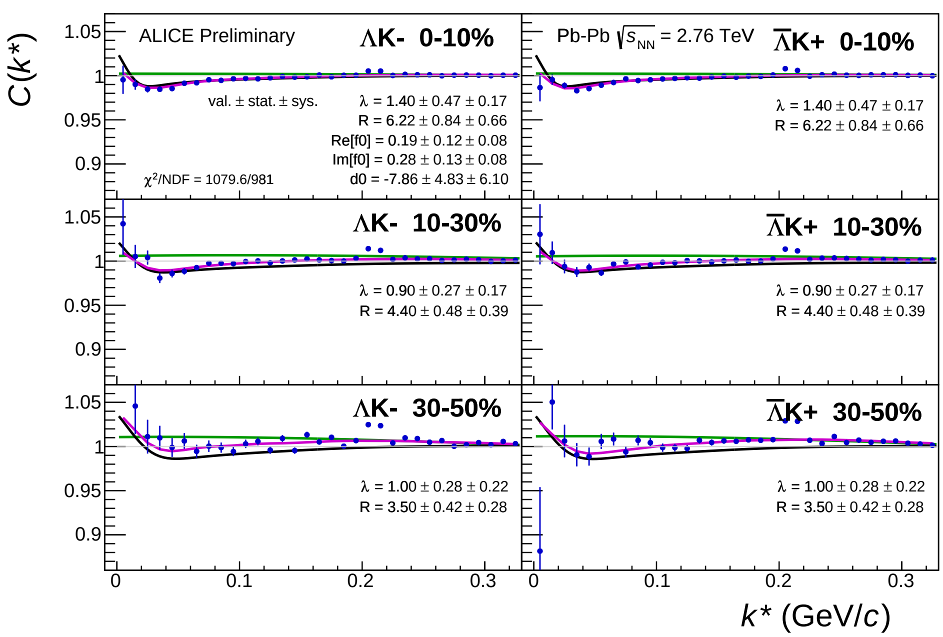

Figure 7.5: Fit results for the ΛK^- (left) and $\bar{\Lambda}K^+$ (right) data in all centrality bins (0–10% in the top, 10–30% in the middle, and 30–50% in the bottom). See text for details.

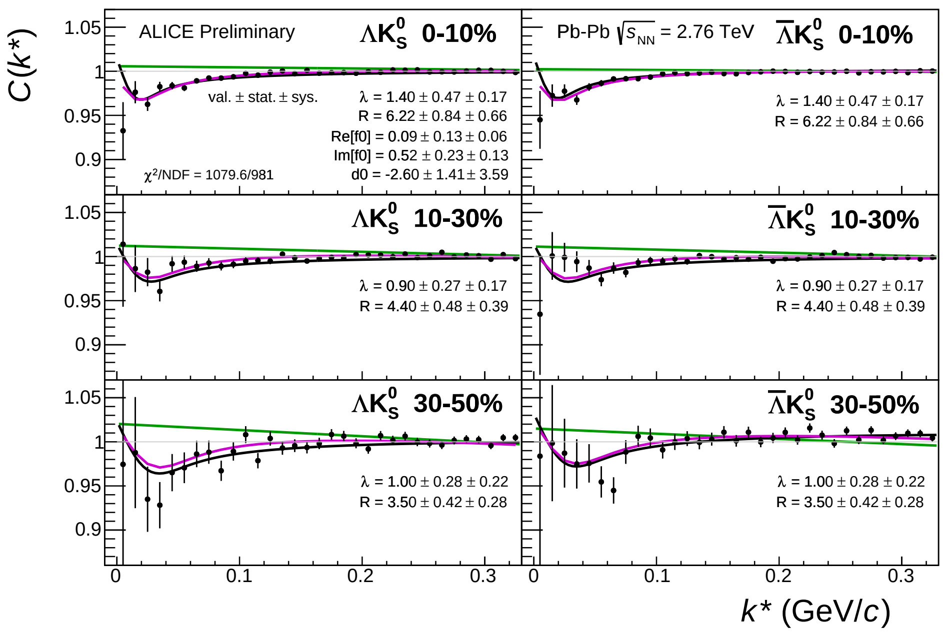

Figure 7.6: Fit results for the ΛK^0_S (left) and $\overline{\Lambda} K^0_S$ (right) data in all centrality bins (0–10% in the top, 10–30% in the middle, and 30–50% in the bottom). See text for details.

Results grouped by centrality bin

The following figures (Figs. 7.7–7.9) contain the same information as Figs. 7.4–7.6), but figures are grouped together by centrality bin instead of analysis type. In these figures, the pair system is shown on the left with its conjugate on the right, the rows differentiate the ΛK charge combinations

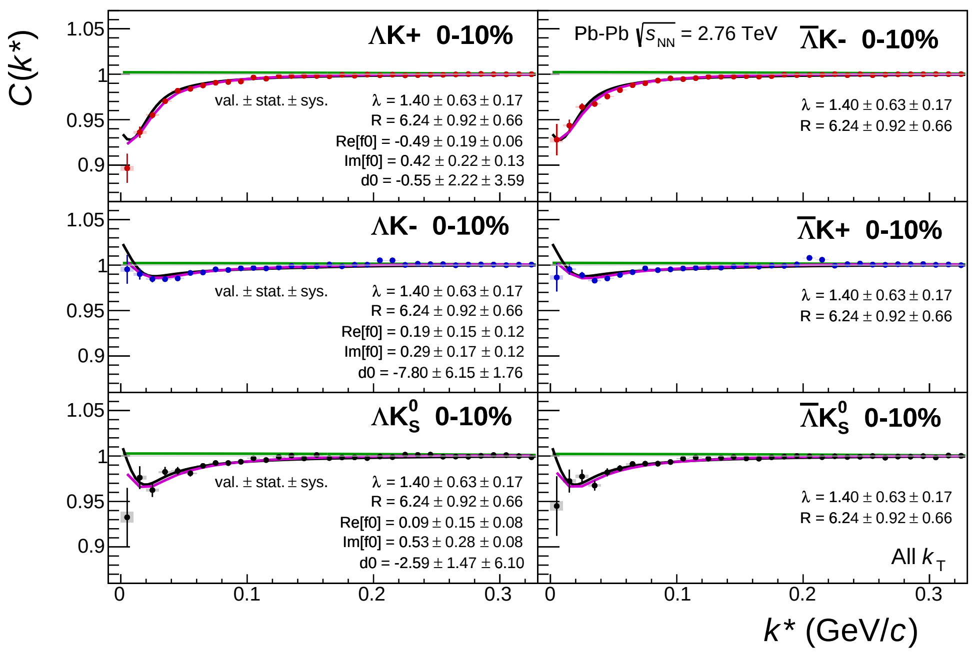

Figure 7.7: Fit results for all ΛK analyses in the 0–10% centrality bin. The pair system (e.g. ΛK^{+}) is shown on the left, and the conjugate pair (e.g. $\overline{\Lambda}K^{-}$) on the right, and the rows differentiate the different ΛK charge combinations (ΛK^{+} in the top, ΛK^{-} in the middle, and ΛK^{0}_{S} in the bottom).

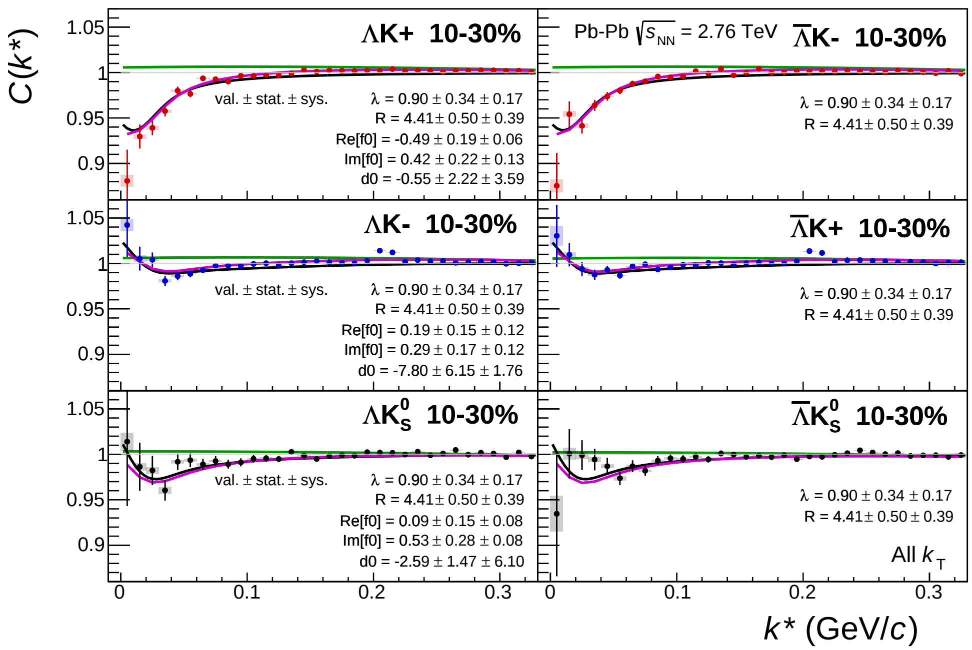

Figure 7.8: Fit results for all ΛK analyses in the 10–30% centrality bin. See legend in Fig. 7.7 for additional information.

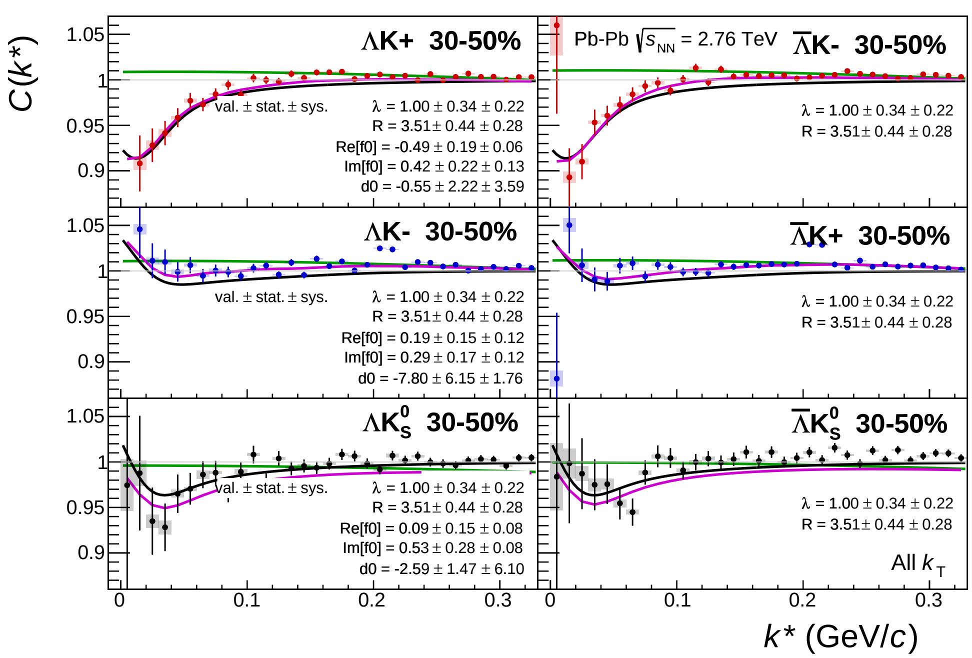

Figure 7.9: Fit results for all ΛK analyses in the 30–50% centrality bin. See legend in Fig. 7.7 for additional information.

7.1.2 Discussion of m_{T}-Scaling

It is clear from the results presented in the previous sections, that the ΛK systems do not conform to the approximate m_{T}-scaling of the pair source sizes in Fig. 7.2. At first thought, this may appear to be a troubling result; the approximate scaling is an observed consequence of the collective behavior of the soft (low-p_{T}) sector of the produced system. The Λ and K particles certainly participate in the collective expansion of the QGP medium, so why do their extracted femtoscopic radii not behave as expected? To get straight to the point: the ΛK systems are comprised of non-identical particles, each with its own unique single-particle source. Each source is, in general, unique both in its overall size, and in its space-time position within the produced medium. The hydrodynamic nature of the medium produces the approximate m_{T}-scaling with respect to these single-particle sources, not the pair sources. The differences in the single-particle sizes and space-time positions, when probing correlations between non-identical particle pairs, leads to extracted radii falling outside of the (identical particle femtoscopy) m_{T}-scaling trend.

Figure 7.10 (which contains the same data as Fig. 7.2), shows again the R_{inv} vs m_{T} plot, but also highlights (with arrows) the approximate individual $\langle m_{\mathrm{T}} \rangle$ values of the single-particle distributions. For identical particle femtoscopy (e.g. the published ALICE data in Fig. 7.10), the pair source is comprised of two identical single-particle sources laying on top of each other. The extracted femtoscopic radii are related to the single-particle source sizes by a factor of $\sqrt{2}$. Therefore, the m_{T}-scaling visible in the identical particle femtoscopic studies presented in Fig. 7.10 is really just a manifestation of the scaling of the single-particle sources.

For the case presented here, sampling single-particle distributions with significantly different m_{T} values translates to sampling distributions differing in size which are separated in space-time. Therefore, our results deviating from the m_{T}-scaling curve of the identical particle studies is not surprising. We emphasize that we do not

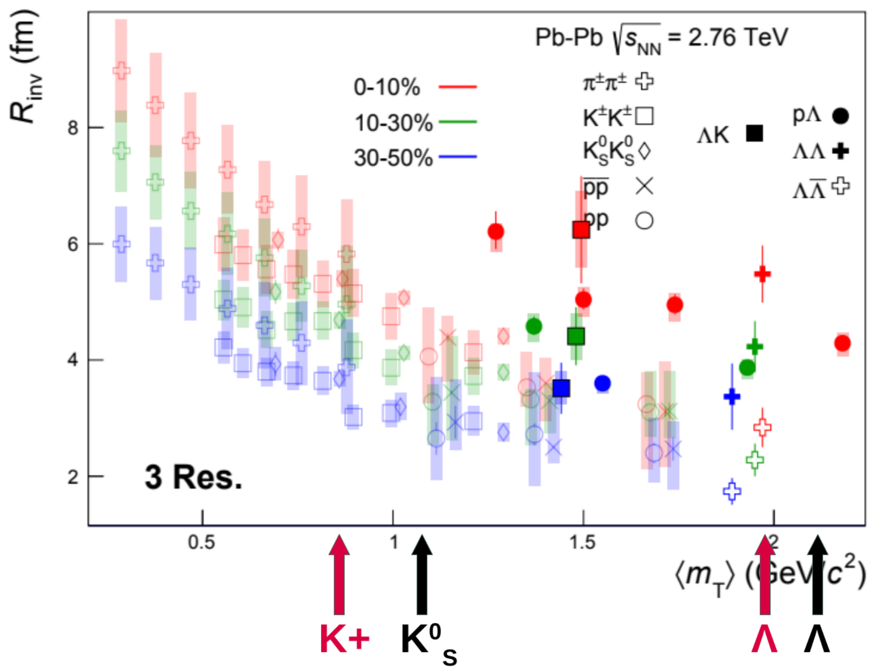

Figure 7.10: Same as Fig. 7.2, but with the individual m_T values for the single-particle distributions identified.

suggest our extracted source sizes indicate any sort of contradiction to the hydrodynamic picture of the system dictating the substructure of the femtoscopic radii. In fact, our results rather support such a picture. The hydrodynamic response of the system not only confines higher-m_T particles to smaller homogeneity regions, it also pushes their average emissions points further in the "out" direction [160]. These effects can inflate the radii extracted using the one-dimensional Lednický model, which assumes a spherically symmetric source about the origin (i.e. $R_{out} = R_{side} = R_{long}$ and $\mu_{out} = \mu_{side} = \mu_{long} = 0$). In the following sections, we support this point through a numerical integration method of the Koonin-Pratt equation (presented below), as well as through varying μ_{out} within the THERMINATOR 2 simulation (presented as the end of this section). Additionally, we will demonstrate with a spherical harmonic decomposition that our systems do exhibit an asymmetry (i.e. offset) in the outward direction (μ_{out}).

We can use Fig. 7.10 to estimate the values of our ΛK radii expected in the absence of any μ_{out} offset. As previously stated, for identical particle studies, the single-particle radii can be obtained from the extracted femtoscopic radii simply by dividing by $\sqrt{2}$. Using the trends shown in Fig. 7.10, with m_{T} values appropriate for our studies, we expect the single-particle source sizes in the 0–10% centrality bin to be $R_{\mathrm{K}} \sim 5/\sqrt{2}$ fm and $R_{\Lambda} \sim 3/\sqrt{2}$ fm. In Eq. 4.43 from Sec. 4.2.5, we found the pair source radius was the sum of the single source radii added in quadrature, $R^2_{ab,i} = R^2_{a,i} + R^2_{b,i}$. Therefore, we would expect the fit algorithm to return $R_{\Lambda\mathrm{K}} \sim$ 4 fm if no outward asymmetry exists, which is clearly below the value we measure. We have also studied the effect of fixing the radii to values calculated using extracted single-particle source sizes from the identical-particle studies, as described above. This procedure fixes the radii to the values one would expect in the absence of any outward asymmetry. The effect of such an assumption can be found in Appendix A.1; in short, this procedure of forcing the radii to be smaller than preferred by the fit algorithm reduces the magnitudes of $\Re f_0$ and $\Im f_0$ in all cases, and causes the sign of $\Re f_0$ to change for the $\Lambda\mathrm{K}^0_{\mathrm{S}}$ analysis (from positive to negative).

To be clear, our model assumes $\mu_{\mathrm{out}} = 0$ because it greatly simplifies the generation of fit correlation functions, but we do not believe this to strictly be the case physically; our radii can be interpreted as effective radii whose larger than expected magnitudes are a result of this outward shift. In order to include a nonzero μ_{out} in the fit, the numerical integration method and/or particle pair simulation method need to be optimized. Additionally, at this point, a smaller source with a nonzero μ_{out} is difficult for us to distinguish from a larger source, as will be discussed below. In the future, our measurement of the scattering parameters may be used in a new fit algorithm to extract the source size and offset, instead of the effective source size quoted in this study.

In summary, we argue that our large extracted radii result from a non-zero μ_{out} in the pair source distribution. Due to the hydrodynamic response of the system created in heavy-ion collisions, we expect higher-m_{T} particles to originate from smaller regions of homogeneity located further in the "out" direction. This difference in single-particle source sizes, in addition to their separation in space-time, can lead to a deviation of non-identical particle studies from the m_{T}-scaling trend observed for identical particle pairs. This is not in contradiction to the hydrodynamic response of the system, but rather in support of it. For non-identical particle studies, the individual particle m_{T} values dictate the single-particle source sizes and positions, which in turn dictate the observed femtoscopic signal. Therefore, when reporting results from non-identical studies, it is vital to report the individual particle m_{T} values, otherwise, comparisons to other measurements will be impossible.

Numerical integration of the Koonin-Pratt equation

We investigated the effect of a non-zero offset in the outward direction, μ_{out}, by numerically integrating the Koonin-Pratt equation (Eq. 4.11), demonstrations of which is shown in Figure 7.11. Before going into the details, we find that increasing μ_{out} leads to a correlation function which is more tightly confined to low-k^* values, i.e. the increase in μ_{out} makes the source appear larger. The nice analytic form for generating fit correlation functions derived by Lednický relies on a spherically symmetric source distribution centered at the origin (i.e. with no offsets, $\mu_{\mathrm{o,s,l}} = 0$). The method of numerical integration allows us to alter the source as we wish, which, in this case, amounts to simply adding an outward shift, μ_{out}, to the spherically symmetric Gaussian profile. The cost of this flexibility is a significant decrease in the speed of generating fit curves, and this numerical integration is currently too slow to be used within our fit framework. Nonetheless, this method offers a simple test ground to study the effect of a non-zero μ_{out}.

For the curves presented in Fig. 7.11, a spherically symmetric Gaussian source ($R_o = R_s = R_l$) is assumed, and the offset in the "out" direction (μ_{out}) is varied. In our numerical integration, we use the appropriate forms of the wave-function and scattering parameters (Eqns. 4.32-4.35), which were presented in Sec. 4.2.5. In the

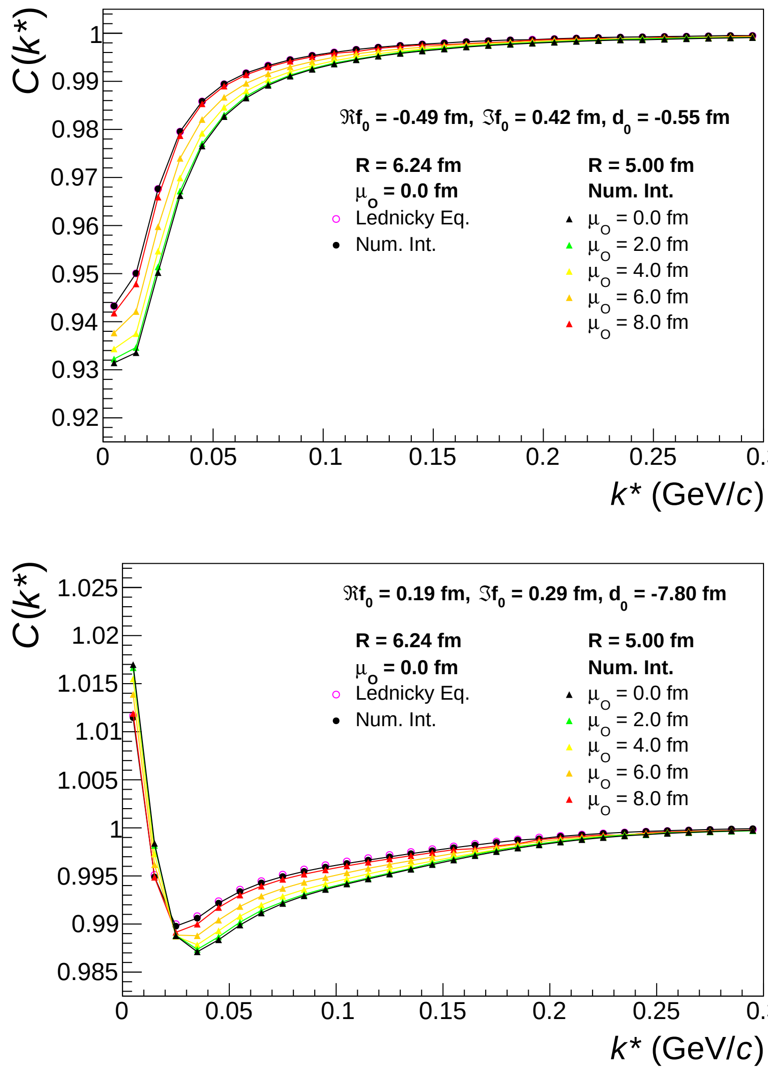

Figure 7.11: Numerical integration of the Koonin-Pratt equation. In the top (bottom), we chose a parameter set to qualitatively match our ΛK^{+} (ΛK^{-}) data. For all, $\mu_{\text{side}} = \mu_{\text{long}} = 0$ fm. Circular (black and magenta) markers assume $R_i = 6.24$ fm (where $i =$ o,s,l) and $\mu_{\text{out}} = 0$ fm. Triangle markers assume $R_i = 5$ fm with varying μ_{out}. The open magenta markers were obtained with the Lednický equation, all others utilize the numerical integration method.

figure, the closed black circles show the curve generated by our numerical integrator for a radius $R_i = 6.24$ fm (where $i =$ o, s, l), $\mu_{\text{out}} = 0$ fm, and the parameter sets listed in the figures ($[\Re f_0, \Im f_0, d_0]$ = [-0.49, 0.42, -0.55] for ΛK^{+} in Fig. 7.11a, and $[\Re f_0, \Im f_0, d_0]$ = [0.19, 0.29, -7.80] for ΛK^{-} in Fig. 7.11b). Note, the radius of

6.24 fm and the parameter sets were chosen to qualitatively match the ΛK^{+} and ΛK^{-} experimental data. The open magenta circles were generated using the analytic Lednický equation (Eqns. 4.44-4.47 from Sec. 4.2.5). The figure shows that our numerical integration method is consistent with the Lednický equation. All of the triangle points assume a radius of 5 fm, again with the parameter sets listed in the legend of the figure, and the different colors correspond to different μ_{out} values.

Figure 7.11 nicely demonstrates the effect of increasing the magnitude of the offset. Specifically, the figure shows that increasing μ_{out} makes the correlation function more concentrated towards the low-k^{*} region, which corresponds to larger extracted radii. Furthermore, for a one-dimensional analysis, we see that a source with $R_i = 6.24$ fm and $\mu_{\mathrm{i}} = 0$ fm (where i = o,s,l) is nearly indistinguishable from a source with $R_i =$ 5 fm and $\mu_{\mathrm{out}} = 8$ fm. Therefore, even with a fast numerical integrator, it would be difficult to disentangle the effects of a larger source radius from a shift in the "out" direction. In order to pursue this direction, outside input constraining these parameters would be necessary. This could be accomplished, for instance, by fixing the pair source size using the single-particle source sizes extracted from identical KK and $\Lambda\Lambda$ results.

Spherical harmonics and varying μ_{out} with THERMINATOR 2

Identical particle femtoscopic studies are able to probe only the size of the emitting region, or, more precisely, the second moment of the emission function. In addition to this, non-identical particle studies are able to measure the relative emission shifts, i.e. the first moments of the emission function. One method to extract information about the emission asymmetries in the system is via a spherical decomposition of the correlation function. With this method, one can draw a wealth of information from just a few components of the decomposition. More specifically, the C_{00} component is similar to the 1D correlation functions typically studied, and probes the overall size of the source. The $\Re C_{11}$ component probes the asymmetry in the system; a non-zero value reveals the asymmetry.

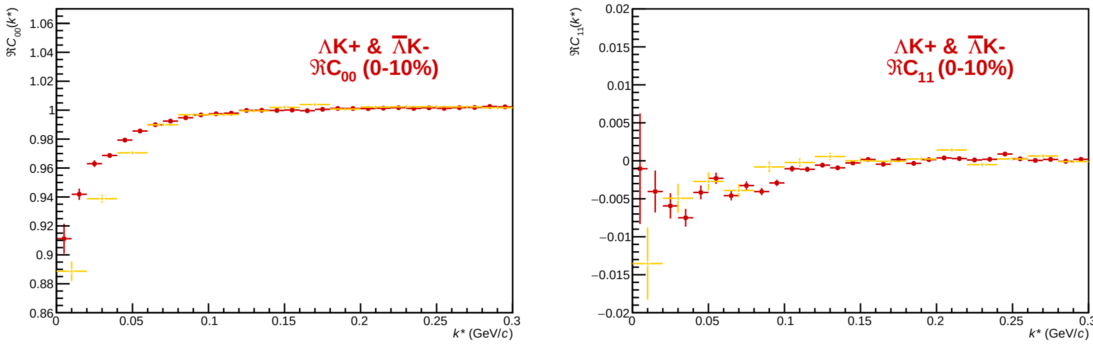

Figure 7.12: C_{00} (left) and $\Re C_{11}$ (right) components of a spherical harmonic decomposition of the ΛK^+ correlation function for the 0–10% centrality bin. The C_{00} component is similar to the 1D correlation functions typically studied, and probes the overall size of the source. The $\Re C_{11}$ component probes the asymmetry in the system; a non-zero value reveals the asymmetry. Results from a THERMINATOR 2 simulation for an impact parameter of b = 2 fm are included (gold stars).

In Fig. 7.12, we show results for the C_{00} and $\Re C_{11}$ components from the spherical decomposition of our ΛK^+ system in the 0–10% centrality bin (red circles). Results for a number of other components within the decomposition, as well as for our ΛK^0_S and ΛK^- systems, are contained in App. B. Along with the experimental data in Fig. 7.12, we have also included results from a THERMINATOR 2 simulation for an impact parameter of b = 2 fm (gold stars). As THERMINATOR 2 does not include any final state interaction effects, we assumed scattering parameters $(\Re f_0, \Im f_0, d_0) =$ (-1.16, 0.51, 1.08) and weighted the numerator pairs with $|\Psi|^2$, as discussed previously in Sec. 6.3 (with regard to Fig. 6.14). Figure 7.12 demonstrates that the C_{00} signal is similar to that observed in our one-dimensional study. The $\Re C_{11}$ component shows a clear deviation from zero, and the negative value signifies that the Λ particles are, on average, emitted further out and/or earlier than the K mesons (in defining our pairs, we take the heavier Λ as our first particle, which is opposite the normal convention). Therefore, as expected, our single-particle Λ and K sources are separated in space-time. Note, for the ΛK^+ system, THERMINATOR 2 predicts $\mu_{\text{out}} \approx 4$ fm for an impact parameter $b = 2$ fm, as shown in Fig. 7.13.

Fig. 7.13 shows a closer look at the THERMINATOR 2 simulation, whose spherical harmonic decomposition was shown along with the data in Fig. 7.12. The top left of Fig. 7.13a shows a fit to the one-dimensional correlation function from THERMINATOR 2. The scattering parameters are known precisely here, as they served as the weights used in the simulation, and are kept constant in the fit. We are interested at looking at the extracted one-dimensional source size here, so the λ parameter is also fixed at unity. The other three plots in Fig. 7.13a show the source distribution in the out (top right), side (bottom left), and long (bottom right) directions (all in the PRF). The source distributions are all fit with a Gaussian form, the result of which is printed within the respective plots. One immediately sees a significant shift in the out direction, $\mu_{\text{out}} \approx 4$ fm, and negligible shift in the other two directions, $\mu_{\text{side}} \approx \mu_{\text{long}} \approx 0$ fm. The figure demonstrates that, within the THERMINATOR 2 model, the Λ is, on average, emitted further out that its K partner. Finally, Fig. 7.13b shows the distribution of the relative time of emittance, again in the PRF. The figure shows that the Λ is, on average, emitted earlier than its K partner. These two results from THERMINATOR 2 are as expected.

We end this section with a brief look at how a spatial separation of the single-particle sources affects the radii extracted from a one-dimensional femtoscopic analysis. To achieve this, we use THERMINATOR 2 in a similar fashion as described above, but with one important difference. Instead of taking the source information from THERMINATOR 2, we draw the source from pre-determined Gaussian distributions. In all cases, we take $\mu_{\text{side}} = \mu_{\text{long}} = 0$ fm, and arbitrarily $R_{\text{out}} = R_{\text{side}} = R_{\text{long}}$ $= 5$ fm. Figure 7.14 shows an example of results obtained from THERMINATOR 2 following this procedure, where $\mu_{\text{out}} = 3$ fm.

In Figure 7.15, we show results for the case of $\mu_{\text{out}} = 1$ fm, $\mu_{\text{out}} = 3$ fm, and μ_{out} $= 6$ fm. In this figure, we do not show the side and long distributions, as they appear identical to those shown in Fig. 7.14. The figure demonstrates that as the separation μ_{out} increases, so do the extracted femtoscopic radii; i.e. the fitted values of R_{inv} are

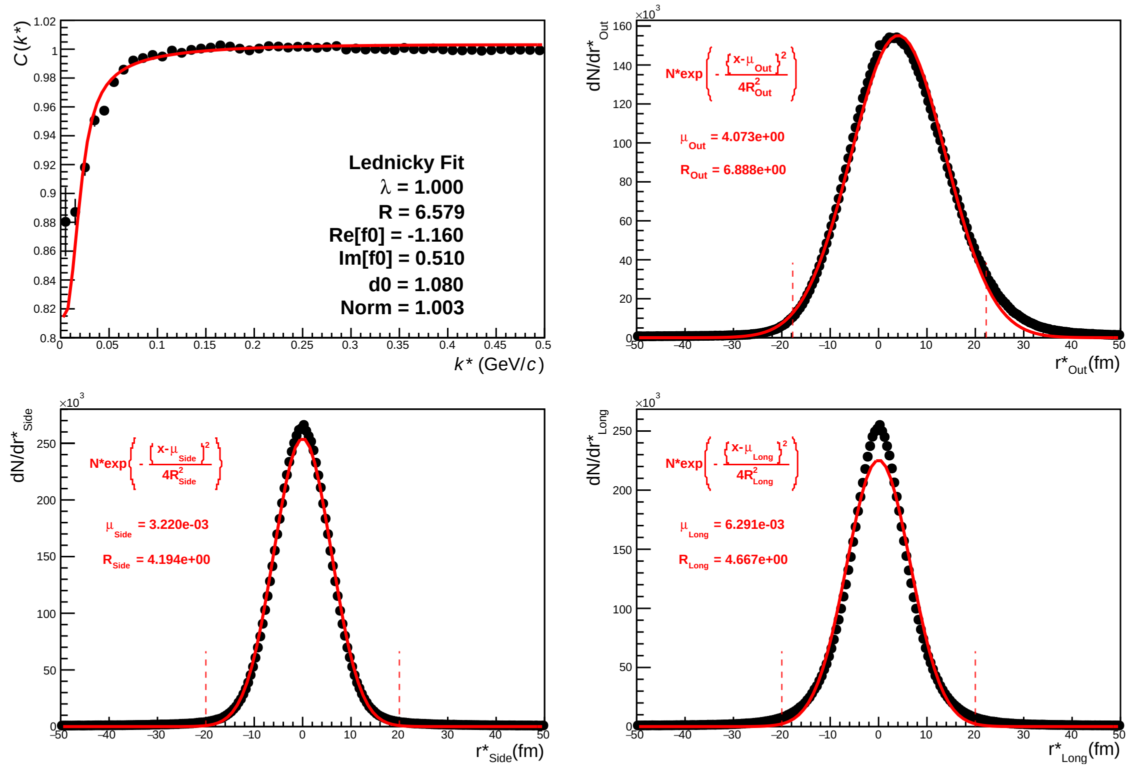

(a) (Top Left) Simple fit on simulation from THERMINATOR 2. Generated source in the (Top Right) out, (Bottom Left) side, and (Bottom Right) long directions.

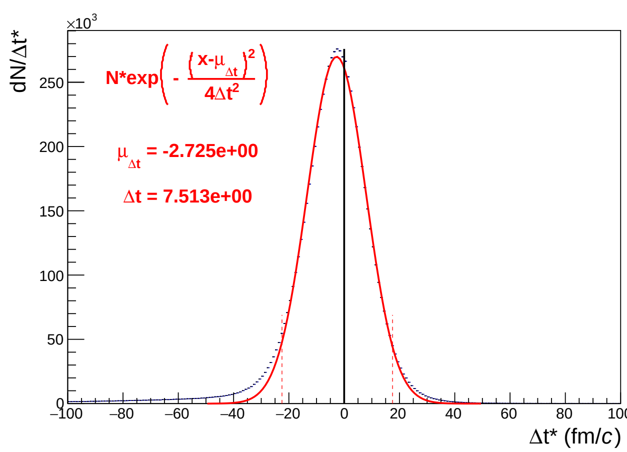

(b) Temporal characteristics of the source.

Figure 7.13: Extracted radius when performing a simple fit on simulation from THERMINATOR 2, along with the spatio-temporal characteristics generated by the simulation.

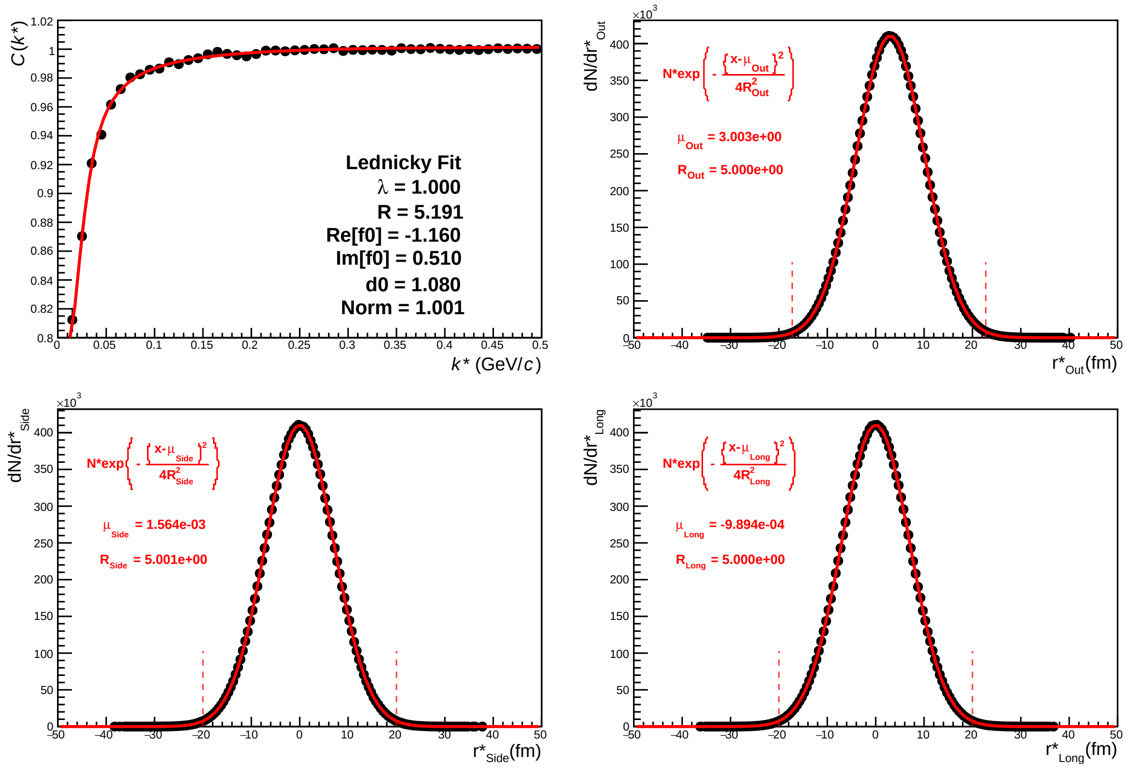

Figure 7.14: THERMINATOR 2 simulation with artificial Gaussian source; the components of the spatial separation for each pair were drawn from Gaussian distributions, with $\sigma_{\mathrm{o,s,l}} = 5$ fm, $\mu_{\mathrm{s,l}} = 0$ fm, and $\mu_{\mathrm{o}} = 3$ fm. The separation of emission in time was taken to be zero. (Top Left) Simple fit of simulation from THERMINATOR 2. Source in the (Top Right) out, (Bottom Left) side, and (Bottom Right) long directions.

correlated with the value of μ_{out}. This is exactly as expected, and in agreement with our qualitative assessment of the curves generated by our numerical Koonin-Pratt integrator described above.

Comparing non-identical to identical particle result

Non-identical femtoscopic analyses cannot be so simply compared to identical particle studies. As introduced in Sec. 4.2.5, assuming the single-particle sources are three dimensional Gaussians with offsets in the "out" direction, the pair source distribution is also a Gaussian with offset in the "out" direction. The form of the

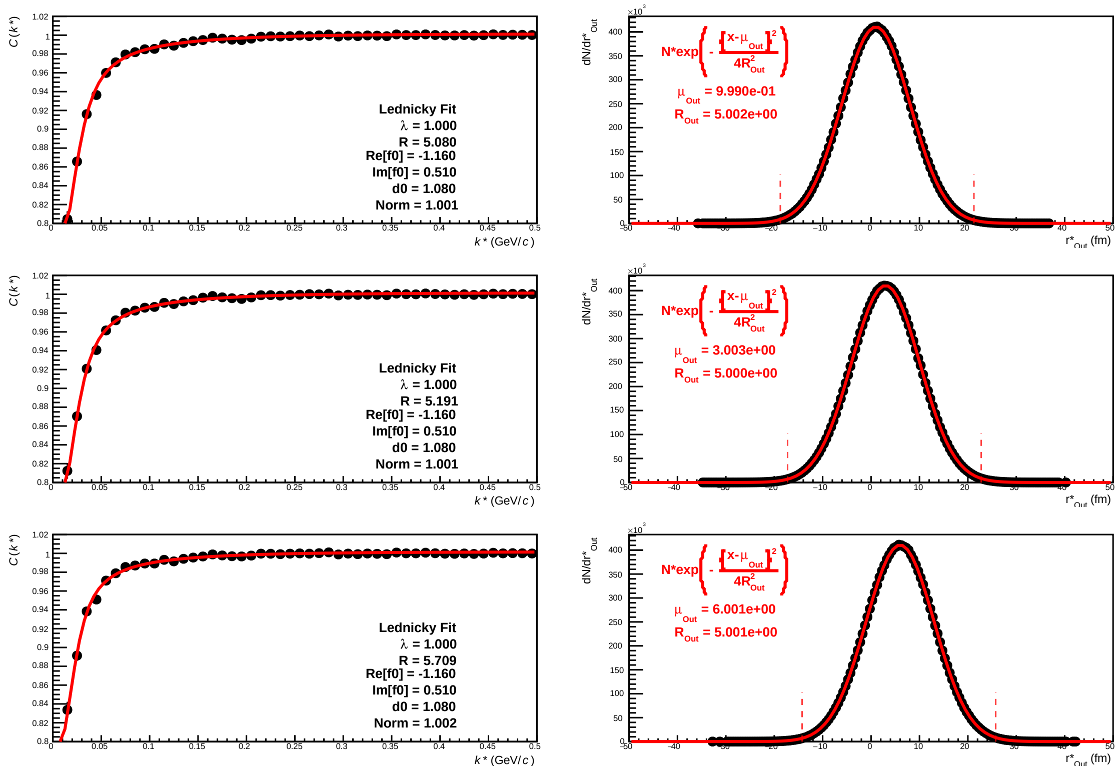

Figure 7.15: Probing the effect of varying the source shift in the outward direction, $\mu_{\rm Out}$, within the THERMINATOR 2 with artificial Gaussian source; the components of the spatial separation for each pair were drawn from Gaussian distributions, with $\sigma_{\rm o,s,l} = 5$ fm, $\mu_{\rm s,l} = 0$ fm, and $\mu_{\rm o} = 0$ fm (top), 3 fm (middle), and 6 fm (bottom). The separation of emission in time was taken to be zero for all. The plots on the left show simple fits corresponding to the adjacent source on the right (the side and long directions are not shown).

Gaussian is given in Eq. 4.43, and reproduced here for convenience.

$$\begin{aligned} S_{AB}(\mathbf{r}) \propto & \exp\left(-\frac{[r_{\rm out} - (\mu_{a,\rm out} - \mu_{b,\rm out})]^2}{2(R^2_{a,\rm out} + R^2_{b,\rm out})}\right) \\ & \times \exp\left(-\frac{r^2_{\rm side}}{2(R^2_{a,\rm side} + R^2_{b,\rm side})}\right) \\ & \times \exp\left(-\frac{r^2_{\rm long}}{2(R^2_{a,\rm long} + R^2_{b,\rm long})}\right) \end{aligned} \tag{7.1}$$

which demonstrates $\mu_{ab,\rm out} = \mu_{a,\rm out} - \mu_{b,\rm out}$, and $R^2_{ab,i} = R^2_{a,i} + R^2_{b,i}$. Unfortunately, with a single femtoscopic measurement, the two single-particle source sizes cannot be extracted. However, a method was presented in which the single-particle source sizes can be extracted using three related femtoscopic measurements, which can then be compared to the results extracted from identical particle studies [136]. Note, this method relies on including μ_{out} in the fit, which is currently not possible with our algorithm.

Performing measurements of the systems πK, πp and Kp permits one to extract the single-particle π, K, and p source sizes. In Ref. [136], the author assumed $R_{\mathrm{out}} = R_{\mathrm{side}} = \sigma_f$, $R_{\mathrm{long}} = 1.3\sigma_f$ and $\mu_{\mathrm{side}} = \mu_{\mathrm{long}} = 0$. Furthermore, having reliable estimates of the scattering parameters for the systems, only two fit parameters, σ_f and μ_{out} were left, and easily extracted. Given the fact that $R^2_{ab,i} = R^2_{a,i} + R^2_{b,i}$, for the three systems we therefore have

$$\begin{aligned}
\sigma_f^{\pi\mathrm{K}} &= \sqrt{\sigma_f^{\pi 2} + \sigma_f^{\mathrm{K}2}} \\
\sigma_f^{\pi\mathrm{p}} &= \sqrt{\sigma_f^{\pi 2} + \sigma_f^{\mathrm{p}2}} \\
\sigma_f^{\mathrm{Kp}} &= \sqrt{\sigma_f^{\mathrm{K}2} + \sigma_f^{\mathrm{p}2}}
\end{aligned} \tag{7.2}$$

These three equations can then be solved for the single-particle source sizes

$$\begin{aligned}
\sigma_f^{\pi} &= \sqrt{\left(\sigma_f^{\pi\mathrm{K}2} + \sigma_f^{\pi\mathrm{p}2} - \sigma_f^{\mathrm{Kp}2}\right)/2} \\
\sigma_f^{\mathrm{K}} &= \sqrt{\left(\sigma_f^{\pi\mathrm{K}2} - \sigma_f^{\pi\mathrm{p}2} + \sigma_f^{\mathrm{Kp}2}\right)/2} \\
\sigma_f^{\mathrm{p}} &= \sqrt{\left(-\sigma_f^{\pi\mathrm{K}2} + \sigma_f^{\pi\mathrm{p}2} + \sigma_f^{\mathrm{Kp}2}\right)/2}
\end{aligned} \tag{7.3}$$

These extracted single-particle source sizes can then be compared to those obtained using identical particle femtoscopy to check for consistency. Unfortunately, with our analysis, we are unable to include μ_{out} in our fit, as the ΛK scattering parameters are unknown and must be left as free parameters. Furthermore, as demonstrated with the numerical integration method previously, discriminating between a larger source with $\mu_{\mathrm{out}} = 0$ fm and a smaller source with non-zero μ_{out} is not trivial. Therefore we are unable to utilize a similar type of solution in our analysis.

7.2 Results: $\Xi K^{\pm}$

The motivation for studying the $\Xi^- K^{\pm}$ system was to investigate the striking difference in the ΛK^+ and ΛK^- correlation functions, as shown explicitly in Fig. 7.16 (originally presented in Sec. 5.7.1, and reproduced here for convenience). Within the femtoscopic framework presented in Section 4, it is clear that there are two important components affecting the femtoscopic signal: the pair emission source distribution, and the interaction between the particles in the pairs. We expect the pair source distribution for ΛK^+ pairs to be similar to that of ΛK^- pairs, therefore, the difference in the femtoscopic signals must be due to a difference in their interactions. As experimentalists, we seek to better understand the ΛK results through the study of the $\Xi^- K^{\pm}$ system. We hope that our ΛK results will motivate the theoretical community to perform for detailed calculations of this system.

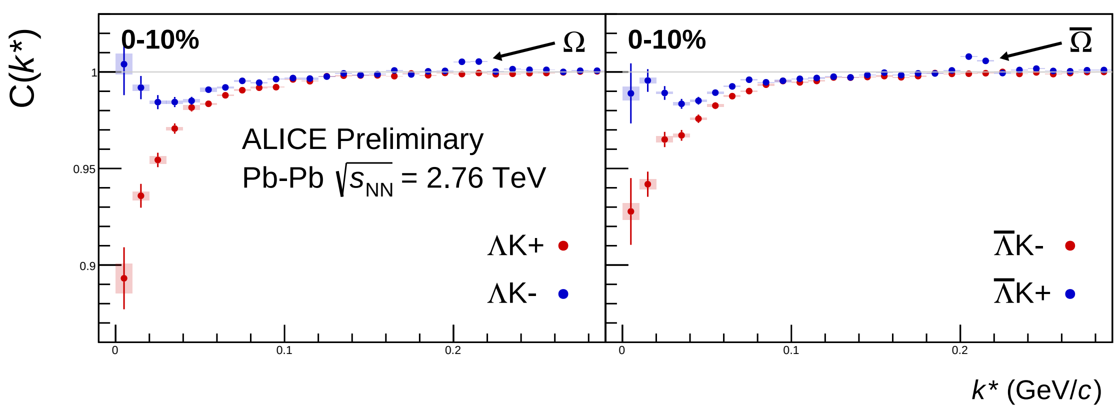

Figure 7.16: Correlation Functions: ΛK^+ vs ΛK^- ($\bar{\Lambda} K^+$ vs $\bar{\Lambda} K^-$) for 0–10% centrality. The peak in ΛK^-($\bar{\Lambda} K^+$) at $k^* \approx 0.2$ GeV/c is due to the Ω^- (and likely the $\Xi(1690)$ resonance, although to a much smaller extent). The lines represent the statistical errors, while boxes represent systematic errors.

Simply, we understand that the observed difference in the femtoscopic signals is due to a difference in the strong interaction in ΛK^+ pairs compared to that in ΛK^- pairs; our extracted scattering parameters demonstrate that. The interesting question to ask is, why does the strong interaction differ so significantly between the two systems? The result could suggest an effect arising from different quark-antiquark interactions between the pairs, i.e. $s\bar{s}$ for ΛK$^+$ and $u\bar{u}$ in ΛK$^-$. This effect could also result from the difference in net strangeness for each system, S=0 for ΛK$^+$ and S=-2 for ΛK$^-$, dictating the available decay channels for each. More specifically, it is possible that a system with less strangeness has more available channels into which it can decay, causing a scarcity of pairs, i.e. a greater suppression, of the correlation function at low k^*. However, such an effect should manifest itself in the imaginary component of the scattering length, $\Im f_0$, not the real component, $\Re f_0$.

In any case, to help find an explanation for this result, it is useful to study another system which we might expect to exhibit similar effects. The Ξ^0K$^\pm$ system is an ideal candidate, as the quark content of the Ξ^0 is *uss*, and therefore studying such correlations would allow for the investigation of the $s\bar{s}$ vs. $u\bar{u}$ quark-antiquark picture. However, the Ξ^0 unfortunately decays as $\Xi^0 \rightarrow \Lambda\pi^0$, and neutral pions are difficult to detect. The next best option is the Ξ^-K$^\pm$ system, as the Ξ^- has quark content *dss*. In this case, we are not able to explore the $s\bar{s}$ vs. $u\bar{u}$ picture, but we are able to investigate $s\bar{s}$ vs. the absence of any $q\bar{q}$ interaction. Furthermore, although the net strangeness in the systems here are different than those in the ΛK$^\pm$ systems (S=−1,−3 instead of S=0,−2), studying Ξ^-K$^\pm$ does allow us to explore the effect of different net strangeness in similar systems. So, in comparing the Ξ^-K$^\pm$ and ΛK$^\pm$ systems, Ξ^-K$^+$ (S=−1, $s\bar{s}$ picture) is analogous to ΛK$^+$ (S=0, $s\bar{s}$ picture), and Ξ^-K$^+$ (S=−3, absence of $q\bar{q}$ picture) is analogous to ΛK$^-$ (S=−2, $u\bar{u}$ picture).

Figure 7.17 presents experimental data from our femtoscopic analysis of Ξ^-K$^\pm$ pairs, along with the conjugate $\overline{\Xi}^+$K$^\pm$ systems. Even without any fits to the data, the fact that the Ξ^-K$^+$ data dips below unity (Fig. 7.17) is exciting, as this cannot occur from a purely Coulomb interaction. We hope that this dip signifies that we are able to peer through the overwhelming contribution from the Coulomb interaction to see the effects arising from the strong interaction.

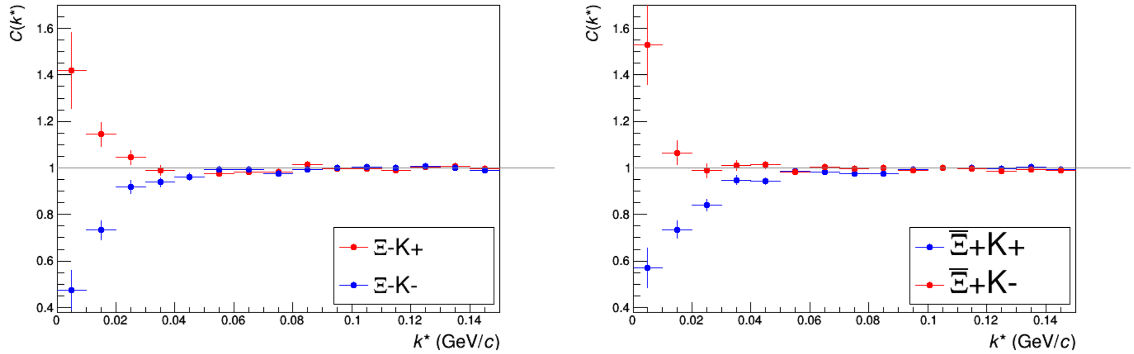

Figure 7.17: $\Xi K^{\pm}$ Results for 0–10% Centrality. (Left) $\Xi^- K^+$ and $\Xi^- K^-$ (Right) $\overline{\Xi}^+ K^+$ and $\overline{\Xi}^+ K^-$

Figure 7.18 demonstrates that the $\Xi^- K^+$ results cannot be described by solely the Coulomb interaction. In this figure, we present the data along with a Coulomb-only band. The Coulomb-only band is spanned by two Coulomb-only curves, whose parameters are given in the figure. The Coulomb-only curves are generated using a technique identical to the generation of the fit function, described in Sec. 6.5, except, of course, with the nuclear scattering parameters all set to zero. The Coulomb-only curves change monotonically with varying λ and with varying radius parameters, therefore, any curves built with parameter sets intermediate to those used in the Coulomb-only band will be contained within the band.

Including the strong interaction into the simulation can change, sometimes dramatically, the resulting correlation function, as shown in Figure 7.19. In the figure, the solid line represents a Coulomb-only curve, i.e. a simulated correlation function with the strong interaction turned off. The dashed lines represent a full simulation, including both the strong and Coulomb interactions. The two dashed lines differ only in the real part of the assumed scattering length: positive $\Re f_0$ in Set 1, and negative $\Re f_0$ in Set 2. In the top figure, for the $\Xi^- K^+$ simulation, we see that both parameter sets lead to a dip below unity. However, the negative $\Re f_0$ of parameter Set 2 causes the simulated curve to dip below unity in a manner more closely matching that of

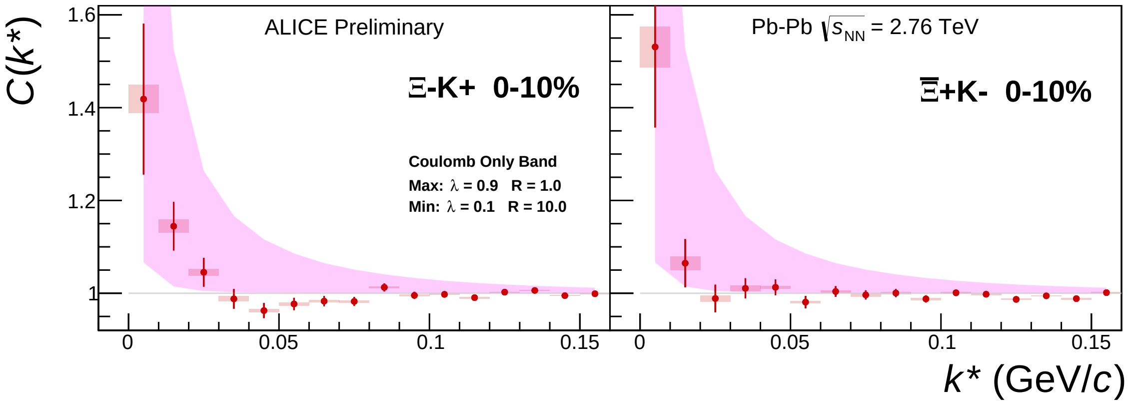

(a) (Left) $\Xi^{-}K^{+}$ and (Right) $\overline{\Xi}^{+}K^{-}$

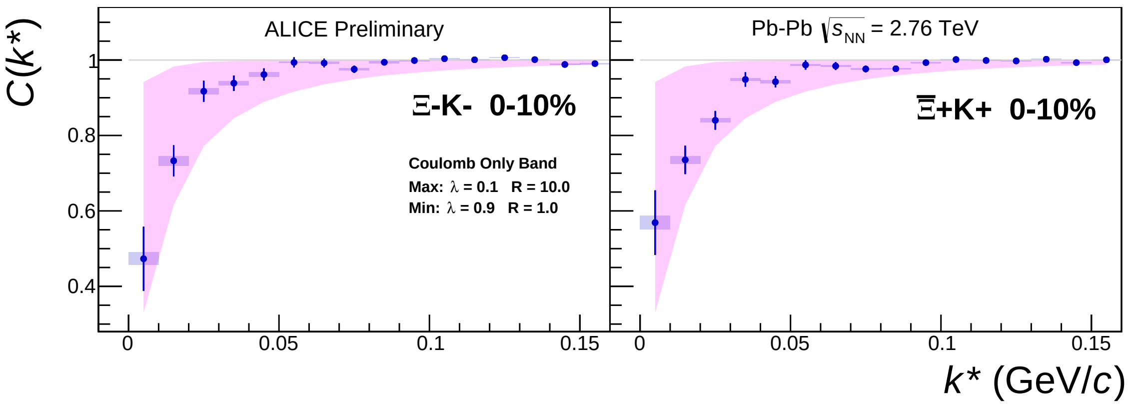

(b) (Left) $\Xi^{-}K^{-}$ and (Right) $\overline{\Xi}^{+}K^{+}$

Figure 7.18: $\Xi K^{\pm}$ data with Coulomb-only bands for the 0–10% centrality bin. The Coulomb-only bands span two sets of Coulomb-only curves: (1) $\lambda = 0.9$, R = 1.0 fm and (2) $\lambda = 0.1$, R = 10.0 fm.

the data. For our ΛK^{+} system, we extracted a negative value of $\Re f_0$, and, as stated previously, if there is a parallel to be drawn between this analysis and the $\Lambda K^{\pm}$ analysis, we expect to see similar effects in the ΛK^{+} system and the $\Xi^{-}K^{+}$ systems. So, this simulation at least moves in the correct direction. However, no real conclusions can be drawn until the fit algorithm is optimized, and a precise fit is performed.

We were asked to perform a global Coulomb-only fit to the data, to ensure that the system truly could not be described simply by the Coulomb interaction. In other words, in the fit, the strong force was turned off, and the $\Xi^{-}K^{+}$, $\overline{\Xi}^{+}K^{-}$, $\Xi^{-}K^{-}$,

$\overline{\Xi}^{+}K^{+}$ systems all share one single radius parameter, while the pair and conjugate pair systems share a λ parameter. The results of this fit are shown in Figures 7.20 and 7.21. In Fig. 7.20, there is a lower limit of 0.1 fm placed on the radius parameter, and the radius parameter is initialized to 3 fm. As is shown in the results, the radius parameter reaches this unrealistic lower bound of 0.1 fm. In Fig. 7.21, the parameters are all unbound, and the radius parameter is initialized to 10 fm. In this case, the radius parameters remains high, and ends at an unrealistic value of 10.84 fm. In both cases, the λ parameters are too low. From these figures, we conclude that a global Coulomb-only fit does not provide a sensible description of the data.

Although the global Coulomb-only fit failed, it is possible that a Coulomb-only fit performed on $\Xi^{-}K^{+}$ and $\overline{\Xi}^{+}K^{-}$ separately from $\Xi^{-}K^{-}$ and $\overline{\Xi}^{+}K^{+}$ could be suitable. The result of such fits are shown in Figure 7.22. Figure 7.22a, shows that the fit is not able to describe the dip in the $\Xi^{-}K^{+}$ data below unity. Of course, this is obviously true for an attractive Coulomb-only fit. The radius parameter of 8.43 fm extracted from this fit is probably too large to describe reality. Figure 7.22b shows the Coulomb-only fit can describe the $\Xi^{-}K^{-}$ data reasonably well. When considering Fig. 7.16, this is not terribly surprising, as the strong effect in the ΛK^{-} (analogous to $\Xi^{-}K^{-}$) is much weaker than that in the ΛK^{+} system (analogous to $\Xi^{-}K^{+}$). In any case, we would expect for the $\Xi^{-}K^{+}$ and $\Xi^{-}K^{-}$ systems to be consistent with each other in their radii, and those extracted from these fits are not.

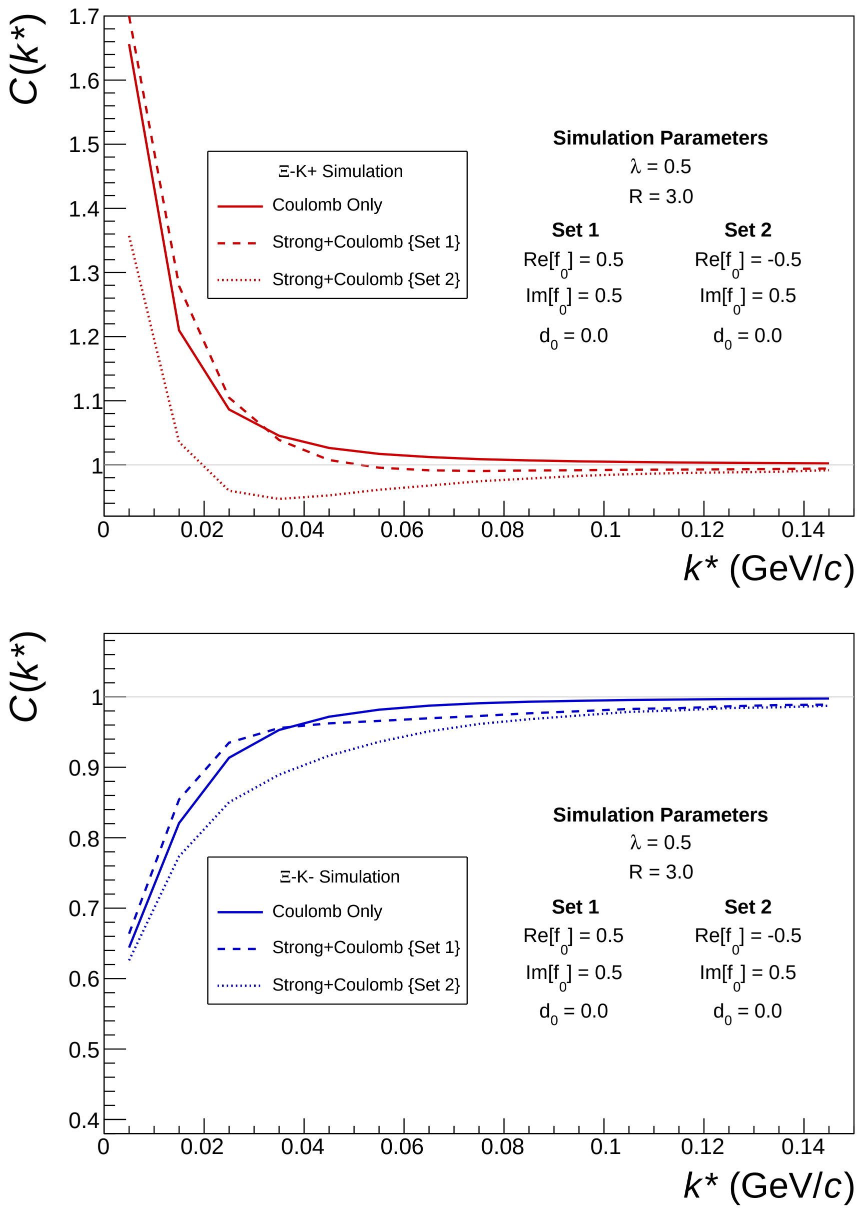

Figure 7.19: Effect on the Coulomb-only curve of including the strong interaction for $\Xi K^{\pm}$ systems. The solid line represents a Coulomb-only curve. The dashed lines represent a full simulation, including both the strong and Coulomb interactions. The two dashed lines differ only in the real part of the assumed scattering length: positive in Set 1, and negative in Set 2.

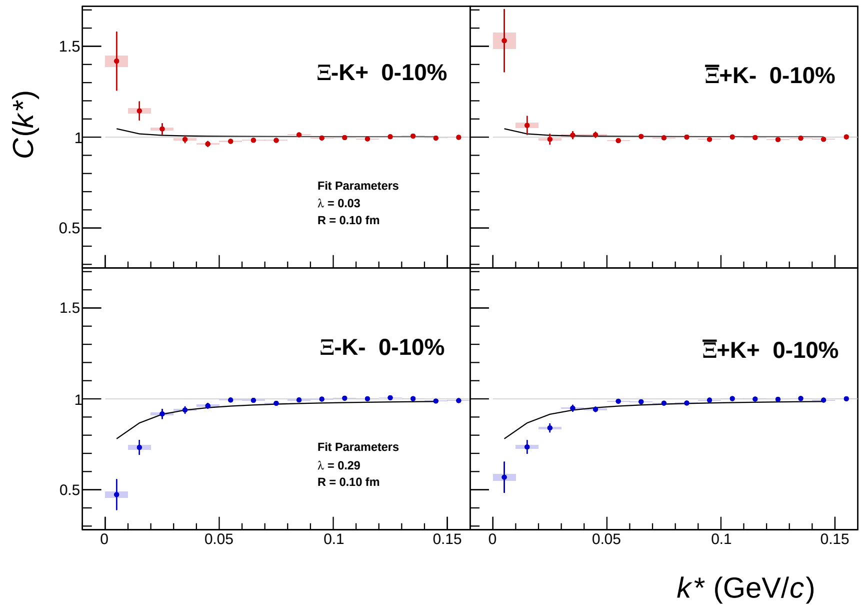

Figure 7.20: ΞK$^{\pm}$ Global Coulomb-only fit (Set 1) for 0–10% centrality. In this fit, there was a lower limit of 0.1 fm placed on the radius parameter, and the radius parameter was initialized to 3 fm.

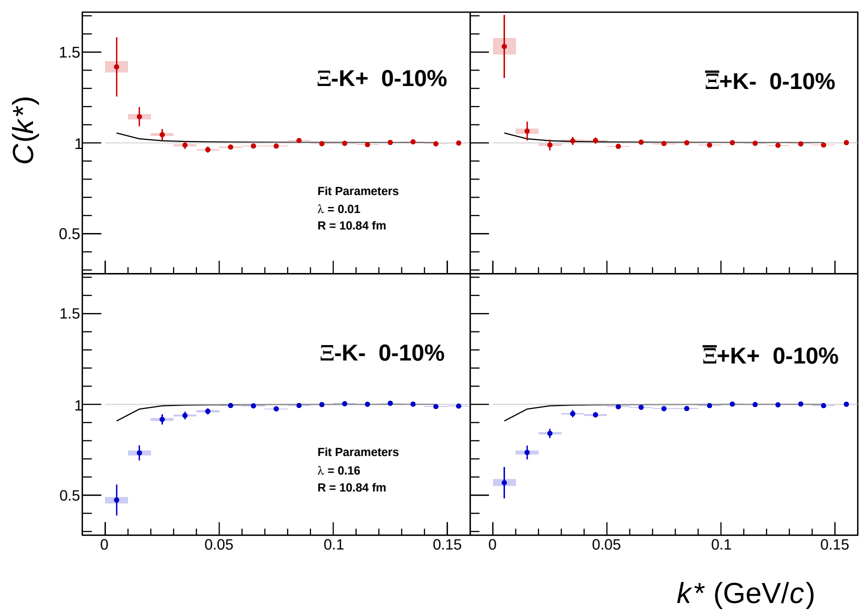

Figure 7.21: ΞK$^{\pm}$ Global Coulomb-only fit (Set 2) for 0–10% centrality. In this fit, the parameters were all unbounded, and the radius parameter was initialized to 10 fm.

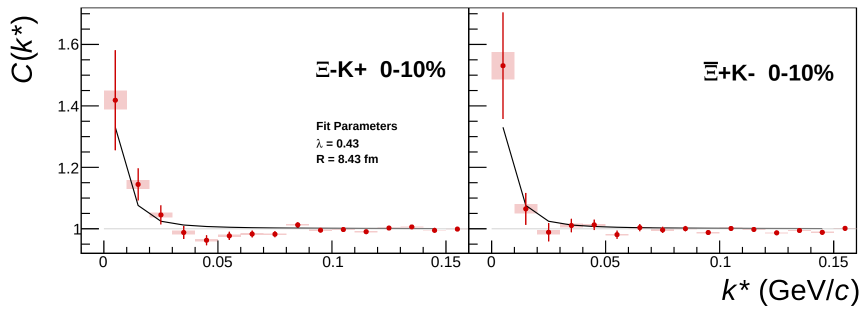

(a) $\Xi^{-}K^{+}$ Coulomb-only fit for 0–10% centrality

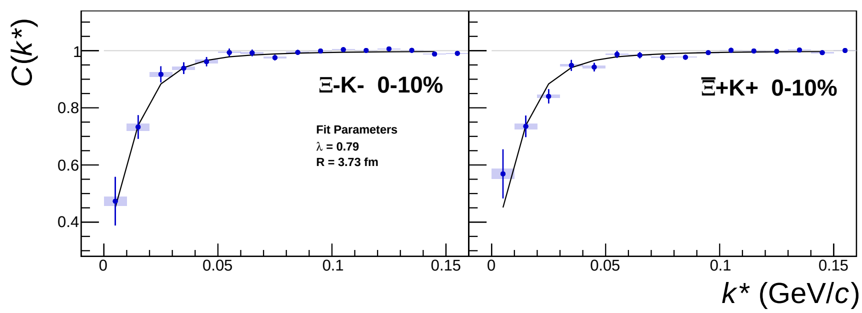

(b) $\Xi^{-}K^{-}$ Coulomb-only fit for 0–10% centrality

Figure 7.22: $\Xi^{-}K^{\pm}$ Coulomb-only fit, with $\Xi^{-}K^{+}$ fit separately from $\Xi^{-}K^{-}$

Chapter 8: Conclusion

In this thesis, we presented a femtoscopic analysis of ΛK correlations in Pb-Pb collisions at $\sqrt{s_{\mathrm{NN}}} = 2.76$ TeV with ALICE at the LHC. Through the femtoscopic method, we measured the scattering parameters of ΛK pairs in all three charge combinations (ΛK^{+}, ΛK^{-}, and ΛK$^{0}_{\mathrm{S}}$) for the first time. The striking difference observed between the ΛK^{+} and ΛK^{-} correlation functions is reflected in their unique scattering parameters. In particular, the ΛK^{+} system exhibits a negative $\Re(f_0)$, while that extracted from the ΛK^{-} system is positive. This implies that the strong interaction is repulsive in the ΛK^{+} system and attractive for the ΛK^{-} (and ΛK$^{0}_{\mathrm{S}}$). Before this measurement, little was known about the ΛK interaction experimentally, and theoretical calculations remain sparse. The ΛK analysis presented here offers low energy QCD measurements, which fall into the notoriously difficult non-perturbative regime. Therefore, the ΛK measurements presented here not only give insight into the strong interaction, they will also help guide future QCD calculations.

We also introduced preliminary results from a Ξ^{-}K$^{\pm}$ femtoscopic analysis, whose initial motivation was the help explain the interesting different between the ΛK^{+} and ΛK^{-} results. The system proved difficult to fit, due to the complications added by the inclusion of the Coulomb interaction. More computationally advanced techniques will need to be utilized in order to model the system, and the development of such techniques was ultimately deemed outside of the scope of this dissertation. Nonetheless, the Ξ^{-}K$^{\pm}$ system remains intriguing, and should be further studied in the future.

The model used to fit the ΛK correlation functions, as developed by Lednický and Lyuboshitz, was presented. The model accounts for particle interactions with an s-wave scattering parametrization of the two-particle wave-function, with an incoming plane wave and an outgoing spherical wave. In the effective range approximation, the complex scattering amplitude is described in terms of the scattering length f_0 and effective range of the interaction d_0. The models assumes the pair source distribution to be a spherically symmetric Gaussian with no offsets (i.e. $R_{\text{out}} = R_{\text{side}} = R_{\text{long}}$ and $\mu_{\text{out}} = \mu_{\text{side}} = \mu_{\text{long}} = 0$). When only quantum statistical and strong final state interaction effects are present, these assumptions allow for the correlation function to be calculated analytically.

Moving forward, a more accurate pair source distribution should be implemented. Instead of modeling with a spherically symmetric Gaussian source, the radii in the "out", "side", and "long" directions should be allowed to differ. Forcing the pair source distribution to exhibit no offset is a good approximation for identical particle studies, where the centers of the two single-particle sources coincide. However, when studying non-identical particle pairs, this approximation becomes less valid. In this case, the two single-particle sources differ both in their space-time positions within the fireball and in their sizes. This is due to the hydrodynamic response of the system, which confines higher-m_{T} particles to smaller homogeneity regions and also pushes their average emission point further in the "out" direction. Through the spherical decomposition of our ΛK correlation functions, we demonstrated that the Λ hyperons are emitted further out and/or earlier than the K mesons. This effect should be accounted for in future fits

The assumption of a spherically symmetric Gaussian source with no offsets in the model resulted in ΛK radii larger than expected from trends set forth in identical particle femtoscopic analyses. Using the THERMINATOR 2 simulation, as well as a numerical integration method, we demonstrated that an offset in the "out" direction results in larger extracted radii within our one-dimensional model. However, even if offsets are permitted in the fit procedure, one should not expect the non-identical particle radii to coincide simply with the trends from identical particle studies. One should, however, expect the single-particle distributions to follow the same trends in either case. For identical particle studies, the extraction of the single-particle source sizes amounts to dividing the pair source radii by a factor of $\sqrt{2}$. For non-identical particle studies, the situation is not as simple. Without any shift in the source, the two-particle radii are obtained as the sum in quadrature of the single-particle radii. Using single-particle radii obtained from previous identical particle studies, the ΛK radii expected in the absence of any shift fell below our extracted radii; a shift in the pair-source is obviously present. When including the appropriate outward shift in the sources, the use of three related femtoscopic measurements can be exploited to extract the single-particle sizes. This was introduced Ref. [136], where πK, πp, and Kp measurements from simulation were used to extract single-particle π, K, and p source sizes.

Unfortunately, the inclusion of the outward shift was not possible for the measurements presented in this thesis. In Ref [136], the πK, πp, and Kp scattering parameters are well known, and could be kept constant during the fit procedure. The ΛK interactions before this work were not known at all, and therefore had to be left as free parameters during the fit. Additionally, the inclusion of an outward shift causes the representation of the correlation function to no longer be analytical, and many of the same computational obstacles suffered in modeling the $\Xi^{-}K^{\pm}$ emerge. Overcoming such obstacles was outside of the scope of this study, and our extracted radii are instead interpreted as effective pair source radii, whose larger than expected value reflect the shift in the outward direction. In the future, the shift in the source should be included in the model. In such a case, the scattering parameters extracted from this analysis may be used, and both the pair-source radii and outward offset can be extracted from the fit. The two-particle radii can then be used, as in Ref. [136], to extract the single-particle source sizes, and to check for consistency amongst the various femtoscopic measurement and within the hydrodynamic picture.

We performed extensive studies with the THERMINATOR 2 and HIJING event generators to account for contributions from residual correlations induced by feed-down from resonances. We found that, in addition to primary pairs, our ΛK pairs originate from a large number of parent systems. We also explained that, in the eyes of femtoscopy, which is sensitive to the source at kinetic freeze-out, the primary categorization also include pairs with a particle born from a parent resonance decaying before last hadronic rescattering. The primary component, contributions from residuals, and contributions from pairs containing one or more misidentified particles, were combined in the fit procedure. The THERMINATOR 2 simulation was useful in estimating the yields of ΛK pairs resulting from various parent systems, which were used in the calculation of the λ_{ij} parameters controlling the relative strength of different component contributions in the fit. The THERMINATOR 2 simulation was further utilized for the generation of transform matrices, which were necessary for calculating the contributions from the residuals to the ΛK correlation functions. The HIJING model was used to estimate the reconstruction efficiencies for ΛK pairs originating from the various components. This was used together with the yields from THERMINATOR 2 to calculate the λ_{ij} parameters.

In this thesis, we used the THERMINATOR 2 simulation to help explain the observed non-femtoscopic background in our correlation functions. We found that the simulation does an excellent job in describing the data. The majority of the background originates due to elliptic flow together with the mixing of events with unlike event-planes in construction of the reference distribution. More specifically, when elliptic flow is present, particles are more likely to be emitted in-plane, and the difference in momenta between pairs of particles tends to be smaller. In the case of mixed-event pairs with unlike event-planes, the collimation effect is absent, and pairs with larger momentum difference are relatively more likely. As a result, the elliptic flow causes an enhancement at low-k^*, followed by a suppression. Due to limited event-plane resolution, binning our events in Ψ_{EP} was not able to rid the correlation functions of the non-femtoscopic background. The THERMINATOR 2 model also revealed that the non-femtoscopic background affects the observed correlation function as a separable scale factor. This fact was exploited in the modeling of the background in our fit procedure. We also demonstrated the effect of utilizing the Stavinskiy method to reduce the observed background. With this method, instead of using mixed-event pairs for the reference distribution, same-event pseudo-pairs are used, which are formed by rotating one particle in a real (same-event) pair by 180° in the transverse plane. This method was shown to be effective in reducing the background both in the data and in the THERMINATOR 2 simulation.

We are currently in the process of publishing the results from the ΛK analysis presented in this dissertation.

References

[1] Edward V. Shuryak. "Quark-Gluon Plasma and Hadronic Production of Leptons, Photons and Psions". *Phys. Lett.* 78B (1978). [Yad. Fiz.28,796(1978)], p. 150. DOI: 10.1016/0370-2693(78)90370-2.

[2] J. C. Collins and M. J. Perry. "Superdense Matter: Neutrons or Asymptotically Free Quarks?" *Phys. Rev. Lett.* 34 (21 1975), pp. 1353–1356. DOI: 10.1103/PhysRevLett.34.1353. URL: https://link.aps.org/doi/10.1103/PhysRevLett.34.1353.

[3] I. Arsene et al. "Quark gluon plasma and color glass condensate at RHIC? The Perspective from the BRAHMS experiment". *Nucl. Phys.* A757 (2005), pp. 1–27. DOI: 10.1016/j.nuclphysa.2005.02.130. arXiv: nucl-ex/0410020 [nucl-ex].

[4] B. B. Back et al. "The PHOBOS perspective on discoveries at RHIC". *Nucl. Phys.* A757 (2005), pp. 28–101. DOI: 10.1016/j.nuclphysa.2005.03.084. arXiv: nucl-ex/0410022 [nucl-ex].

[5] John Adams et al. "Experimental and theoretical challenges in the search for the quark gluon plasma: The STAR Collaboration's critical assessment of the evidence from RHIC collisions". *Nucl. Phys.* A757 (2005), pp. 102–183. DOI: 10.1016/j.nuclphysa.2005.03.085. arXiv: nucl-ex/0501009 [nucl-ex].

[6] K. Adcox et al. "Formation of dense partonic matter in relativistic nucleus-nucleus collisions at RHIC: Experimental evaluation by the PHENIX collaboration". *Nucl. Phys.* A757 (2005), pp. 184–283. DOI: 10.1016/j.nuclphysa.2005.03.086. arXiv: nucl-ex/0410003 [nucl-ex].

[7] Y. Aoki et al. "The Order of the quantum chromodynamics transition predicted by the standard model of particle physics". *Nature* 443 (2006), pp. 675–678. DOI: 10.1038/nature05120. arXiv: hep-lat/0611014 [hep-lat].

[8] A. Bazavov et al. "Equation of state in (2+1)-flavor QCD". *Phys. Rev.* D90 (2014), p. 094503. DOI: 10.1103/PhysRevD.90.094503. arXiv: 1407.6387 [hep-lat].

[9] Francois Gelis and Bjoern Schenke. "Initial State Quantum Fluctuations in the Little Bang". *Ann. Rev. Nucl. Part. Sci.* 66 (2016), pp. 73–94. DOI: 10.1146/annurev-nucl-102115-044651. arXiv: 1604.00335 [hep-ph].

[10] Betty Abelev et al. "Centrality determination of Pb-Pb collisions at $\sqrt{s_{\mathrm{NN}}} =$ 2.76 TeV with ALICE". *Phys. Rev.* C88.4 (2013), p. 044909. DOI: 10.1103/PhysRevC.88.044909. arXiv: 1301.4361 [nucl-ex].

[11] Michael L. Miller et al. "Glauber modeling in high energy nuclear collisions". *Ann. Rev. Nucl. Part. Sci.* 57 (2007), pp. 205–243. DOI: 10.1146/annurev.nucl.57.090506.123020. arXiv: nucl-ex/0701025 [nucl-ex].

[12] Betty Bezverkhny Abelev et al. "Performance of the ALICE Experiment at the CERN LHC". *Int. J. Mod. Phys.* A29 (2014), p. 1430044. DOI: 10.1142/S0217751X14300440. arXiv: 1402.4476 [nucl-ex].

[13] B. Alver et al. "The PHOBOS Glauber Monte Carlo" (2008). arXiv: 0805.4411 [nucl-ex].

[15] Kenneth Aamodt et al. "Centrality dependence of the charged-particle multiplicity density at mid-rapidity in Pb-Pb collisions at $\sqrt{s_{\mathrm{NN}}} = 2.76$ TeV". *Phys. Rev. Lett.* 106 (2011), p. 032301. DOI: 10.1103/PhysRevLett.106.032301. arXiv: 1012.1657 [nucl-ex].

[16] Georges Aad et al. "Measurement of the centrality dependence of the charged particle pseudorapidity distribution in lead-lead collisions at $\sqrt{s_{\mathrm{NN}}} = 2.76$ TeV with the ATLAS detector". *Phys. Lett.* B710 (2012), pp. 363–382. DOI: 10.1016/j.physletb.2012.02.045. arXiv: 1108.6027 [hep-ex].

[17] Serguei Chatrchyan et al. "Dependence on pseudorapidity and centrality of charged hadron production in PbPb collisions at a nucleon-nucleon centre-of-mass energy of 2.76 TeV". *JHEP* 08 (2011), p. 141. DOI: 10.1007/JHEP08(2011)141. arXiv: 1107.4800 [nucl-ex].

[18] M.C. Abreu et al. "Scaling of charged particle multiplicity in PbPb collisions at SPS energies". *Physics Letters B* 530.1 (2002), pp. 43 –55. ISSN: 0370-2693. DOI: https://doi.org/10.1016/S0370-2693(02)01353-9. URL: http://www.sciencedirect.com/science/article/pii/S0370269302013539.

[19] I. G Bearden et al. "Charged particle densities from Au+Au collisions at $\sqrt{s_{\mathrm{NN}}}$ = 130 GeV". *Phys. Lett.* B523 (2001), pp. 227–233. DOI: 10.1016/S0370-2693(01)01333-8. arXiv: nucl-ex/0108016 [nucl-ex].

[20] I. G. Bearden et al. "Pseudorapidity distributions of charged particles from Au+Au collisions at the maximum RHIC energy". *Phys. Rev. Lett.* 88 (2002),

p. 202301. DOI: 10.1103/PhysRevLett.88.202301. arXiv: nucl-ex/0112001 [nucl-ex].

[21] K. Adcox et al. “Centrality dependence of charged particle multiplicity in Au-Au collisions at $\sqrt{s_{\rm NN}} = 130$ GeV”. *Phys. Rev. Lett.* 86 (2001), pp. 3500–3505. DOI: 10.1103/PhysRevLett.86.3500. arXiv: nucl-ex/0012008 [nucl-ex].

[22] B. Alver et al. “Phobos results on charged particle multiplicity and pseudorapidity distributions in Au+Au, Cu+Cu, d+Au, and p+p collisions at ultra-relativistic energies”. *Phys. Rev.* C83 (2011), p. 024913. DOI: 10.1103/PhysRevC.83.024913. arXiv: 1011.1940 [nucl-ex].

[23] B. I. Abelev et al. “Systematic Measurements of Identified Particle Spectra in $pp, d+$ Au and Au+Au Collisions from STAR”. *Phys. Rev.* C79 (2009), p. 034909. DOI: 10.1103/PhysRevC.79.034909. arXiv: 0808.2041 [nucl-ex].

[24] Jaroslav Adam et al. “Charged-particle multiplicities in protonproton collisions at $\sqrt{s} = 0.9$ to 8 TeV”. *Eur. Phys. J.* C77.1 (2017), p. 33. DOI: 10.1140/epjc/s10052-016-4571-1. arXiv: 1509.07541 [nucl-ex].

[25] V. Khachatryan et al. “Pseudorapidity distribution of charged hadrons in protonproton collisions at $\sqrt{s} = 13$TeV”. *Physics Letters B* 751 (2015), pp. 143 –163. ISSN: 0370-2693. DOI: https://doi.org/10.1016/j.physletb.2015.10.004. URL: http://www.sciencedirect.com/science/article/pii/S0370269315007558.

[26] J. Adam et al. “Pseudorapidity and transverse-momentum distributions of charged particles in protonproton collisions at $\sqrt{s} = 13$TeV”. *Physics Letters B* 753 (2016), pp. 319 –329. ISSN: 0370-2693. DOI: https://doi.org/10.1016/j.physletb.2015.12.030. URL: http://www.sciencedirect.com/science/article/pii/S0370269315009788.

[27] B. Abelev et al. “Pseudorapidity Density of Charged Particles in p+Pb Collisions at $\sqrt{s_{\rm NN}}$=5.02 TeV”. *Phys. Rev. Lett.* 110 (3 2013), p. 032301. DOI: 10.1103/PhysRevLett.110.032301. URL: https://link.aps.org/doi/10.1103/PhysRevLett.110.032301.

[28] B. B. Back et al. “Pseudorapidity distribution of charged particles in d + Au collisions at $\sqrt{s_{\rm NN}} = 200$ GeV”. *Phys. Rev. Lett.* 93 (2004), p. 082301. DOI: 10.1103/PhysRevLett.93.082301. arXiv: nucl-ex/0311009 [nucl-ex].

[14] Jaroslav Adam et al. “Centrality dependence of the charged-particle multiplicity density at midrapidity in Pb-Pb collisions at $\sqrt{s_{\rm NN}} = 5.02$ TeV”. *Phys. Rev. Lett.* 116.22 (2016), p. 222302. DOI: 10.1103/PhysRevLett.116.222302. arXiv: 1512.06104 [nucl-ex].

[29] J. D. Bjorken. “Highly Relativistic Nucleus-Nucleus Collisions: The Central Rapidity Region”. *Phys. Rev.* D27 (1983), pp. 140–151. DOI: 10.1103/PhysRevD.27.140.

[30] Jaroslav Adam et al. “Measurement of transverse energy at midrapidity in Pb-Pb collisions at $\sqrt{s_{\mathrm{NN}}} = 2.76$ TeV”. *Phys. Rev.* C94.3 (2016), p. 034903. DOI: 10.1103/PhysRevC.94.034903. arXiv: 1603.04775 [nucl-ex].

[34] Serguei Chatrchyan et al. “Measurement of the pseudorapidity and centrality dependence of the transverse energy density in PbPb collisions at $\sqrt{s_{\mathrm{NN}}} = 2.76$ TeV”. *Phys. Rev. Lett.* 109 (2012), p. 152303. DOI: 10.1103/PhysRevLett.109.152303. arXiv: 1205.2488 [nucl-ex].

[31] S. S. Adler et al. “Systematic studies of the centrality and $\sqrt{s_{\mathrm{NN}}}$ dependence of the $dE_{\mathrm{T}}/d\eta$ and $dN_{\mathrm{ch}}/d\eta$ in heavy ion collisions at mid-rapidity”. *Phys. Rev.* C71 (2005). [Erratum: Phys. Rev.C71,049901(2005)], p. 034908. DOI: 10.1103/PhysRevC.71.049901,10.1103/PhysRevC.71.034908. arXiv: nucl-ex/0409015 [nucl-ex].

[32] K. J. Eskola et al. “Scaling of transverse energies and multiplicities with atomic number and energy in ultrarelativistic nuclear collisions”. *Nucl. Phys.* B570 (2000), pp. 379–389. DOI: 10.1016/S0550-3213(99)00720-8. arXiv: hep-ph/9909456 [hep-ph].

[33] Thorsten Renk et al. “Systematics of the charged-hadron P_T spectrum and the nuclear suppression factor in heavy-ion collisions from $\sqrt{s_{\mathrm{NN}}} = 200$ GeV to $\sqrt{s_{\mathrm{NN}}} = 2.76$ TeV”. *Phys. Rev.* C84 (2011), p. 014906. DOI: 10.1103/PhysRevC.84.014906. arXiv: 1103.5308 [hep-ph].

[35] J. Adams et al. “Measurements of transverse energy distributions in Au + Au collisions at $\sqrt{s_{\mathrm{NN}}} = 200$ GeV”. *Phys. Rev.* C70 (2004), p. 054907. DOI: 10.1103/PhysRevC.70.054907. arXiv: nucl-ex/0407003 [nucl-ex].

[36] A. Adare et al. “Transverse energy production and charged-particle multiplicity at midrapidity in various systems from $\sqrt{s_{\mathrm{NN}}} = 7.7$ to 200 GeV”. *Phys. Rev.* C93.2 (2016), p. 024901. DOI: 10.1103/PhysRevC.93.024901. arXiv: 1509.06727 [nucl-ex].

[37] Ulrich W. Heinz. “Concepts of heavy ion physics”. *2002 European School of high-energy physics, Pylos, Greece, 25 Aug-7 Sep 2002: Proceedings.* 2004, pp. 165–238. arXiv: hep-ph/0407360 [hep-ph]. URL: http://doc.cern.ch/yellowrep/CERN-2004-001.

[38] Ulrich Heinz and Raimond Snellings. "Collective flow and viscosity in relativistic heavy-ion collisions". *Ann. Rev. Nucl. Part. Sci.* 63 (2013), pp. 123–151. DOI: 10.1146/annurev-nucl-102212-170540. arXiv: 1301.2826 [nucl-th].

[39] Ekkard Schnedermann, Josef Sollfrank, and Ulrich W. Heinz. "Thermal phenomenology of hadrons from 200-A/GeV S+S collisions". *Phys. Rev.* C48 (1993), pp. 2462–2475. DOI: 10.1103/PhysRevC.48.2462. arXiv: nucl-th/9307020 [nucl-th].

[40] K. Yagi, T. Hatsuda, and Y. Miake. *Quark-Gluon Plasma*. Cambridge: Cambridge University Press, 2005.

[41] S. Esumi et al. "Transverse flow at ultrarelativistic energies". *Phys. Rev. C* 55 (5 1997), R2163–R2166. DOI: 10.1103/PhysRevC.55.R2163. URL: https://link.aps.org/doi/10.1103/PhysRevC.55.R2163.

[42] Jerzy Bartke. *Introduction to relativistic heavy ion physics*. 2009.

[43] Betty Abelev et al. "Centrality dependence of π, K, p production in Pb-Pb collisions at $\sqrt{s_{\mathrm{NN}}} = 2.76$ TeV". *Phys. Rev.* C88 (2013), p. 044910. DOI: 10.1103/PhysRevC.88.044910. arXiv: 1303.0737 [hep-ex].

[44] S. S. Adler et al. "Identified charged particle spectra and yields in Au+Au collisions at $\sqrt{s_{\mathrm{NN}}} = 200$ GeV". *Phys. Rev.* C69 (2004), p. 034909. DOI: 10.1103/PhysRevC.69.034909. arXiv: nucl-ex/0307022 [nucl-ex].

[45] Ulrich W. Heinz. "Strange messages: Chemical and thermal freezeout in nuclear collisions". *J. Phys.* G25 (1999), pp. 263–274. DOI: 10.1088/0954-3899/25/2/014. arXiv: nucl-th/9810056 [nucl-th].

[46] Wojciech Florkowski. *Phenomenology of Ultra-Relativistic Heavy-Ion Collisions*. 2010. ISBN: 9789814280662.

[47] A. Andronic et al. "Hadron yields, the chemical freeze-out and the QCD phase diagram". *J. Phys. Conf. Ser.* 779.1 (2017), p. 012012. DOI: 10.1088/1742-6596/779/1/012012. arXiv: 1611.01347 [nucl-th].

[48] Betty Abelev et al. "Pion, Kaon, and Proton Production in Central Pb–Pb Collisions at $\sqrt{s_{\mathrm{NN}}} = 2.76$ TeV". *Phys. Rev. Lett.* 109 (2012), p. 252301. DOI: 10.1103/PhysRevLett.109.252301. arXiv: 1208.1974 [hep-ex].

[49] Betty Bezverkhny Abelev et al. "K^0_S and Λ production in Pb-Pb collisions at $\sqrt{s_{\mathrm{NN}}} = 2.76$ TeV". *Phys. Rev. Lett.* 111 (2013), p. 222301. DOI: 10.1103/PhysRevLett.111.222301. arXiv: 1307.5530 [nucl-ex].

[50] Betty Bezverkhny Abelev et al. "Multi-strange baryon production at mid-rapidity in Pb-Pb collisions at $\sqrt{s_{\mathrm{NN}}} = 2.76$ TeV". *Phys. Lett.* B728 (2014). [Erratum: Phys. Lett.B734,409(2014)], pp. 216–227. DOI: 10.1016/j.physletb.2014.05.052, 10.1016/j.physletb.2013.11.048. arXiv: 1307.5543 [nucl-ex].

[51] Betty Bezverkhny Abelev et al. "$K^*(892)^0$ and (1020) production in Pb-Pb collisions at $\sqrt{s_{\mathrm{NN}}} = 2.76$ TeV". *Phys. Rev.* C91 (2015), p. 024609. DOI: 10.1103/PhysRevC.91.024609. arXiv: 1404.0495 [nucl-ex].

[52] Jaroslav Adam et al. "${}^{3}_{\Lambda}\mathrm{H}$ and ${}^{3}_{\Lambda}\overline{\mathrm{H}}$ production in Pb-Pb collisions at $\sqrt{s_{\mathrm{NN}}} = 2.76$ TeV". *Phys. Lett.* B754 (2016), pp. 360–372. DOI: 10.1016/j.physletb.2016.01.040. arXiv: 1506.08453 [nucl-ex].

[53] Jaroslav Adam et al. "Production of light nuclei and anti-nuclei in pp and Pb-Pb collisions at energies available at the CERN Large Hadron Collider". *Phys. Rev.* C93.2 (2016), p. 024917. DOI: 10.1103/PhysRevC.93.024917. arXiv: 1506.08951 [nucl-ex].

[54] Simone Schuchmann. "Modification of K^0_{S} and $\Lambda(\overline{\Lambda})$ transverse momentum spectra in Pb-Pb collisions at $\sqrt{s_{\mathrm{NN}}} = 2.76$ TeV with ALICE". PhD thesis. New York: Frankfurt U., 2015-04-14. DOI: 10.1007/978-3-319-43458-2. URL: http://www.springer.com/gp/book/9783319434575.

[55] M. M. Aggarwal et al. "Observation of direct photons in central 158 AGeV Pb-208 + Pb-208 collisions". *Phys. Rev. Lett.* 85 (2000), pp. 3595–3599. DOI: 10.1103/PhysRevLett.85.3595. arXiv: nucl-ex/0006008 [nucl-ex].

[56] S. S. Adler et al. "Centrality dependence of direct photon production in $\sqrt{s_{\mathrm{NN}}}$ = 200 GeV Au + Au collisions". *Phys. Rev. Lett.* 94 (2005), p. 232301. DOI: 10.1103/PhysRevLett.94.232301. arXiv: nucl-ex/0503003 [nucl-ex].

[57] Jaroslav Adam et al. "Direct photon production in Pb-Pb collisions at $\sqrt{s_{\mathrm{NN}}} = 2.76$ TeV". *Phys. Lett.* B754 (2016), pp. 235–248. DOI: 10.1016/j.physletb.2016.01.020. arXiv: 1509.07324 [nucl-ex].

[58] Chun Shen et al. "Thermal photons as a quark-gluon plasma thermometer reexamined". *Phys. Rev.* C89.4 (2014), p. 044910. DOI: 10.1103/PhysRevC.89.044910. arXiv: 1308.2440 [nucl-th].

[59] Jean-Franois Paquet et al. "Production of photons in relativistic heavy-ion collisions". *Phys. Rev.* C93.4 (2016), p. 044906. DOI: 10.1103/PhysRevC.93.044906. arXiv: 1509.06738 [hep-ph].

[60] Hendrik van Hees, Min He, and Ralf Rapp. "Pseudo-critical enhancement of thermal photons in relativistic heavy-ion collisions?" *Nucl. Phys.* A933 (2015), pp. 256–271. DOI: 10.1016/j.nuclphysa.2014.09.009. arXiv: 1404.2846 [nucl-th].

[61] Rupa Chatterjee et al. "Collision centrality and τ_0 dependence of the emission of thermal photons from fluctuating initial state in ideal hydrodynamic calculation". *Phys. Rev.* C85 (2012), p. 064910. DOI: 10.1103/PhysRevC.85.064910. arXiv: 1204.2249 [nucl-th].

[62] O. Linnyk et al. "Hadronic and partonic sources of direct photons in relativistic heavy-ion collisions". *Phys. Rev.* C92.5 (2015), p. 054914. DOI: 10.1103/PhysRevC.92.054914. arXiv: 1504.05699 [nucl-th].

[63] Arthur M. Poskanzer and S. A. Voloshin. "Methods for analyzing anisotropic flow in relativistic nuclear collisions". *Phys. Rev.* C58 (1998), pp. 1671–1678. DOI: 10.1103/PhysRevC.58.1671. arXiv: nucl-ex/9805001 [nucl-ex].

[64] S. Voloshin and Y. Zhang. "Flow study in relativistic nuclear collisions by Fourier expansion of Azimuthal particle distributions". *Z. Phys.* C70 (1996), pp. 665–672. DOI: 10.1007/s002880050141. arXiv: hep-ph/9407282 [hep-ph].

[65] Raimond Snellings. "Elliptic Flow: A Brief Review". *New J. Phys.* 13 (2011), p. 055008. DOI: 10.1088/1367-2630/13/5/055008. arXiv: 1102.3010 [nucl-ex].

[66] Jaroslav Adam et al. "Anisotropic flow of charged particles in Pb-Pb collisions at $\sqrt{s_{\mathrm{NN}}} = 5.02$ TeV". *Phys. Rev. Lett.* 116.13 (2016), p. 132302. DOI: 10.1103/PhysRevLett.116.132302. arXiv: 1602.01119 [nucl-ex].

[67] Betty Abelev et al. "Anisotropic flow of charged hadrons, pions and (anti-)protons measured at high transverse momentum in Pb-Pb collisions at $\sqrt{s_{\mathrm{NN}}}$=2.76 TeV". *Phys. Lett.* B719 (2013), pp. 18–28. DOI: 10.1016/j.physletb.2012.12.066. arXiv: 1205.5761 [nucl-ex].

[68] Nicolas Borghini, Phuong Mai Dinh, and Jean-Yves Ollitrault. "Flow analysis from multiparticle azimuthal correlations". *Phys. Rev. C* 64 (5 2001), p. 054901. DOI: 10.1103/PhysRevC.64.054901. URL: https://link.aps.org/doi/10.1103/PhysRevC.64.054901.

[69] K. Aamodt et al. "Higher harmonic anisotropic flow measurements of charged particles in Pb-Pb collisions at $\sqrt{s_{\mathrm{NN}}}$=2.76 TeV". *Phys. Rev. Lett.* 107 (2011), p. 032301. DOI: 10.1103/PhysRevLett.107.032301. arXiv: 1105.3865 [nucl-ex].

[70] Jacquelyn Noronha-Hostler, Matthew Luzum, and Jean-Yves Ollitrault. "Hydrodynamic predictions for 5.02 TeV Pb-Pb collisions". *Phys. Rev.* C93.3 (2016), p. 034912. DOI: 10.1103/PhysRevC.93.034912. arXiv: 1511.06289 [nucl-th].

[71] H. Niemi et al. "Predictions for 5.023 TeV Pb + Pb collisions at the CERN Large Hadron Collider". *Phys. Rev.* C93.1 (2016), p. 014912. DOI: 10.1103/PhysRevC.93.014912. arXiv: 1511.04296 [hep-ph].

[72] Ulrich W. Heinz. "Hydrodynamics at RHIC - How well does it work, where and how does it break down?" *J. Phys.* G31 (2005), S717–S724. DOI: 10.1088/0954-3899/31/6/012. arXiv: nucl-th/0412094 [nucl-th].

[73] Huichao Song, Steffen A. Bass, and Ulrich Heinz. "Viscous QCD matter in a hybrid hydrodynamic+Boltzmann approach". *Phys. Rev.* C83 (2011), p. 024912. DOI: 10.1103/PhysRevC.83.024912. arXiv: 1012.0555 [nucl-th].

[74] Hao-jie Xu, Zhuopeng Li, and Huichao Song. "High-order flow harmonics of identified hadrons in 2.76A TeV Pb + Pb collisions". *Phys. Rev.* C93.6 (2016), p. 064905. DOI: 10.1103/PhysRevC.93.064905. arXiv: 1602.02029 [nucl-th].

[75] Chun Shen et al. "The iEBE-VISHNU code package for relativistic heavy-ion collisions". *Comput. Phys. Commun.* 199 (2016), pp. 61–85. DOI: 10.1016/j.cpc.2015.08.039. arXiv: 1409.8164 [nucl-th].

[76] S. A. Bass et al. "Microscopic models for ultrarelativistic heavy ion collisions". *Prog. Part. Nucl. Phys.* 41 (1998). [Prog. Part. Nucl. Phys.41,225(1998)], pp. 255–369. DOI: 10.1016/S0146-6410(98)00058-1. arXiv: nucl-th/9803035 [nucl-th].

[77] Jaroslav Adam et al. "Higher harmonic flow coefficients of identified hadrons in Pb-Pb collisions at $\sqrt{s_{\mathrm{NN}}} = 2.76$ TeV". *JHEP* 09 (2016), p. 164. DOI: 10.1007/JHEP09(2016)164. arXiv: 1606.06057 [nucl-ex].

[79] Betty Bezverkhny Abelev et al. "Elliptic flow of identified hadrons in Pb-Pb collisions at $\sqrt{s_{\mathrm{NN}}} = 2.76$ TeV". *JHEP* 06 (2015), p. 190. DOI: 10.1007/JHEP06(2015)190. arXiv: 1405.4632 [nucl-ex].

[80] C. Adler et al. "Elliptic flow from two and four particle correlations in Au+Au collisions at $\sqrt{s_{\mathrm{NN}}} = 130$ GeV". *Phys. Rev.* C66 (2002), p. 034904. DOI: 10.1103/PhysRevC.66.034904. arXiv: nucl-ex/0206001 [nucl-ex].

[78] S. A. Voloshin. "Anisotropic flow". *Nucl. Phys.* A715 (2003), pp. 379–388. DOI: 10.1016/S0375-9474(02)01450-1. arXiv: nucl-ex/0210014 [nucl-ex].

[81] Panagiota Foka and Magorzata Anna Janik. “An overview of experimental results from ultra-relativistic heavy-ion collisions at the CERN LHC: Hard probes”. *Rev. Phys.* 1 (2016), pp. 172–194. DOI: 10.1016/j.revip.2016.11.001. arXiv: 1702.07231 [hep-ex].

[82] Serguei Chatrchyan et al. “Study of high-pT charged particle suppression in PbPb compared to *pp* collisions at $\sqrt{s_{\rm NN}} = 2.76$ TeV”. *Eur. Phys. J.* C72 (2012), p. 1945. DOI: 10.1140/epjc/s10052-012-1945-x. arXiv: 1202.2554 [nucl-ex].

[83] K. Aamodt et al. “Suppression of Charged Particle Production at Large Transverse Momentum in Central Pb-Pb Collisions at $\sqrt{s_{\rm NN}} = 2.76$ TeV”. *Phys. Lett.* B696 (2011), pp. 30–39. DOI: 10.1016/j.physletb.2010.12.020. arXiv: 1012.1004 [nucl-ex].

[84] M. M. Aggarwal et al. “Transverse mass distributions of neutral pions from Pb-208 induced reactions at 158 AGeV”. *Eur. Phys. J.* C23 (2002), pp. 225–236. DOI: 10.1007/s100520100886. arXiv: nucl-ex/0108006 [nucl-ex].

[85] David G. d’Enterria. “Indications of suppressed high p(T) hadron production in nucleus - nucleus collisions at CERN-SPS”. *Phys. Lett.* B596 (2004), pp. 32–43. DOI: 10.1016/j.physletb.2004.06.071. arXiv: nucl-ex/0403055 [nucl-ex].

[86] A. Adare et al. “Suppression pattern of neutral pions at high transverse momentum in Au + Au collisions at $\sqrt{s_{\rm NN}} = 200$ GeV and constraints on medium transport coefficients”. *Phys. Rev. Lett.* 101 (2008), p. 232301. DOI: 10.1103/PhysRevLett.101.232301. arXiv: 0801.4020 [nucl-ex].

[87] J. Adams et al. “Transverse momentum and collision energy dependence of high p(T) hadron suppression in Au+Au collisions at ultrarelativistic energies”. *Phys. Rev. Lett.* 91 (2003), p. 172302. DOI: 10.1103/PhysRevLett.91.172302. arXiv: nucl-ex/0305015 [nucl-ex].

[88] A. Dainese, C. Loizides, and G. Paic. “Leading-particle suppression in high energy nucleus-nucleus collisions”. *Eur. Phys. J.* C38 (2005), pp. 461–474. DOI: 10.1140/epjc/s2004-02077-x. arXiv: hep-ph/0406201 [hep-ph].

[89] Ivan Vitev and Miklos Gyulassy. “High p_T tomography of d + Au and Au+Au at SPS, RHIC, and LHC”. *Phys. Rev. Lett.* 89 (2002), p. 252301. DOI: 10.1103/PhysRevLett.89.252301. arXiv: hep-ph/0209161 [hep-ph].

[90] Ivan Vitev. “Jet tomography”. *J. Phys.* G30 (2004), S791–S800. DOI: 10.1088/0954-3899/30/8/019. arXiv: hep-ph/0403089 [hep-ph].

[91] Carlos A. Salgado and Urs Achim Wiedemann. “Calculating quenching weights”. *Phys. Rev.* D68 (2003), p. 014008. DOI: 10.1103/PhysRevD.68.014008. arXiv: hep-ph/0302184 [hep-ph].

[92] Nestor Armesto et al. “Testing the color charge and mass dependence of parton energy loss with heavy-to-light ratios at RHIC and CERN LHC”. *Phys. Rev.* D71 (2005), p. 054027. DOI: 10.1103/PhysRevD.71.054027. arXiv: hep-ph/0501225 [hep-ph].

[93] Betty Abelev et al. “Centrality Dependence of Charged Particle Production at Large Transverse Momentum in Pb–Pb Collisions at $\sqrt{s_{\rm NN}} = 2.76$ TeV”. *Phys. Lett.* B720 (2013), pp. 52–62. DOI: 10.1016/j.physletb.2013.01.051. arXiv: 1208.2711 [hep-ex].

[94] Serguei Chatrchyan et al. “Measurement of isolated photon production in *pp* and PbPb collisions at $\sqrt{s_{\rm NN}} = 2.76$ TeV”. *Phys. Lett.* B710 (2012), pp. 256–277. DOI: 10.1016/j.physletb.2012.02.077. arXiv: 1201.3093 [nucl-ex].

[95] Serguei Chatrchyan et al. “Study of Z boson production in PbPb collisions at $\sqrt{s_{\rm NN}} = 2.76$ TeV”. *Phys. Rev. Lett.* 106 (2011), p. 212301. DOI: 10.1103/PhysRevLett.106.212301. arXiv: 1102.5435 [nucl-ex].

[96] Serguei Chatrchyan et al. “Study of W boson production in PbPb and *pp* collisions at $\sqrt{s_{\rm NN}} = 2.76$ TeV”. *Phys. Lett.* B715 (2012), pp. 66–87. DOI: 10.1016/j.physletb.2012.07.025. arXiv: 1205.6334 [nucl-ex].

[97] Betty Bezverkhny Abelev et al. “Transverse momentum dependence of inclusive primary charged-particle production in p-Pb collisions at $\sqrt{s_{\rm NN}} =$ 5.02 TeV”. *Eur. Phys. J.* C74.9 (2014), p. 3054. DOI: 10.1140/epjc/s10052-014-3054-5. arXiv: 1405.2737 [nucl-ex].

[98] Lyndon Evans and Philip Bryant. “LHC Machine”. *Journal of Instrumentation* 3.08 (2008), S08001–S08001. DOI: 10.1088/1748-0221/3/08/s08001. URL: https://doi.org/10.1088%2F1748-0221%2F3%2F08%2Fs08001.

[99] “LHC Guide”. https://cds.cern.ch/record/2255762. 2017. URL: https://cds.cern.ch/record/2255762.

[100] Esma Mobs. “The CERN accelerator complex. Complexe des acclrateurs du CERN” (2016). General Photo. URL: https://cds.cern.ch/record/2197559.

[101] K. Aamodt et al. “The ALICE experiment at the CERN LHC”. *JINST* 3 (2008), S08002. DOI: 10.1088/1748-0221/3/08/S08002.

[116] *ALICE Collaboration Home Page*. http://cds.cern.ch/record/451098.

[102] B Abelev et al and The ALICE Collaboration. "Technical Design Report for the Upgrade of the ALICE Inner Tracking System". *Journal of Physics G: Nuclear and Particle Physics* 41.8 (2014), p. 087002. URL: http://stacks.iop.org/0954-3899/41/i=8/a=087002.

[103] J. Alme et al. "The ALICE TPC, a large 3-dimensional tracking device with fast readout for ultra-high multiplicity events". *Nucl. Instrum. Meth.* A622 (2010), pp. 316–367. DOI: 10.1016/j.nima.2010.04.042. arXiv: 1001.1950 [physics.ins-det].

[104] P Cortese. *ALICE transition-radiation detector: Technical Design Report*. Technical Design Report ALICE. Geneva: CERN, 2001. URL: http://cds.cern.ch/record/519145.

[105] *ALICE Time-Of-Flight system (TOF): Technical Design Report*. Technical Design Report ALICE. Geneva: CERN, 2000. URL: http://cds.cern.ch/record/430132.

[106] P Cortese. *ALICE Time-Of Flight system (TOF): addendum to the Technical Design Report*. Technical Design Report ALICE. Geneva: CERN, 2002. URL: http://cds.cern.ch/record/545834.

[107] Franois Piuz et al. *ALICE high-momentum particle identification: Technical Design Report*. Technical Design Report ALICE. Geneva: CERN, 1998. URL: http://cds.cern.ch/record/381431.

[108] V I Man'ko et al. *ALICE Photon Spectrometer (PHOS): Technical Design Report*. Technical Design Report ALICE. Geneva: CERN, 1999. URL: http://cds.cern.ch/record/381432.

[109] ALICE Collaboration et al. "ALICE: Physics Performance Report, Volume I". *Journal of Physics G: Nuclear and Particle Physics* 30.11 (2004), pp. 1517–1763. DOI: 10.1088/0954-3899/30/11/001. URL: https://doi.org/10.1088%2F0954-3899%2F30%2F11%2F001.

[110] Christian Wolfgang Fabjan et al. "ALICE: Physics performance report, volume II". *J. Phys.* G32 (2006). Ed. by B Alessandro et al., pp. 1295–2040. DOI: 10.1088/0954-3899/32/10/001.

[111] M Gallio et al. *ALICE Zero-Degree Calorimeter (ZDC): Technical Design Report*. Technical Design Report ALICE. Geneva: CERN, 1999. URL: http://cds.cern.ch/record/381433.

[112] *ALICE Photon Multiplicity Detector (PMD): Technical Design Report*. Technical Design Report ALICE. Geneva: CERN, 1999. URL: http://cds.cern.ch/record/451099.

[113] P Cortese et al. *ALICE forward detectors: FMD, TO and VO: Technical Design Report*. Technical Design Report ALICE. Submitted on 10 Sep 2004. Geneva: CERN, 2004. URL: http://cds.cern.ch/record/781854.

[114] *ALICE dimuon forward spectrometer: Technical Design Report*. Technical Design Report ALICE. Geneva: CERN, 1999. URL: http://cds.cern.ch/record/401974.

[115] A. Fernndez et al. "ACORDE a Cosmic Ray Detector for ALICE". *Nucl. Instrum. Meth.* A572 (2007), pp. 102–103. DOI: 10.1016/j.nima.2006.10.336. arXiv: physics/0606051 [physics.ins-det].

[117] G. Dellacasa et al. "ALICE: Technical design report of the time projection chamber" (2000).

[118] P Cortese et al. "ALICE technical design report on forward detectors: FMD, T0 and V0" (2004).

[119] E. Abbas et al. "Performance of the ALICE VZERO system". *JINST* 8 (2013), P10016. DOI: 10.1088/1748-0221/8/10/P10016. arXiv: 1306.3130 [nucl-ex].

[120] R. Hanbury Brown and R. Q. Twiss. "A New type of interferometer for use in radio astronomy". *Phil. Mag. Ser.7* 45 (1954), pp. 663–682. DOI: 10.1080/14786440708520475.

[121] R. Hanbury Brown and R. Q. Twiss. "Correlation between Photons in two Coherent Beams of Light". *Nature* 177 (1956), pp. 27–29. DOI: 10.1038/177027a0.

[122] Gerson Goldhaber et al. "Influence of Bose-Einstein Statistics on the Antiproton-Proton Annihilation Process". *Phys. Rev.* 120 (1 1960), pp. 300–312. DOI: 10.1103/PhysRev.120.300. URL: https://link.aps.org/doi/10.1103/PhysRev.120.300.

[123] Michael Annan Lisa et al. "Femtoscopy in relativistic heavy ion collisions". *Ann. Rev. Nucl. Part. Sci.* 55 (2005), pp. 357–402. DOI: 10.1146/annurev.nucl.55.090704.151533. arXiv: nucl-ex/0505014 [nucl-ex].

[124] Ulrich W. Heinz and Barbara V. Jacak. "Two particle correlations in relativistic heavy ion collisions". *Ann. Rev. Nucl. Part. Sci.* 49 (1999), pp. 529–

579. DOI: 10.1146/annurev.nucl.49.1.529. arXiv: nucl-th/9902020 [nucl-th].

[125] Michael Annan Lisa and Scott Pratt. "Femtoscopically Probing the Freeze-out Configuration in Heavy Ion Collisions". *Relativistic Heavy Ion Physics*. Ed. by R. Stock. 2010. DOI: 10.1007/978-3-642-01539-7_21. arXiv: 0811.1352 [nucl-ex].

[126] Richard Lednicky. "Finite-size effects on two-particle production in continuous and discrete spectrum". *Phys. Part. Nucl.* 40 (2009), pp. 307–352. DOI: 10.1134/S1063779609030034. arXiv: nucl-th/0501065 [nucl-th].

[127] D. Anchishkin, U. Heinz, and P. Renk. "Final state interactions in two-particle interferometry". *Phys. Rev. C* 57 (3 1998), pp. 1428–1439. DOI: 10.1103/PhysRevC.57.1428. URL: https://link.aps.org/doi/10.1103/PhysRevC.57.1428.

[128] S. E. Koonin. "Proton Pictures of High-Energy Nuclear Collisions". *Phys. Lett.* B70 (1977), pp. 43–47. DOI: 10.1016/0370-2693(77)90340-9.

[129] S. Pratt, T. Csorgo, and J. Zimanyi. "Detailed predictions for two pion correlations in ultrarelativistic heavy ion collisions". *Phys. Rev.* C42 (1990), pp. 2646–2652. DOI: 10.1103/PhysRevC.42.2646.

[130] S.V. Akkelin and Yu.M. Sinyukov. "The HBT-interferometry of expanding sources". *Physics Letters B* 356.4 (1995), pp. 525 –530. ISSN: 0370-2693. DOI: https://doi.org/10.1016/0370-2693(95)00765-D. URL: http://www.sciencedirect.com/science/article/pii/037026939500765D.

[131] Scott Chapman, J. Rayford Nix, and Ulrich W. Heinz. "Extracting source parameters from Gaussian fits to two particle correlations". *Phys. Rev.* C52 (1995), pp. 2694–2703. DOI: 10.1103/PhysRevC.52.2694. arXiv: nucl-th/9505032 [nucl-th].

[132] Urs Achim Wiedemann and Ulrich W. Heinz. "Particle interferometry for relativistic heavy ion collisions". *Phys. Rept.* 319 (1999), pp. 145–230. DOI: 10.1016/S0370-1573(99)00032-0. arXiv: nucl-th/9901094 [nucl-th].

[133] Jaroslav Adam et al. "One-dimensional pion, kaon, and proton femtoscopy in Pb-Pb collisions at $\sqrt{s_{\mathrm{NN}}}$ =2.76 TeV". *Phys. Rev.* C92.5 (2015), p. 054908. DOI: 10.1103/PhysRevC.92.054908. arXiv: 1506.07884 [nucl-ex].

[134] R. Lednicky and V. L. Lyuboshits. "Final State Interaction Effect on Pairing Correlations Between Particles with Small Relative Momenta". *Sov. J. Nucl. Phys.* 35 (1982). [Yad. Fiz.35,1316(1981)], p. 770.

[135] R. Lednicky et al. “How to measure which sort of particles was emitted earlier and which later”. *Phys. Lett.* B373 (1996), pp. 30–34. DOI: 10.1016/0370-2693(96)00124-4.

[136] Adam Kisiel. “Non-identical particle femtoscopy at $\sqrt{s_{\rm NN}} = 200$ GeV in hydrodynamics with statistical hadronization”. *Phys. Rev.* C81 (2010), p. 064906. DOI: 10.1103/PhysRevC.81.064906. arXiv: 0909.5349 [nucl-th].

[137] Landau L.D. and E.M. Lifshitz. *Quantum Mechanics: Non-Relativistic Theory (Course on Theoretical Physics, Vol. 3)*. Oxford: Pergamon Press, 1977.

[138] M.G. Bowler. “Coulomb corrections to Bose-Einstein corrections have greatly exaggerated”. *Physics Letters B* 270.1 (1991), pp. 69 –74. ISSN: 0370-2693. DOI: https://doi.org/10.1016/0370-2693(91)91541-3. URL: http://www.sciencedirect.com/science/article/pii/0370269391915413.

[139] Yu.M. Sinyukov et al. “Coulomb corrections for interferometry analysis of expanding hadron systems”. *Physics Letters B* 432.3 (1998), pp. 248 –257. ISSN: 0370-2693. DOI: https://doi.org/10.1016/S0370-2693(98)00653-4. URL: http://www.sciencedirect.com/science/article/pii/S0370269398006534.

[140] G. I. Kopylov. “Like particle correlations as a tool to study the multiple production mechanism”. *Phys. Lett.* B50 (1974). [,39(1974)], pp. 472–474. DOI: 10.1016/0370-2693(74)90263-9.

[141] Zbigniew Chajecki and Mike Lisa. “Global Conservation Laws and Femtoscopy of Small Systems”. *Phys. Rev.* C78 (2008), p. 064903. DOI: 10.1103/PhysRevC.78.064903. arXiv: 0803.0022 [nucl-th].

[142] D. A. Brown et al. “Imaging three dimensional two-particle correlations for heavy-ion reaction studies”. *Phys. Rev. C* 72 (5 2005), p. 054902. DOI: 10.1103/PhysRevC.72.054902. URL: https://link.aps.org/doi/10.1103/PhysRevC.72.054902.

[143] Adam Kisiel and David A. Brown. “Efficient and robust calculation of femtoscopic correlation functions in spherical harmonics directly from the raw pairs measured in heavy-ion collisions”. *Phys. Rev.* C80 (2009), p. 064911. DOI: 10.1103/PhysRevC.80.064911. arXiv: 0901.3527 [nucl-th].

[144] K. Aamodt et al. “Two-pion Bose-Einstein correlations in central Pb-Pb collisions at $\sqrt{s_{\rm NN}} = 2.76$ TeV”. *Phys. Lett.* B696 (2011), pp. 328–337. DOI: 10.1016/j.physletb.2010.12.053. arXiv: 1012.4035 [nucl-ex].

[145] M. A. Lisa et al. “Bombarding Energy Dependence of π^- Interferometry at the Brookhaven AGS”. *Phys. Rev. Lett.* 84 (13 2000), pp. 2798–2802. DOI:

10.1103/PhysRevLett.84.2798. URL: https://link.aps.org/doi/10.1103/PhysRevLett.84.2798.

[146] C. Alt et al. “Bose-Einstein correlations of $\pi^-\pi^-$ pairs in central Pb+Pb collisions at $20A, 30A, 40A, 80A$, and $158A$ GeV”. *Phys. Rev. C* 77 (6 2008), p. 064908. DOI: 10.1103/PhysRevC.77.064908. URL: https://link.aps.org/doi/10.1103/PhysRevC.77.064908.

[147] S. V. Afanasiev et al. “Energy dependence of pion and kaon production in central Pb + Pb collisions”. *Phys. Rev.* C66 (2002), p. 054902. DOI: 10.1103/PhysRevC.66.054902. arXiv: nucl-ex/0205002 [nucl-ex].

[148] D. Adamov et al. “Beam energy and centrality dependence of two pion Bose-Einstein correlations at SPS energies”. *Nucl. Phys.* A714 (2003), pp. 124–144. DOI: 10.1016/S0375-9474(02)01369-6. arXiv: nucl-ex/0207005 [nucl-ex].

[149] B. I. Abelev et al. “Pion Interferometry in Au+Au and Cu+Cu Collisions at RHIC”. *Phys. Rev.* C80 (2009), p. 024905. DOI: 10.1103/PhysRevC.80.024905. arXiv: 0903.1296 [nucl-ex].

[150] B. B. Back et al. “Transverse momentum and rapidity dependence of Hanbury-Brown–Twiss correlations in Au+Au collisions at $\sqrt{s_{\mathrm{NN}}} = 62.4$ and 200 GeV”. *Phys. Rev. C* 73 (3 2006), p. 031901. DOI: 10.1103/PhysRevC.73.031901. URL: https://link.aps.org/doi/10.1103/PhysRevC.73.031901.

[151] B. B. Back et al. “Charged-particle pseudorapidity distributions in Au+Au collisions at $\sqrt{s_{\mathrm{NN}}} = 62.4$ GeV”. *Phys. Rev. C* 74 (2 2006), p. 021901. DOI: 10.1103/PhysRevC.74.021901. URL: https://link.aps.org/doi/10.1103/PhysRevC.74.021901.

[152] B. B. Back et al. “Significance of the Fragmentation Region in Ultrarelativistic Heavy-Ion Collisions”. *Phys. Rev. Lett.* 91 (5 2003), p. 052303. DOI: 10.1103/PhysRevLett.91.052303. URL: https://link.aps.org/doi/10.1103/PhysRevLett.91.052303.

[153] J. Adams et al. “Pion interferometry in Au+Au collisions at $\sqrt{s_{\mathrm{NN}}} = 200$ GeV”. *Phys. Rev.* C71 (2005), p. 044906. DOI: 10.1103/PhysRevC.71.044906. arXiv: nucl-ex/0411036 [nucl-ex].

[154] Jaroslav Adam et al. “Centrality dependence of pion freeze-out radii in Pb-Pb collisions at $\sqrt{s_{\mathrm{NN}}} = 2.76$ TeV”. *Phys. Rev.* C93.2 (2016), p. 024905. DOI: 10.1103/PhysRevC.93.024905. arXiv: 1507.06842 [nucl-ex].

[155] M. Herrmann and G. F. Bertsch. "Source dimensions in ultrarelativistic heavy ion collisions". *Phys. Rev.* C51 (1995), pp. 328–338. DOI: 10.1103/PhysRevC.51.328. arXiv: hep-ph/9405373 [hep-ph].

[156] A. Adare et al. "Azimuthal-angle dependence of charged-pion-interferometry measurements with respect to second- and third-order event planes in Au+Au collisions at $\sqrt{s_{\mathrm{NN}}} = 200$ GeV". *Phys. Rev. Lett.* 112.22 (2014), p. 222301. DOI: 10.1103/PhysRevLett.112.222301. arXiv: 1401.7680 [nucl-ex].

[157] S. Acharya et al. "Azimuthally-differential pion femtoscopy relative to the third harmonic event plane in Pb-Pb collisions at $\sqrt{s_{\mathrm{NN}}} = 2.76$ TeV". *Phys. Lett.* B785 (2018), pp. 320–331. DOI: 10.1016/j.physletb.2018.06.042. arXiv: 1803.10594 [nucl-ex].

[158] Michael Annan Lisa. "Azimuthally sensitive interferometry and the source lifetime at RHIC". *Acta Phys. Polon.* B35 (2004), pp. 37–46. arXiv: nucl-ex/0312012 [nucl-ex].

[159] Dagmar Adamova et al. "Azimuthally differential pion femtoscopy in Pb-Pb collisions at $\sqrt{s_{\mathrm{NN}}} = 2.76$ TeV". *Phys. Rev. Lett.* 118.22 (2017), p. 222301. DOI: 10.1103/PhysRevLett.118.222301. arXiv: 1702.01612 [nucl-ex].

[160] Fabrice Retiere and Michael Annan Lisa. "Observable implications of geometrical and dynamical aspects of freeze out in heavy ion collisions". *Phys. Rev.* C70 (2004), p. 044907. DOI: 10.1103/PhysRevC.70.044907. arXiv: nucl-th/0312024 [nucl-th].

[161] Ashutosh Kumar Pandey. "Pion-kaon femtoscopy in Pb−Pb collisions at $\sqrt{s_{\mathrm{NN}}} =$ 2.76 TeV measured with ALICE". *Nucl. Phys.* A982 (2019), pp. 351–354. DOI: 10.1016/j.nuclphysa.2018.10.048. arXiv: 1807.10072 [hep-ex].

[162] Adam Kisiel. "CorrFit - a program to fit arbitrary two-particle correlation functions". *Nukleonika* 49.suppl.2 (2004), s81–s83.

[163] J. Adams et al. "Pion-kaon correlations in Au+Au collisions at $\sqrt{s_{\mathrm{NN}}} = 130$ GeV". *Phys. Rev. Lett.* 91 (2003), p. 262302. DOI: 10.1103/PhysRevLett.91.262302. arXiv: nucl-ex/0307025 [nucl-ex].

[164] C. Patrignani et al. "Review of Particle Physics". *Chin. Phys.* C40.10 (2016), p. 100001. DOI: 10.1088/1674-1137/40/10/100001.

[165] A.V. Stavinskiy et al. "Some new aspects of femtoscopy at high energy". *Nukleonika* 49 (Supplement 2) (2004), S23.

[166] Adam Kisiel, Hanna Zbroszczyk, and Maciej Szymaski. "Extracting baryon-antibaryon strong interaction potentials from p$\bar{\Lambda}$ femtoscopic correlation functions". *Phys. Rev.* C89.5 (2014), p. 054916. DOI: 10.1103/PhysRevC.89.054916. arXiv: 1403.0433 [nucl-th].

[167] Mikolaj Chojnacki et al. "THERMINATOR 2: THERMal heavy IoN generATOR 2". *Comput. Phys. Commun.* 183 (2012), pp. 746–773. DOI: 10.1016/j.cpc.2011.11.018. arXiv: 1102.0273 [nucl-th].

[168] A Kisiel. "Non-identical Particle Correlation Analysis in the Presence of Non-femtoscopic Correlations". *Acta Physica Polonica B* 48 (Apr. 2017), p. 717. DOI: 10.5506/APhysPolB.48.717.

[169] Yan-Rui Liu and Shi-Lin Zhu. "Meson-baryon scattering lengths in HB chi PT". *Phys. Rev.* D75 (2007), p. 034003. DOI: 10.1103/PhysRevD.75.034003. arXiv: hep-ph/0607100 [hep-ph].

[170] Maxim Mai et al. "Aspects of meson-baryon scattering in three and two-flavor chiral perturbation theory". *Phys. Rev.* D80 (2009), p. 094006. DOI: 10.1103/PhysRevD.80.094006. arXiv: 0905.2810 [hep-ph].

Appendix A: Results: ΛK^0_S and $\Lambda K^\pm$ (Additional Figures)

This appendix presents fit results obtained using different methods and variations of our fit procedure. The purpose here is to offer a more in depth and transparent look at how the various assumptions made for our final fit procedure affect our results. For all cases, the interesting result remains of the ΛK^+ system exhibiting a negative $\Re f_0$, the ΛK^- positive, and the ΛK^0_S system somewhere between.

For our final results, we have chosen to include three residual contributors, as this best matches the experimental situation. These three contributors include: ($\Sigma^0 K$, $\Xi^0 K$, $\Xi^- K$) $\rightarrow \Lambda K$. Moving to ten contributors, we additionally include feed-down from ($\Sigma^{*(+,-,0)} K^{*0}$, ΛK^{*0}, $\Sigma^0 K^{*0}$, $\Xi^0 K^{*0}$, $\Xi^- K^{*0}$) $\rightarrow \Lambda K$. As stated in Sec. 6.2, femtoscopic analyses are sensitive to the pair emission structure at kinetic freeze-out, therefore any particle born from a resonance decaying before last rescattering is seen as primary. The Σ^* and K^* resonances have proper decay lengths $c\tau \approx 5$ fm and 4 fm, respectively. Although some of these will decay after, we expect that most will decay before kinetic freeze-out. Therefore, it is best to treat Λ and K particles originating from these resonances as primary, and therefore include only three residual contributors in our fit procedure. However, it is still interesting to observe how these additional sources of residuals would affect our fit results, as the actual situation lies somewhere between the two cases (although, weighted much more towards the three residuals case). For a more precise treatment (not warranted here, when considering all of the approximations in the measurement), one should estimate the number of

Σ^* and K^* resonances decaying after kinetic freeze-out, and use this information to adjust the λ parameters.

In Appendix A.1 we present summary plots demonstrating the effect on the extracted fit parameter sets of utilizing the different fit techniques. The comparisons include the effect of using different numbers of residual contributors, fixing the overall λ_{Fit} parameter compared to allowing it to be free, fitting a correlation function built with the Stavinskiy method compared to the normal construction method, sharing radii among all ΛK systems compared to sharing radii between only the $\Lambda K^{\pm}$ systems, and using the experimental $\Xi^{-}K^{\pm}$ data compared to modeling it with a Coulomb-only curve in the residuals treatment.

The final three subsections include a more thorough look into utilizing three (App. A.2), ten (App. A.3), and no (App. A.4) residual contributors in the fit routine. These subsections match closely the structure of Sec. 7.1, where we presented the final results for our ΛK study. Each begins with a summary plot compactly showing the extracted fit parameters, and each contains figures showing the fit plotted on top of the experimental data. Different from Sec. 7.1, the correlations are shown out to ~ 1 GeV/c (instead of ~ 0.3 GeV/c), to show both the signal region and the non-femtoscopic background. Furthermore, Appendices A.2 and A.3 contain figures showing the final fit with the components describing the different residual contributions, on top of the experimental data.

As with the results presented in Sec. 7.1, unless otherwise noted, the following hold true: All correlation functions were normalized in the range $0.32 < k^* < 0.40$ GeV/c, and fit in the range $0.0 < k^* < 0.30$ GeV/c. For the ΛK^- and $\overline{\Lambda}K^+$ analyses, the region $0.19 < k^* < 0.23$ GeV/c was excluded from the fit to exclude the bump caused by the Ω^- resonance. The non-femtoscopic backgrounds for the ΛK^+ and ΛK^- systems were modeled by a 6^{th}-order polynomial fit to THERMINATOR 2 simulation, while those for the ΛK^0_S were fit with a simple linear form. All analyses were fit simultaneously across all centralities, with a single radius and normalization

$\lambda_{\rm Fit}$ parameter for each centrality bin. Scattering parameters ($\Re f_0$, $\Im f_0$, d_0) were shared between pair-conjugate systems, but assumed unique between the different ΛK charge combinations (i.e. a parameter set describing the ΛK^+ & $\overline{\Lambda}K^-$ system, a second set describing the ΛK^- & $\overline{\Lambda}K^+$ system, and a third for the ΛK^0_S & $\overline{\Lambda}K^0_S$ system). Each correlation function received a unique normalization parameter. The fits were corrected for finite momentum resolution effects, non-femtoscopic backgrounds, and residual correlations resulting from the feed-down from resonances. Lines and boxes on the experimental data represent statistical and systematic errors, respectively.

In the figures showing experimental correlation functions with fits, the black solid curve represents the primary (ΛK) correlation's contribution to the fit. The green line shows the fit to the non-flat background. The purple points show the fit after all residual contributions have been included, and momentum resolution and non-flat background corrections have been applied. The extracted fit values with uncertainties are printed as (fit value) ± (statistical uncertainty) ± (systematic uncertainty).

A.1 Fit method comparisons

The figures in this appendix show comparisons of extracted fit parameters obtained using different fit techniques. Fig. A.1 shows a comparison of results obtained using three, ten, and no residual contributors. In Fig. A.2, we demonstrate the effect of fixing the overall $\lambda_{\rm Fit}$ parameter compared to allowing it to be free (see Eq. 6.2 in Sec. 6.2). Fig. A.5 compares our normal fit results to those obtained when the correlation functions are built using the Stavinskiy method (see Sec. 5.7.2). Fig. A.6 shows the difference between sharing radii among all ΛK systems versus only sharing radii between the $\Lambda K^{\pm}$ systems. Finally, Fig. A.7 shows the effect of using the experimental $\Xi^- K^{\pm}$ data compared to modeling it with a Coulomb-only curve for use in the residuals treatment (see Sec. 6.2).

All of the figures follow the same four-panel structure: [Top Left]: $\Im f_0$ vs. $\Re f_0$, together with d_0 to the right. [Top Right (Bottom Left, Bottom Right)]: λ vs. Radius for the 0–10% (10–30%, 30–50%) bin. The ΛK^+ system is always presented with red markers, the ΛK^- with blue, and the ΛK^0_S with black. In the case of all ΛK analyses sharing radii, the markers are gold. In the case of only the $\Lambda K^\pm$ analyses sharing radii, the markers are magenta. The square symbols in the first column of the legends are to signify the color scheme. The black symbols in the second column of the legend describe the fit procedure used.

To better explain the description in the legends, take Fig. A.1 as an example. The square symbols in the first column of the top left figure indicate that the ΛK^+ scattering parameters are shown in red, the ΛK^- in blue, and the ΛK^0_S in black. The symbols in the second column of the top left figure indicate that the case of three residual contributors is shown with closed circles, ten residual contributors with open crosses, and no residuals with open triangles. For the λ vs. radii plots, the square symbol describing the color scheme in the first column of the top right figure shows that all ΛK analyses share common radii and are shown with gold markers.

Fig. A.6 is a bit more involved example, in terms of the markers, so it is worthwhile to explain as a second example. The square symbols in the first column of the top left figure indicate that the ΛK^+ scattering parameters are shown in red, the ΛK^- in blue, and the ΛK^0_S in black. The symbols in the second column of the top left figure indicate that the case where all ΛK analyses share common radii is shown with closed circles, the case of only $\Lambda K^\pm$ analyses sharing radii is shown with open crosses, and the ΛK^0_S system being fit alone is shown with open triangles. For the λ vs. radii plots, the square symbols describing the color scheme in the first column of the top right figure show that the case where all ΛK analyses share common radii is drawn with gold (in addition to being closed circles, as just described) markers, only $\Lambda K^\pm$ analyses sharing radii is shown with magenta (in addition to open crosses, as just described) markers, and the ΛK^0_S system being fit alone is shown with black (in addition to open triangles, as just described) markers.

Fig. A.1 shows a comparison of results obtained using three, ten, and no residual contributors. A more detailed look of the fits with the experimental data can be found in Appendices A.2 - A.4. As shown, the scattering parameters vary significantly between the different cases. For the case of no residual contributors, we would expect the λ_{Fit} parameters to be closer to $\lambda_{\text{Fit}} \sim 0.5$, when considering the value extracted for primary pairs using simulation in Table 6.2. For the case of 10 residual contributors, the figure shows the magnitude of the scattering parameters tends to increase, as do the λ_{Fit} parameters. The improper treatment of the residuals places less emphasis on the primary interaction, as conveyed through the relative strength of the λ_{Fit} parameters between the three and ten residuals case, presented in Tables 6.2 and 6.3. More emphasis is placed on the residual contributors, whose signal is effectively flattened after being run through the appropriate transform matrices (as shown in Figs. 6.7 and 6.8 of Sec. 6.2). This leads to a lot of mostly-flat contributions, as shown e.g. in Fig. A.19 in App. A.3. These two effects could account for the (mostly) larger in magnitude scattering parameters and λ_{Fit} parameters extracted when assuming 10 residual contributors.

In Fig. A.2 we demonstrate the effect of fixing the overall λ_{Fit} parameter compared to allowing it to be free (see Eq. 6.2 in Sec. 6.2). As shown, the extracted scattering parameters are mostly unaffected by this choice. The radii behave as expected, when considering the λ_{Fit} and R parameters are strongly correlated. For instance, forcing λ_{Fit} to decrease, as in the 0–10% centrality bin shown in the top right of the figure, causes the fit radius to also decrease.

In Figures A.3 and A.4 we investigate the effect of setting the radii equal to values calculated using extracted single-particle source sizes from the identical-particle studies (for the case of free λ_{Fit} and λ_{Fit} fixed to unity, respectively). This amounts essentially to forcing $\mu_{\text{out}} = 0$ in reality. To be clear, our model assumes $\mu_{\text{out}} = 0$ because it greatly simplifies the generation of fit correlation functions, but we do not believe this to strictly be the case physically; our radii can be interpreted as effective

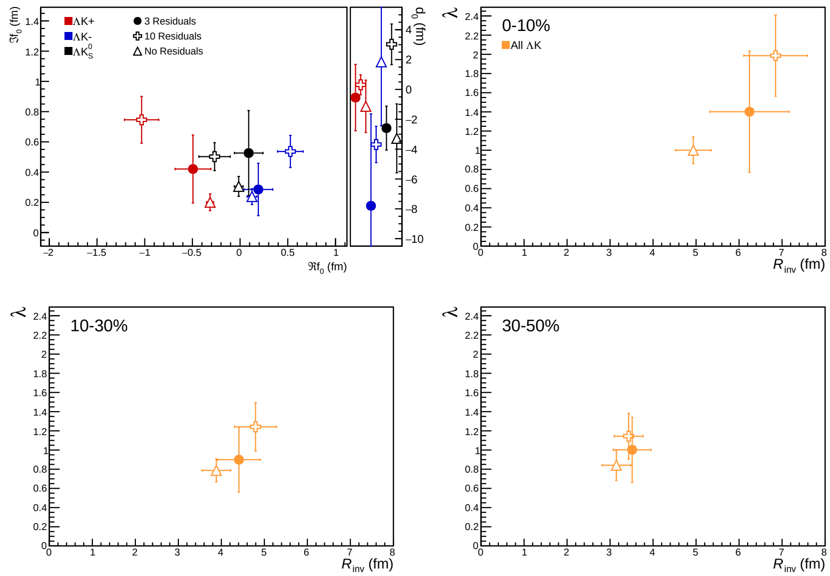

Figure A.1: Results shown for the case of 3 (closer, circles), 10 (open, crosses), and no (open, triangles) residual contributors included in the fit. See text at beginning of section for color scheme information.

radii whose larger than expected magnitudes are a cause of this outward shift. As explained in Sec. 4.2.5 and Sec. 7.1.2, the pair source radius is the sum of the single source radii added in quadrature, $R^2_{ab,i} = R^2_{a,i} + R^2_{b,i}$, and the extracted offset is the difference in the single-particle distribution shifts $\mu_{ab,\,\mathrm{out}} = \mu_{a,\,\mathrm{out}} - \mu_{b,\,\mathrm{out}}$. In the case of identical-particle studies, this amounts to $R^2_{aa} = 2R^2_a$ and $\mu_{aa,\,\mathrm{out}} = 0$. From the m_{T}-scaling plot (Fig. 7.10 in Sec. 7.1.2), we estimated the single-particle K and Λ source sizes using the $\mathrm{K^0_S K^0_S}$ results at $\langle m_{\mathrm{T}} \rangle \approx 1.03$ GeV/c and the $\Lambda\bar{\Lambda}$ results for $\langle m_{\mathrm{T}} \rangle \approx 1.95$ GeV/c. The radii for the ΛK fits in Figures A.3 and A.4 were fixed to (4.13 fm, 3.34 fm, 2.59 fm) for (0–10%, 10–30%, 30–50%), as shown in Table A.1. In both cases (λ_{Fix} left free or set to unity), this procedure forces the radii to be smaller than preferred by the fit algorithm, and reduces the magnitudes of $\Re f_0$ and $\Im f_0$ for all ΛK systems, and causes the sign of $\Re f_0$ to change for the $\Lambda \mathrm{K^0_S}$ analysis (from positive to negative).

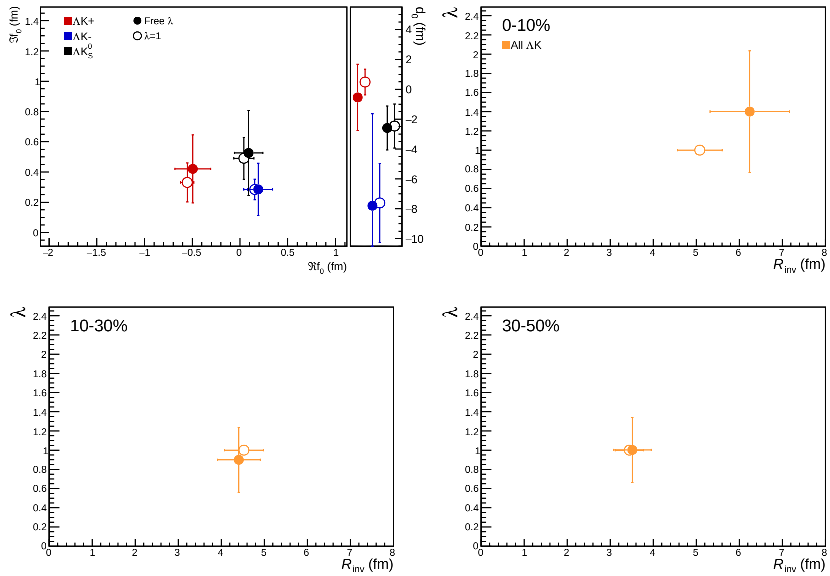

Figure A.2: Results shown for λ_{Fit} parameters left free (closed, circles) and fixed to 1 (open, circles). See text at beginning of section for color scheme information and Eq. 6.2 in Sec. 6.2 for more information on the λ_{Fit} parameter.

Fig. A.5 compares our normal fit results to those obtained when the correlation functions are built using the Stavinskiy method (see Sec. 5.7.2). As shown in the figure, with the exception of the d_0 parameters (which are difficult for us to resolve experimentally), the results from the two methods are within errors of each other. As implemented in this analysis, the Stavinskiy method does a good job of reducing the non-femtoscopic background, but does not completely eliminate it. Nonetheless, it is a simple and elegant method, and should be investigated further in the future.

Fig. A.6 shows the difference between sharing radii among all ΛK systems versus only sharing radii between the $\Lambda K^{\pm}$ systems. As shown in the figure, the $\Lambda K^{\pm}$ systems give consistent results whether or not the ΛK^0_S system is included in the fit. The ΛK^0_S system, however, gives significantly different results when fit by itself. The ΛK^0_S system suffers the most from low statistics, and is the most difficult to fit (for instance, when fit by itself, the λ_{Fit} parameter has to be limited between [0.6, 1.1] to give realistic results). As shown, when fit alone, the ΛK^0_S fit settles on much smaller

Centrality	Pair size (fm)		Single size (fm)		Pair size (fm)
	$K^0_S K^0_S$	$\Lambda\bar{\Lambda}$	Λ	K	ΛK
0–10%	5.07	2.90	3.59	2.05	4.13
10–30%	4.12	2.30	2.91	1.63	3.34
30–50%	3.19	1.8	2.26	1.27	2.59

Table A.1: ΛK source sizes estimated using single-particle K and Λ source sizes extracted from the $K^0_S K^0_S$ results at $\langle m_T \rangle \approx 1.03$ GeV/c and the $\Lambda\bar{\Lambda}$ results for $\langle m_T \rangle \approx 1.95$ GeV/c (see Fig. 7.10).

radii compared to the $\Lambda K^{\pm}$ systems. As we expect the ΛK^0_S system to share similar radii with the $\Lambda K^{\pm}$ systems, we choose to join the three together to combat the low statistics available to the ΛK^0_S. The purpose of this figure is mainly to demonstrate how the inclusion of the ΛK^0_S affects the $\Lambda K^{\pm}$ results, not the other way around.

Finally, Fig. A.7 shows the effect of using the experimental $\Xi^- K^{\pm}$ data compared to modeling it with a Coulomb-only curve for use in the residuals treatment (see Sec. 6.2). As shown, the results are consistent. The use of a the experimental data is preferable in that no assumption need to be made about the parent system's correlation function. However, the low statistics of the parent $\Xi^- K^{\pm}$ data (especially in the 30–50% centrality bin) could be reason to instead use the Coulomb-only curve. In our description, we choose to use the experimental data, although, as shown in the figure, the choice does not matter much.

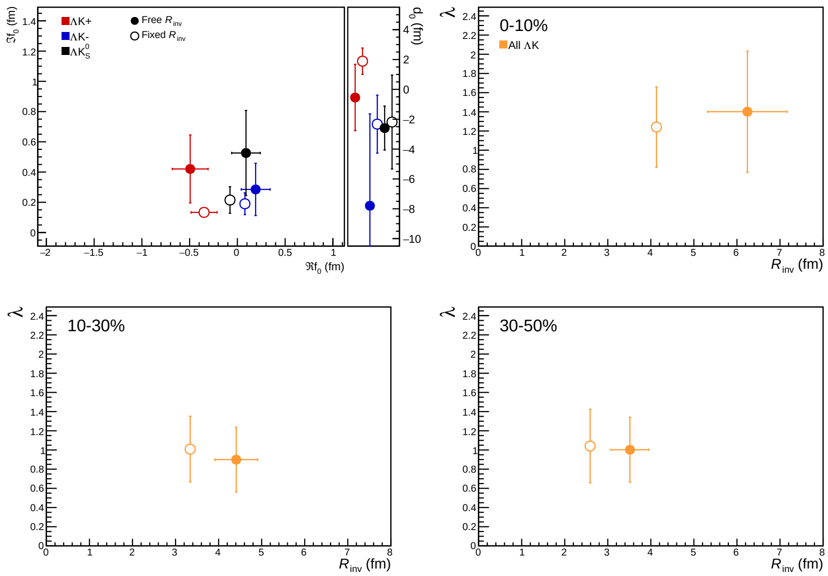

Figure A.3: Results shown for free (closed circles) and fixed radii (open circles) with λ_{Fit} left free. The fixed radii values were estimated using single-particle K and Λ source sizes extracted from the $\mathrm{K^0_S K^0_S}$ results, see Tab. A.1. See text at beginning of section for color scheme information.

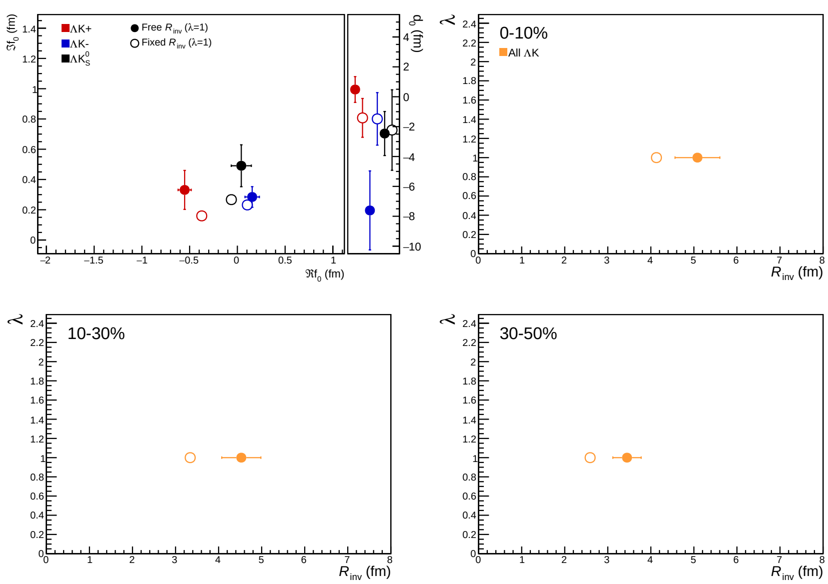

Figure A.4: Results shown for free (closed circles) and fixed radii (open circles) with λ_{Fit} fixed to unity. The fixed radii values were estimated using single-particle K and Λ source sizes extracted from the $\mathrm{K^0_S K^0_S}$ results, see Tab. A.1. See text at beginning of section for color scheme information.

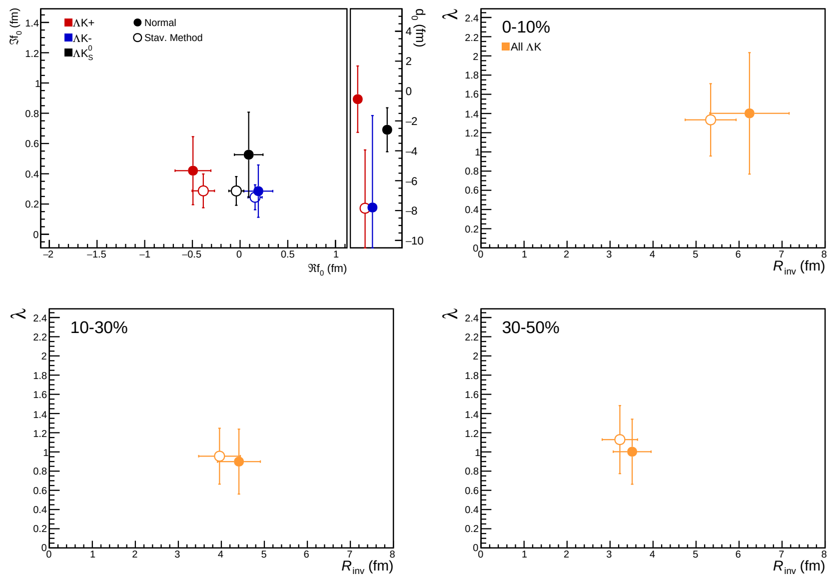

Figure A.5: Results shown for normal correlation function construction (closed, circles) and when built using the Stavinskiy method (open, circles). See text at beginning of section for color scheme information and Sec. 5.7.2 for more information on the Stavinskiy method.

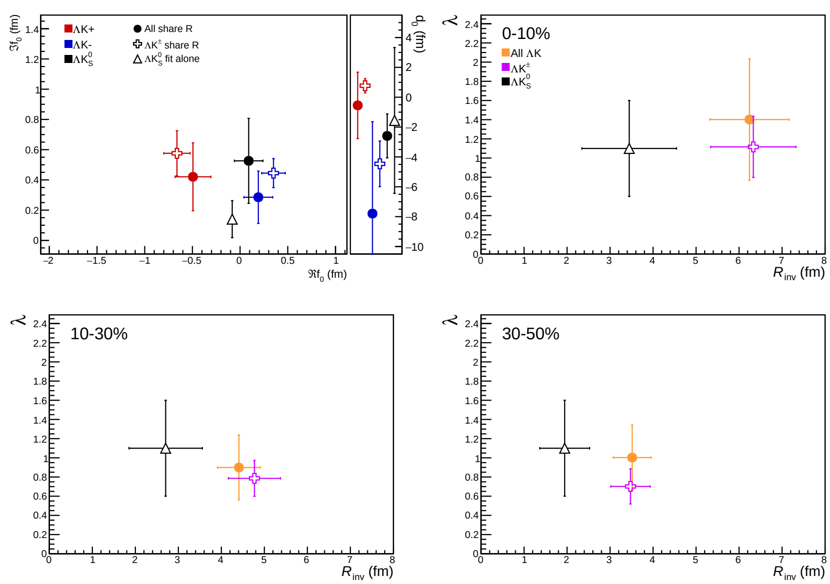

Figure A.6: Results shown for the case of all ΛK analyses sharing radii (closed, circles) and only the $\Lambda K^{\pm}$ analyses sharing radii (open, crossed), with the ΛK^0_S system fit separately (open, triangles). See text at beginning of section for color scheme information.

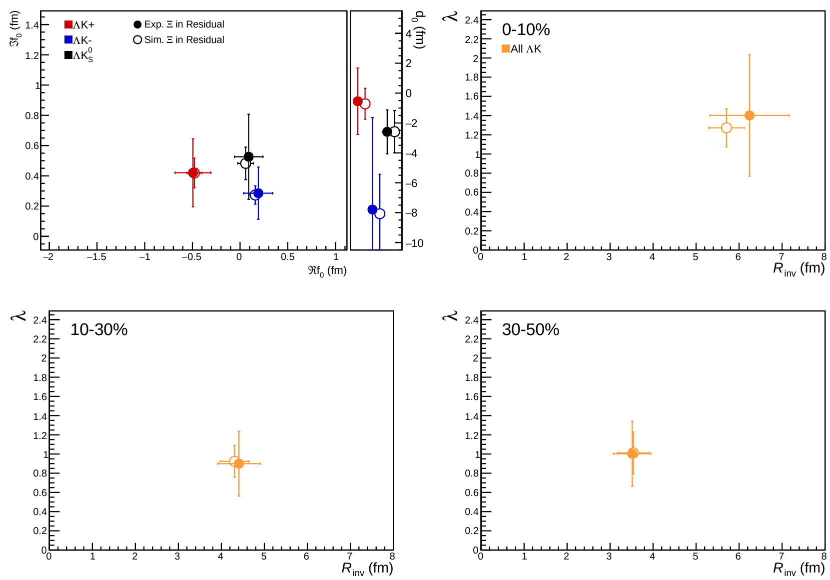

Figure A.7: Results shown when using experimental $\Xi^- K^\pm$ data (closed, circles) and when simulating the $\Xi^- K^\pm$ correlation function with a Coulomb-only curve (open, circles) for use in the treatment of the residual. See text at beginning of section for color scheme information, and Sec. 6.2 for more information on the $\Xi^- K^\pm$ simulation.

A.2 3 residual contributors included in fit

This section presents our final results, for which three residual contributors were assumed. These three contributors include: (Σ^0K, Ξ^0K, Ξ^-K) $\rightarrow$ ΛK. The figures presented do contain supplemental information to that presented in Sec. 7.1, but are here largely for convenience in comparing to the cases of including 10 (App. A.3) and no (App. A.4) residual contributors.

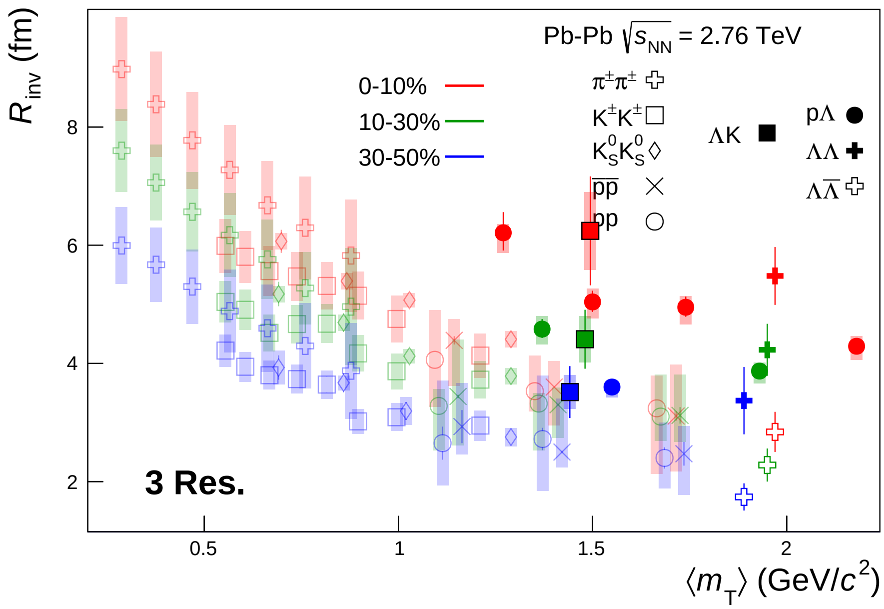

Figure A.8: 3 residual correlations in ΛK fits. Extracted R_{inv} fit parameters as a function of pair transverse mass (m_{T}) for various pair systems over several centralities. The ALICE published data [133] are shown with transparent, open symbols. The new ΛK results are shown with opaque, filled symbols. The m_{T} value for the ΛK system is an average of those for the ΛK^+, $\bar{\Lambda}K^-$, and ΛK^0_S systems.

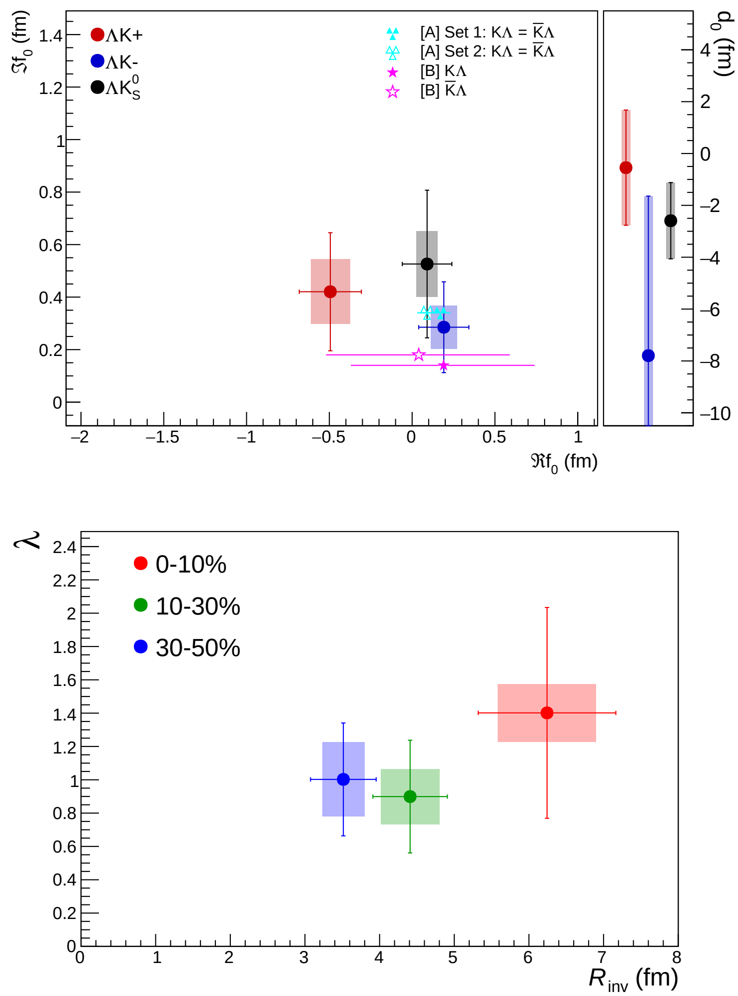

Figure A.9: Extracted fit parameters for the case of 3 residual contributors for all of our ΛK systems. [Top]: $\Im f_0$ vs. $\Re f_0$, together with d_0 to the right. [Bottom]: λ vs. Radius for the 0–10% (blue), 10–30% (green), and 30–50% (red) centrality bins. In the fit, all ΛK systems share common radii. The color scheme used in the panel are to be consistent with those in Fig. A.8. The cyan ([A] = Ref. [169]) and magenta ([B] = Ref. [170]) points show theoretical predictions made using chiral perturbation theory.

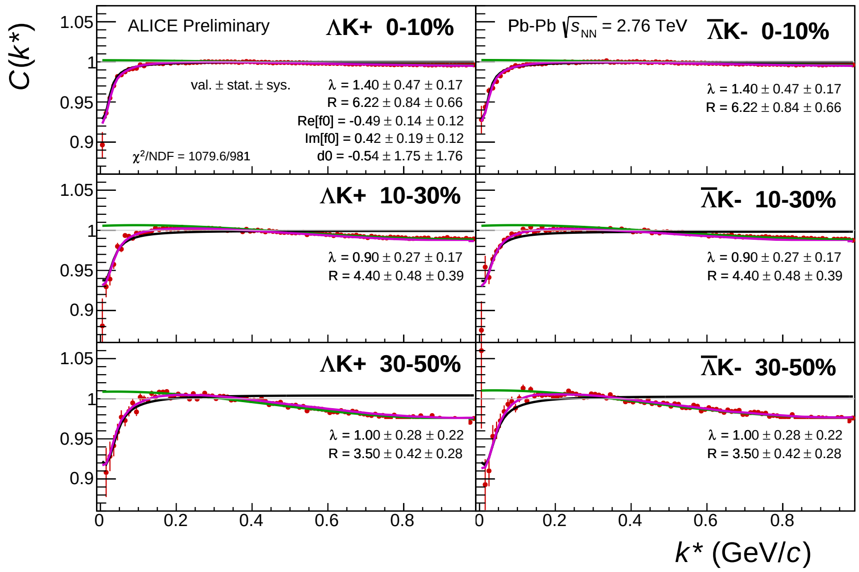

Figure A.10: Fit results, with 3 residual correlations included, for the ΛK^+ and $\overline{\Lambda} K^-$ data. The ΛK^+ data is shown in the left column, the $\overline{\Lambda} K^-$ in the right, and the rows differentiate the different centrality bins (0–10% in the top, 10–30% in the middle, and 30–50% in the bottom).

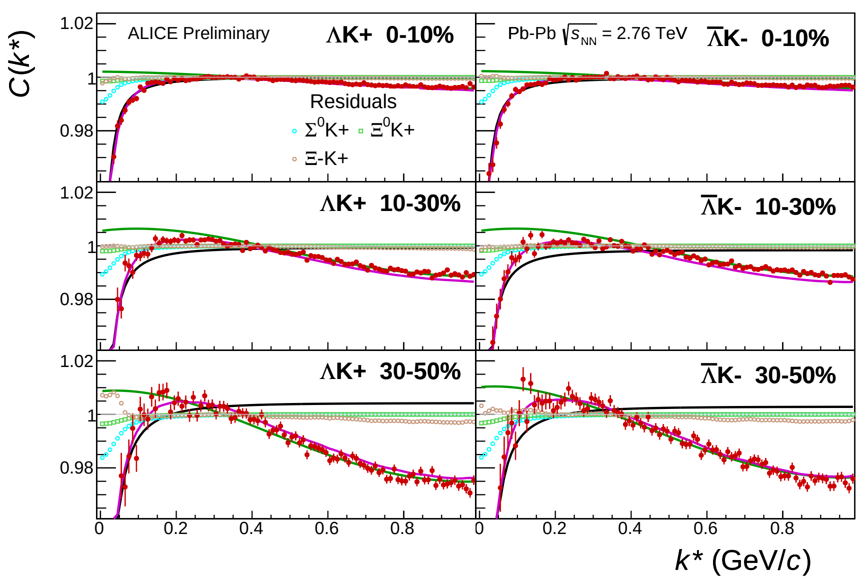

Figure A.11: Fit results with the 3 residual contributions shown, for the ΛK^+ and $\overline{\Lambda} K^-$ data. The ΛK^+ data is shown in the left column, the $\overline{\Lambda} K^-$ in the right, and the rows differentiate the different centrality bins (0–10% in the top, 10–30% in the middle, and 30–50% in the bottom).

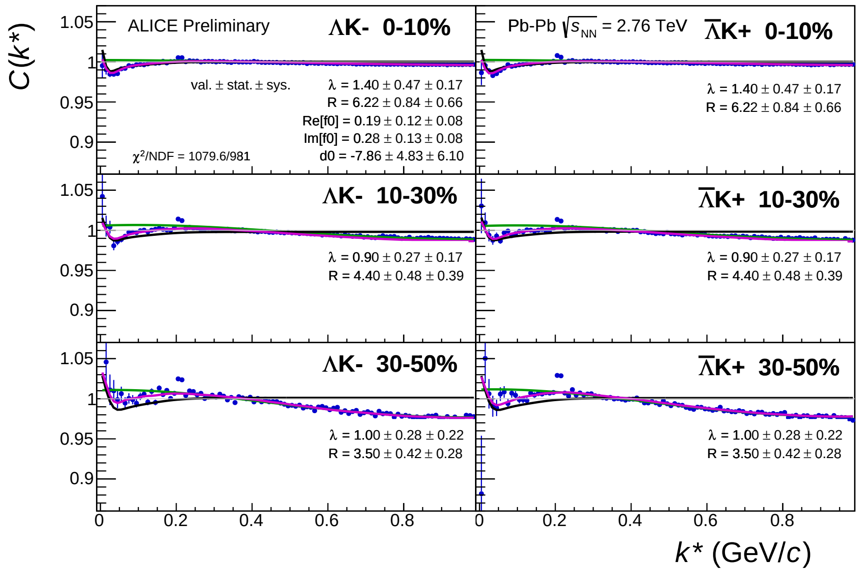

Figure A.12: Fit results, with 3 residual correlations included, for the ΛK^- and $\overline{\Lambda} K^+$ data. The ΛK^- data is shown in the left column, the $\overline{\Lambda} K^+$ in the right, and the rows differentiate the different centrality bins (0–10% in the top, 10–30% in the middle, and 30–50% in the bottom).

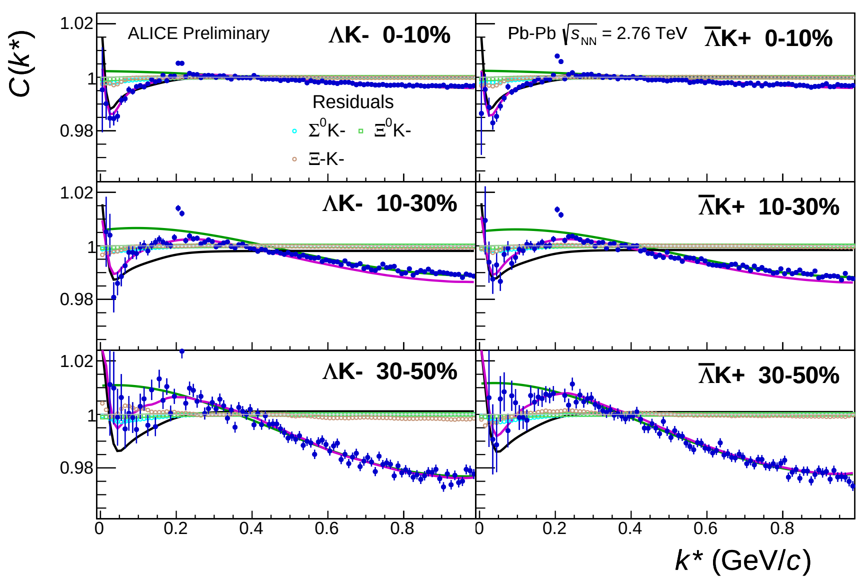

Figure A.13: Fit results with the 3 residual contributions shown, for the ΛK^- and $\overline{\Lambda} K^+$ data. The ΛK^- data is shown in the left column, the $\overline{\Lambda} K^+$ in the right, and the rows differentiate the different centrality bins (0–10% in the top, 10–30% in the middle, and 30–50% in the bottom).

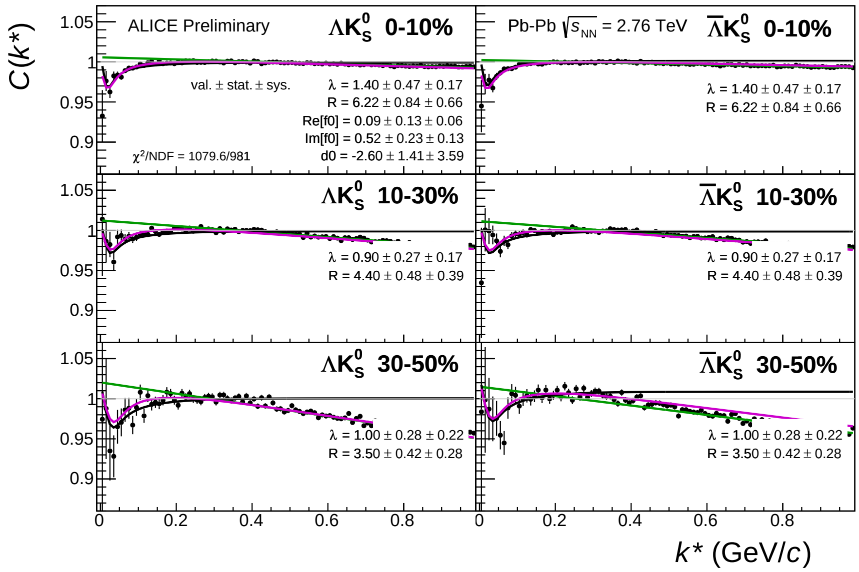

Figure A.14: Fit results, with 3 residual correlations included, for the ΛK^0_S and $\overline{\Lambda}K^0_S$ data. The ΛK^0_S data is shown in the left column, the $\overline{\Lambda}K^0_S$ in the right, and the rows differentiate the different centrality bins (0–10% in the top, 10–30% in the middle, and 30–50% in the bottom).

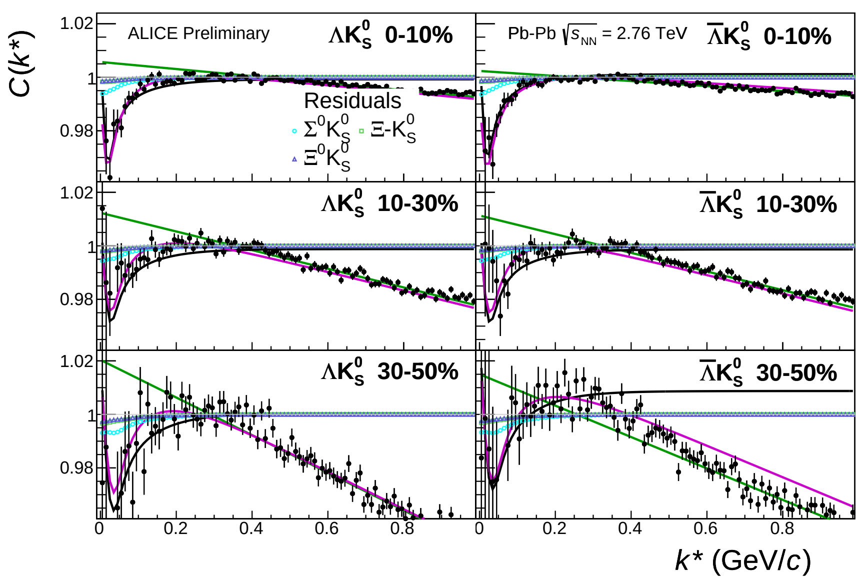

Figure A.15: Fit results with the 3 residual contributions shown, for the ΛK^0_S and $\overline{\Lambda}K^0_S$ data. The ΛK^0_S data is shown in the left column, the $\overline{\Lambda}K^0_S$ in the right, and the rows differentiate the different centrality bins (0–10% in the top, 10–30% in the middle, and 30–50% in the bottom).

A.3 10 residual contributors included in fit

This section presents fit results for which 10 residual contributors were assumed. These contributors include those shared by the three contributor case (App. A.2), (Σ^0K, Ξ^0K, Ξ^-K) → ΛK, and additionally the contributors ($\Sigma^{*(+,-,0)}K^{*0}$, ΛK^{*0}, $\Sigma^0 K^{*0}$, $\Xi^0 K^{*0}$, $\Xi^- K^{*0}$) → ΛK. As stated at the beginning of App. A, most of the Σ^* and K^* resonances will have decayed before kinetic freeze-out, and therefore it is best to treat Λ and K particles originating from these resonances as primary, i.e. only using three residual contributors. However, it is still interesting to examine how these additional shorter lived sources affect our fit result, as presented below. For a comparison of these results to the case of three residual contributors, see Fig. A.1 in App. A.1

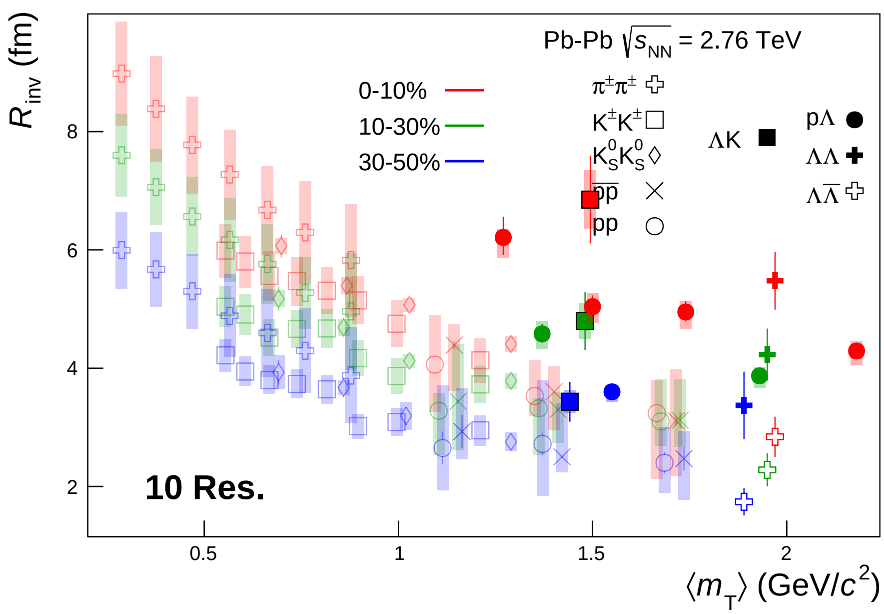

Figure A.16: 10 residual correlations in ΛK fits. Extracted R_{inv} fit parameters as a function of pair transverse mass (m_{T}) for various pair systems over several centralities. The ALICE published data [133] are shown with transparent, open symbols. The new ΛK results are shown with opaque, filled symbols. The m_{T} value for the ΛK system is an average of those for the ΛK^+, $\bar{\Lambda}K^-$, and ΛK^0_S systems.

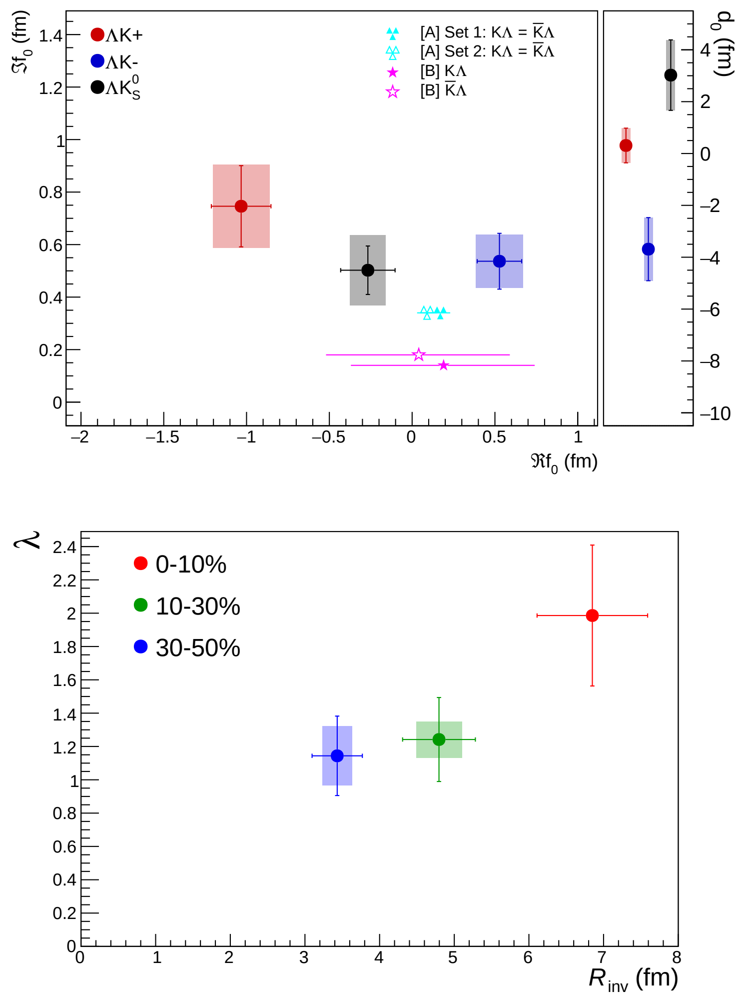

Figure A.17: Extracted fit parameters for the case of 10 residual contributors for all of our ΛK systems. [Top]: $\Im f_0$ vs. $\Re f_0$, together with d_0 to the right. [Bottom]: λ vs. Radius for the 0–10% (blue), 10–30% (green), and 30–50% (red) centrality bins. In the fit, all ΛK systems share common radii. The color scheme used in the panel are to be consistent with those in Fig. A.16. The cyan ([A] = Ref. [169]) and magenta ([B] = Ref. [170]) points show theoretical predictions made using chiral perturbation theory.

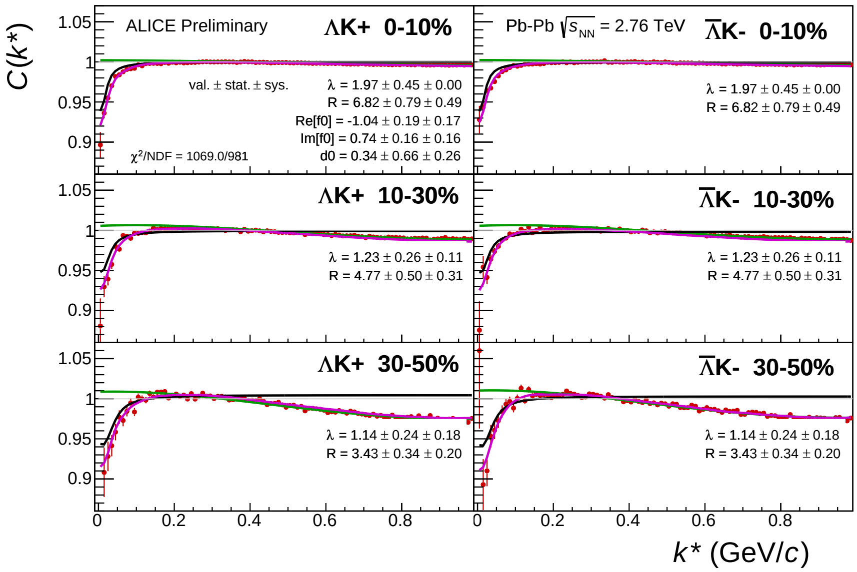

Figure A.18: Fit results, with 10 residual correlations included, for the ΛK^+ and $\overline{\Lambda}K^-$ data. The ΛK^+ data is shown in the left column, the $\overline{\Lambda}K^-$ in the right, and the rows differentiate the different centrality bins (0–10% in the top, 10–30% in the middle, and 30–50% in the bottom).

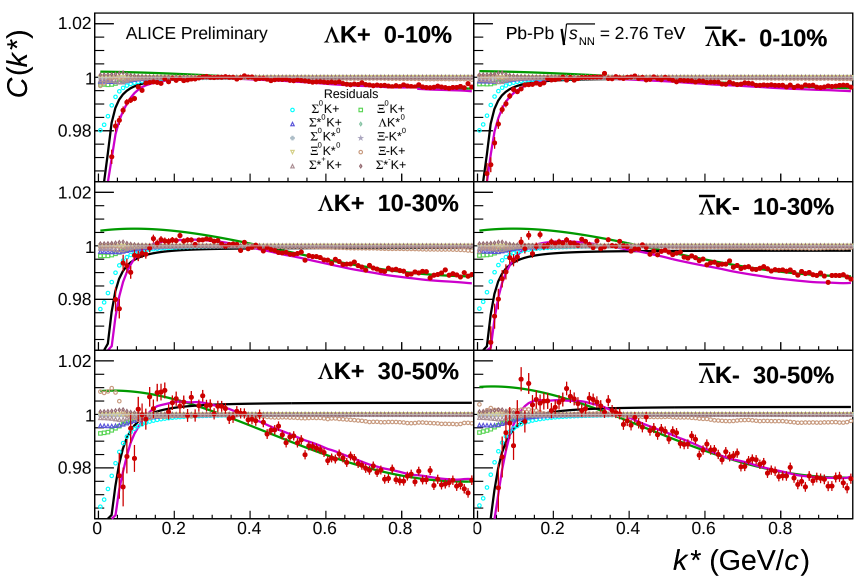

Figure A.19: Fit results with the 10 residual contributions shown, for the ΛK^+ and $\overline{\Lambda}K^-$ data. The ΛK^+ data is shown in the left column, the $\overline{\Lambda}K^-$ in the right, and the rows differentiate the different centrality bins (0–10% in the top, 10–30% in the middle, and 30–50% in the bottom).

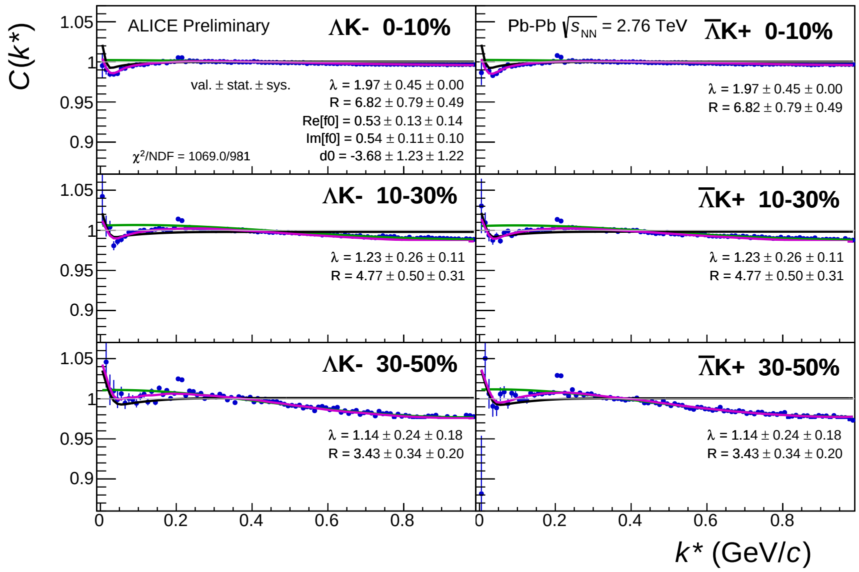

Figure A.20: Fit results, with 10 residual correlations included, for the ΛK^- and $\overline{\Lambda}K^+$ data. The ΛK^- data is shown in the left column, the $\overline{\Lambda}K^+$ in the right, and the rows differentiate the different centrality bins (0–10% in the top, 10–30% in the middle, and 30–50% in the bottom).

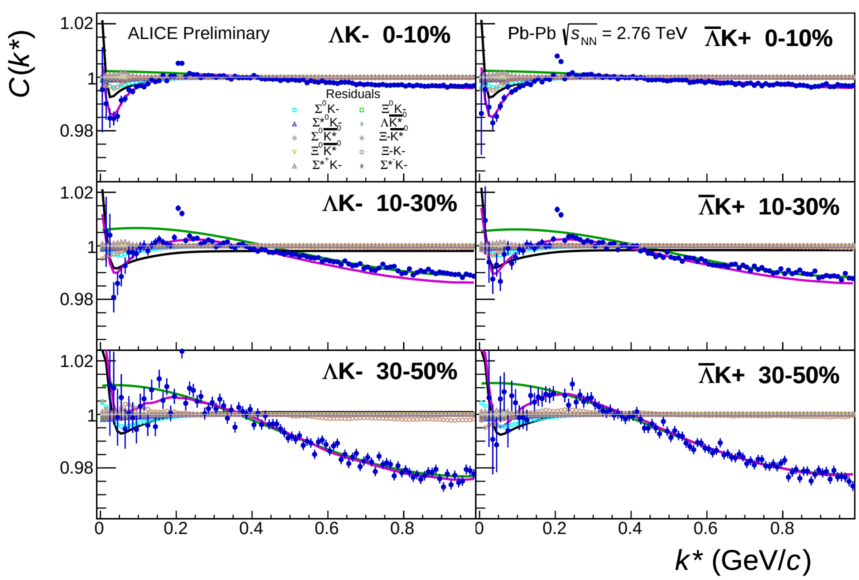

Figure A.21: Fit results with the 10 residual contributions shown, for the ΛK^- and $\overline{\Lambda}K^+$ data. The ΛK^- data is shown in the left column, the $\overline{\Lambda}K^+$ in the right, and the rows differentiate the different centrality bins (0–10% in the top, 10–30% in the middle, and 30–50% in the bottom).

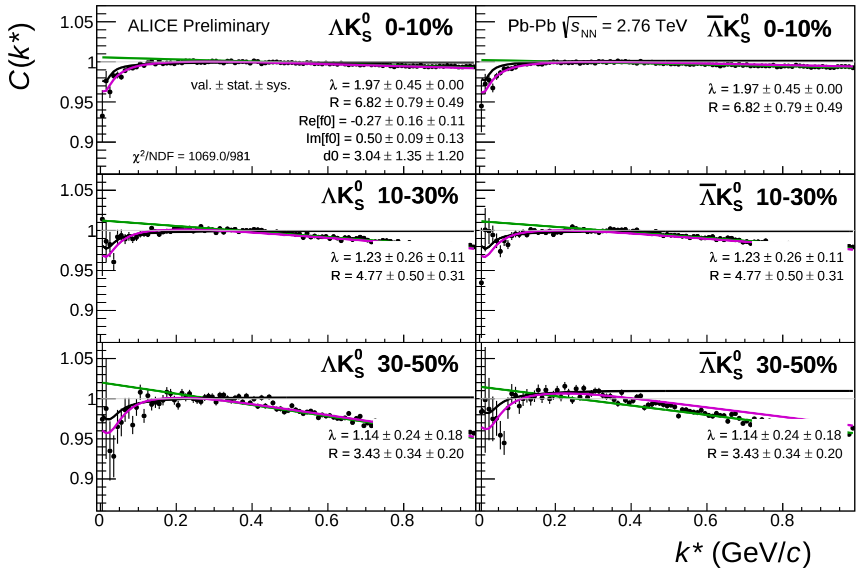

Figure A.22: Fit results, with 10 residual correlations included, for the ΛK^0_S and $\overline{\Lambda}K^0_S$ data. The ΛK^0_S data is shown in the left column, the $\overline{\Lambda}K^0_S$ in the right, and the rows differentiate the different centrality bins (0–10% in the top, 10–30% in the middle, and 30–50% in the bottom).

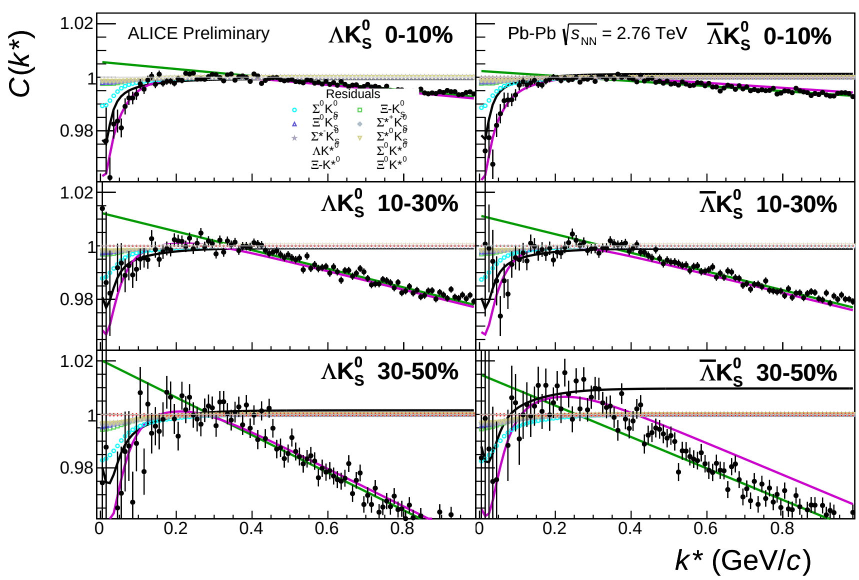

Figure A.23: Fit results with the 10 residual contributions shown, for the ΛK^0_S and $\overline{\Lambda}K^0_S$ data. The ΛK^0_S data is shown in the left column, the $\overline{\Lambda}K^0_S$ in the right, and the rows differentiate the different centrality bins (0–10% in the top, 10–30% in the middle, and 30–50% in the bottom).

A.4 No residual contributors included in fit

This section presents fit results for which no residual contributors were assumed. This is a typical starting point for femtoscopic analyses such as ours, and the effects of residual contributions are sometimes ignored. Therefore, it is interesting to observe the effects of neglecting residual feed-down from our fit description. For a comparison of these results to the case of three residual contributors, see Fig. A.1 in App. A.1

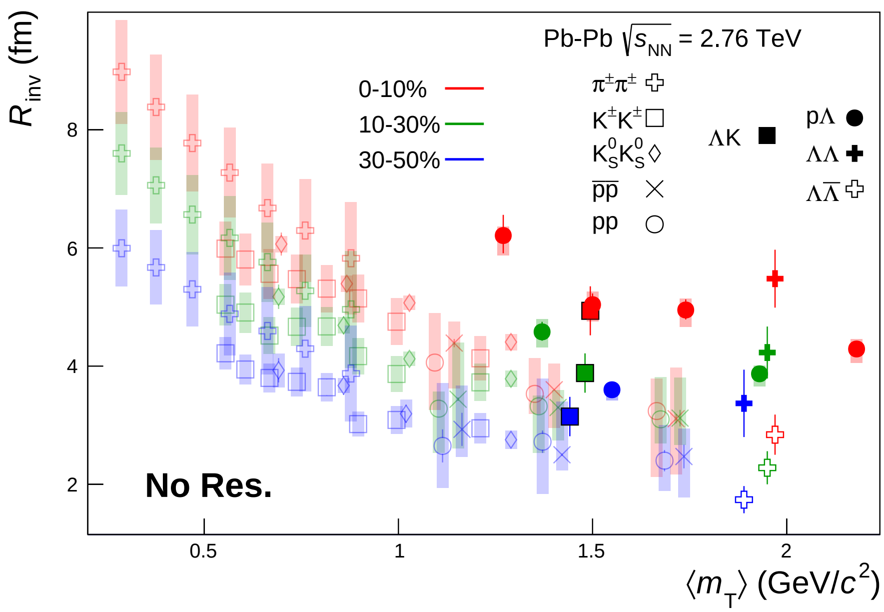

Figure A.24: No residual correlations in ΛK fits. Extracted R_{inv} fit parameters as a function of pair transverse mass (m_{T}) for various pair systems over several centralities. The ALICE published data [133] are shown with transparent, open symbols. The new ΛK results are shown with opaque, filled symbols. The m_{T} value for the ΛK system is an average of those for the ΛK^+, $\overline{\Lambda}K^-$, and ΛK^0_S systems.

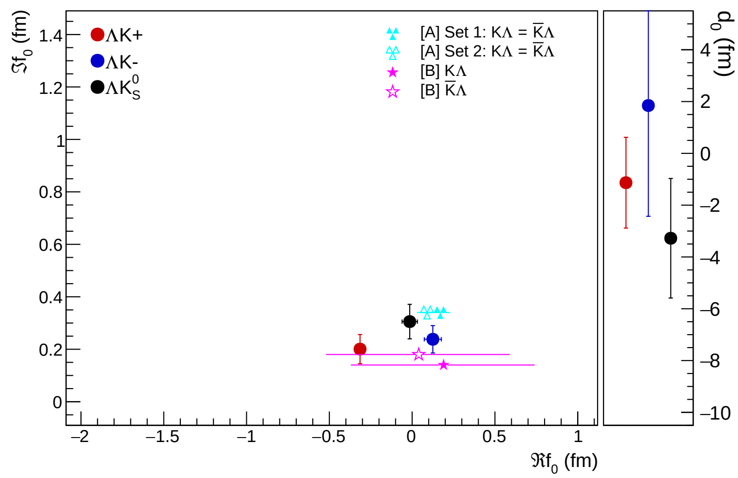

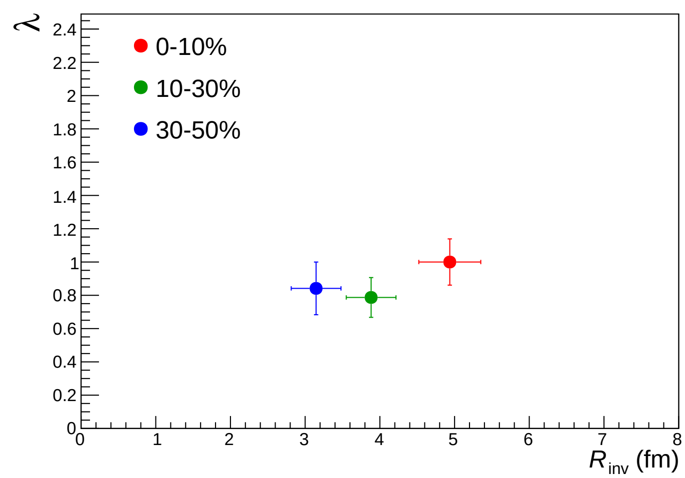

Figure A.25: Extracted fit parameters for the case of no residual contributors for all of our ΛK systems. [Top]: $\Im f_0$ vs. $\Re f_0$, together with d_0 to the right. [Bottom]: λ vs. Radius for the 0–10% (blue), 10–30% (green), and 30–50% (red) centrality bins. In the fit, all ΛK systems share common radii. The color scheme used in the panel are to be consistent with those in Fig. A.24. The cyan ([A] = Ref. [169]) and magenta ([B] = Ref. [170]) points show theoretical predictions made using chiral perturbation theory.

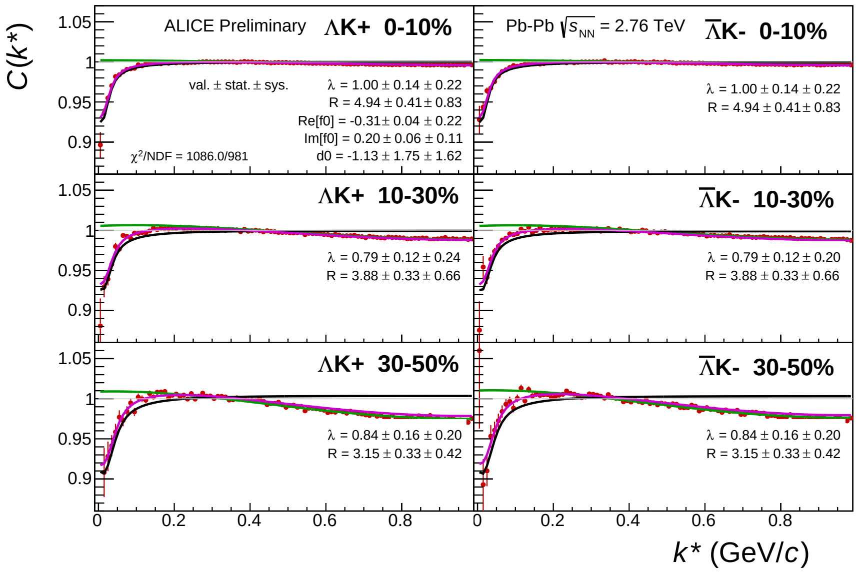

Figure A.26: Fit results, with no residual correlations included, for the ΛK^+ and $\overline{\Lambda}K^-$ data. The ΛK^+ data is shown in the left column, the $\overline{\Lambda}K^-$ in the right, and the rows differentiate the different centrality bins (0–10% in the top, 10–30% in the middle, and 30–50% in the bottom).

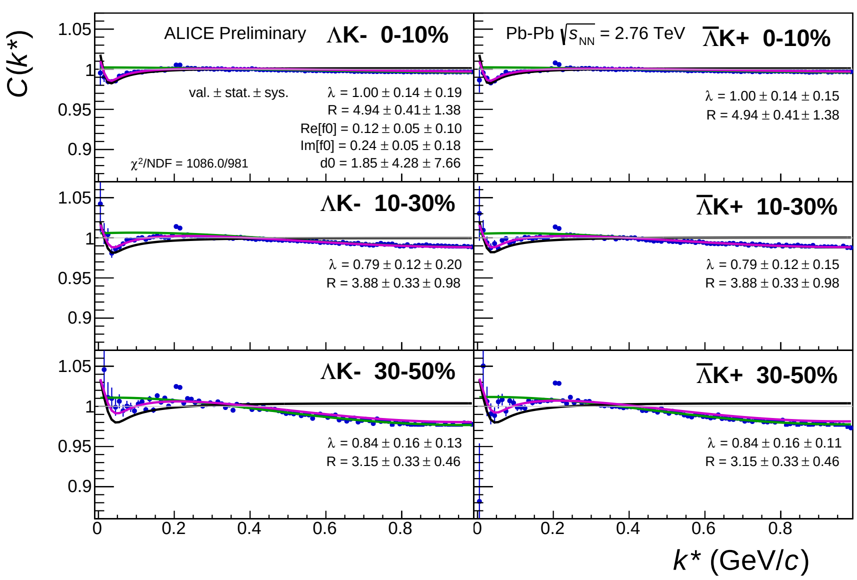

Figure A.27: Fit results, with no residual correlations included, for the ΛK^- and $\overline{\Lambda}K^+$ data. The ΛK^- data is shown in the left column, the $\overline{\Lambda}K^+$ in the right, and the rows differentiate the different centrality bins (0–10% in the top, 10–30% in the middle, and 30–50% in the bottom).

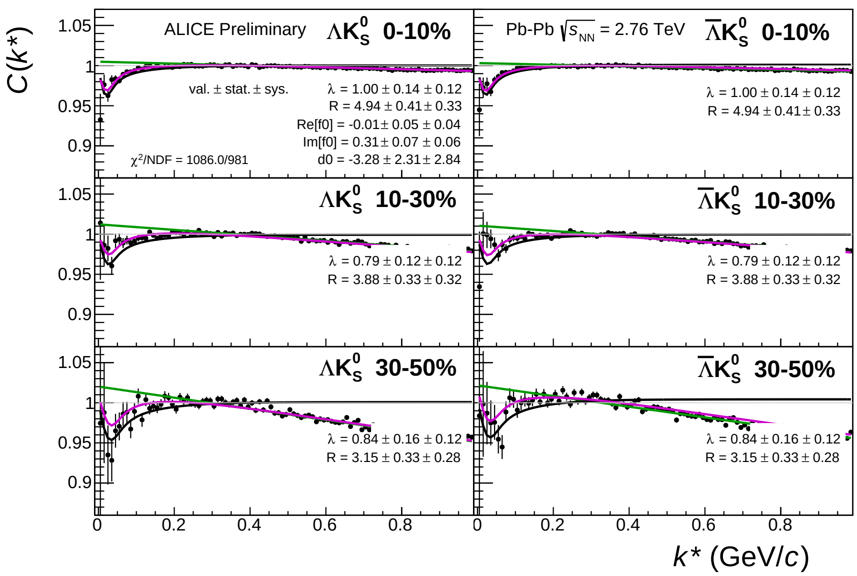

Figure A.28: Fit results, with no residual correlations included, for the ΛK^0_S and $\overline{\Lambda} K^0_S$ data. The ΛK^0_S data is shown in the left column, the $\overline{\Lambda} K^0_S$ in the right, and the rows differentiate the different centrality bins (0–10% in the top, 10–30% in the middle, and 30–50% in the bottom).

Appendix B: Spherical Harmonics

This appendix shows a spherical harmonic decomposition of our ΛK correlation functions; see Sec. 4.3.1 for a more detailed introduction to spherical harmonics in femtoscopy. For our purposes, the most interesting components are C_{00} and $\Re C_{11}$, which are presented in Figures B.1 - B.3. In each of the figures, the left column shows C_{00}, the right column $\Re C_{11}$, and the rows separate the centrality bins. For the the 0–10% bin, results are also included from a THERMINATOR 2 simulation for an impact parameter $b = 2$ fm (gold stars) and assumed scattering parameters ($\Re f_0$, $\Im f_0$, d_0) = (-1.16, 0.51, 1.08), (0.41, 0.47, -4.89), and (-0.41, 0.20, 2.08) for the ΛK^+, ΛK^-, and ΛK^0_S systems, respectively. The coefficient C_{00} quantifies the overall angle-integrated strength of the correlation function, similar to that studied in our 1D analysis. The $\Re C_{11}$ term is sensitive to the asymmetry in the outward direction, a component interesting for non-identical particle studies. In our analysis, we have taken the Λ to be the first particle in our pairs, and a negative value of $\Re C_{11}$ signifies the Λ particles are emitted, on average, further out and/or earlier than the K mesons. For completeness, the first six components of the spherical harmonic decompositions are shown in Figures B.4 - B.6

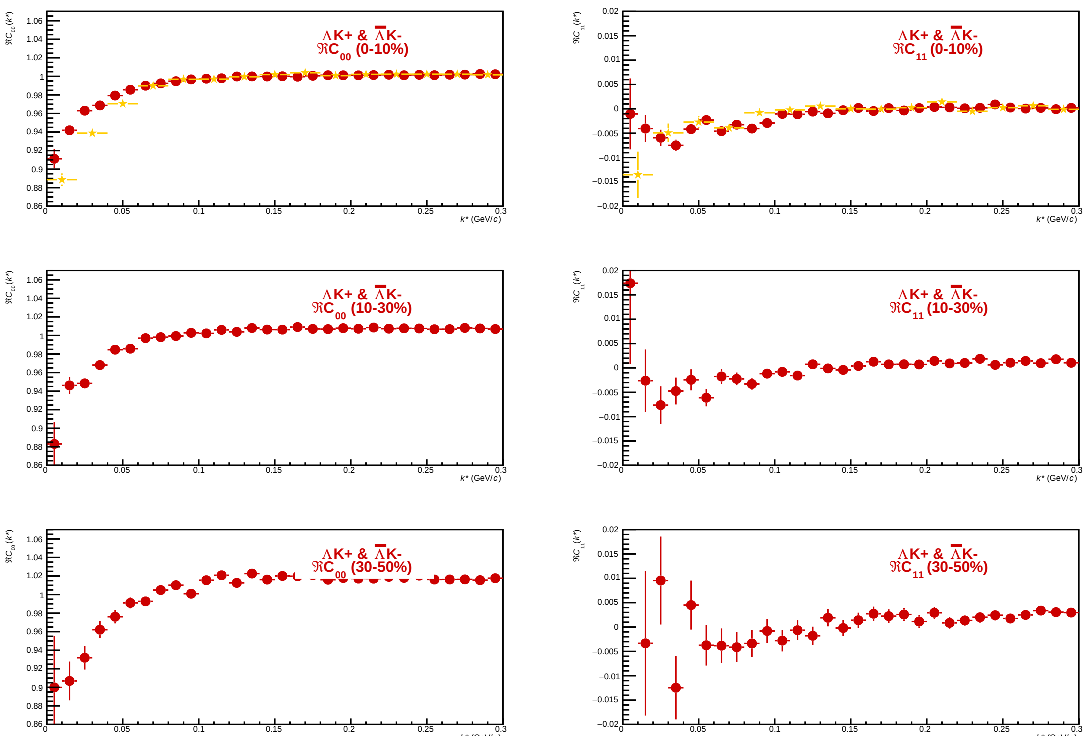

Figure B.1: C_{00} (left) and $\Re C_{11}$ (right) components of a spherical harmonic decomposition of the ΛK^{+} correlation function for the 0–10% (top), 10–30% (middle), and 30–50% (bottom) centrality bins. For the the 0–10% bin, results are also included from a THERMINATOR 2 simulation for an impact parameter $b = 2$ fm (gold stars) and assumed scattering parameters ($\Re f_0$, $\Im f_0$, d_0) = (-1.16, 0.51, 1.08).

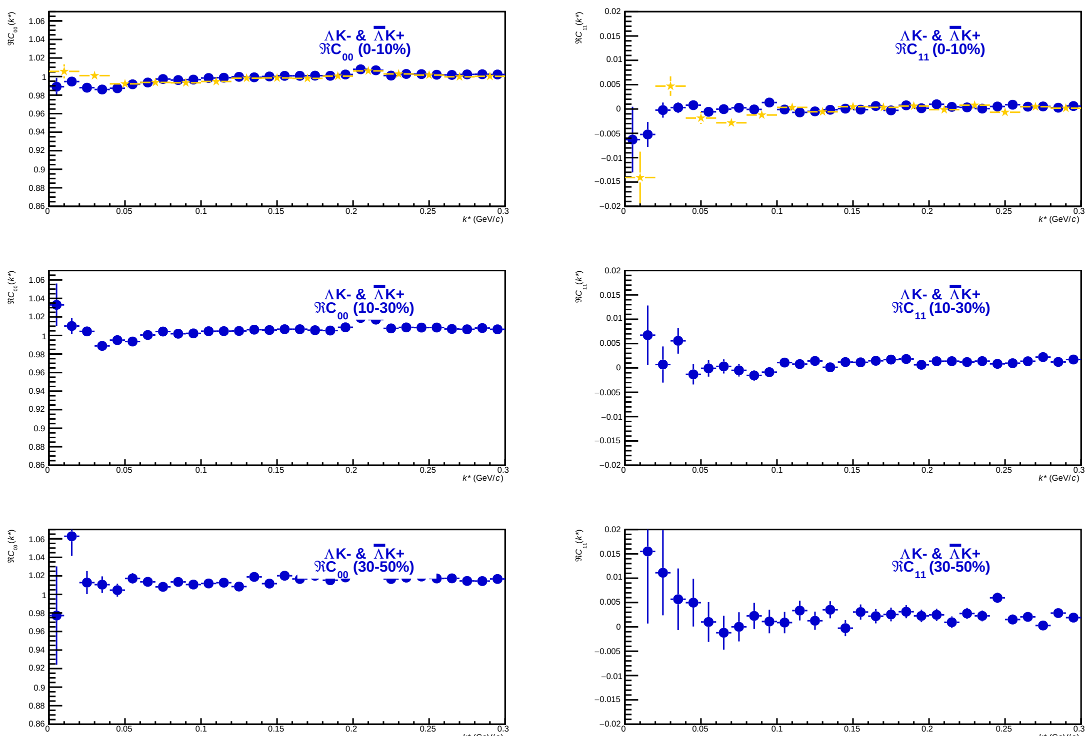

Figure B.2: C_{00} (left) and $\Re C_{11}$ (right) components of a spherical harmonic decomposition of the ΛK$^-$ correlation function for the 0–10% (top), 10–30% (middle), and 30–50% (bottom) centrality bins. For the the 0–10% bin, results are also included from a THERMINATOR 2 simulation for an impact parameter $b = 2$ fm (gold stars) and assumed scattering parameters ($\Re f_0$, $\Im f_0$, d_0) = (0.41, 0.47, -4.89).

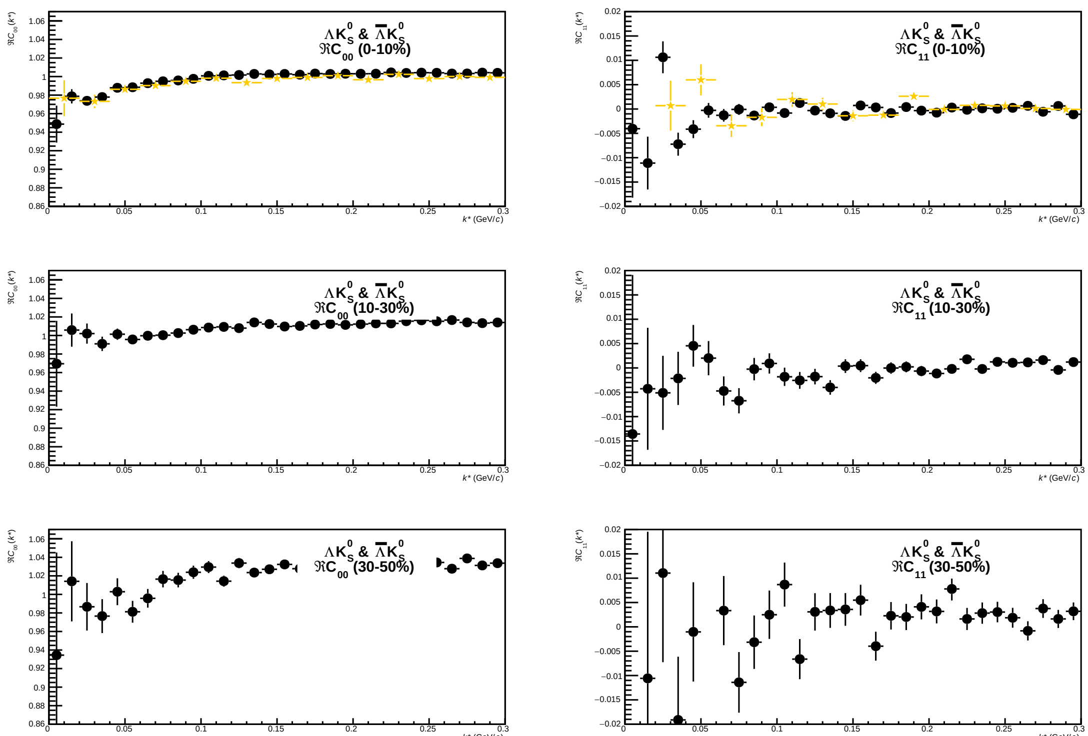

Figure B.3: C_{00} (left) and $\Re C_{11}$ (right) components of a spherical harmonic decomposition of the ΛK^0_S correlation function for the 0–10% (top), 10–30% (middle), and 30–50% (bottom) centrality bins. For the the 0–10% bin, results are also included from a THERMINATOR 2 simulation for an impact parameter $b = 2$ fm (gold stars) and assumed scattering parameters ($\Re f_0$, $\Im f_0$, d_0) = (-0.41, 0.20, 2.08).

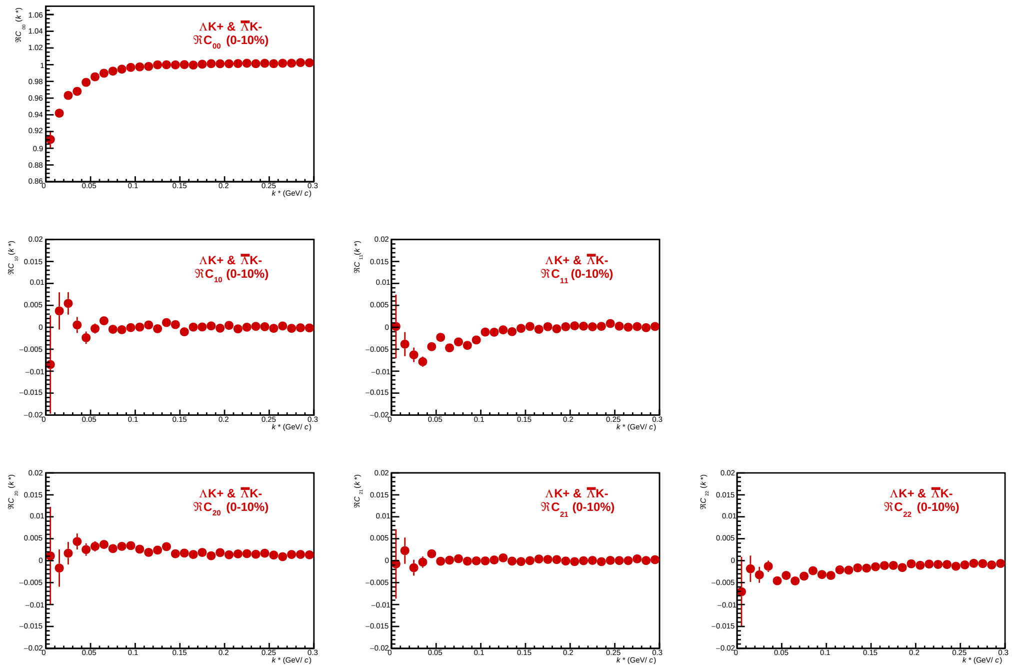

(a) Real components, $\Re C_{lm}$

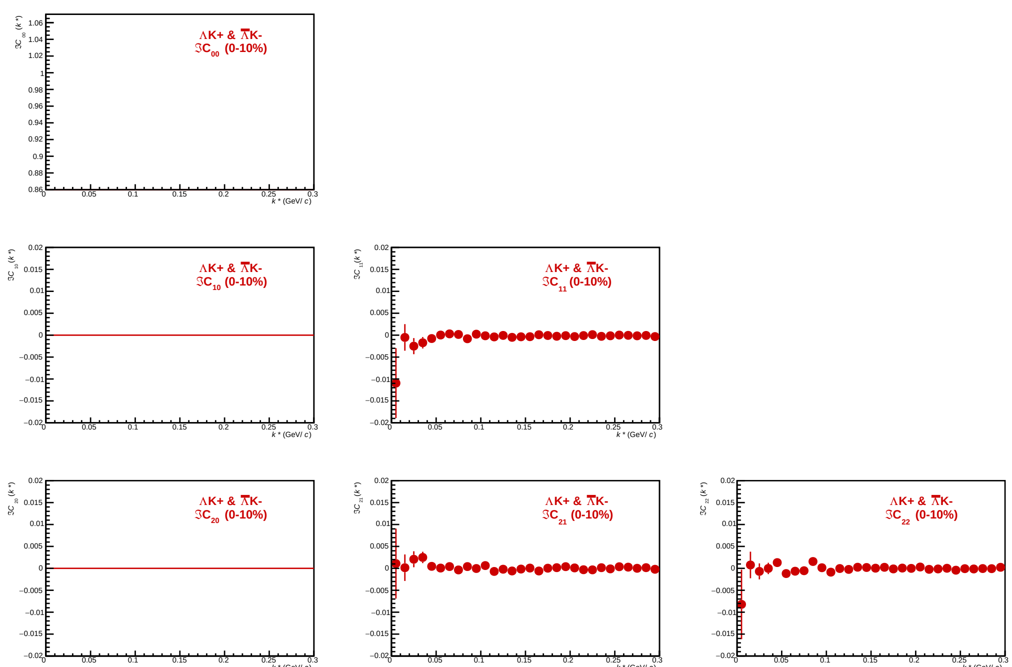

(b) Imaginary components, $\Im C_{lm}$

Figure B.4: First six components ($C_{00}, C_{10}, C_{11}, C_{20}, C_{21}, C_{22}$) of the spherical harmonic decomposition of the ΛK^{+} correlation function for the 0–10% centrality bin. Note, $\Im C_{00}$, $\Im C_{10}$, and $\Im C_{20}$ are zero by definition.

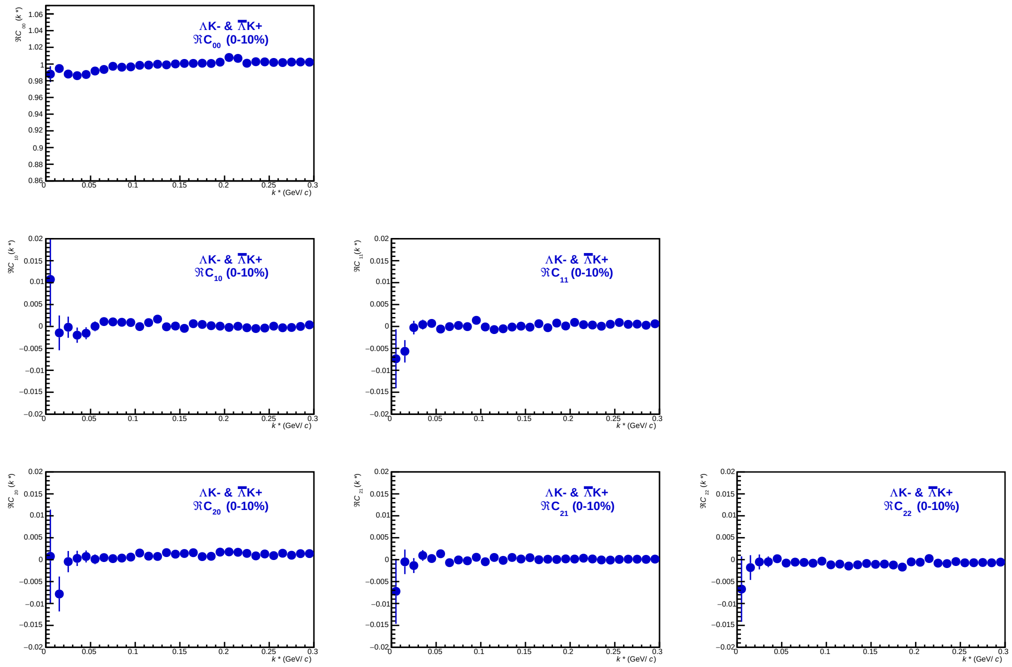

(a) Real components, $\Re C_{lm}$

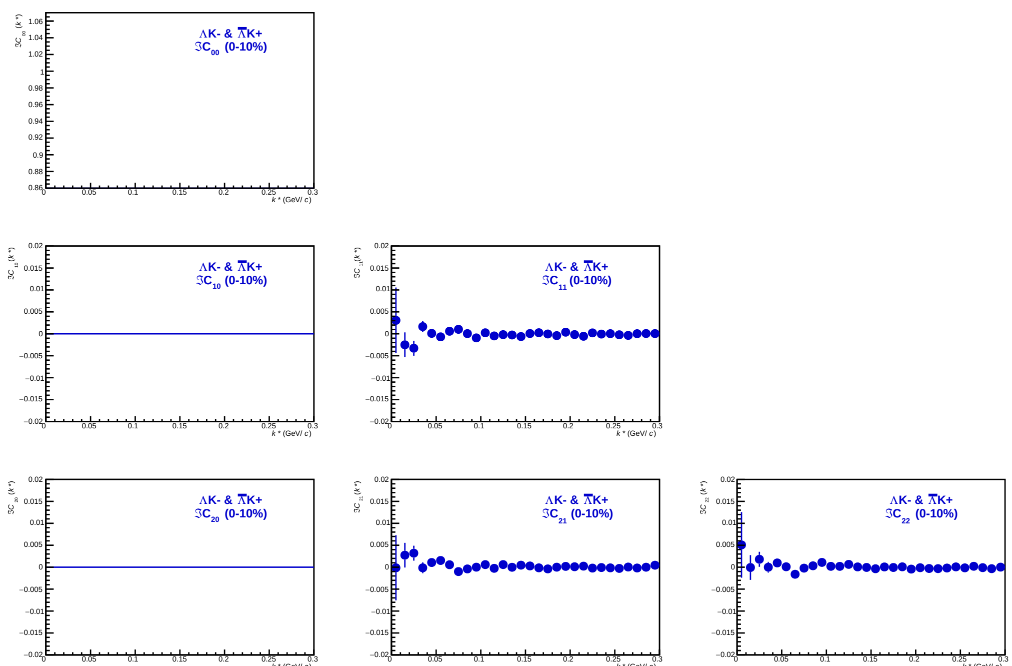

(b) Imaginary components, $\Im C_{lm}$

Figure B.5: First six components $(C_{00}, C_{10}, C_{11}, C_{20}, C_{21}, C_{22})$ of the spherical harmonic decomposition of the $\Lambda\mathrm{K}^-$ correlation function for the 0–10% centrality bin. Note, $\Im C_{00}$, $\Im C_{10}$, and $\Im C_{20}$ are zero by definition.

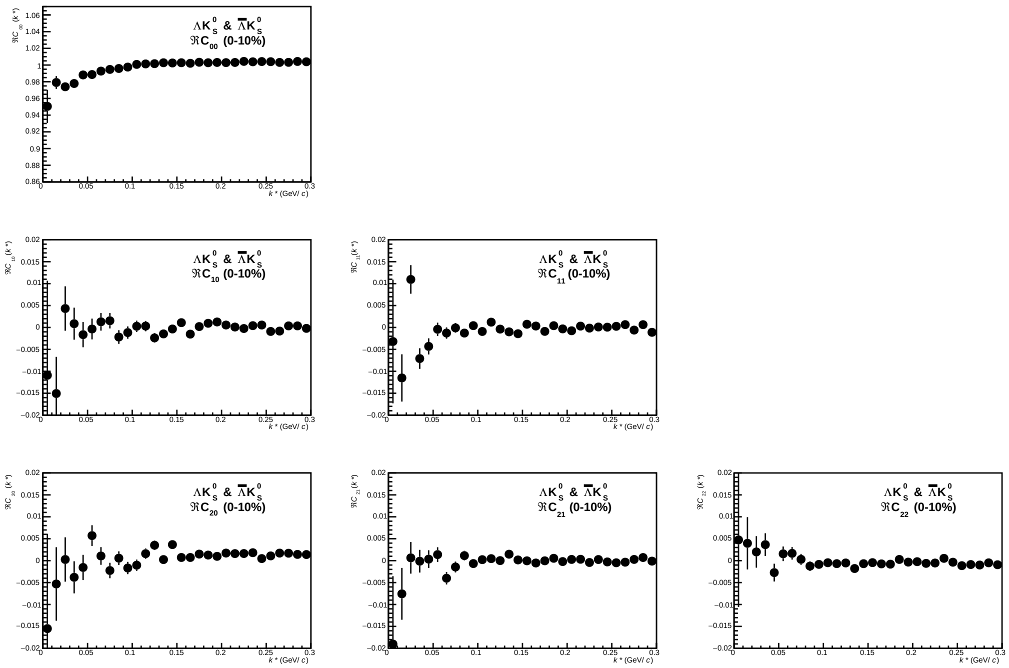

(a) Real components, $\Re C_{lm}$

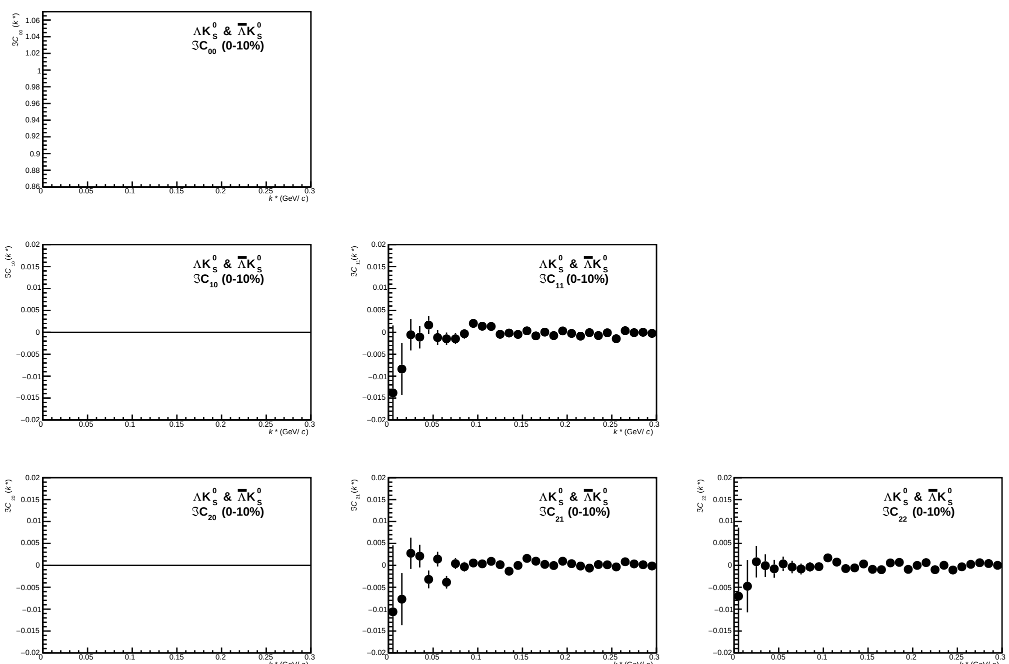

(b) Imaginary components, $\Im C_{lm}$

Figure B.6: First six components $(C_{00}, C_{10}, C_{11}, C_{20}, C_{21}, C_{22})$ of the spherical harmonic decomposition of the ΛK^0_S correlation function for the 0–10% centrality bin. Note, $\Im C_{00}$, $\Im C_{10}$, and $\Im C_{20}$ are zero by definition.

Appendix C: Useful Gaussian Integrals

C.1 Simple univariate Gaussian integral

$$
\begin{aligned}
I &= \int_{-\infty}^{\infty} e^{-x^2/2\sigma^2} dx \\
\rightarrow I^2 &= \int_{-\infty}^{\infty} e^{-x^2/2\sigma^2} dx \int_{-\infty}^{\infty} e^{-y^2/2\sigma^2} dy = \int_{-\infty}^{\infty}\int_{-\infty}^{\infty} e^{-(x^2+y^2)/2\sigma^2} dx dy \\
&= \int_{0}^{\infty}\int_{0}^{2\pi} e^{-r^2/2\sigma^2} r dr d\theta = -2\pi\sigma^2 \int_{0}^{\infty} e^{-r^2/2\sigma^2} \frac{-r}{\sigma^2} dr = 2\pi\sigma^2 \\
\Rightarrow I &= \sigma\sqrt{2\pi}
\end{aligned}
\tag{C.1}
$$

This also implies

$$\int_{-\infty}^{\infty} e^{-(x-\mu)^2/2\sigma^2} dx = \sigma\sqrt{2\pi} \tag{C.2}$$

This can be shown by making the substitution $x \rightarrow x - \mu$; but, intuitively this makes sense, as the area under a Gaussian curve does not depend on where the curve is located.

C.2 Product of two univariate Gaussian integrals

The purpose of this section is to derive the integral of the product of two Gaussian integrals

$$\int_{-\infty}^{\infty} f(x)g(x)dx = \int_{-\infty}^{\infty} \frac{1}{\sigma_f\sqrt{2\pi}} e^{-\frac{(x-\mu_f)^2}{2\sigma_f^2}} \frac{1}{\sigma_g\sqrt{2\pi}} e^{-\frac{(x-\mu_g)^2}{2\sigma_g^2}} \tag{C.3}$$

$$
\begin{aligned}
f(x) &= \frac{1}{\sigma_f\sqrt{2\pi}} \exp\left[-\frac{(x-\mu_f)^2}{2\sigma_f^2}\right] \\
g(x) &= \frac{1}{\sigma_g\sqrt{2\pi}} \exp\left[-\frac{(x-\mu_g)^2}{2\sigma_g^2}\right] \\
\Rightarrow f(x)g(x) &= \frac{1}{2\pi\sigma_f\sigma_g} \exp\left[-\frac{(x-\mu_f)^2}{2\sigma_f^2} - \frac{(x-\mu_g)^2}{2\sigma_g^2}\right] \\
&\equiv \frac{1}{2\pi\sigma_f\sigma_g} \exp[-\beta]
\end{aligned} \tag{C.4}
$$

$$
\begin{aligned}
\beta &= \frac{(x-\mu_f)^2}{2\sigma_f^2} + \frac{(x-\mu_g)^2}{2\sigma_g^2} \\
&= \frac{2\sigma_g^2[x^2 - 2\mu_f x + \mu_f^2] + 2\sigma_f^2[x^2 - 2\mu_g x + \mu_g^2]}{4\sigma_f^2\sigma_g^2} \\
&= \frac{(\sigma_f^2+\sigma_g^2)x^2 - 2(\mu_f\sigma_g^2 + \mu_g\sigma_f^2)x + \mu_f^2\sigma_g^2 + \mu_g\sigma_f^2}{2\sigma_f^2\sigma_g^2} \\
&= \frac{x^2 - 2\frac{\mu_f\sigma_g^2+\mu_g\sigma_f^2}{\sigma_f^2+\sigma_g^2}x + \frac{\mu_f^2\sigma_g^2+\mu_g^2\sigma_f^2}{\sigma_f^2+\sigma_g^2}}{2\frac{\sigma_f^2\sigma_g^2}{\sigma_f^2+\sigma_g^2}} \\
\text{Define} : \alpha &\equiv \frac{\mu_f\sigma_g^2+\mu_g\sigma_f^2}{\sigma_f^2+\sigma_g^2} \Rightarrow \beta = \frac{(x^2 - 2\alpha x + \alpha^2) - \alpha^2 + \frac{\mu_f^2\sigma_g^2+\mu_g^2\sigma_f^2}{\sigma_f^2+\sigma_g^2}}{2\frac{\sigma_f^2\sigma_g^2}{\sigma_f^2+\sigma_g^2}}
\end{aligned} \tag{C.5}
$$

$$
\begin{aligned}
\frac{\mu_f^2\sigma_g^2+\mu_g^2\sigma_f^2}{\sigma_f^2+\sigma_g^2} - \alpha^2 &= \frac{\mu_f^2\sigma_g^2+\mu_g^2\sigma_f^2}{\sigma_f^2+\sigma_g^2} - \left(\frac{\mu_f\sigma_g^2+\mu_g\sigma_f^2}{\sigma_f^2+\sigma_g^2}\right)^2 \\
&= \frac{1}{(\sigma_f^2+\sigma_g^2)^2}\left[(\mu_f^2\sigma_g^2+\mu_g^2\sigma_f^2)(\sigma_f^2+\sigma_g^2) - (\mu_f\sigma_g^2+\mu_g\sigma_f^2)^2\right] \\
&= \frac{1}{(\sigma_f^2+\sigma_g^2)^2}\left[\mu_f^2\sigma_f^2\sigma_g^2 + \mu_g^2\sigma_f^2\sigma_g^2 + \mu_f^2\sigma_g^4 + \mu_g^2\sigma_f^4\right. \\
&\qquad \left. - \mu_f^2\sigma_g^4 - \mu_g^2\sigma_f^4 - 2\mu_f\mu_g\sigma_f^2\sigma_g^2\right] \\
&= \frac{\sigma_f^2\sigma_g^2}{(\sigma_f^2+\sigma_g^2)^2}\left[\mu_f^2 - 2\mu_f\mu_g + \mu_g^2\right] = \frac{\sigma_f^2\sigma_g^2}{(\sigma_f^2+\sigma_g^2)^2}(\mu_f-\mu_g)^2
\end{aligned} \tag{C.6}
$$

$$\beta = \frac{(x^2 - 2\alpha x + \alpha^2) - \alpha^2 + \frac{\mu_f^2\sigma_g^2 + \mu_g^2\sigma_f^2}{\sigma_f^2+\sigma_g^2}}{2\frac{\sigma_f^2\sigma_g^2}{\sigma_f^2+\sigma_g^2}} = \frac{(x-\alpha)^2 + \frac{\sigma_f^2\sigma_g^2}{(\sigma_f^2+\sigma_g^2)^2}(\mu_f - \mu_g)^2}{2\frac{\sigma_f^2\sigma_g^2}{\sigma_f^2+\sigma_g^2}}$$
$$\text{Define : } \gamma^2 = \frac{\sigma_f^2\sigma_g^2}{\sigma_f^2+\sigma_g^2} \Rightarrow \beta = \frac{(x-\alpha)^2}{2\gamma^2} + \frac{(\mu_f-\mu_g)^2}{2(\sigma_f^2+\sigma_g^2)} \tag{C.7}$$

$$\begin{aligned}
f(x)g(x) &= \frac{1}{2\pi\sigma_f\sigma_g}e^{-\beta} = \frac{1}{2\pi\sigma_f\sigma_g}\exp\left[-\frac{(x-\alpha)^2}{2\gamma^2}\right]\exp\left[\frac{(\mu_f-\mu_g)^2}{2(\sigma_f^2+\sigma_g^2)}\right] \\
&= \frac{1}{\sigma_f\sigma_g}\gamma\sqrt{(\sigma_f^2+\sigma_g^2)} \times \frac{1}{\gamma\sqrt{2\pi}}\exp\left[-\frac{(x-\alpha)^2}{2\gamma^2}\right] \\
&\quad \times \frac{1}{\sqrt{(\sigma_f^2+\sigma_g^2)}\sqrt{2\pi}}\exp\left[\frac{(\mu_f-\mu_g)^2}{2(\sigma_f^2+\sigma_g^2)}\right] \\
\Rightarrow f(x)g(x) &= \frac{1}{\gamma\sqrt{2\pi}}\exp\left[-\frac{(x-\alpha)^2}{2\gamma^2}\right]S_{fg} \\
S_{fg} &= \frac{\gamma\sqrt{(\sigma_f^2+\sigma_g^2)}}{\sigma_f\sigma_g}\frac{1}{\sqrt{(\sigma_f^2+\sigma_g^2)}\sqrt{2\pi}}\exp\left[-\frac{(\mu_f-\mu_g)^2}{2(\sigma_f^2+\sigma_g^2)}\right] \\
&= \frac{1}{\sqrt{2\pi(\sigma_f^2+\sigma_g^2)}}\exp\left[-\frac{(\mu_f-\mu_g)^2}{2(\sigma_f^2+\sigma_g^2)}\right]
\end{aligned} \tag{C.8}$$

$$\begin{aligned}
\int_{-\infty}^{\infty} f(x)g(x)dx &= \frac{S_{fg}}{\gamma\sqrt{2\pi}}\int_{-\infty}^{\infty}\exp\left[-\frac{(x-\alpha)^2}{2\gamma^2}\right] = S_{fg} \\
&= \frac{1}{\sqrt{2\pi(\sigma_f^2+\sigma_g^2)}}\exp\left[-\frac{(\mu_f-\mu_g)^2}{2(\sigma_f^2+\sigma_g^2)}\right]
\end{aligned} \tag{C.9}$$

C.3 Univariate Gaussian with linear term in exponential

$$I = \int_{-\infty}^{\infty}\exp\left[-\frac{x^2}{2\sigma^2} + Jx\right] \tag{C.10}$$

Just as above, the idea is to complete the square

$$\begin{aligned}\frac{x^2}{2\sigma^2} - Jx &= \frac{1}{2\sigma^2}\left[x^2 - 2\sigma^2 Jx + (\sigma^2 J)^2 - (\sigma^2 J)^2\right] \\ &= \frac{1}{2\sigma^2}\left(x - \sigma^2 J\right)^2 - \frac{1}{2\sigma^2}(\sigma^2 J)^2 = \frac{\left(x - \sigma^2 J\right)^2}{2\sigma^2} - \frac{(\sigma J)^2}{2}\end{aligned} \tag{C.11}$$

Therefore, I find:

$$\begin{aligned}I &= \int_{-\infty}^{\infty} \exp\left[-\frac{x^2}{2\sigma^2} + Jx\right] = \int_{-\infty}^{\infty} \exp\left[\frac{\left(x - \sigma^2 J\right)^2}{2\sigma^2} - \frac{(\sigma J)^2}{2}\right] \\ &= \sigma\sqrt{2\pi}\exp\left[\frac{(\sigma J)^2}{2}\right]\end{aligned} \tag{C.12}$$

Appendix D: Derivations from Femtoscopy Formalism

Equation 4.31 from Sec. 4.2.5 is reproduced for convenience:

$$\begin{aligned}|\Psi|^2 = &\frac{j+1}{2(2j+1)}\left|\psi_{p_1p_2}(x_1,x_2)+(-1)^{2j}\psi_{p_2p_1}(x_1,x_2)\right|^2\\ &+\frac{j}{2(2j+1)}\left|\psi_{p_1p_2}(x_1,x_2)-(-1)^{2j}\psi_{p_2p_1}(x_1,x_2)\right|^2\end{aligned} \tag{D.1}$$

D.1 Non-interacting identical particles

$$\begin{aligned}\psi_{p_1p_2}(x_1,x_2) &= e^{ip_1\cdot x_1}e^{ip_2\cdot x_2} = e^{i\frac{P}{2}\cdot(x_1+x_2)}e^{ik\cdot r}\\ \psi_{p_2p_1}(x_1,x_2) &= e^{ip_2\cdot x_1}e^{ip_1\cdot x_2} = e^{i\frac{P}{2}\cdot(x_1+x_2)}e^{-ik\cdot r}\end{aligned} \tag{D.2}$$

Therefore, the modulus squared terms from Eq. D.1 are

$$\begin{aligned}&\left|\psi_{p_1p_2}(x_1,x_2)\pm(-1)^{2j}\psi_{p_2p_1}(x_1,x_2)\right|^2 =\\ &= \left(e^{i\frac{P}{2}\cdot(x_1+x_2)}e^{ik\cdot r}\pm(-1)^{2j}e^{i\frac{P}{2}\cdot(x_1+x_2)}e^{-ik\cdot r}\right)\\ &\quad\times\left(e^{-i\frac{P}{2}\cdot(x_1+x_2)}e^{-ik\cdot r}\pm(-1)^{2j}e^{-i\frac{P}{2}\cdot(x_1+x_2)}e^{ik\cdot r}\right)\\ &= 1+(-1)^{4j}\pm(-1)^{2j}e^{2ik\cdot r}\pm(-1)^{2j}e^{-2ik\cdot r}\\ &= 2\pm(-1)^{2j}e^{2ik\cdot r}\pm(-1)^{2j}e^{-2ik\cdot r}\\ &= 2\left[1\pm(-1)^{2j}\cos(2k\cdot r)\right]\end{aligned} \tag{D.3}$$

Inserting this result into Eq. D.1, I find

$$
\begin{aligned}
|\Psi|^2 &= \\
&= \quad \frac{j+1}{2(2j+1)} \left\{2\left[1+(-1)^{2j}\cos(2k\cdot r)\right]\right\} \\
&\quad + \frac{j}{2(2j+1)} \left\{2\left[1-(-1)^{2j}\cos(2k\cdot r)\right]\right\} \\
&= \frac{1}{2(2j+1)} \left\{2\left[1+(-1)^{2j}\cos(2k\cdot r)\right]\right\} + \frac{2j}{2j+1} \\
&= \frac{1}{2j+1}\left[1+(-1)^{2j}\cos(2k\cdot r)\right] + \frac{2j}{2j+1} \\
&= 1 + \frac{(-1)^{2j}}{2j+1}\cos(2k\cdot r) = 1 + g_0\cos(2k\cdot r)
\end{aligned}
\tag{D.4}
$$

where $g_0 = (-1)^{2j}/(2j+1)$.

Therefore, in the case of identical non-interacting spin-0 bosons, $g_0 = 1$, and we have

$$
|\Psi|^2 = 1 + \cos(2k\cdot r) \tag{D.5}
$$

D.2 Interacting identical particles

In this case, we have $\psi_{p_1p_2} \approx e^{-ik\cdot r} + \phi_{p_1p_2}(r)$, where $\phi_{p_1p_2}(r)$ is independent of the directions of the vectors $\boldsymbol{k}$ and $\boldsymbol{r}$ [135]. The modulus squared terms in Eq. D.1 become:

$$
\begin{aligned}
&\left|\psi_{p_1p_2} \pm (-1)^{2j}\psi_{p_2p_1}\right|^2 = \\
&= \quad \left[\left(e^{-ik\cdot r} + \phi_{p_1p_2}(r)\right) \pm (-1)^{2j}\left(e^{ik\cdot r} + \phi_{p_2p_1}(r)\right)\right] \\
&\quad \times \left[\left(e^{ik\cdot r} + \tilde{\phi}_{p_1p_2}(r)\right) \pm (-1)^{2j}\left(-e^{ik\cdot r} + \tilde{\phi}_{p_2p_1}(r)\right)\right] \\
&= \quad 2 \pm (-1)^{2j}\left[e^{2ik\cdot r} + e^{-2ik\cdot r}\right] + 2\left[1 \pm (-1)^{2j}\right]|\phi_{p_1p_2}(r)|^2 \\
&\quad + 2\left[1 \pm (-1)^{2j}\right]\Re[\phi_{p_1p_2}(r)]\left[e^{ik\cdot r} + e^{-ik\cdot r}\right] \\
&= 2\left\{1 \pm (-1)^{2j}\cos(2k\cdot r) + \left[1 \pm (-1)^{2j}\right]\left[|\phi_{p_1p_2}(r)|^2 + 2\Re[\phi_{p_1p_2}(r)]\cos(k\cdot r)\right]\right\}
\end{aligned}
\tag{D.6}
$$

Still assuming the final state interactions are independent of the spin state, for identical interacting particles, Eq. D.1 becomes:

$$
\begin{aligned}
|\Psi|^2 &= \frac{1}{2(2j+1)} \left|\psi_{p_1p_2}(x_1,x_2) + (-1)^{2j}\psi_{p_2p_1}(x_1,x_2)\right|^2 \\
&\quad + \frac{j}{2(2j+1)} \left|\psi_{p_1p_2}(x_1,x_2) + (-1)^{2j}\psi_{p_2p_1}(x_1,x_2)\right|^2 \\
&\quad + \frac{j}{2(2j+1)} \left|\psi_{p_1p_2}(x_1,x_2) - (-1)^{2j}\psi_{p_2p_1}(x_1,x_2)\right|^2 \\
&= \frac{1}{2j+1} \left[1 + (-1)^{2j}\cos(2k\cdot r) + \left[1+(-1)^{2j}\right]\left[|\phi_{p_1p_2}(r)|^2 + 2\Re[\phi_{p_1p_2}(r)]\cos(k\cdot r)\right]\right] \\
&\quad + \frac{2j}{2j+1}\left[1 + |\phi_{p_1p_2}(r)|^2 + 2\Re[\phi_{p_1p_2}(r)]\cos(k\cdot r)\right] \\
&= 1 + g_0\cos(2k\cdot r) + \left[\frac{1}{2j+1} + g_0 + \frac{2j}{2j+1}\right]\left[|\phi_{p_1p_2}(r)|^2 + 2\Re[\phi_{p_1p_2}(r)]\cos(k\cdot r)\right] \\
&= 1 + g_0\cos(2k\cdot r) + [1+g_0]\left[|\phi_{p_1p_2}(r)|^2 + 2\Re[\phi_{p_1p_2}(r)]\cos(k\cdot r)\right] \\
&= 1 + g_0\cos(2k\cdot r) + g_i\left[|\phi_{p_1p_2}(r)|^2 + 2\Re[\phi_{p_1p_2}(r)]\cos(k\cdot r)\right] \\
\Rightarrow |\Psi|^2 &= 1 + g_0\cos(2k\cdot r) + g_i\left\{|\phi_{p_1p_2}(r)|^2 + 2\Re[\phi_{p_1p_2}(r)]\cos(k\cdot r)\right\}
\end{aligned}
\tag{D.7}
$$

where, as before, $g_0 = (-1)^{2j}/(2j+1)$, and $g_i = 1 + g_0$.

D.3 Interacting non-identical particles

For the case of interacting non-identical particles, we need not worry about the symmetrization of the wave-function

$$
\begin{aligned}
|\Psi_{p_1p_2}|^2 &= \left[e^{-ik\cdot r} + \phi_{p_1p_2}(r)\right]\left[e^{ik\cdot r} + \tilde{\phi}_{p_1p_2}(r)\right] \\
&= 1 + |\phi_{p_1p_2}(r)|^2 + e^{ik\cdot r}\phi_{p_1p_2}(r) + e^{-ik\cdot r}\tilde{\phi}_{p_1p_2}(r) \\
&= 1 + |f(k^*)\Phi_{p_1p_2}(r)|^2 + e^{ik\cdot r}f(k^*)\Phi_{p_1p_2}(r) + e^{-ik\cdot r}\tilde{f}(k^*)\tilde{\Phi}_{p_1p_2}(r)
\end{aligned}
\tag{D.8}
$$

where $\tilde{f}(k^*)$ and $\tilde{\Phi}_{p_1p_2}(r)$ are the complex conjugates of $f(k^*)$ and $\Phi_{p_1p_2}(r)$.

To obtain an expression more closely resembling previous interacting identical results, we first rewrite the $e^{ik\cdot r}f\Phi + e^{-ik\cdot r}\tilde{f}\tilde{\Phi}$ term in the first line as:

$$
\begin{aligned}
& e^{ik\cdot r} f\Phi + e^{-ik\cdot r}\tilde{f}\tilde{\Phi} = \\
& = e^{ik\cdot r} f\Phi + e^{-ik\cdot r}\tilde{f}\tilde{\Phi} + \frac{1}{2}(e^{-ik\cdot r} f\Phi - e^{-ik\cdot r} f\Phi) + \frac{1}{2}(e^{ik\cdot r}\tilde{f}\tilde{\Phi} - e^{ik\cdot r}\tilde{f}\tilde{\Phi}) \\
& = \frac{1}{2}\left[(e^{ik\cdot r} + e^{-ik\cdot r})(f\Phi + \tilde{f}\tilde{\Phi})\right] + \frac{1}{2}\left[(e^{ik\cdot r} - e^{-ik\cdot r})(f\Phi - \tilde{f}\tilde{\Phi})\right] \\
& = 2\Re[f\Phi]\cos(k\cdot r) - 2\Im[f\Phi]\sin(k\cdot r)
\end{aligned}
\tag{D.9}
$$

Then, it immediately follows that:

$$
\begin{aligned}
|\Psi_{p_1p_2}|^2 &= 1 + |f(k^*)\Phi_{p_1p_2}|^2 + e^{ik\cdot r} f(k^*)\Phi_{p_1p_2} + e^{-ik\cdot r}\tilde{f}(k^*)\tilde{\Phi}_{p_1p_2} \\
&= 1 + |f(k^*)\Phi_{p_1p_2}|^2 + 2\Re[f(k^*)\Phi_{p_1p_2}]\cos(k\cdot r) - 2\Im[f(k^*)\Phi_{p_1p_2}]\sin(k\cdot r)
\end{aligned}
\tag{D.10}
$$

D.4 Interacting identical particles (spin dependent)

If we allow the interaction, and therefore the two-particle wave-function, to depend on the total spin S of the system (but not on the spin projections), things change slightly. Instead of grouping all odd and even spins together, we need to keep track of their individual contributions, as their wave-functions will be different. Therefore, instead of Eq. D.6, we should consider

$$
\begin{aligned}
& \left|\psi^S_{p_1p_2} \pm \psi^S_{p_2p_1}\right|^2 = \\
& \quad = \quad \left[\left(e^{-ik\cdot r} + \phi^S_{p_1p_2}(r)\right) \pm \left(e^{ik\cdot r} + \phi^S_{p_2p_1}(r)\right)\right] \\
& \qquad \times \left[\left(e^{ik\cdot r} + \tilde{\phi}^S_{p_1p_2}(r)\right) \pm \left(e^{-ik\cdot r} + \tilde{\phi}^S_{p_2p_1}(r)\right)\right] \\
& \quad = 2\left\{1 \pm \cos(2k\cdot r) + [1\pm 1]\left[|\phi^S_{p_1p_2}(r)|^2 + 2\Re[\phi^S_{p_1p_2}(r)]\cos(k\cdot r)\right]\right\}
\end{aligned}
\tag{D.11}
$$

From Eq. 4.30, we see that for even spin states, which for both fermions and bosons are accompanied by symmetric spatial wave-functions (i.e. $\pm \to +$), the contribution to the total is

$$
\left|\psi^S_{p_1p_2} + \psi^S_{p_2p_1}\right|^2 \propto 2\left\{1 + \cos(2k\cdot r) + 2\left[|\phi^S_{p_1p_2}(r)|^2 + 2\Re[\phi^S_{p_1p_2}(r)]\cos(k\cdot r)\right]\right\}
\tag{D.12}
$$

Similarly, for odd spin states, which for both fermions and bosons are accompanied by antisymmetric spatial wave-functions (i.e. $\pm \to -$), the contribution to the total is

$$\left|\psi^S_{p_1p_2} - \psi^S_{p_2p_1}\right|^2 \propto 2\left\{1 - \cos(2k \cdot r)\right\} \tag{D.13}$$

When combining all of the various states with different spin S, they must be combined with a weight factor ρ_S, the normalized emission probability for such a state ($\sum_S \rho_s = 1$). Now, the modulus squared of the total wave-function, combining contributions from all spin states, will be

$$\begin{aligned}
|\Psi|^2 &= \frac{1}{2}\sum_{S=\text{even}} 2\rho_S \left\{1 + \cos(2k\cdot r) + 2\left[|\phi^S_{p_1p_2}(r)|^2 + 2\Re[\phi^S_{p_1p_2}(r)]\cos(k\cdot r)\right]\right\} \\
&\quad + \frac{1}{2}\sum_{S=\text{odd}} 2\rho_S\left\{1 - \cos(2k\cdot r)\right\} \\
&= \sum_S \rho_S + \left(\sum_{S=\text{even}} \rho_S - \sum_{S=\text{odd}} \rho_S\right)\cos(2k\cdot r) \\
&\quad + 2\sum_{S=\text{even}} \rho_S\left\{|\phi^S_{p_1p_2}(r)|^2 + 2\Re[\phi^S_{p_1p_2}(r)]\cos(k\cdot r)\right\} \\
&= 1 + \left(\sum_{S=\text{even}} \rho_S - \sum_{S=\text{odd}} \rho_S\right)\cos(2k\cdot r) \\
&\quad + 2\sum_{S=\text{even}} \rho_S\left\{|\phi^S_{p_1p_2}(r)|^2 + 2\Re[\phi^S_{p_1p_2}(r)]\cos(k\cdot r)\right\} \\
&= 1 + g'_0\cos(2k\cdot r) + 2\sum_{S=\text{even}} \rho_S\left\{|\phi^S_{p_1p_2}(r)|^2 + 2\Re[\phi^S_{p_1p_2}(r)]\cos(k\cdot r)\right\}
\end{aligned} \tag{D.14}$$

where $g'_0 = \sum_{S=\text{even}} \rho_S - \sum_{S=\text{odd}} \rho_S$. In the case of unpolarized emission for identical particle pairs, $\rho_S = (2S+1)/(2j+1)^2$, and we have $g'_0 = g_0 = (-1)^{2j}/(2j+1)$.